

PHYSIK-DEPARTMENT



Precision Tracking and Electromagnetic Calorimetry
Towards a Measurement of the
Pion Polarisabilities at COMPASS

Dissertation

von

Anna-Maria Elisabeth Dinkelbach



TECHNISCHE UNIVERSITÄT
MÜNCHEN

TECHNISCHE UNIVERSITÄT MÜNCHEN
Physik Department E18

Precision Tracking and Electromagnetic Calorimetry
Towards a Measurement of the
Pion Polarisabilities at COMPASS

Anna-Maria Elisabeth Dinkelbach

Vollständiger Abdruck der von der Fakultät für Physik der Technischen Universität München zur Erlangung des akademischen Grades eines

Doktors der Naturwissenschaften (Dr. rer. nat.)

genehmigten Dissertation.

Vorsitzende: Univ.-Prof. Dr. Nora Brambilla

Prüfer der Dissertation:

1. Univ.-Prof. Dr. Stephan Paul
2. Jun.-Prof. Dr. Laura Fabbietti

Die Dissertation wurde am 23.06.2010 bei der Technischen Universität München eingereicht und durch die Fakultät für Physik am 20.07.2010 angenommen.

Abstract

In 2004 the COMPASS experiment at CERN SPS measured soft reactions with a beam of negatively charged pions on various nuclear targets. For this measurement, a silicon micro-strip telescope was installed in the target region. For the first time 5 silicon detector stations were operated simultaneously in the COMPASS experiment. A novel method of time calibration, with a clustering algorithm accordingly adapted, and refined alignment corrections were implemented in the analysis software. The spatial resolution of a silicon detector was determined to be 5 – 14 μm and the time resolution 2 – 3 ns. Combining the time information of all stations, a track time resolution of 530 ps from the silicon telescope could be reached.

One of the key points of this experiment was the observation of Primakoff events, namely pions scattering off quasi-real photons in the Coulomb field of a heavy nucleus. The production of real photons corresponds to pion Compton scattering in inverse kinematics which is sensitive to the pion polarisabilities α_π and β_π . Key ingredient for such measurements is a precise knowledge of the performance of the electromagnetic calorimeter. This includes a study of the instabilities of calorimeter cells and an improved reconstruction algorithm. A data-driven shower model was developed, which was used for a time-dependent recalibration of the calorimeter. A new cluster refitting method was used to recover position and energy of clusters containing passive or saturated cells and detects double-hit clusters. The latter are important, as the main background to the Primakoff Compton events stems from neutral pions misinterpreted as single-photon hits.

The physics analysis comprised the selection of Primakoff events and the necessary steps to obtain the pionic polarisabilities. The measurement was limited by systematic effects of the apparatus also determined within this thesis.

Kurzfassung

Am COMPASS Experiment am CERN SPS wurden im Jahr 2004 weiche Streureaktionen mit negativ geladenen Pionen einer Energie von 190 GeV an verschiedenen Targetmaterialien gemessen. Für diese Messung wurde ein Siliziummikrostreifenteleskop im Bereich des Targets installiert. Erstmals kamen dabei fünf Siliziumstationen gleichzeitig zum Einsatz. In der Analysesoftware wurde ein Clusteralgorithmus, basierend auf einer neuen Methode zur Zeitkalibrierung, sowie Korrekturen zur Ausrichtung der Siliziumdetektoren, implementiert. Die Ortsauflösung der Siliziumdetektoren liegt abhängig von der Anzahl getroffener Streifen im Bereich 5 – 14 μm und die Zeitauflösung bei 2 - 3 ns. Kombiniert man die Zeitinformationen aller Siliziumstationen, wird für die Teilchenspur im Siliziumteleskop eine Zeitauflösung von 530 ps erreicht. Im Fokus des Experiments stand die Beobachtung von sogenannten Primakoff-Ereignissen. Dabei streut ein Pion an einem quasi-reellen Photon des Coulombfelds eines schweren Nukleons. Wird bei diesem Streuprozess ein reelles Photon erzeugt, so entspricht dieser Prozess der Comptonstreuung in inverser Kinematik, und es können die elektromagnetischen Polarisierbarkeiten α_π und β_π des Pions untersucht werden. Um Primakoff-Ereignisse beobachten zu können, muss das Verhalten des elektromagnetischen Kalorimeters, in welchem diese nachgewiesen werden, sehr gut bekannt sein. Daher wurde die Stabilität der Kalorimeterblöcke im Einzelnen untersucht. Um diese Kalorimeterblöcke (zeitabhängig) neu zu kalibrieren, wurde ein auf experimentellen Daten basierendes Schauermodell entwickelt. Aus diesem Schauermodell wurde eine Fitmethode abgeleitet, welche die Position und Energie eines Schauers wieder herstellen kann, auch wenn dabei passive oder instabile Kalorimeterblöcke getroffen wurden. Die Fitmethode ist sensitiv auf die Form des Schauers, z.B. wenn zwei hochenergetische Photonen des neutralen Pionzerfalls fälschlicherweise als ein zusammenhängender Schauer identifiziert wurden. Diese Eigenschaft des Fits ist nützlich, da der Untergrund bei Primakoffereignissen hauptsächlich von neutralen Pionen stammt. Für den hier betrachteten Physikkanal wird die beobachtete Statistik diskutiert sowie Gründe, weshalb die Polarisierbarkeiten aus der Messung in 2004 nicht extrahiert werden konnten.

Summary

The COMPASS experiment is a fixed target experiment at the CERN SPS. In a pilot run in 2004 with incoming pion beam, soft reactions with a beam of negatively charged pions on various nuclear targets were studied. One aim of this experiment was the measurement of the electric α_π and the magnetic β_π pion polarisabilities. In order to study the response of an unstable particle to an external electromagnetic field, COMPASS exploited the *Primakoff effect*, where ultra-relativistic charged pions scatter off the Coulomb field of a nucleus thereby emitting a hard photon. Deviations of the measured cross section from that expected for a point-like particle gives the pion polarisabilities α_π and β_π . From theory like Chiral Perturbation Theory (ChPT) we expect structural effects resulting in values for the polarisabilities $(\alpha - \beta)_\pi = (5.7 \pm 1.0) \cdot 10^{-4} \text{fm}^3$. Measurements by various experiments using different physics reactions give no conclusive answer and range between $(\alpha - \beta)_\pi = (15.6 \pm 6.4 \pm 4.4) \cdot 10^{-4} \text{fm}^3$ and $(\alpha - \beta)_\pi = (4.4 \pm 3.2) \cdot 10^{-4} \text{fm}^3$. This work covers many experimental aspects involved in precision measurement of the electromagnetic polarisabilities of the charged pion.

Silicon micro-strip detectors are one of the key detector elements for this measurement. They are used in COMPASS for the definition of the incoming beam and for the reconstruction of particles emerging from the target, since they have excellent time and spatial resolution. For the measurement of the pion polarisabilities α_π and β_π , a telescope of silicon micro-strip detectors was installed in the target region. Ten silicon micro-strip detectors were operated simultaneously in the COMPASS experiment for the first time. An alignment of the silicon telescope was performed and the realisation of a simple vertexing algorithm in the online monitoring programme leads to a very fast characterisation of the target region during the pion beam in 2004. As a result, the experimental setup could be optimised for the desired measurement programme, aiming at the reactions with extremely small scattering angles.

From the analysis of electronic signals generated by charged particles traversing the silicon micro-strip detector, time and corresponding precision can be reconstructed. An analytical function was found relating the electronic signals to the signal time of the charged particle traversing the detector. The parameters of this function have to be determined using a novel method of time calibration. The spatial resolution of a silicon detector was determined to be 5 – 14 μm depending on the number of strips hit and the time resolution was 2–3 ns. Combining the time information of the stations, a track time resolution of 530 ps from the silicon telescope could be reached.

The precise study of the Primakoff reaction requires excellent reconstruction of the emerging photon. Reliable efficiency and good energy reconstruction are a prerequisite for a reliable analysis. An electromagnetic calorimeter placed far downstream from the target is used for this task. In course of the data analysis, it became clear that a detailed understanding of the calorimeter required dedicated work. At first, stabilities of the individual calorimeter cells (blocks of lead glass) were studied. In the region of the electromagnetic calorimeter most important for events resulting from Primakoff reactions, several cells (about 10%) were passive and showed instabilities, respectively. The electromagnetic calorimeter is optimised to measure the electromagnetic shower component (total energy) of impinging particles, e.g. electrons. Such a shower is distributed over several cells in the calorimeter. The energy deposited per cell is related to the measured electronic signal via a proportionality constant. These constants (unique for each cell) were determined by a calibration with electrons of known energies once only for the pilot run in 2004. In order to get a measure about the stability of these constants over time (in scales of hours), a method was developed to recalibrate the cells of the electromagnetic calorimeter. For this purpose, electrons and positrons of background reactions like photon conversion $\gamma \rightarrow e^+e^-$ were proven to be useful. This new method is based on a data-driven model generated from the observed response of the calorimeter to electrons. This data-driven model is used by a fit on the electromagnetic shower in order to derive the energy and position of the impinging particle. In the region of unstable cells, the fit enhances the resolution in energy and position of clusters containing passive or unstable cells. Yet, the resolution is not sufficient to fully recover the events for the desired physics analysis. Due to the underlying data-driven shower model, the cluster fit is sensitive to background of neutral pions, originating from two photons with high energies misidentified as one shower. This is important since the main background to the Primakoff Compton events stems from neutral pions misinterpreted as single-photon hits.

In the last section of this thesis a detailed study is presented, showing the path from the event identification towards the extraction of physics quantities α_π and β_π . Also systematic effects present in the COMPASS spectrometer in 2004 and their effects on the analysis are shown. They comprise geometrical constraints, performance problems of the electromagnetic calorimeter, detector materials and a trigger inefficiency. These systematic effects lead to distortions of the observed differential $\pi\gamma$ count rates from which the pion polarisabilities α_π and β_π have to be extracted. The distortions were too severe to be simulated precise enough and thus no reliable values for α_π and β_π could be determined.

In 2009 a new Primakoff measurement was performed which took more emphasise on the stability of the spectrometer. The measurement of the pion polarisabilities is an important ingredient for the understanding of QCD at low energies. A full beam time will be dedicated to the measurement of the pion polarisabilities at COMPASS in 2012 in order to clarify the presently inconsistent picture of the experimental results obtained so far.

Contents

1	Introduction	1
2	The COMPASS Experiment	3
2.1	The COMPASS Physics Program	3
2.1.1	Physics with Hadron Beam	3
2.1.2	Physics with Muon Beam	4
2.2	The Experimental Setup	6
2.2.1	The Different Spectrometer Regions	7
2.2.2	The COMPASS Detector Components	7
2.2.3	Beam Requirements	11
2.2.4	The 2004 Hadron Setup	12
2.2.5	The Specific Components of the Muon Setup	15
2.3	Data Processing and Analysis Software	16
2.3.1	Online Filter	16
2.3.2	The ROOT Analysis Framework	17
2.3.3	Online Monitoring with COOOL	17
2.3.4	COMgeant- the Monte Carlo Setup	17
2.3.5	CORAL - Reconstruction Software	18
2.3.6	Data Analysis with PHAST	19
3	The COMPASS Silicon Micro-Strip Detector	21
3.1	The Basic Principle	21
3.2	The COMPASS Silicon Detector Setup	22
3.2.1	System Requirements	22
3.2.2	The Wafer Design	22
3.2.3	The Detector Module	23
3.2.4	Electronics and Readout Chain	25
3.2.5	The Silicon Detector Station	27
3.2.6	The Detector Station in COMPASS	27

CONTENTS

3.3	Cryogenic Development - an Outlook	32
4	Characterisation of the COMPASS Silicon Detector	33
4.1	Detector Signal	33
4.2	Time Reconstruction	35
4.3	Determination of the Signal Shape from the Data	37
4.4	Time Calibration	41
4.5	Clustering	46
4.5.1	Cluster Finding	47
4.5.2	Determination of Cluster Position	51
4.6	Results	54
4.6.1	Time Resolution	54
4.6.2	Spatial Resolution	55
4.7	Summary	62
5	Silicon Detectors in Hadron Run 2004	63
5.1	Operation	63
5.2	Alignment for Hadron Run	66
5.3	Trending of Silicon Time	69
5.4	Performance Test with COOL	70
5.5	Summary	72
6	Calibration of the Electromagnetic Calorimeter	73
6.1	Motivation	73
6.2	Operation Principle of an Electromagnetic Calorimeter	74
6.3	The COMPASS Electromagnetic Calorimeter	76
6.3.1	The Detector Setup	76
6.3.2	A Glimpse on the Shower Reconstruction	77
6.4	Calibration Method	78
6.4.1	Event Selection	79
6.4.2	Shower Model	80
6.4.3	Calibration Values from Application of the Shower Model	93
6.4.4	LED Analysis	95
6.5	Cluster Fit	100
6.6	Checking the Calibration	104
6.6.1	Electron Track Analysis	104
6.6.2	Primakoff Compton Analysis	114
6.7	Performance of ECAL2 in Hadron Run 2004	122

6.7.1	Problematic Cells	122
6.7.2	Energy and Spatial Resolution	122
6.8	Summary and Conclusion	129
7	Compton Scattering and Pion Polarisability	131
7.1	Motivation and Cross Section	131
7.2	Effect of Pion Polarisabilities	136
7.3	Radiative Corrections	138
8	Data Analysis	139
8.1	Event Selection	139
8.2	Background Reactions	144
8.3	Simulation and Acceptance	145
8.3.1	He-Gas Pipe of the RICH	147
8.3.2	Trigger Efficiency	152
8.4	Discussion	152
8.5	Conclusion	158
A	Coordinate Systems	161
B	Hadron Run 2004	163
B.1	History of Hadron Run 2004	163
C	Silicon Detectors in COMPASS	167
D	Silicon Detector Analysis - Technical Information	171
D.1	Calibrations with COOL	171
D.1.1	Alignment	173
D.1.2	Time Calibration	174
D.2	Silicon Detectors in CORAL	174
D.2.1	New Silicon CORAL Options	175
D.2.2	CORAL Configurations for Silicon Data Analysis	175
E	ECAL2 in COMPASS	179
E.1	ECAL2 Mapping	179
E.2	Technical Information for ECAL2 Calibration	180
E.2.1	Functions for Generating Energy Ratio Distributions	180
E.2.2	Functions for Generating the Calibration Parameters	182
E.2.3	Run Lists	182
E.2.4	Description of the Cluster Refit	184

CONTENTS

E.3 Various Distributions of the Electron Analysis 185

F Primakoff Statistics 191

List of Figures 193

List of Tables 197

Bibliography 199

Chapter 1

Introduction

This work covers the many experimental aspects of the challenging precision measurement of the electromagnetic polarisabilities of the charged pion with the COMPASS experiment at CERN. In order to measure the electric α_π and the magnetic β_π pion polarisabilities, the COMPASS experiment exploits the *Primakoff effect*, where ultra-relativistic charged pions scatter off the Coulomb field of a nuclei by emitting a hard photon. Chiral Perturbation Theory (χ PT) predicts a significant contribution of the polarisabilities α_π and β_π , but compared with the results of various experiments, there is no coherent picture of the pion polarisabilities yet.

The COMPASS experiment is a fixed target experiment at CERN SPS. Chapter 2 gives a brief overview over the different physics topics which are of interest to the COMPASS collaboration. This chapter also introduces the reader to the spectrometer setup with its detector components. Since COMPASS measures with both, muon and hadron beams, the difference concerning the spectrometer setup is emphasized. The specific hadron setup will be described in more detail, because the pion polarisability measurement is performed with a pion beam. A first data set was taken in a pilot hadron run in 2004.

The silicon micro-strip detectors are one of the key detectors in this measurement. Silicon micro-strip detectors are used in COMPASS for beam definition, and during the hadron pilot run also for track reconstruction downstream the target, since they have excellent time and spatial resolution. Chapter 3 gives an introduction to the specific COMPASS silicon micro-strip detector. The signal time reconstruction of the silicon detectors, the time calibration as well as the clustering algorithm are explained in chapter 4. The results on the time and spatial resolution of the detectors are presented at the end of this chapter. The performance in the run 2004 is discussed in chapter 5. Therein the focus is on the alignment procedure of the silicon telescope and fast analysis with the COMPASS online monitoring program.

Another important detector for the analysis of the pion polarisabilities is the electromagnetic calorimeter, where the photon produced in the Primakoff reaction is detected. While analysing the hadron data, it turned out, that a detailed understanding of the perfor-

1 INTRODUCTION

mance of the electromagnetic calorimeter is necessary. In chapter 6, the COMPASS electromagnetic calorimetry is briefly discussed. A new time dependent calibration method for the calorimeter cells, a new cluster fit procedure as well as the performance of the detector in the 2004 pilot hadron run are described in detail.

A short overview about the experimental and theoretical aspects of the Primakoff-reaction and pion polarisabilities are given in chapter 7 followed by the analysis of the data set of the 2004 hadron pilot run in chapter 8. There, the selection criteria are explained, that are applied to the data set. This chapter also points out the experimental limits for analysing the pion polarisabilities α_π and β_π .

Chapter 2

The COMPASS Experiment

COMPASS (COmmon MUon and Proton Apparatus for Structure and Spectroscopy) is a high luminosity fixed target experiment at the CERN SPS [COM96]. Various very different physics questions can be studied either with hadron or polarised muon beams. This chapter gives a glimpse at the diverse physics topics for the hadron and muon program. The second part describes the spectrometer layout and goes into the specific spectrometer details for the two different programs but with a higher emphasis on the hadron program, since the physics analysis of this thesis deals with a topic of the hadron program. The chapter closes with an overview on the specific analysis software of COMPASS.

2.1 The COMPASS Physics Program

2.1.1 Physics with Hadron Beam

2.1.1.1 Primakoff Reaction

Chiral perturbation theory (χ PT) is established in describing many strong interaction systems at low energies as e.g. pion-pion scattering lengths. It makes definite predictions for measurable quantities like the electromagnetic polarisabilities of the pion and the kaon, as well as for the chiral axial anomaly amplitudes. Such processes can be studied with the Primakoff reaction. In the Coulomb field of high Z -nuclei, pions scatter inelastically by the reactions $\pi + \gamma^* \rightarrow \pi' + \gamma$ and $\pi + \gamma^* \rightarrow \pi' + \pi^0$ which provide access to the polarisabilities and axial anomaly amplitudes respectively. In chapter 7 and 8 the Primakoff reaction and the measurement by COMPASS are discussed in detail.

2.1.1.2 Exotic States

In the picture of the constituent quark model, many observations are consistent with mesons being $q\bar{q}$ states and baryons being qqq states. Within the theory of QCD, the pic-

ture is much more multi-faceted of possible states, and in addition there are experimental evidences for new states.

Gluons carry colour charge by themselves and therefore should be able to form bound states among each other, so called *glueballs*. The lowest glueball mass is predicted by Lattice QCD to be a $J^{PC} = 0^{++}$ state with a width of 100-150 MeV/ c^2 in an estimated mass range of 1500 to 1800 MeV/ c^2 . The glueballs can be identified by their production characteristics, decay patterns and the relation to other mesons which carry the same parity and spin.

QCD also includes the existence of *hybrids* ($qg\bar{q}$) which are $q\bar{q}$ systems coupled to excitations of the gluonic string, that binds the quark and antiquark. They can be seen in the observation of excited states with not allowed quantum numbers for $q\bar{q}$ systems for the three light flavours. The lowest predicted hybrid has quantum numbers $J^{PC} = 1^{+-}$, 0^{-+} and 1^{--} at a mass of approximately 1.9 GeV/ c^2 .

Even more exotic states like *tetraquarks* ($qq\bar{q}\bar{q}$) and meson-meson molecules are under discussion which also acquire exotic quantum numbers. For both, hybrids and glueballs, it is important to come to know the complete information of all neighbouring states. Therefore it is necessary to reconstruct the final states of both neutral and charged particles, to observe the same meson resonance in several different channels, and to produce the exotic resonances via different reactions. With COMPASS it is possible to study charged exotic states by diffractive scattering, e.g. $\pi^- p \rightarrow X^- p$ and $K^- p \rightarrow X^- p$ or neutral states via the central production mechanism $\pi^- p \rightarrow \pi^- X^0 p_s$ and photo-production of neutral $\mu^- p \rightarrow \mu^- X^0 p$.

2.1.1.3 Charmed Baryons

Very little is known about masses, life time and decay width of baryons containing two charm quarks, so called *doubly charmed baryons*. They are interesting due to the high mass of the charm quark of 1.15 to 1.35 GeV/ c^2 , and such states should be well described by perturbative QCD. The radius of doubly charmed baryons may be large, if it is dominated by the light quark orbiting the tightly bound cc-pair. Constraints on models of quark-quark forces can be found by studying such configurations and by their weak decay.

2.1.2 Physics with Muon Beam

2.1.2.1 Gluon Polarisation

For the last twenty years, it has been an important topic in deep inelastic scattering (DIS) to investigate the decomposition of the nucleon spin in terms of contributions from its constituents. In the quark-parton model, the total spin of the nucleon is calculated from

the following components (in units of \hbar):

$$(2.1) \quad \frac{1}{2} = \frac{1}{2} \Delta\Sigma + \Delta G + L_q + L_G ,$$

with $\Delta\Sigma$ the sum of the spin contents of the quark and anti-quarks, ΔG the gluon spin contribution and $L_{q,G}$ the orbital angular momentum of the quarks and the gluons. At first the EMC (European Muon Collaboration), the preceding experiment of COMPASS and various other experiments observed, that only a small fraction of the nucleon spin in the order of 20% to 30% percent is carried by the quarks which is in contrast to the 60% expected by the quark-parton model — the famous spin riddle. Some missing contribution to the nucleon spin was expected to be ΔG originating from the spin of the gluons. Its determination was one of the main goals to set up COMPASS.

In polarised semi-inclusive DIS, the polarisation $\Delta G/G$ of gluons carrying a fraction x_g of the nucleon momentum is obtained from the cross-section helicity asymmetries of the photon-gluon fusion (PGF) $\gamma^* g \rightarrow q\bar{q}$. The PGF is a second order process, and the photon interacts with the gluon via an intermediate quark line. It is selected via the final state and in COMPASS the following processes are studied.

Open charm: The production of heavy quark pairs via PGF, like $c\bar{c}$ -pairs, are dominant in leading order. One of the charm quarks fragments into a D meson which is reconstructed using the invariant mass of the D -decay. The gluon polarisation $\Delta G/G$ are accessed via the cross-section asymmetry for different spin orientations of the photon and the nucleon of this process. The statistic is limited by the small cross-section and a significant background contribution. The COMPASS result is $\Delta G/G = -0.49 \pm 0.27$ (stat) ± 0.11 (sys) at a scale of $\mu^2 \approx 13$ (GeV/c)² and at an average gluon momentum fraction $\langle x \rangle \approx 0.11$ [COM09c] which supersedes the result of [COM08a].

High- p_T : Another access to $\Delta G/G$ is to select events with two hadrons at high transverse momentum p_T . This procedure has large statistics but a significant fraction of background events, which have to be estimated by simulations. COMPASS determined the gluon polarisation: $\Delta G/G = 0.024 \pm 0.089$ (stat) ± 0.057 (syst) at $x_g = 0.095$ (momentum fraction carried by the gluon) and $\mu^2 \approx 3$ (GeV/c)² [COM06].

2.1.2.2 Longitudinal Spin Structure Function

Semi-inclusive measurements of deep inelastic scattering (DIS) of polarised leptons on longitudinal polarised deuteron targets make it possible to study the deuteron longitudinal spin asymmetry A_1^d and the deuteron spin-dependent structure function g_1^d [COM05b], [COM07d]. With a precise measurement of g_1^d it is possible to evaluate the fraction of the nucleon spin carried by the quarks $\Delta\Sigma = 0.33 \pm 0.03$ (stat) ± 0.05 (sys) [COM07b]. COMPASS also determined the polarised valence quark distributions [COM08b] and flavour separated helicity distributions [COM09b].

2.1.2.3 Transverse Spin Asymmetries

The Collins and Sivers mechanisms can be extracted and disentangled from the measurement of single-spin asymmetries in cross-sections for semi-inclusive DIS of leptons on transversely polarised nucleons (in respect of the beam polarisation) by detecting the hadron with the highest momentum originating from the extraction vertex. COMPASS measured the Collins and Sivers asymmetries for charged pions, charged kaons and neutral kaons on a transversely polarised deuteron target. All asymmetries are small, but compatible with zero within the statistical errors, see [COM05a], [COM07c] and [COM09a]. The results of Collins and Sivers asymmetry on a transversely polarised proton target are not yet published.

2.1.2.4 Λ and $\bar{\Lambda}$ Polarisation

Information on the polarisation of strange quarks and/or antiquarks can be retrieved by measuring the longitudinal polarisation of Λ and $\bar{\Lambda}$ baryons. With the semi-inclusive reaction $\mu^+ N^+ \rightarrow \mu' \Lambda^+ X$ the spin transfer from the longitudinally polarised target nucleon (with respect to the beam polarisation) to the final state hyperon can be studied. The spin transfer coefficient of the longitudinal spin transfer to Λ is small with $D_{LL}^{\Lambda} = -0.012 \pm 0.047 \pm 0.024$ at $x_F = 0.22$ (the Feynman variable) and is larger to $\bar{\Lambda}$ with $D_{LL}^{\bar{\Lambda}} = 0.249 \pm 0.056 \pm 0.049$ at $x_F = 0.20$. These COMPASS results are conformable with previous measurements, but with a much better statistical precision [COM09d].

In the simplest process of unpolarised inclusive hyperon production $\mu N \rightarrow \mu' H X$, the polarisation of the hyperon does not depend on the spin states of the beam or the target particle. Due to the spin conservation in strong and electromagnetic interactions, the polarisation is directed normal to the production plane spanned by the incoming beam and outgoing hyperon which is referred as *transverse* polarisation. It is related to properties of the hadronisation process and has still open questions. The present measurements of Λ and Ξ hyperons with COMPASS data can be found in [Wie04] and [Gru06].

2.2 The Experimental Setup

COMPASS is a fixed target experiment and its challenging physics goals require large luminosity and high statistics. In order to achieve high luminosity, the COMPASS setup has to have high data rate capability, particle identification and a wide angular and momentum acceptance. Also the precise kinematic reconstruction of events is necessary as well as a good mass resolution. The high statistics is achieved with beam rates in the order of 10^8 particles per SPS cycle¹ and trigger rates up to 100 kHz (design goal). High precision can be reached with the two stage spectrometer. In 2001 the spectrometer was prepared to be commissioned, and physics data with a muon beam were taken in 2002, 2003 and

¹A SPS cycle consists of a 4.8 s long spill where protons are extracted within a period of 16.8 s.

2004. In 2004 the COMPASS setup was prepared for the first time for a three weeks period of collecting data with a 190 GeV pion beam which was dedicated for measuring the pion polarisability via the Primakoff reaction. After the CERN accelerator shutdown in 2005, COMPASS continued in 2006 with collecting data.

Since COMPASS is designed for two different physics programs, some elements of the spectrometer are specific for the hadron and the muon programs which will be described separately in subsection 2.2.4 and subsection 2.2.5. If no other literature is cited all information and numbers concerning the spectrometer and its components are taken from [COM07a].

2.2.1 The Different Spectrometer Regions

The layout of the spectrometer can be divided into three regions. The region upstream of the target, followed by the Large Angle Spectrometer (LAS) and the Small Angle Spectrometer (SAS).

In the region upstream and around the target, a telescope of fast and high resolution detectors is located for precise track reconstruction. It is equipped with veto detectors to separate the beam from the beam-halo and to define the beam spot-size. Due to the different targets and tracking requirements this region differs most between the two spectrometer setups of the muon and the hadron program, see Fig. 2.1 and Fig. 2.2.

The LAS which is close to the target, covers a momentum range of about 1 - 20 GeV. In order to cover 180 mrad polar acceptance, the LAS has a dipole magnet named SM1 with a field integral of 1.0 Tm. The magnet is sandwiched by a telescope of tracking detectors. SM1 is followed by a Ring Imaging Cherenkov detector (RICH) to identify charged hadrons with momenta of a few ten GeV/c. After the RICH a hadron calorimeter HCAL1 is located, with a central hole matching the acceptance of the second spectrometer. The LAS ends with a filter to identify muons (Muon-Filter 1).

The SAS detects particles with small angles (± 30 mrad) and momenta higher than 5 GeV/c. The 4 m dipole magnet SM2, with a field integral of 4.4 Tm is located just behind the LAS. The SM2 is also surrounded by tracking detectors. In the SAS an electron calorimeter ECAL2 for photon and electron detection is located just before the hadron calorimeter HCAL2. At the end of the SAS a second muon filter (Muon-Filter2) is placed.

2.2.2 The COMPASS Detector Components

2.2.2.1 The Tracking Detectors

In COMPASS, a variety of different tracking detector types are installed to cover the overall spectrometer acceptance. Especially for detectors close to the beam, a high particle rate capability, excellent space resolution and a minimal amount of material is required. Some

2 THE COMPASS EXPERIMENT

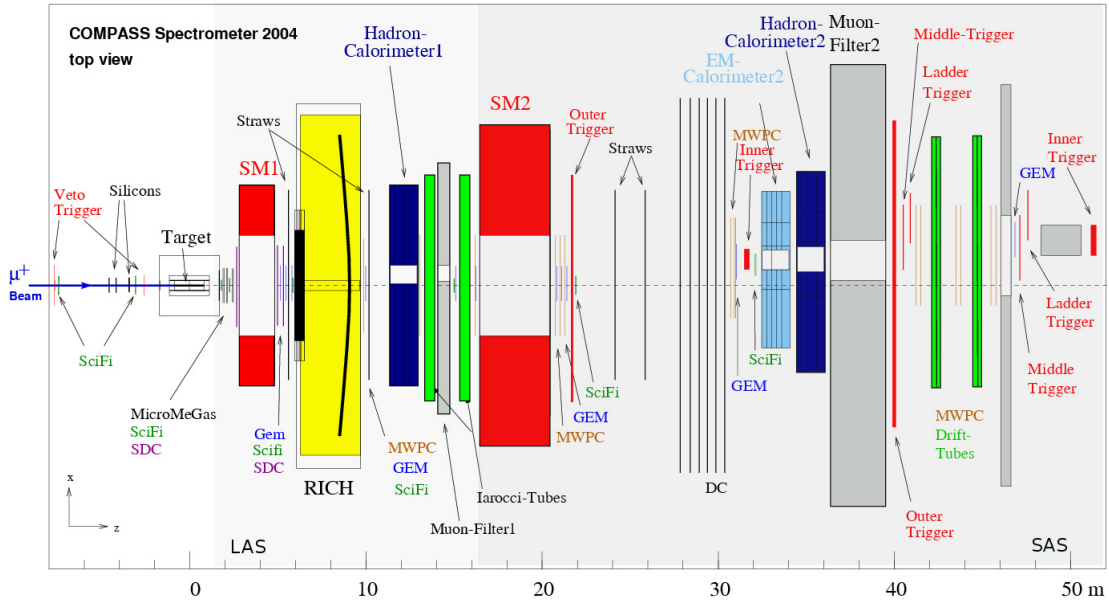


Figure 2.1: A sketch of the COMPASS muon spectrometer setup 2004 from the top, the figure is not to scale along the x-axis.

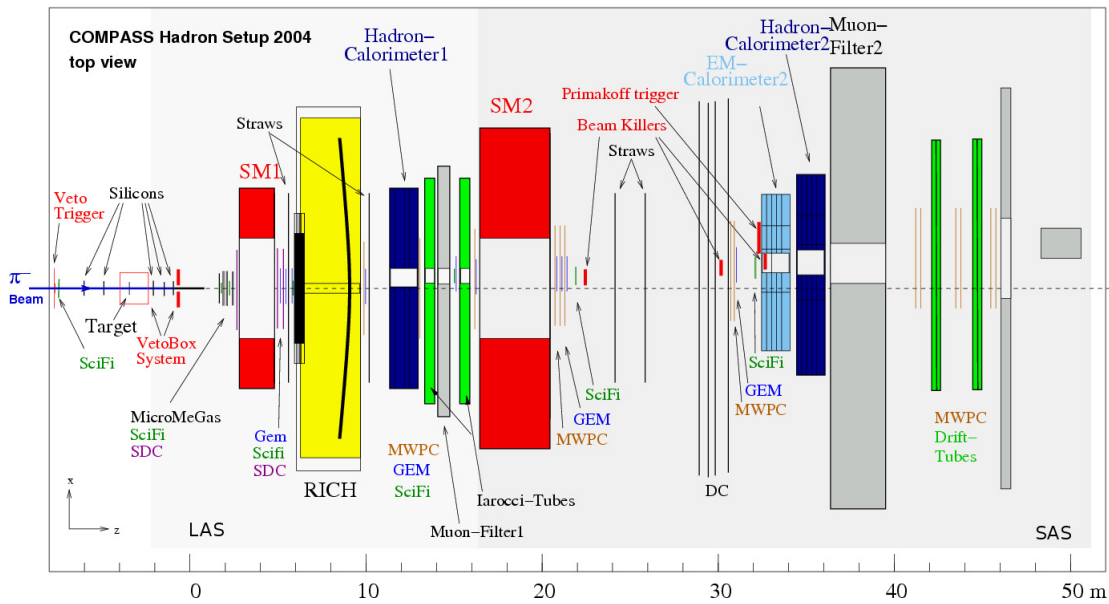


Figure 2.2: A sketch of the COMPASS hadron spectrometer setup 2004 from the top, the figure is not to scale along the x-axis.

relevant information about the various detectors, like resolution in space and time, different projections, number of channels, active area and the number of detector stations are listed in Table B.2.

Very Small Area Trackers (VSAT) are needed for precise track reconstruction of the beam and the scattered particle. Due to the high hit rate of $3 \cdot 10^6$ per SPS cycle in the muon and hadron beam respectively, hits are attached to the track due to their time correlation. Scintillating fibre (SciFi) detectors with their very good time resolution in the order of 400 ps are placed along the spectrometer to measure charged reaction products close to the beam. Depending on the position along the beam axis and beam divergence, the active area increases downstream from $5.3 \times 5.3 \text{ cm}^2$ to $12 \times 12 \text{ cm}^2$. Silicon micro-strip detectors are essential due to their excellent space resolution of about 4 - 14 μm for beam reconstruction and precise angular resolution. The detectors have double sided readout to minimise multiple scattering effects and a radiation hard wafer design to stand the high intensities. A detailed description of this detector is given in chapter 3, and its characterisation in chapter 4 and 5.

Small Area Trackers (SAT) are used to detect particles with distances larger than 2.5 cm to the nominal beam axis. The COMPASS experiment profited from the development of two new high-rate capable gaseous detector types. The three Micromegas (Micromesh Gaseous Structure) stations with an active area of $40 \times 40 \text{ cm}^2$ detect track particles in the region between the polarised target solenoid and SM1. The 22 GEM (Gas Electron Multiplier) detectors cover the region downstream of SM1 until the end of the spectrometer. Each GEM detector, with a size of $31 \times 31 \text{ cm}^2$ records two perpendicular projections. Both detectors, Micromegas and GEM, have a good space resolution in the order of 70 - 90 μm and a time resolution in the range of 9 - 12 ns.

Large Area Trackers (LAT) have to cover the large angle acceptance. One out of three Drift Chambers (DC) is located before SM1 and two are placed downstream of SM1. They have a size of $1.8 \times 1.8 \text{ m}^2$ and a 30 cm diameter dead zone in the central region. One straw tube chamber (Straw) with 6 double layer planes is installed in the SAS stage of the spectrometer. Further downstream, three straw tube chambers with $3.2 \times 3.2 \text{ m}^2$ and an inactive zone of $10 \times 20 \text{ cm}^2$ are mounted to provide tracking of charged particles with large scattering angles (15 - 200 mrad). The 11 multi-wire proportional chambers (MWPC) with a 16 - 20 cm non sensitive central zone belong also to the LAS detector set. Downstream of SM2 six large drift chambers with a size of $5.2 \times 2.6 \text{ m}^2$ and a 50 cm diameter central dead zone complete the track telescope of the SAS. The space resolution of the different detectors is in the order of 0.2 mm - 1.6 mm, see Table B.2.

2.2.2.2 Particle Identification

In order to identify muons in COMPASS, the last detectors of LAS and SAS are the muon filters which consist of an absorber layer sandwiched between tracker stations. The absorber layer has to be thick enough to stop incoming hadrons. If a track can be found with hits in the muon wall detectors before and after the absorber, then it is identified

as a muon. In the LAS, the muon filter 1 is placed with a 60 cm iron absorber in front of SM2. The muon filter 1 is preceded and followed by two stations of muon wall 1 (MW1) which are gaseous wire detectors (Mini Drift Tubes) with moderate space resolution. The muon filtering system in SAS consists of a 2.4 m thick concrete wall (muon filter 2) and the tracking behind SM2 and two dedicated stations of MW2 and three MWPC stations.

The Ring Imaging Cherenkov Detector (RICH) separates hadrons into pions, kaons and protons in between an energy range of 5-50 GeV/c. It consists of a large vessel of 80 m³ volume which is filled with the radiator gas C₄F₁₀. The emitted Cherenkov photons are reflected by two spherical mirror surfaces and converted to electrons by CsI photon detectors. The 8 photon sensitive surfaces (567 × 1152 mm²) are equipped with MWPCs which detect the converted electrons. The RICH covers the whole angular acceptance of the LAS, except a central dead zone of 10 cm diameter.

2.2.2.3 Calorimeter

The spectrometer is equipped with two hadron calorimeters, HCAL1 and HCAL2 which are installed in front of the muon filters of LAS and SAS. In order to measure the energy of the hadrons, the hadron calorimeters consist of stacks of iron and scintillator plates, where the absorbed energy of the hadronic shower particles is reemitted as light and via light guides transferred to photo multiplier tubes (PMT). HCAL1 consists of 480 modules, each 40 layers of 20 mm iron and 5 mm scintillator plates. The modules cover an active area of 10.8 m² with a window for high momentum and beam particles of the size 8 × 4 modules, with a cross section of 14.2 × 14.6 cm² each. The energy resolution as a function of the pion energy (in GeV) can be parametrised by $\sigma(E)/E = (59.4 \pm 2.9)\%/\sqrt{E/\text{GeV}} \oplus (7.6 \pm 0.4)\%$. For the spatial resolution $\sigma_{x,y} = 14 \pm 2$ mm is obtained. HCAL2 consists of 22 × 10 modules each with a cross section of 20 × 20 cm² and 25 mm steel and 5 mm scintillator stacks with mostly 36 layers. The central hole has a size of 2 × 2 modules to pass the high intensity beam. HCAL2 has a good linearity in the energy range 10-100 GeV and an energy resolution of $\sigma(E)/E = (66/\sqrt{E/\text{GeV}} \oplus 5)\%$.

The electromagnetic calorimeter ECAL2 is located in SAS in front of the hadron calorimeter and the muon filter 2. It consists of lead glass modules where each has the size 38 × 38 × 450 mm³ arranged in a matrix of 64 × 48 modules. Since in the centre of ECAL2 the beam intensity is high, there is left a hole. Its size is adjusted to the demands of the hadron or muon beam. Electrons and photons induce an electromagnetic shower inside the lead glass. The Cherenkov light of the shower electrons and positrons is collected by a PMT which is mounted at the end of each block. The collected light is proportional to the energy deposit of the incident particle. Detailed information about the calibration and the performance of ECAL2 is given in chapter 6.

2.2.3 Beam Requirements

The CERN SPS accelerator M2 beam line can be tuned for secondary hadron beams as well as tertiary muon and electron beams. The SPS primary proton beam of 400 GeV/c hits a beryllium target which can be chosen in different thicknesses depending on the required beam intensity. Whether pions and kaons as secondary particles, or muons and electrons as tertiary particles follow the transfer line, depends on the polarity of the bending magnets and the presence of collimator and absorber, see Fig. 2.3.

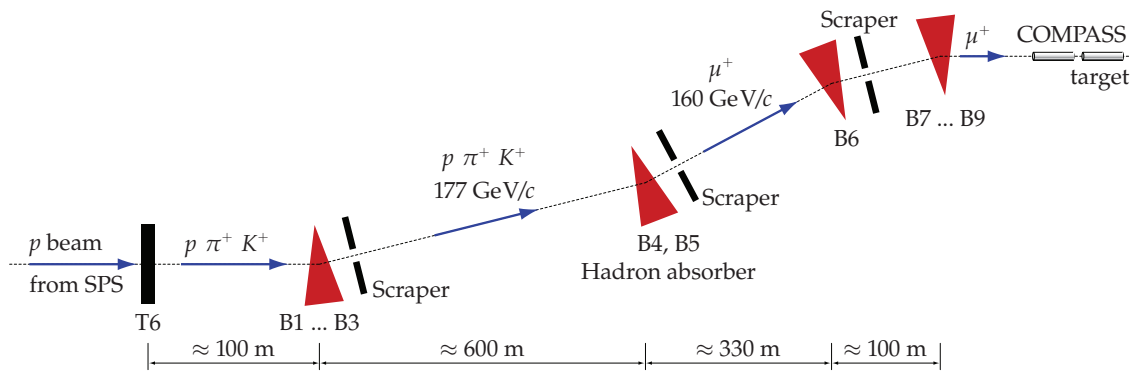


Figure 2.3: The M2 beam line for the COMPASS muon beam, Fig. from [Gru06].

2.2.3.1 Muon Beam

For the muon beam, the pion and kaon decay channel is used. At the end of a 600 meters decay section, the remaining hadrons are stopped by a 9.9 m thick beryllium hadron absorber, Fig. 2.3. The generated muons are momentum-selected by bending magnets. Before they reach the COMPASS experimental area, the beam is additionally purified by a heavy concrete absorber placed before the entrance to the experimental hall. The muon beam can be tuned for momenta between 60 and 190 GeV/c of both polarities. The spot size for the muon beam is typically $7 \times 8 \text{ mm}^2$ RMS in the horizontal and vertical plane with a divergence of less than $0.5 \text{ mrad} \times 1 \text{ mrad}$. The flux of the beam is up to $2 \cdot 10^8$ muons per SPS cycle and limited by radio-protection-guidelines [Gat01].

2.2.3.2 Hadron Beam

The secondary hadron beam is guided from the production target through the beam line. The main difference to the muon beam setup is the absence of the hadron absorber which is moved out. For negative hadron beams the electron content can be reduced, if wanted, by a 5 mm lead converter. The momentum of the hadron beam can be adjusted within a range of 40 to 280 GeV/c and a maximum allowed flux of 10^8 hadrons per SPS cycle. It is possible to focus the beam to $1.1 \times 1.5 \text{ mm}^2$ RMS [Gat01].

Beam parameters	Measured
Beam momentum	190 GeV/c
Proportion of negative pions	92 %
Proportion of negative kaons	4.5 %
Proportion of negative muons	3 %
Other components (antiprotons, electrons)	$\sim 0.4\%$, $\sim 0.1\%$
Typical spot size at COMPASS target ($\sigma_x \times \sigma_y$)	$\approx 3 \times 3 \text{ mm}^2$

Table 2.1: Parameters and performance of the 190 GeV/c negative hadron beam in 2004.

2.2.3.3 Electron Beam

The electron beam is a tertiary beam. From the secondary hadron beam, only low momentum particles in the order of 100 GeV/c are focused to a 5 mm lead converter which serves as a secondary target. The obtained electron flux is 10^3 to 10^4 electrons per SPS cycle with an momentum range of 30 to 60 GeV/c and a spot size in the order of 8 mm in diameter [Gat01]. This electron beam is used in COMPASS for the absolute calibration of the electron calorimeters.

2.2.4 The 2004 Hadron Setup

The hadron setup in the year 2004 was dedicated to measure Primakoff scattering and diffractive dissociation processes. The Primakoff and the diffractive program share a very similar experimental spectrometer setup which has to fulfil certain requirements. For the Primakoff process, the reconstruction of the incident and scattered pion angle is necessary as well as the separation of the scattered pions and pions which did not interact in the target material [Fer05]. Important is also the measurement of the emitted photon energy with a good energy resolution of σ_E/E better than 2%. Especially for the diffractive process, the possibility to reject hard interactions in the target is of advantage.

2.2.4.1 Hadron Targets

Data was taken with different target materials in order to study the dependency of Z^2 (the charge of the target nucleus) on the cross section of the Primakoff scattering process. Different materials are also needed to determine the ratio between Coulomb and diffractive scattering cross sections. The targets are discs with a diameter of 30 mm, centred on the incoming beam axis. As target materials serves lead, copper and carbon, whereby the thickness depends on the required radiation and interaction length. This is a trade-off between achieving high statistics and avoiding photo conversion in the target material and significant effects of multiple scattering. For systematic studies and better understanding of the spectrometer, data was also taken without a specific target, called empty target. In Table 2.2 all target configurations, their geometries and properties are summarised.

Target material	Beam	A	Z	ρ [g/cm ³]	Width [mm]	R.L. X_0	θ_0 [μ rad]
Pb	π^-	207.2	82	11.35	3.0	0.54	52.3
Pb	π^-	207.2	82	11.35	1.6	0.29	38.1
Pb	π^-, μ^-	207.2	82	11.35	2.0 + 1.0	0.36 + 0.18	42.6 + 30.0
Cu	π^-	63.5	29	8.96	3.55	0.25	35.5
C	π^-	12.0	6	2.2	23.5	0.12	25.1
Empty target	π^-, μ^-						

Table 2.2: Different target configurations for the hadron pilot run in 2004. There are listed the target material, the various beam configurations, the atomic number A, the atomic charge Z, the density of the target, the thickness of the target disc which is a disc of 30 mm in diameter, the radiation length of the material and the multiple scattering angle θ_0 .

2.2.4.2 Specific Hadron Components

The target is surrounded by a veto box to measure low energy target fragments. The veto box is a barrel shaped detector and consists of scintillating counters followed by an electromagnetic calorimeter. The target is preceded and followed by a silicon micro-strip telescope at a distance of about 1 m which is needed for a precise measurement of the pion scattering angle and good vertex reconstruction, see Fig. 3.8 on page 31. Two silicon detector stations are placed upstream and three stations downstream of the target. Two sandwiches of scintillating counters and lead foils are supposed to be used to veto on photons and particles emitted by large angles.

In order to minimise the contributions of multiple scattering and photon conversion, sequentially scintillator modules were removed from the spectrometer setup (SciFi 4, 6, 7). The main important changes are listed in appendix B.1 of the setup during this hadron beam time. For the same purpose the vessel of the RICH was filled with nitrogen gas. In ECAL2 the central hole was optimised to the size of 7.7×7.7 cm² to fit the hadron beam. The bending power of SM2 was increased from nominal 4000 A to 5000 A due to the higher hadron beam momentum (190 GeV/c) compared to the muon beam (160 GeV/c). The momentum of the hadron beam is not measured for each incoming particle, but is only known by the beam optics.

Since the pion beam has a kaon content of about 4.5%, see Table 2.1, two CEDARs (Cherenkov Differential counters with Achromatic Ring focus) were placed in a row in the hadron beam at the entrance of the experimental area. For a given particle mass and momentum at a fixed pressure of the radiator gas, the Cherenkov light is emitted into a fixed angle which passes the diaphragm. By adjusting the pressure of the radiator gas, the CEDAR can be made sensitive to certain particles. With two CEDARs in a row, one with a threshold setting for pions and the other for kaons, particles can be identified by the coincidence with the trigger. The CEDARs can distinguish kaons from pions up to 300 GeV/c [Bov82].

2.2.4.3 The Hadron Triggers

Mainly two physics trigger types, Primakoff and diffractive trigger were implemented in the 2004 hadron run. Both types have common trigger requirements.

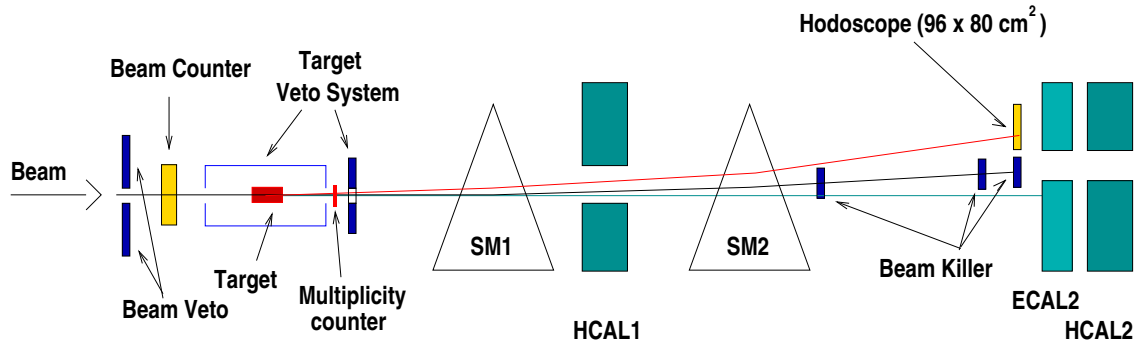


Figure 2.4: Schematic view of the hadron trigger system in 2004.

Common hadronic trigger: The beam trigger selects particles pointing to the target. The beam is triggered by the coincidence of two scintillator counters of 5 cm diameter which are centred on the beam trajectory and placed 10 and 5 m respectively upstream of the target.

A veto system rejects beam particles outside of the apparatus acceptance. It consists of a $250 \times 320 \text{ cm}^2$ veto detector with a 4 cm diameter hole in the centre of the beam trajectory at the entrance of the experimental area. The second part is a sandwich detector placed after the veto box with a 4 cm diameter hole. It rejects either events with photons and charged particles emitted by angles large enough, that they are falling outside the acceptance of the electromagnetic and hadronic calorimeter, or which are simply not crossing the target disc.

If the pions do not interact in the target, except multiple scattering, they are detected by three plastic scintillator discs of 5 mm thickness and 5 cm in diameter, so called Beam Killers which are placed along the beam trajectory between SM2 and ECAL2.

The common hadronic trigger consists of the beam counter in anti-coincidence with the Beam Killers and the veto system.

Primakoff triggers: Apart from the common trigger, an event has a typical Primakoff signature if there is a scattered pion with a momentum below $150 \text{ GeV}/c$ in coincidence with a high energy photon.

PRIM1: For the detection of the scattered pion a hodoscope with 20 slabs of $6 \times 90 \text{ cm}^2$ is placed in front of ECAL2. It covers a momentum range from $20 \text{ GeV}/c$ to $110 \text{ GeV}/c$. The Primakoff trigger (PRIM1) requires a coincidence with the hodoscope and a minimum threshold on the summed ECAL2 energy to select events with high photon energy or

electromagnetic decays of neutral particles. The energy deposition in ECAL2 has to be larger than 50 GeV and in HCAL2 larger than 18 GeV which is an indication for a hit of the scattered pion.

PRIM2: A second Primakoff trigger covers the kinematic region for events with an energy in the laboratory frame below 20 GeV of the scattered pion. For those events, no signal will be seen in the hodoscope, but in order to detect them the summed energy deposited in ECAL2 has to be higher than 90 GeV.

For both Primakoff triggers the energy deposit in HCAL1 is demanded to be smaller than 6 GeV/c, [Tri].

Diffraction trigger: A diffractive trigger is applied to select diffractive processes like the η -meson production. The decay mode $\eta \rightarrow \pi^+ \pi^- \pi^0$ requires at least two charged particles hitting a scintillator counter, located between the veto system and the silicon telescope. In the diffractive trigger, the hit multiplicity of the scintillator counter has to be at least two, combined in coincidence with the common trigger. The diffractive trigger covers the full kinematic range of the scattered pion.

Charge exchange trigger: A charge exchange trigger is implemented for calibration purposes. It selects the reaction $\pi^- p \rightarrow \pi^0 n$. For this trigger, it is required that there is no hit in the multiplicity counter and a minimum energy threshold of 50 GeV in the ECAL2.

2.2.5 The Specific Components of the Muon Setup

The muon program relies mainly on the measurement of various spin asymmetries. A polarised muon beam with a momentum of 160 GeV/c hits a polarised deuterium target. Compared to the hadron setup, the main differences of the spectrometer are the measurement of the beam momentum and the layout of the target region, including the target itself.

The muon beam has a large momentum spread about 5%, defined by the beam optics. A Beam Momentum Station (BMS) is placed in the beam line upstream the experimental hall in order to measure the momentum of each muon. It consists of three consecutive dipole magnets which belong to the beam optics, with a large vertical bend (30 mrad), and scintillating fibre hodoscopes. Three of the hodoscopes are placed before and after the magnet each. The momentum of each muon track can be determined to a precision better than 1 %.

A silicon telescope with three stations is placed in front of the target in order to determine precisely the beam trajectory.

As target material, deuterated lithium (${}^6\text{LiD}$) is used which reaches a high degree of deuteron polarisation (> 40%) since ${}^6\text{Li}$ can be approximated as a Spin-0 ${}^4\text{He}$ nucleus and a deuteron. The nucleons are polarised via *Dynamic Nucleon Polarisation* (DNP): Irradiation with microwaves polarises paramagnetic centres (impurities with free electrons) in

the material which can then transfer their polarisation to the nucleons [Wie04]. A homogeneous magnetic field along the beam direction is provided by a 2.5 T superconducting solenoid to built up and sustain the polarisation. In order to measure asymmetries, the polarised target is build out of two 60 cm long and 3 cm diameter target cells which are separated 10 cm from each other and placed in a row. The spins in the two cells are polarised in opposite direction. Acceptance effects are mainly cancelled out by rotating the spin direction. e.g. in 2004 three times a day, the spin direction was inverted by rotating the solenoid field.

The RICH vessel is filled with the radiator gas C_4F_{10} , allowing particle identification of hadrons in the range of 5 to 43 GeV/c for pions, kaons and protons.

The central hole of ECAL2 is enlarged compared to the hadron setup from 2×2 to 10×10 lead blocks, fitting the muon beam size.

The trigger system and composition of the muon program is designed for a minimum bias selection of inelastic scattering events which means triggering on scattered muons. The physics trigger composition is completed by a beam veto system, rejecting events where the muon did not pass the target. Since the complex muon trigger system will not be relevant within this thesis it is not further discussed here, for more information see [COM07a].

2.3 Data Processing and Analysis Software

If a trigger event occurs and gives the signal to readout all front-end electronics of the detectors, these data are transferred to the event builder computers, where all data fragments are combined to one so called *event*. Events are combined into a file with 1 GByte maximum size, named *chunk*. Such chunks are numbered by packages up to 200 SPS cycles which are denominated as *runs* and stored on tape at the CERN CASTOR system, the CERN Advanced STORage manager [CAS]. The COMPASS Data Acquisition (DAQ) has to handle rates of 50000 events in muon run as well as 86000 events in hadron run per SPS cycle with an average size of a single event of about 35 kByte for the muon run in 2004 and 25 kByte for the hadron run which accumulates to 350 TByte/year, see [Gru06] for detailed descriptions.

The following subsections are a brief introduction to the various software packages of COMPASS starting from online monitoring to event reconstruction and data analysis tools.

2.3.1 Online Filter

A cleaning of the trigger and an efficient way of data reduction is achieved by the online-filter Cinderella [Nag05], [Kuh07] which is basically a software trigger. It was used for the first time in 2004. Events are only stored in case the beam momentum station, the silicon

telescope and the fibre stations upstream of the target have recorded a sufficient number of hits from the beam particle. These have to be in coincidence with the trigger times and hit times of the particles measured by the detectors, taking into account their particular time resolution. The filter achieved for the muon run in 2004 a reduction by 23% with an associated inefficiency of 0.4%. During the hadron run the diffractive trigger rate was reduced by 45%. The filter has the side-effect, that it is very sensitive to the detector performance. During data acquisition, the filter rates are calculated after each SPS cycle. A drop in the filter rates may be an indication for certain detector problems.

2.3.2 The ROOT Analysis Framework

ROOT is an object-oriented framework written in C++ and developed at CERN in the mid-90's as successor of the previous FORTRAN-based analysis tool PAW. ROOT covers the special needs for high energy physicists. At COMPASS the online monitoring program COOL (subsection 2.3.3) is based on ROOT. In order to analyse data with ROOT, the library PHAST (2.3.6) provides the required linking tools with the COMPASS data reconstruction software CORAL (2.3.5). Within this thesis the methods of ROOT are used, e.g. for creating histograms and displaying data, as well as the fitting routines. ROOT is designed to handle huge amounts of data. Data are stored in so-called `TTree`s. Those objects of the `TTree` class are optimised to reduce disc space and enhance data access. Detailed information about ROOT can be found in [ROO] and [Bru97].

2.3.3 Online Monitoring with COOL

COOL is the online monitoring program of COMPASS [COO], [Ber04]. During data acquisition various detector types can be examined online. COOL provides access to off-line data as well. COOL is based on ROOT which provides the framework for generating histograms and for the graphical user interface. It can also produce a `TTree` containing data and performance histograms of the detectors. In COOL also a simple tracking routine is implemented which is sufficient for detector studies and quick quality checks.

2.3.4 COMgeant- the Monte Carlo Setup

COMgeant is an application of the GEANT 3.21 simulation program to simulate the COMPASS spectrometer [COM]. Generators for lepton, photon and hadron interactions can be linked to COMgeant. COMgeant creates geometry files with the detector positions which are then used by the reconstruction software CORAL, see subsection 2.3.5. The COMPASS spectrometer with its material budget due to different material types of the various detector components are described in so called *material maps*, which are used by COMgeant. In the target material, the interactions are generated using random distributions, reflecting the statistical nature of the interactions. COMgeant simulates the

tracks and secondary tracks propagated through the spectrometer. The response of each detector is simulated as a first step in CORAL.

2.3.5 CORAL - Reconstruction Software

The event reconstruction software CORAL (COmpass Reconstruction and AnaLysis project) is a program written in C++ [COR]. Input files are either the raw detector information recorded by the DAQ system or files from the Monte Carlo simulation software. In order to reconstruct an event (track parameters, vertices, calorimeter clusters, RICH probabilities etc.), several steps are executed by CORAL:

- **Decoding:** Information of the detector signals (wire, pad, cell) is extracted from the raw data (digit). In case of Monte Carlo, this process is replaced by the so called digitisation which is the simulation of the detector response based on the particle trajectory and the detector resolution.
- **Clustering:** Neighbouring detector channels are grouped together and the new cluster position is calculated.
- **Tracking:** With the information of the tracking detectors, the particle trajectories can be reconstructed. Different steps are necessary:
 - For pattern recognition, the spectrometer is split into 5 zones along the beam direction. For each zone, track segments are reconstructed, for each detector projection separately.
 - A space track segment is formed by associating of the tracks of at least two projections.
 - Bridging corrects tracks of the different zones to build a full track through the spectrometer, including the bending effect in the spectrometer magnets. The time information of several detectors is used to calculate the needed track time, e.g by the drift-like detectors.
 - In the track fitting method, all track parameters of the charged particles and the corresponding error matrices are determined by the Kalman fit method.
- **Calorimeter reconstruction:** The known parametrisation of the shower profile leads to an estimation of the deposited energy in the calorimeter cells. With a special fitting procedure the position of the cluster and the energy are determined.
- **RICH reconstruction:** Particles that crossed the radiator gas of the RICH detector radiate Cherenkov photons under an angle given by the particle mass. The package calculates the probabilities of the hypotheses of the particle being a proton, a pion or a kaon.

- **Vertexing:** The vertexing algorithm is searching for the position of the primary interaction and the decays of neutral particles. The primary interaction vertex contains the beam track and the track of the scattered particle. The Point Of Closest Approach (POCA) is first calculated for all track combinations and those below a certain threshold are selected. With the inverse Kalman filter algorithm the track parameters at the vertex and the error matrix are determined.

The reconstructed events are stored in ROOT `TTree`s, so called *mini Data Summary Trees* (mDST). These mDST data are the basis for all physics analysis. The data size, compared to the raw information, is reduced by a factor of about 100 for muon data and a factor of 4 for hadron data in 2004. mDSTs which contain additional raw information of selected detectors for detector analysis are named GigaDSTs.

The production of mDST data can start, when all detector calibration constants, e.g. time calibration, energy calibration are generated by the particular detector experts and an *alignment* of the whole spectrometer is performed. The alignment procedure determines the rotation between the detector coordinate system and the COMPASS coordinate system including the effects of the various magnetic fields within the spectrometer. It optimises the effective detector pitch and evaluates the positions of the detector centres. All relevant geometrical information of the detectors needed in CORAL are stored in a text file, the official COMPASS alignment file. An alignment is performed once per week during the beam time.

2.3.6 Data Analysis with PHAST

PHysics Analysis Software Tools (PHAST) is a framework for the analysis of the COMPASS data at mDST level. In order to generate such mDST files, PHAST is linked to CORAL. PHAST was developed to have an easy access to all important information which are needed for physics analysis. In order to analyse the mDST files, PHAST has a specific user section. A `UserEvent` function which loops over all events, is the place for the user to write the code for the specific analysis either for physics or in case of GigaDST also for detector studies. The output of this function can be a ROOT file containing histograms or a `TTree` which can be further handled within the ROOT framework. It can also be used to filter the data for the special needs of the analysis to reduce the amount of data and create so-called μ DST files. PHAST keeps also an environment to include further code and algorithm developments which are of interest for the physics analysis.

Chapter 3

The COMPASS Silicon Micro-Strip Detector

3.1 The Basic Principle

In high energy experiments, silicon detectors are used for position measurement when excellent spatial resolution is required. They typically consist of a n-type silicon bulk of 300 μm thickness with low impurity concentration of donors (e.g. phosphor) and a thin region in the order of 1 μm with a high concentration of acceptors (e.g. boron) on the upper side, so called p^+ -implants, see Fig. 3.1. The p^+ -implants build with the n-type silicon bulk a p-n junction, forming a diode. There the free charge carriers, electrons of the n-type silicon bulk and holes of the p^+ -implants, recombine and a depletion zone is generated, where no free charge carriers exist. This zone is strongly asymmetric and reaches deep into the n-type silicon bulk since the donator concentration is orders of magnitude smaller than the acceptor concentration of the p^+ -implants.

By applying a bias voltage in reverse direction on the p-n junction, the whole n-type silicon bulk can be depleted which serves as the active volume of this particle detector. The behaviour is resistor like which means no current is drawn under the applied voltage. A charged particle which passes the depleted silicon bulk generates pairs of electrons and holes along the trajectory which drift to the n- and p-readout electrodes, respectively, of the applied bias voltage. In order to be position sensitive, the p- and n-electrode are split in a series of strips or pads which are placed on the same silicon base. Detailed descriptions of the operation mode of silicon detectors can be found in [Leo94], [Pei92] and [Spi05].

3.2 The COMPASS Silicon Detector Setup

3.2.1 System Requirements

The COMPASS silicon micro-strip detectors are used for beam definition and scattered particle track reconstruction. The high beam rates in COMPASS of the order of 10^8 particles per SPS cycle¹ require a radiation hard detector design and an excellent time resolution. In order to achieve measurements with high resolution, the material budget needs to be minimised, because the spatial resolution is dominated by multiple scattering contributions. Especially for the hadron program (section 2.1.1) a good angular resolution of the vertex silicon telescope is needed. The angles of scattered particles for reactions of interest in this work are as low as $150 \mu\text{rad}$ [COM96]. The muon beam has a very broad beam spot of $10 \times 8 \text{ mm}^2$ (Gaussian sigmas), so the active area of the detector has to fit at least this beam size. In the range downstream of the target, the detectors have to cover the small scattering angle area, where the following detectors have dead zones.

3.2.2 The Wafer Design

The silicon wafer, optimised for high fluences, was originally designed and developed for the HERA-B experiment [SP95] by the Semiconductor Laboratory (HLL) of the Max-Planck-Institutes in Munich and produced by SINTEF in Oslo (Norway) [Sin97]. The special feature of this silicon detector is its design for double-sided readout which reduces the material budget by a factor of two compared to single-sided readout. A detailed description of this wafer is given in [Ric96] and [Abt00].

The $280 \mu\text{m}$ thick n-type wafer has an active area of $5 \times 7 \text{ cm}^2$ and a resistivity about $2\text{-}3 \text{ k}\Omega\text{cm}$. The 1280 strips on the n-side ($54.6 \mu\text{m}$ pitch) are perpendicular to the 1024 strips on the p-side ($51.7 \mu\text{m}$ pitch), so that with one detector, a two-dimensional position information can be obtained. The strips are tilted by 2.5° with respect to the wafer edge, see Fig. 3.5, optimised for the required geometry of HERA-B vertex detector [Bau00].

The wafer design was developed to stand an equivalent annual fluence of $3 \cdot 10^{14}$ minimum ionising particles (MIP) per cm^2 exceeded for the innermost edge of the sensors [Bau02], [Pug99]. Radiation damage induces high leakage currents (up to 1000 nA [Abt96]), so readout via capacitive coupling is necessary. The aluminium readout strips are separated from the implanted strips by a layer of silicon dioxide and silicon nitride. In order to operate the detector up to 500 V , a controlled gradual drop of the potential from the detector rim towards the potential of the undepleted substrate is needed. This is realised by a multi-guard-ring structure around the wafer [Abt96]. The bias voltage is applied to the bias ring which is connected via $1 \text{ M}\Omega$ polysilicon resistors to the strips. [Rie98] shows that the noise remains constant in high radiation environment with strip biasing compared to the punch-through biasing, where the bias voltage is not connected via resistors to the bias ring.

¹A SPS cycle consists of a 4.8 s long spill where protons are extracted with a period of typically 16.8 s .

On double sided silicon detectors, the n^+ -strips have to be insulated from each other to avoid a short which is realized by p-stop implants in between as separation method on the n-side. On the p-side intermediate strips improve the spatial resolution, since they distribute their collected charge via capacitive coupling to the adjacent strips, see Fig. 3.1 and Fig. 3.2.

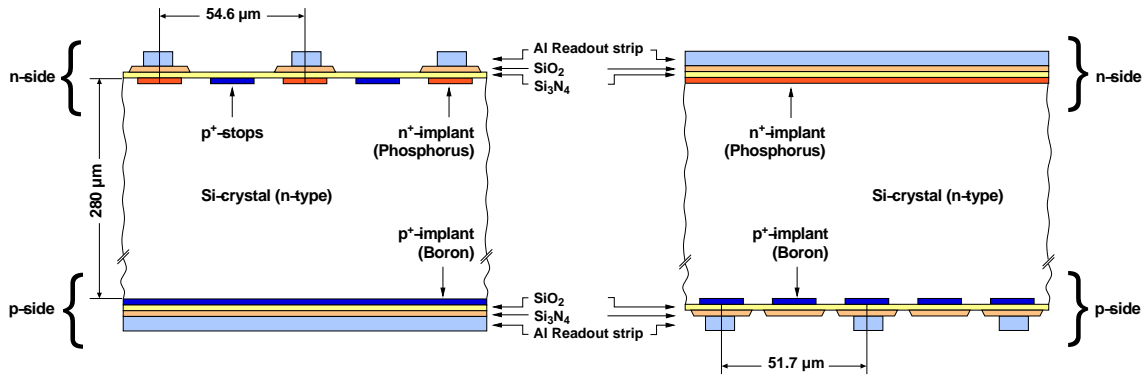


Figure 3.1: Cross section of the silicon wafer.

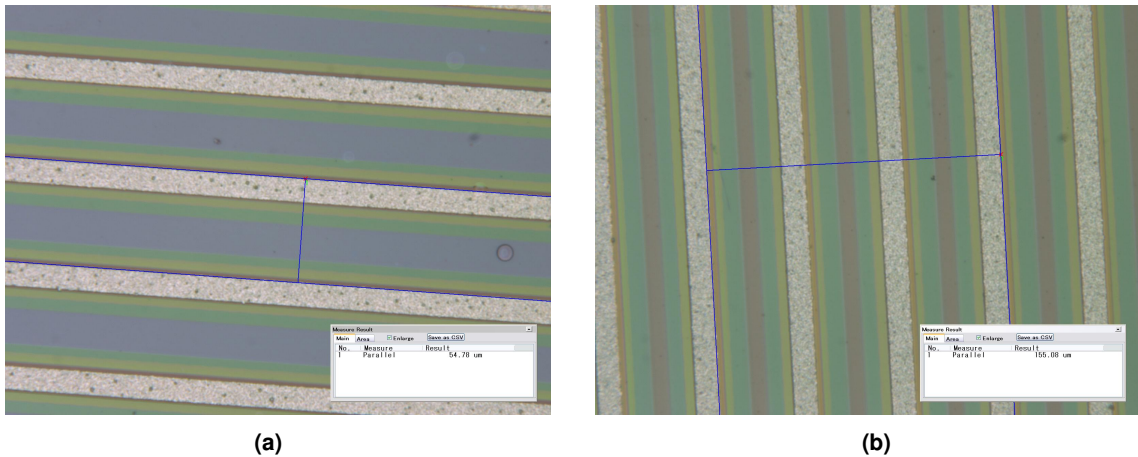


Figure 3.2: Image of the silicon wafer surface. On both pictures the read-out strips can be clearly seen in light grey. On the left picture, the n-side of the wafer is shown. The pitch between the strips is $54.78 \mu\text{m}$. On the right, the p-side of the wafer is shown. The pitch was determined to be $51.83 \mu\text{m}$. Between the readout strips, the intermediate strips are located which appear in a fine brown tone.

3.2.3 The Detector Module

The silicon wafer is glued with silicone glue in between two L-shaped Printed Circuit Boards (PCBs), so called *L-Boards*. They provide the connections for data transmission, power lines, a configuration bus clock and trigger information as well as pads for the

3 THE COMPASS SILICON MICRO-STRIP DETECTOR

silicon bias voltage and temperature readout. The two L-boards are on different potentials due to the applied depletion voltage. The frontend chip APV25² [Jon], see subsection 3.2.4, and the pitch adaptor which matches the output pattern of the APV frontend chip and the bonding pad, are glued onto the L-board. The 1280 readout strips on the n-side and 1024 readout strips on the p-side of the detector are connected via bonds and the pitch adaptor to the 10 and 8 APV25 readout chips, respectively, with 128 channels each. Along two wafer edges a capillary³ is soldered on the back side of the L-board and is electrically insulated by a connector of epoxy material. The capillary is flushed with about 400 l/h gaseous nitrogen to cool the APV25 chip which dissipates 0.4 W each (7 W per module). The temperature is measured by PT100 temperature sensors. Keeping the temperature at 55° C on the PBC close to the APV chip turned out to be sufficient. A COMPASS silicon detector module with all its components is shown in Fig. 3.3.

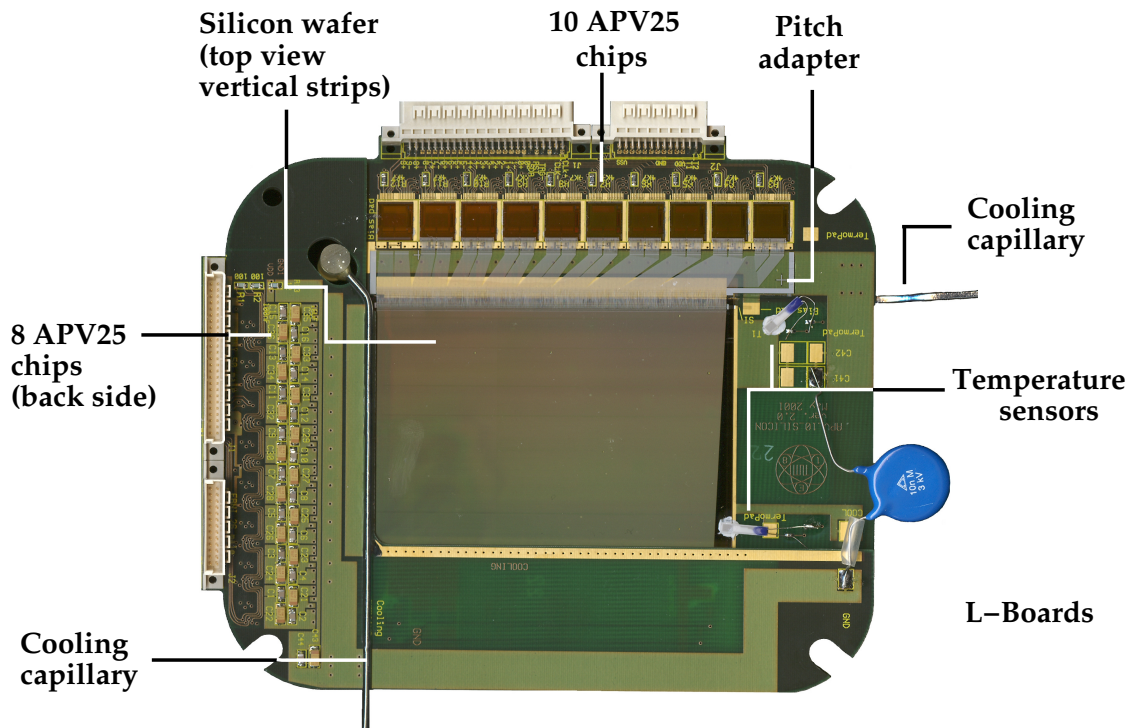


Figure 3.3: The COMPASS silicon detector module.

²The APV25 frontend chip is an analogue pipeline ASIC intended for readout of silicon strip detectors in the CMS silicon trackers at LHC at CERN.

³Material: Cu/Ni, 1.3 mm inner and 1.6 mm outer diameter

3.2.4 Electronics and Readout Chain

3.2.4.1 The Frontend Chip APV

The APV25 frontend chip is an analog pipeline ASIC⁴ developed for reading out the silicon trackers of the CMS⁵ experiment at CERN. The APV25 frontend chip combines analog signals with digital control. Each of the 128 channels of the APV25 frontend chip consists of a low noise CR-RC type shaping amplifier and a 192 samples deep analog pipeline. The amplifier integrates the analog signals arriving from the micro-strips of the silicon module and transforms it into a well defined voltage pulse. The APV frontend chip continuously samples the signals at a frequency of 38.88 MHz, synchronous to the reference clock of the Trigger Control System (TCS) of the experiment.

The analog memory pipeline is used to compensate the latency of the first level trigger. The pipeline consists of switched capacitor elements. 160 out of the 192 memory cells are acting as a ring buffer. All incoming data are cached in the capacitor array and can be stored up to 4 μ s (at sampling rate of 38.88 MHz) with respect to the signal time. The trigger pointer of the ring buffer flags the pipeline column in case of an external trigger signal for read out. This pipeline column is transferred to one of the remaining 32 memory elements which are organised like a FIFO⁶. There, the data are buffered until sent out multiplexed onto one single differential output line.

In COMPASS the APV25 frontend chip is operated in the multi-mode which means the trigger flags three consecutive pipeline columns for readout. From these three samples a precise time information for the silicon detectors can be extracted, see section 4.2. For more information about the APV25 frontend chip see [Jon].

3.2.4.2 The Readout Chain

The readout chain of the silicon detectors is shown in Fig. 3.4. The APV25 chips are connected via short flat cables (~ 10 cm) to the repeater card. This card supplies the APV25 chips with power (± 1.3 V) and amplifies the analog differential output signals of the APV25 chips by high-speed operational amplifiers. It also provides trigger and clock lines as well as the separation of the temperature sensors from the data flow.

The amplified signals of one projection are digitised by an ADC⁷ card, named SGADC card which is connected with 0.5 m long flat cables to the repeater card. The SGADC card has a pipelined architecture and the digitisation is done by 10 bit differential ADCs at a sampling rate of 20 MHz. Two FPGAs⁸ at the SGADC do the main data processing.

⁴Application Specific Integrated Circuit

⁵Compact Muon Solenoid, see [CMS].

⁶First In - First Out, principle of data structure processing technique

⁷An Analog to Digital Converter (ADC) converts continuous analog signals into a sequence of discrete digital values that correspond to the signal amplitude [Gru06].

⁸Field Programmable Gate Array; an FPGA is a semiconductor device containing programmable logic components [Wik].

3 THE COMPASS SILICON MICRO-STRIP DETECTOR

The data rate is reduced by a zero suppression logic which sorts out channels containing low amplitude-noise [Gru01]. This zero suppression algorithm subtracts on-chip loaded values for the baseline of each individual channel, so-called pedestals, and the remaining value of the signal is compared with a level depending on the noise of each channel. A correction is applied to the collective changes of the pedestals, the common noise. The common mode noise are fluctuations of all 128 channels of a APV chip due to small fluctuations of the power supply voltage [Wie04]. In the end only signals which are above a certain threshold, e.g. four times above noise level, are formatted to a 32 bit word and sent via optical fibres of 50 m length to the GEM and Silicon Control and Acquisition module (GeSiCA). Since the ADC cards have an optical connection to the GeSiCA, the silicon detector station is electrically decoupled from the GeSiCA. This is necessary, because due to the depletion voltage on the silicon detectors, the n- and p-sides have a different potential and so do the L-board, the repeater card and the ADC cards of one detector side. A detailed grounding scheme can be found in [DeM04].

The GeSiCA modules distribute the TCS clock and transfer reset and trigger signals to the frontend cards. The data stream can be multiplexed of up to four ADC cards into one serial data stream which is sent via an optical S-Link to the Data Acquisition (DAQ) system. There is also a small bidirectional interface to configure the frontend cards. The successor of the GeSiCA module is the HotGeSiCA, which was first used during the hadron run 2004, see section 5.1. For more details about the readout chain and the zero suppression algorithm, see [Gru01], [Gru06] and [COM07a].

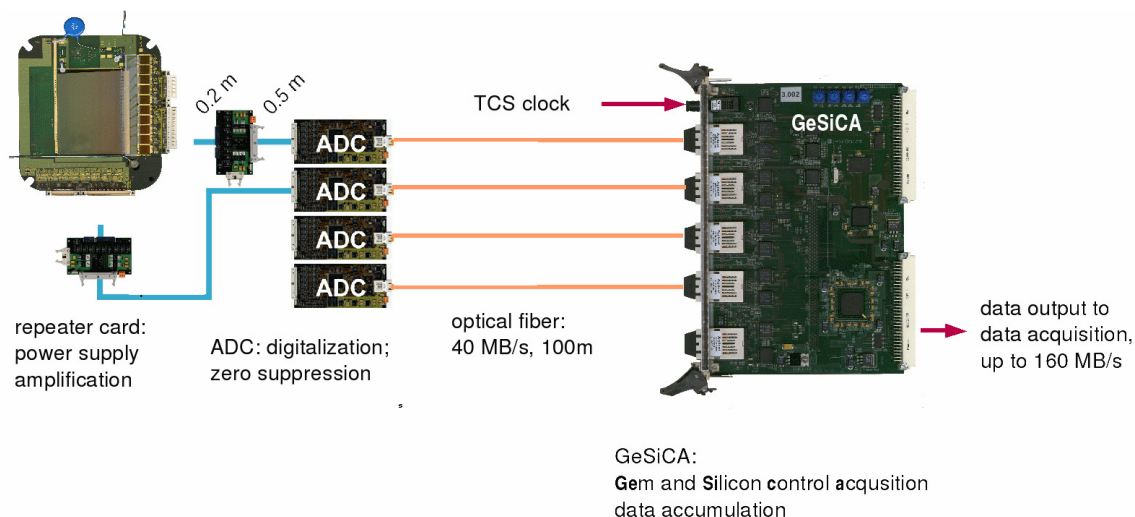


Figure 3.4: Readout chain of the COMPASS silicon detector.

3.2.5 The Silicon Detector Station

Two of these silicon detector modules are grouped into one silicon station. They are mounted on a glass-fibre frame (Stesalit), such that one detector measures the horizontal (X) and vertical (Y) coordinates of a particle trajectory, while the other is rotated with respect to the beam axis by 5° , providing two additional projections (U,V), see Fig. 3.5. The wafers are oriented such that the X and U planes constitute the n-side and the Y and V planes the p-side of the wafer, respectively. These projections X, Y, U and V are supposed to have rotation angles with respect to the COMPASS main reference system of 0° , 90° , 5° , and -85° , see Fig. A.1, since tracking works in projections, see subsection 2.3.5. In direction of the Z-axis they keep the following order U, V, Y and X.

Fig. 3.6 shows a photo of the open cryostat with the detectors inside. The cryostat was designed in view of cooling the detector with liquid nitrogen, requiring vacuum shielding, see subsection 3.3. This cryostat provides connections for vacuum equipment and serves as electrical shielding. A first version of vacuum feedthroughs for the electronic consisted of two PCB connectors which were sealed with epoxy glue into aluminium flanges with two thin feedthroughs. In the actual setup, developed in 2008, they are replaced by more appropriate commercial chrome sealings [Fri10]. The front and back sides of the cryostat are covered by light tight detector flanges that are optimised for low mass density. The window of the flange has the size of 260 cm^2 and is covered with aluminised mylar foil with a mass density of 3.48 mg/cm^2 . Together with a Kevlar support structure, the window was developed for vacuum applications as well and could reach a mass density of only 6.73 mg/cm^2 [Din03]. In the final design (2008), the Kevlar yarn is replaced by a carbon mesh, but the principle of supporting an aluminised mylar foil was kept. Further information with detailed descriptions of the COMPASS silicon detector modules and stations are given in [Ang03], [Wie04], [DeM04] and [Wag01].

Each silicon module is attributed a unique name with pattern e.g. SIL12, SIL13 and so on. A complete silicon station as it is mounted in the experiment is referred to as SI01 to SI05. In the following text, a single projection of a silicon station will be named e.g. SI02X, SI04V, SI05Y and a silicon module e.g. SI01XY, SI03UV.

3.2.6 The Detector Station in COMPASS

The beam in COMPASS enters the experimental area in 315.2 cm height over the floor level. In the COMPASS experiment, the silicon stations are placed on a optical bench on top of concrete blocks in 240 cm height. This optical bench is made of highly braced iron bars with 120 cm long granite rails.

The use of silicon detectors in COMPASS depends on the physics program which COMPASS follows. Since the commissioning phase of COMPASS (in the year 2001) till September 2004, the experiment was running with a muon beam. For the muon program, the silicon stations were used for beam definition. In the muon run 2002, two silicon stations were used as beam telescope, while for 2003, 2004 and 2006 three silicon stations were

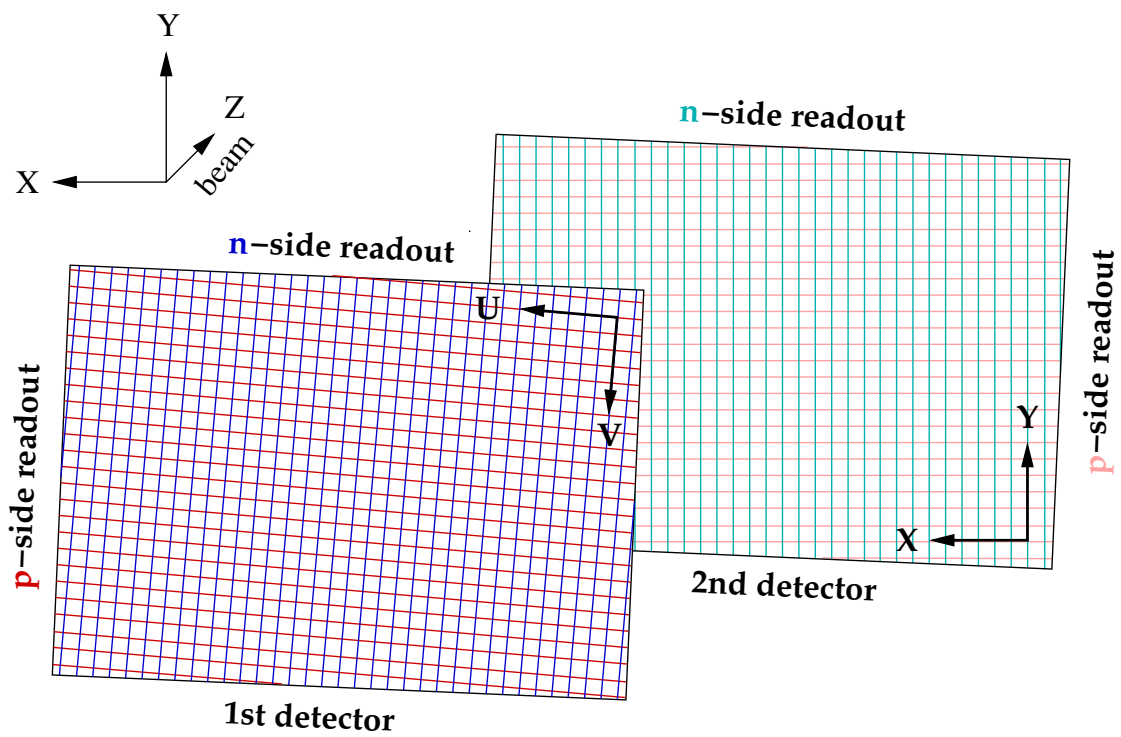


Figure 3.5: Scheme of the geometry of the silicon detectors mounted in a cryostat.

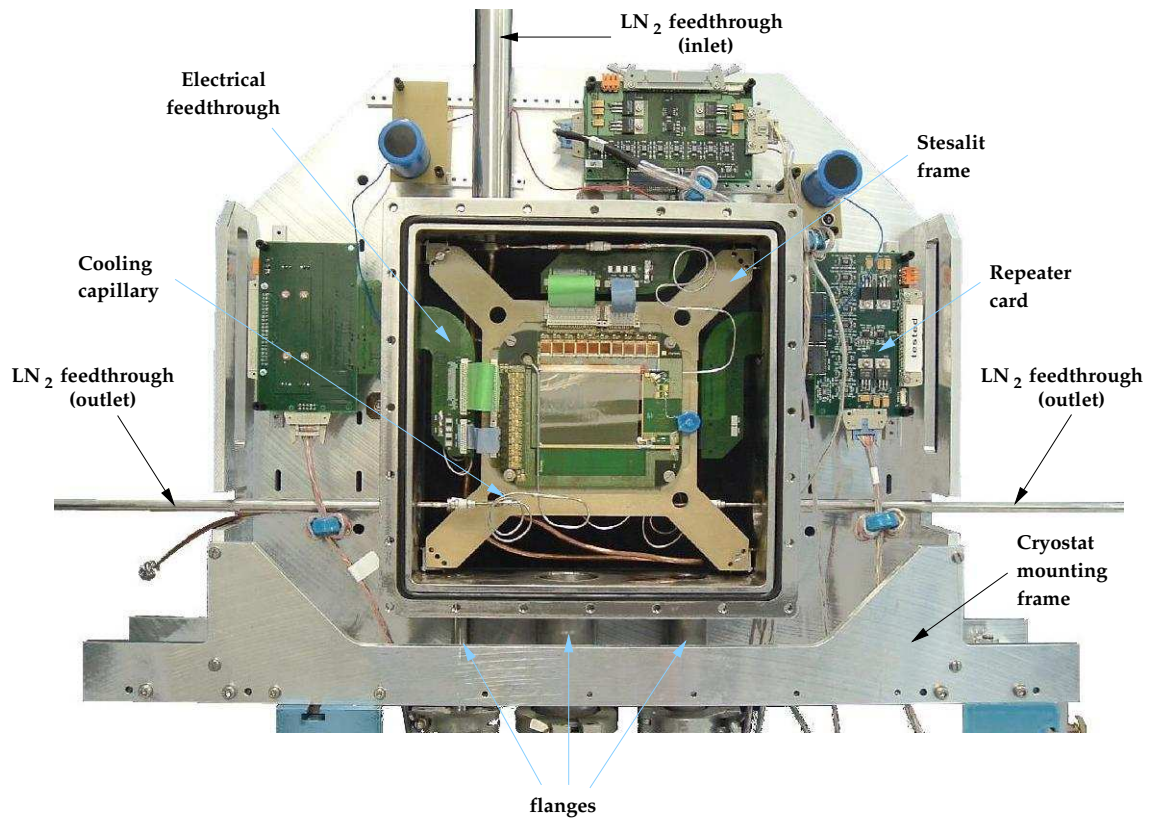


Figure 3.6: Silicon station: At the bottom sides, flanges for vacuum equipment are implemented. Electrical feedthroughs for the front-end electronics are placed on flanges at the sides and the top of the cryostat. Feedthroughs for liquid nitrogen are situated at the top (inlet) and the sides (outlets) which are dismantled when the silicon station is operated at room temperature, Fig. from [Bec04].

3 THE COMPASS SILICON MICRO-STRIP DETECTOR

installed, including 6 silicon modules determining 3×4 projections. Table 3.1 lists all detectors and their corresponding station names which were in use during these years. Fig. 3.7 shows a drawing of the typical setup of the target region for a muon run and on top a photo of the setup for the year 2004. In all muon periods of collecting data, each silicon detector was exposed to a fluence of about $5 - 8 \cdot 10^{13}$ muons/cm² in the central region [Gra09]. An increase of noise combined with a decrease of the signal amplitude due to radiation damage was observed for the central region of the silicon detectors. The leakage current, e.g. for SIL11, increased from about 70 μ A to 270 μ A within the beam time in 2004 and 140 μ A to 700 μ A in 2006 [Gra09]. Up to now these effects have been compensated by increasing the depletion voltage about 15 - 20 V on average for each year of muon run.

Year	Installed SI-Stations		
2002	SI01	SI02	–
2003	SI01	SI02	SI03
2004	SI01	SI02	SI05
2006	SI01	SI02	SI03
Names of the modules			
UV	SIL11	SIL08	SIL16
XY	SIL10	SIL12	SIL13

Table 3.1: Number and names of silicon stations and silicon modules installed during the muon beam times 2002 to 2006.

For the physics with hadron beams, it is necessary to have precise track reconstruction downstream the target and a good vertex resolution. During the first hadron beam time of COMPASS, two silicon stations were placed upstream the target for beam definition and three stations downstream the target for track reconstruction, see Fig. 3.8. In total 10 silicon modules were determining 5×4 projections. All silicon detectors which came into operation during the hadron run are listed in Table 3.2, sorted by their module and station names. More detailed information about the performance of the detectors during the hadron run in 2004 is given in chapter 5.

SI-Station	SI01	SI02	SI03	SI04	SI05
UV	SIL20	SIL22	SIL16	SIL11	SIL08
XY	SIL18	SIL21	SIL13	SIL10	SIL12

Table 3.2: Silicon modules installed during hadron beam time 2004.

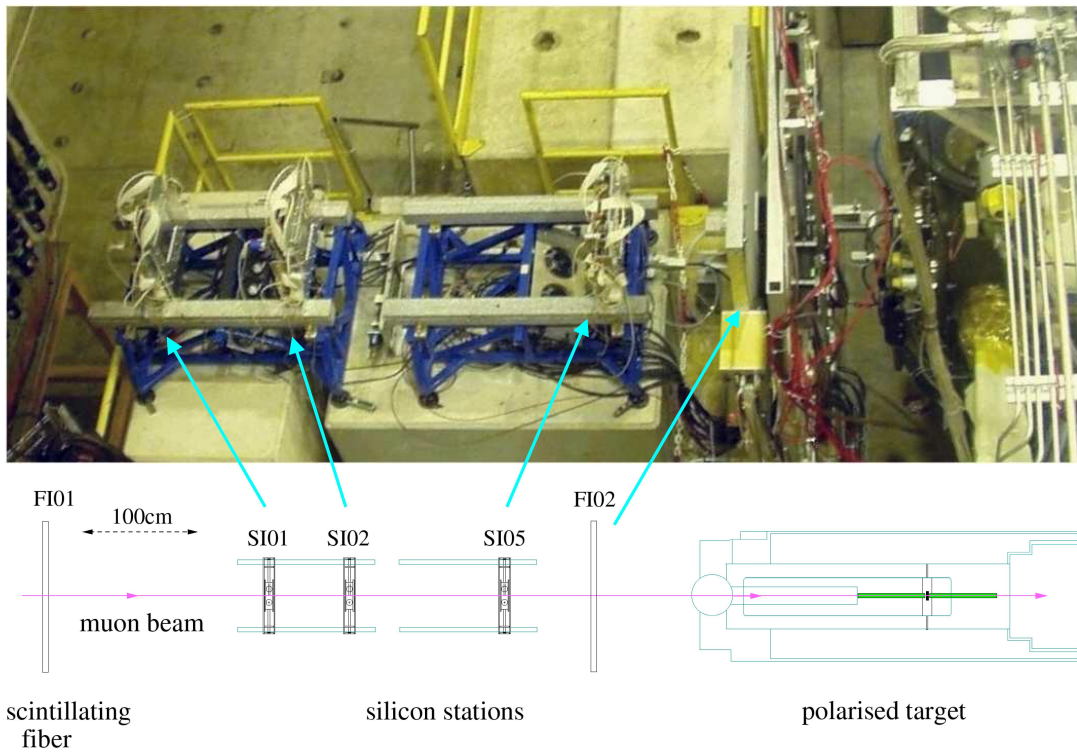


Figure 3.7: Silicon stations in muon run 2004.

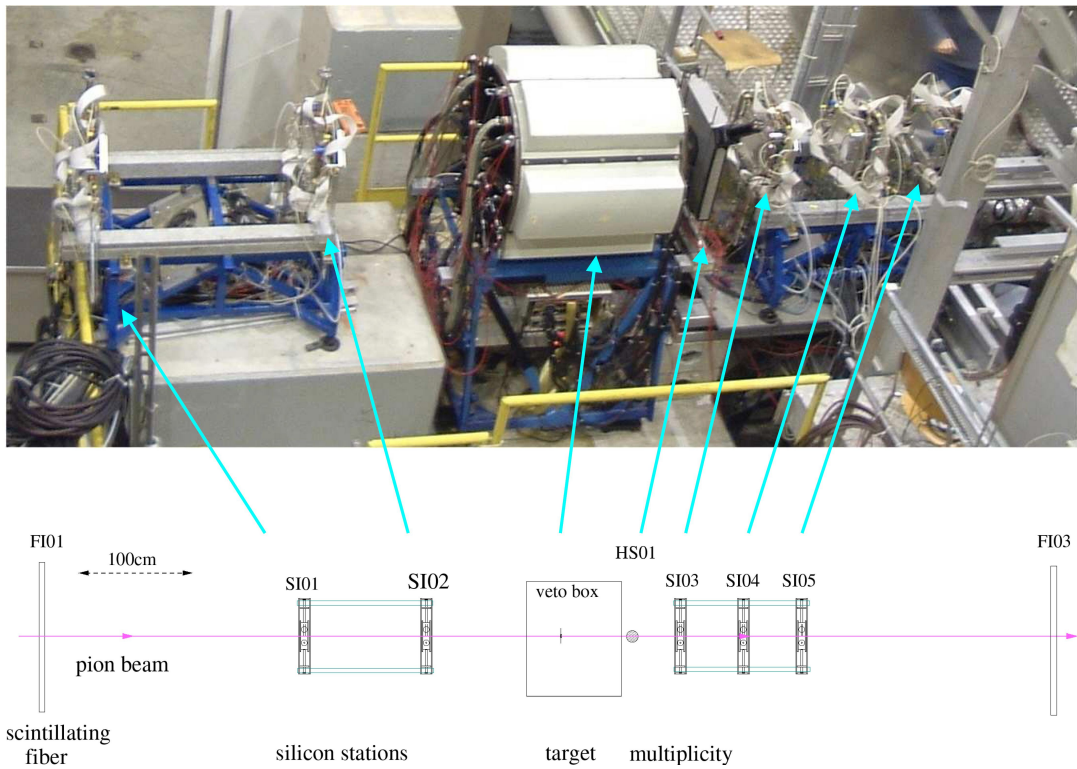


Figure 3.8: Silicon stations in hadron run 2004.

3.3 Cryogenic Development - an Outlook

For the future COMPASS hadron beam times, the beam intensity is foreseen for up to 10^8 hadrons per spill which means the silicon detectors will be damaged by radiation. The design goal of the COMPASS silicon detectors is to increase the radiation hardness by exploiting the Lazarus effect [Pal98] for irradiated detectors which causes a partial recovery of the charge collection efficiency (CCE) at cryogenic temperatures. It has been determined experimentally, that the CCE recovery has its maximum for cryogenic operation at 130 K. The operation of a silicon detector at 130 K requires a special infrastructure on the detector modules and at the silicon station. A first design of the silicon module and the cryostat in order to cool the detector with liquid nitrogen is described in [Wie04] and [DeM04]. Such a cryogenic operated silicon station needs a distribution system for the liquid nitrogen [Bec04] and a steering and safety system [See04]. During a two weeks test beam in 2003 a test setup was installed in the COMPASS beam telescope. One detector station was operated at 130 K, the results are presented in [Din03]. Recently, the cryogenic setup was completely revised with the support of the COMPASS groups from Torino and Saclet. In the beam time 2008 and 2009 the silicon detector stations were successfully put in stable operation at cryogenic temperatures [Fri10], [Gra10].

Chapter 4

Characterisation of the COMPASS Silicon Detector

This chapter describes how the spatial and time information of the particle trajectories traversing the silicon detectors are reconstructed from amplitude signals. This is called the *clustering process* of the detectors. In the following, the results on the time resolution for a single silicon plane, the track time resolution of the silicon telescope and the achieved spatial resolution are presented.

4.1 Detector Signal

A particle traversing the silicon sensor creates a cylindrical volume of electron-hole pairs around the track. Typically, a minimum ionising particle creates on average about 80 electron-hole pairs per μm path length in silicon, statistically varying such that the deposited energy is Landau-Vavilov distributed [Spi05]. Due to the electric field of the applied bias voltage, the electrons move to the n-side (on positive bias voltage), and the holes to the p-side. The charge collection time in a typical fully-depleted, 300 μm thick silicon detector is about 10 ns for electrons, and 25 ns for holes [PDG06]. The drifting charge induces a current in the metalised readout strips which are capacitively decoupled from the silicon bulk, see 3.2.2. Fig. 4.1 shows exemplarily the signal current for a double-sided micro-strip detector. The pulse duration is determined by the collection time, with different shapes on the two sides [Spi05]. Each strip is read out by a charge sensitive amplifier followed by a switchable unity gain converter to allow both p- and n-strip readout. The low noise CR-RC-shaping unit¹ transforms the integrated charge-pulse into a well defined voltage pulse. The signal, which is digitised by the ADC and finally sent to the DAQ, is determined by the convolution of the detector signal and the behaviour of the APV25 shaper. The response of this APV25 frontend chip for a δ -like input from

¹CR-RC: A preamplifier is followed by a low-pass and high-pass filter which have the function of a "Differentiator" and "Integrator", respectively, to a signal.

4 CHARACTERISATION OF THE COMPASS SILICON DETECTOR

a pulse generator was studied in [Wie04]. The response function may be approximated by a combination of two exponentials which is motivated by the pure capacitor-resistor network,

$$(4.1) \quad A(t) = A_0 \cdot e^{-(t-t_0)/\tau_{\text{fall}}} \cdot (1 - e^{-(t-t_0)/\tau_{\text{rise}}})$$

where $\tau_{\text{rise}} \approx 22 \text{ ns}$ and $\tau_{\text{fall}} \approx 100 \text{ ns}$ are the time constants of the shaping circuit of the rising and the falling components, valid for the APV25s at room temperature, A_0 is the amplitude and t_0 the arrival time of the signal. In Fig. 4.2 the fit to the response function is shown.

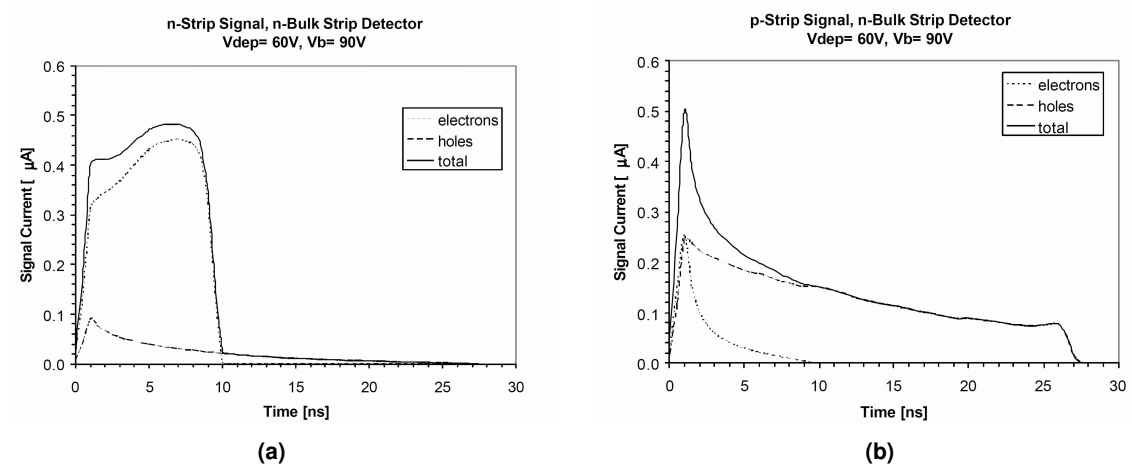


Figure 4.1: The signal current of a double-sided n-bulk strip detector with 60 V depletion voltage operated at a bias voltage of 90 V. The electron (e) and hole (h) components are shown together with the total signal (bold), from [Spi05]. Due to the capacitive coupling at very early times both charge components contribute, while later only the faster e^- or slower (holes) drifting charges are seen.

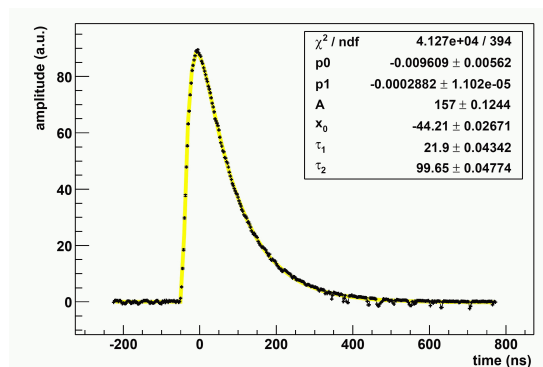


Figure 4.2: Response function of the APV25 frontend chip for a δ -like input signal fitted by eq. (4.1) plus a first order polynomial, from [Wie04].

4.2 Time Reconstruction

The APV25 frontend chip continuously samples the analog signals of the micro-strips at a frequency of 38.88 MHz, synchronised with the reference clock of the trigger control system (TCS) of the experiment. The signals are stored for up to 4 μ s in a capacitor array acting as a ring buffer (as described in subsection 3.2.4). Upon trigger, the stored data are marked for readout at a latency which is adjusted to the trigger delay, so that the raising edge of signals coincident with the trigger is recorded. Since the sampling happens prior to the trigger generation, the adjustment of the latency is made only in steps of the clock period of about 25.8 ns. In order to extract the timing information with higher precision, the trigger time is measured with respect to the TCS clock. The difference between the rising edge of the TCS clock and the trigger time is called *TCS phase* and gives the respective correction:

$$(4.2) \quad t_{\text{TCS phase}} = t_{\text{TCS clock}} - t_{\text{trigger}}$$

The APV25 is operated in the so called *multi-mode*, meaning that with every event the APV25 writes out three samples of the signal shape $A(t)$ consecutive in time, so spaced by the period of $\Delta = 25.8$ ns of the TCS clock cycle. The three samples are the amplitudes

$$(4.3) \quad a_0 = A(t_2 - 2\Delta), \quad a_1 = A(t_2 - \Delta) \quad \text{and} \quad a_2 = A(t_2)$$

of the signal with respect to the time t_2 of the a_2 readout. This represents the partial determination of the signal shape $A(t)$, from which the signal time can be reconstructed with much higher resolution as described in detail in the following.

Since the energy loss distribution of a particle in the silicon detector can be approximated by a modified Landau distribution, the signal amplitude per particle varies. In order to be independent of the varying amplitude of the signals, in the following the ratios of these amplitudes are considered:

$$(4.4) \quad r_{02}(t) = \frac{a_0}{a_2} \quad \text{and} \quad r_{12}(t) = \frac{a_1}{a_2}$$

Here, it is assumed that the signal shape $A(t)$ factorises as $A(t) = A_0 \cdot r(t)$, with $r(t)$ which turns out to be correct within the precision relevant here. The signal timing functions r_{02} (and r_{12}) can be extracted from the experimental data with no necessity for a model as e.g. eq. (4.1).

The time dependence of the amplitude ratios r_{02} and r_{12} is displayed in Fig. 4.3. Within the black lines, the optimal latency configuration l is marked, where both amplitudes a_0 and a_1 lie on the rising edge of the signal. It also shows the ratio correlations for off-time events in case the detector was readout one clock cycle too early (negative time difference, $l + 1$). In that case, the distribution runs towards zero, since the particle has not yet crossed the detector. If the readout was one clock cycle too late, ($l - 1$), e.g. due to a late trigger, the ratios approach a constant value, reflecting the exponential decay of

4 CHARACTERISATION OF THE COMPASS SILICON DETECTOR

the detector signal. In principle, the amplitude ratio functions should be deducible by the characteristics of the electronics with its shaping and integration parameters. From the theoretical shape of the signal, the ratio function could be calculable. However, it turned out that the signal response of the detector, the properties of the APV-preamplifier and ADC readout chain is not sufficiently understood to follow this method and an other approach has been followed. The ratio distributions are found by a detailed investigation

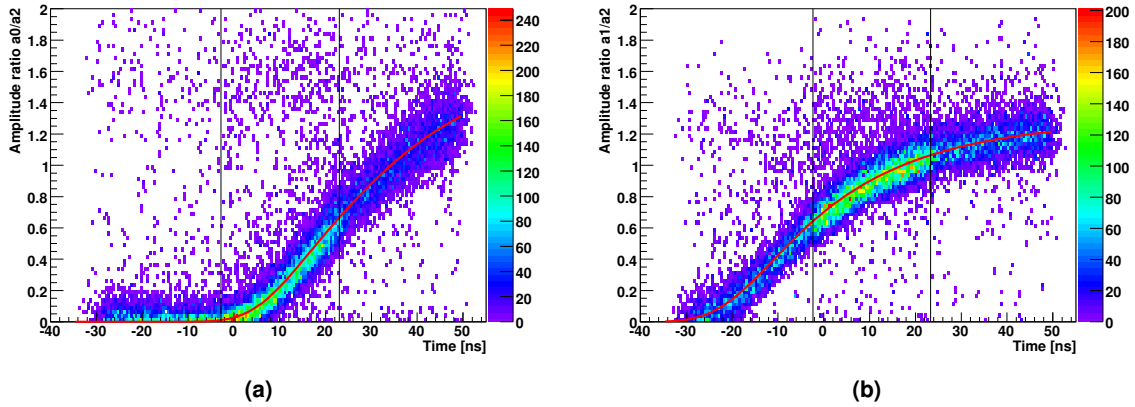


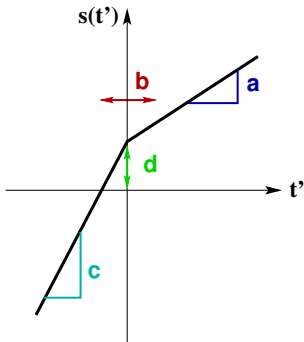
Figure 4.3: Typical dependence of in-time signal ratios $r_{02}(t)$ (left) and $r_{12}(t)$ (right) on the 25.8 ns long TCS clock cycle marked out by the black lines. The ratio correlations for off-time events in case the detector was read out one clock cycle too early (negative time difference) and one cycle too late (time difference larger than 25.8 ns) can clearly be seen. These two distributions belonging to the detector plane SI01Y (silicon module SIL10) were produced in conjunction with the time calibration for muon beam time in 2006, see section 4.4. The red curve is the function eq. (4.5) with the parameter set determined by the time calibration.

of the experimental data to follow the parametrisation [Fri04]

$$(4.5) \quad r(t) = r_0 \cdot \exp[-\exp[-s(t')]]$$

$$\text{with } s(t') = \left(\frac{a+c}{2} \cdot t' + \frac{a-c}{2} \left(\sqrt{t'^2 + b^2} - |b| \right) \right) + d$$

$$\text{and } t' = t - t_0$$



with fit parameters a , b , c , d , r_0 , t_0 and the signal time t with respect to the TCS phase. r_0 is the maximum ratio, where the function converges, and t_0 is the inflection point. The parameter d is responsible for the value of the ratio at this inflection point. The function $s(t')$ consists of two parts whereby the sum and the difference of the parameters a and c determine the gradient of each part. The parameter b is the transition width of merging these two parts.

This parametrisation is sufficiently flexible to describe all observed signal shapes, including those measured at cryogenic operation, see subsection 3.3, where the signal is significantly faster [Ang03]. In addition, this parameterisation is analytic and allows an exact error propagation from the known error on the amplitude measurement to the timing information. The parameters were optimised for the 2004/2006 muon setup and 2004 hadron setup which are listed as an example in the appendix, see Table D.3. Due to its compact and numerically rapidly evaluable form, it is possible to use it also in the COMPASS online filter (subsection 2.3.1) where in fact this algorithm was first implemented [Nag05]. Here, the beneficial property of being invertible is used:

$$(4.6) \quad \begin{aligned} t(r) &= t_0 - s^{-1} \left(\log \left[-\log \left(\frac{r}{r_0} \right) \right] \right) \\ \text{with } s^{-1}(x) &= \frac{1}{2ac} \left[(a+c) \cdot f(x) - (a-c) \cdot \sqrt{f(x)^2 + acb^2} \right] \\ \text{and } f(x) &= x - d + \frac{b}{2} \cdot (a-c) \end{aligned}$$

The parameters of eq. (4.5) are determined by the time calibration procedure which is described in section 4.4.

4.3 Determination of the Signal Shape from the Data

The signal shape $a(t)$ can be deduced from this parameter set which is determined by the time calibration. According to eq. (4.3) and eq. (4.4), the ratio $r(t)$ can be calculated

$$(4.7) \quad r(t) = \frac{a(t)}{a(t+\Delta)} \quad \Rightarrow \quad a(t) = r(t) \cdot a(t+\Delta)$$

with $\Delta = 25.8$ ns of the TCS clock cycle. So, the signal shape $a(t)$ can be written as the products

$$(4.8) \quad a(t) = \left(\prod_i^{N-1} r(t+i\Delta) \right) \cdot a(t+N\Delta)$$

with N the number of time intervals. If the amplitude $a(t+N\Delta)$ is far in the falling edge of the signal which (presumably) follows an exponential decay, the ratio $r(t)$ is at a constant maximum value r_0 which corresponds to the parameter r_0 of eq. (4.5). So, the last term of the product in eq. (4.8) can be approximated to a very good precision

$$(4.9) \quad a(t+N\Delta) = r_0 \cdot a(t+(N+1)\Delta), \quad N \gtrsim 8$$

4 CHARACTERISATION OF THE COMPASS SILICON DETECTOR

and modelled by an exponential with the decay constant τ which is related to r_0 via

$$(4.10) \quad e^{-(t+N\Delta)/\tau} = r_0 \cdot e^{-(t+(N+1)\Delta)/\tau}$$

$$(4.11) \quad r_0 = e^{\Delta/\tau} \Rightarrow \tau = \frac{\Delta}{\log(r_0)}$$

So, the signal shape $a(t)$ can be calculated with

$$(4.12) \quad a(t) = \left(\prod_i^{N-1} r(t+i\Delta) \right) \cdot e^{-(t+N\Delta)/\tau},$$

choosing N such that $a(t+N\Delta)$ is safely in the falling signal part for the considered times t .

The top graph in Fig. 4.4 shows the signal time structure as determined by the ratio functions, indicated in the two lower plots for the amplitude ratios a_0/a_2 and a_1/a_2 . The calculation is performed according to eq. (4.12) and the needed set of fit parameters was extracted from experimental data, see section 4.4. The signal shapes are normalised with its maximum value and the used number of time intervals is $N = 8$. The two lower plots in Fig. 4.4 show a typical shape of the corresponding functions $r_{02}(t)$ and $r_{12}(t)$. Since three amplitudes a_0 , a_1 and a_2 are measured, two independent timings can be extracted. The upper graph shows the two time evolutions eq. (4.6) of the amplitude calculated from $r_{02}(t)$ and $r_{12}(t)$. The difference (shaded in green) between the two signal shapes is less than a few percent, this is the region where a_2 is not sensitive to the signal. This confirms, that both parameter sets determine independently the same signal shape. Obviously, this fact can be used also as constraint in the parameter fitting procedure.

In order to calculate a common time value (strip-time) t out of $t_0(r_{02})$ and $t_1(r_{02})$, the error on both values has to be taken into account. For each of the three measured amplitudes, their common uncertainty σ_a is known due to the regular measurement (once per week) of the pedestal of the chip and noise values. The absolute error on a ratio $r_x = a_x/a_2$ can be determined by the error propagation of the amplitude uncertainties:

$$(4.13) \quad \sigma_{rx} = \frac{a_x}{a_2} \sqrt{\left(\frac{\sigma_a}{a_x}\right)^2 + \left(\frac{\sigma_a}{a_2}\right)^2} = \frac{\sigma_a}{a_2} \cdot \sqrt{a_x^2 + a_2^2}.$$

However, due to the strong curvature of $t(r)$, a Gaussian error makes not much sense, and the error has to be treated asymmetrically and is split in an "downward" error σ_{tx}^- and "upward" error σ_{tx}^+

$$(4.14) \quad \sigma_{tx}^+ = t_x(r) - t_x(r + \sigma_{rx}), \quad \sigma_{tx}^- = t_x(r - \sigma_{rx}) - t_x(r).$$

For each measured amplitude-set per detector channel, the ratios, the time and their asymmetric errors (r_{02} , t_0 , $\sigma_{t_0}^-$, $\sigma_{t_0}^+$ and r_{12} , t_1 , $\sigma_{t_1}^-$, $\sigma_{t_1}^+$) are calculated. The combined strip-time t can be estimated as the mean value of t_0 and t_1 and each weighted by the

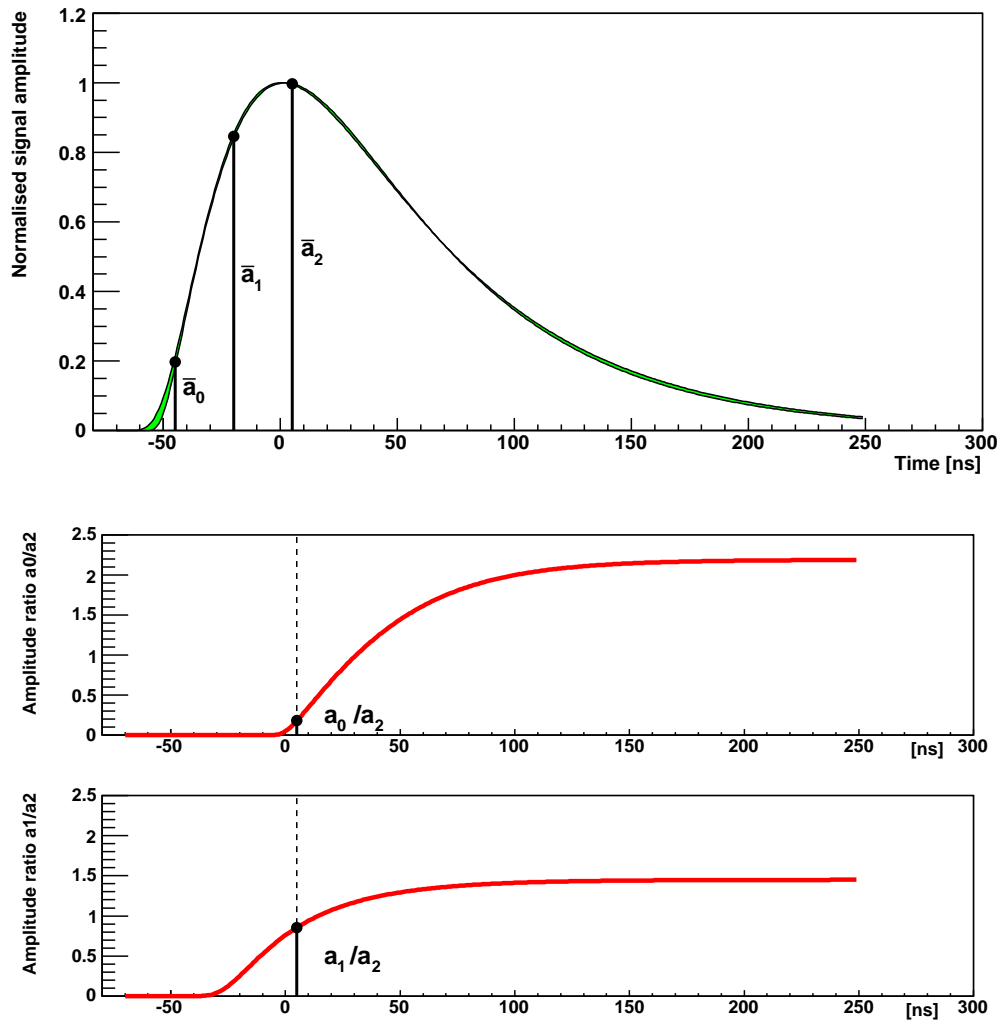


Figure 4.4: The top graph displays the signal time structure as determined by the ratio functions, indicated in the two lower plots for the amplitude ratios a_0/a_2 and a_1/a_2 . Since three amplitudes are measured, two independent timings can be extracted. The upper graph shows the two time evolutions eq. (4.6) of the amplitude calculated from $r_{02}(t)$ and $r_{12}(t)$. This confirms that both parametrisations follow from the same signal shape on the level of a few percent, as it should be.

4 CHARACTERISATION OF THE COMPASS SILICON DETECTOR

uncertainty in the direction of the other

$$(4.15) \quad t = \frac{t_1 \sigma_0^2 + t_0 \sigma_1^2}{\sigma_0^2 + \sigma_1^2}$$

The asymmetric errors of the combined strip-time σ_t^+ and σ_t^- are calculated separately in each direction by error propagation

$$(4.16) \quad \sigma_t^+ = \frac{1}{\sqrt{\frac{1}{(\sigma_{t0}^+)^2} + \frac{1}{(\sigma_{t1}^+)^2}}}, \quad \sigma_t^- = \frac{1}{\sqrt{\frac{1}{(\sigma_{t0}^-)^2} + \frac{1}{(\sigma_{t1}^-)^2}}}.$$

The combined strip-time and the appropriate error calculations are essential for the clustering algorithm. A more detailed discussion of the time error propagation can be found in [Nag05].

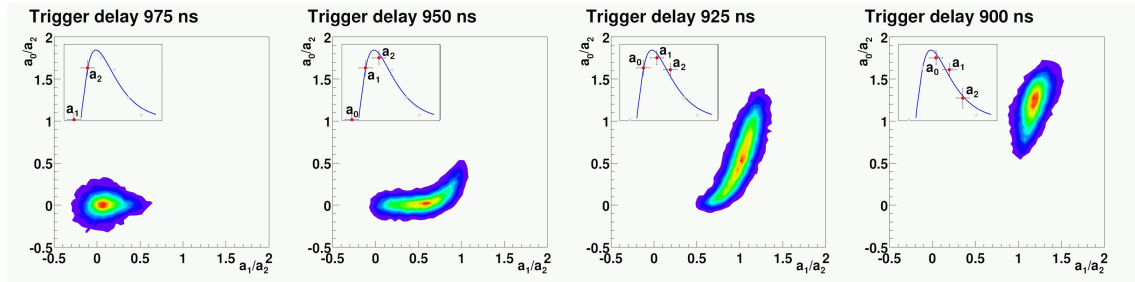


Figure 4.5: The correlations of the amplitude ratios a_0/a_2 and a_1/a_2 for four different trigger delays and latencies, respectively. For each configuration the position of the three amplitudes with respect to the silicon signal is given. The second panel shows a correct adjustment of the latency. The amplitude ratios were blurred to avoid artifacts since they are fractions of small integer values, from [Wag01].

Fig. 4.5 illustrates for four different latency adjustments and trigger delays, respectively, the correlation of the two amplitude ratios r_{02} and r_{12} . For each configuration, the position of the three amplitudes with respect to the silicon signal is given. If the readout of the signal amplitudes starts too early, e.g. due to a wrong latency adjustment, the signal amplitude a_2 has to be at least 4σ above noise level. The measured amplitudes for a_0 and a_1 are dominated by the noise. The corresponding amplitude ratios r_{02} and r_{12} are filled around zero. For a later sampling, a_1 picks up the signal amplitude at the rising edge, but a_0 still measures noise. The amplitude ratio r_{12} starts to rise while r_{02} remain at zero. In an optimal configuration, the latency is adjusted such that a_0 and a_1 pick up the rising edge. This leads to the bending of the amplitude ratio distribution. In case of a late timing and too small latency, respectively, all three signal amplitudes lie on the falling edge of the signal. Since the falling edge follows an exponential, the amplitude ratios reach a constant value.

4.4 Time Calibration

The time calibration of the silicon detectors is part of the commissioning procedure of the COMPASS spectrometer at the beginning of each beam time. Fig. 4.6 outlines a possible work flow of this phase. When the beam starts, first the trigger logic is tested and timed-in. As soon as at least the beam trigger, see 2.2.4.3, is adjusted, the scintillating fibre detectors (SciFi/FI) and the silicon detectors can start with dedicated runs for their time calibration. Valid time calibrations of the SciFi detectors are a requirement for the time calibration procedure of the silicon detectors. Also other detectors have to perform calibration runs which are needed before the first alignment of the spectrometer can be determined. Afterwards, the production of mDST data, see 2.3, can be started. Usually within about two weeks, all detectors are set up and prepared for collecting physics data. The silicon time calibration is needed for the online filter, see 2.3.1, and for the off-line analysis of the data.

Time calibration of the silicon detectors means to determine the parameters of the function (4.5) which describes the analytical relation of calculating the signal time from the signal amplitude ratios. Several different steps are necessary to derive these parameters for each silicon detector plane.

At the beginning of each beam time, dedicated calibration runs for the silicon time calibration have to be taken with different latency adjustments. The latency is set in units of 25.8 ns clock cycles. It is sufficient for the time calibration to cover a time window of about 200 ns which corresponds to eight latency steps². For these calibration runs, it is convenient to reduce the beam intensity from $2 \cdot 10^8$ particles per SPS cycle to a lower intensity in the order of $1 \cdot 10^6$ particles per SPS cycle. This has the advantage that multi-hit ambiguities and pile-up events are much reduced and the signal for calibration is much cleaner.

Until the time calibration is available, the detectors have to be adjusted in the right time window and latency step, respectively, which is the case if the three signal amplitudes a_0 , a_1 and a_2 lie at the rising edge of the signal, see top graph in Fig. 4.4. A hint, if the detector is adjusted in the right time window gives the correlation between amplitude ratios r_{02} and r_{12} , as shown in ratio plot e.g. Fig. 4.7 generated online by COOOL (the COMPASS online monitoring program, see 2.3.3). The black box marks the region in which all events, initiated by the trigger signal, should lie in if the detector is timed in.

For the time calibration, only amplitude signals related to the particle initialising the trigger are of interest. Those signals are enriched with respect to the background if the corresponding track is reconstructed and the time of the track can e.g. be restricted by other information of the detector. Therefore, the runs for the latency scan are analysed with COOOL using its tracking method. The straight line tracking is activated for the silicon telescope and the scintillating fibre detectors, usually FI01 and FI02 for muon run

²The typical latency value for the silicon detectors with the trigger in the years 2000 - 2009 is 70. This value is predefined by the cable length which the trigger signal has to pass until it arrives the readout system of the detector.

4 CHARACTERISATION OF THE COMPASS SILICON DETECTOR

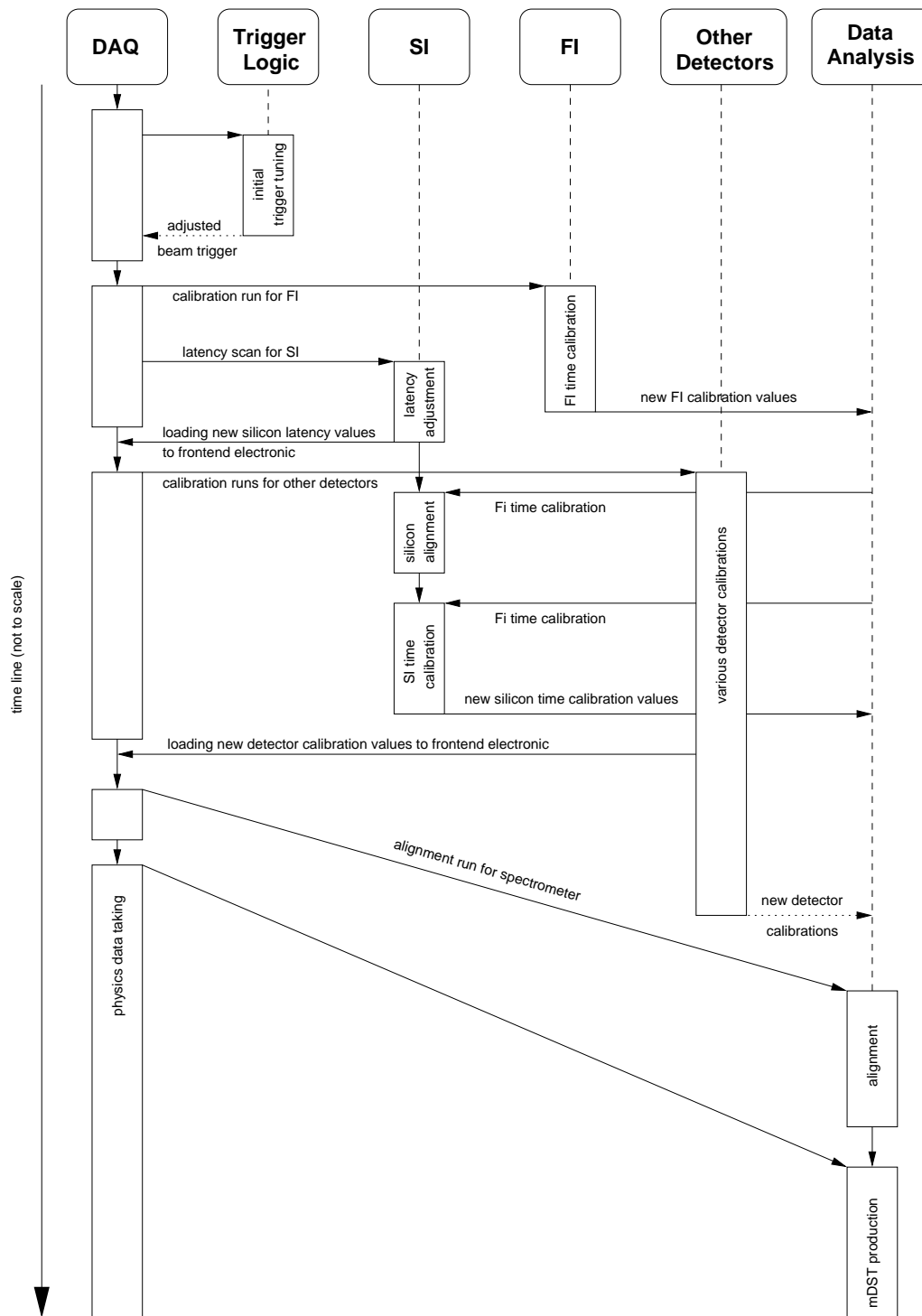


Figure 4.6: A possible work flow of the commissioning phase for the COMPASS beam time from the point of view of the silicon detector group.

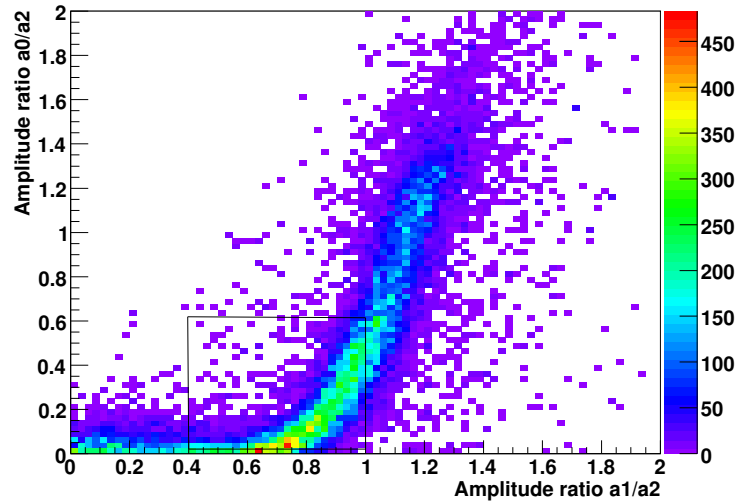


Figure 4.7: The correlation between the amplitude ratios r_{02} and r_{12} . In case the latency of a silicon detector plane is correctly adjusted, the amplitudes lie at the rising edge of the signal and their ratios r_{02} and r_{12} can be found in the region indicated by the black box (see Fig. 4.5). This histogram was generated for SI01Y (silicon module SIL10) of the run 47779 in muon beam time 2006.

and FI01 and FI03 for hadron run, see Fig. 3.7 and Fig. 3.8 on page 31. This tracking is sufficiently fast to loop over all hit combinations since the track determination involves only a single matrix inversion.

Usually by the time when the calibration is performed, an official COMPASS alignment file, see end of subsection 2.3.5, is not yet available because e.g. the silicon time calibration files are missing, see Fig. 4.6. With the help of the COOOL tracking package, it is possible to perform independently a quick pre-alignment of the silicon telescope. The only necessity are time-calibrated SciFi detectors in the target region and at least one trigger (usually the beam trigger) in its final configuration. If the tracking in COOOL is active, the residual δ of the track position x_{track} and the position of the hit x_{hit} of each silicon and SciFi plane are calculated

$$(4.17) \quad \delta = x_{\text{track}} - x_{\text{hit}}$$

and written in a ROOT-TTree. COOOL is configured such, that only a part of the detectors are considered by the tracking algorithm and the other detectors stay passive. Those active trackers act as pivot elements and the mean shifts of the residuals of the passive detectors according to these pivot detectors are determined.

The residual distributions are fitted by a Gaussian distribution, and the detector positions in the alignment file are corrected by the mean value of the fit. The newly calculated detector positions are written in a new alignment file and the data sample is processed once again in a new iteration. From iteration to iteration, the pivot planes for tracking are

changed. This procedure is finished until the χ^2/ndf -distribution of the tracks can not be enhanced by a further iteration, see Fig. 4.8. In appendix D.1 technical details of this alignment procedure are documented, including the specific configurations of COOOL and the used macros. More on the alignment of a silicon telescope with COOOL can be found in [Din03].

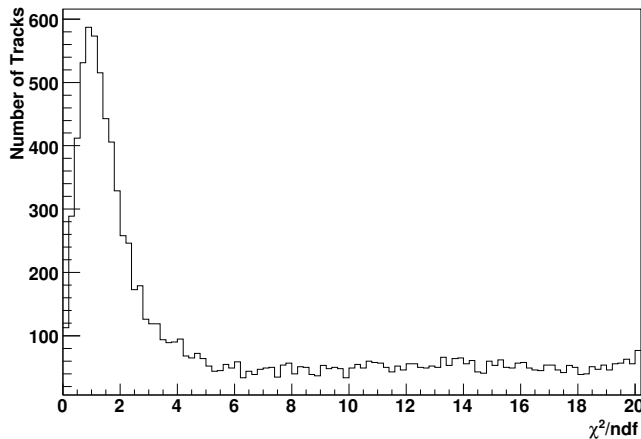


Figure 4.8: χ^2/ndf -distribution of beam tracks after an alignment with COOOL performed on a chunk of run 47779 of 2006 muon data.

With the silicon telescope aligned, only hits are stored in the final ROOT-TTree that are associated with tracks having a $\chi^2/ndf < 10$. In addition, only tracks are selected where the hits in FI01 and FI02 have a time difference of less than 2 ns, so that noise and background tracks due to pile-up and beam halo are massively reduced. The time gate between the scintillating fibres and the trigger time is opened up to 100 ns in order to have tracks in the sample which are off-time. Fig. 4.3 exemplarily shows the walk of in-time signal ratios r_{02} and r_{12} for the projection SI01Y (SIL10 p-side) in muon run 2006. Those distributions are generated for all silicon planes and each latency step of the calibration runs. In order to receive the time calibration parameters, the walk of in-time signal ratios are fitted by the eq. (4.5). To avoid a complicated 2D-fit, these histograms of Fig. 4.3 are split up into bins of 0.5 ns along the time axis. Each of these 1D-distributions are fitted by a simple Gaussian function as it is shown in Fig. 4.9. This is done for all latency steps of each detector plane, and the mean values of the Gauss fits are combined into one histogram, see Fig. 4.11. The stability of the Gauss fits is monitored by a performance histogram, see Fig. 4.10 for the example plane SI01Y, where the parameters of each single Gauss fit are displayed: the σ , the number of events per entries and the χ^2/ndf . For ratio r_{02} the χ^2/ndf gets worse for negative time values. The reason is that the first amplitude a_0 is taken well before the signal raises, so a_0 is expected to be zero and thus the ratio r_{02} as well. In reality, it is not zero and it represents the noise level at this stage where very small values are measured. In case those ratios are smaller than 0.04 the algorithm sets them manually to zero applied with a comparatively large error of 0.05. The mean values and

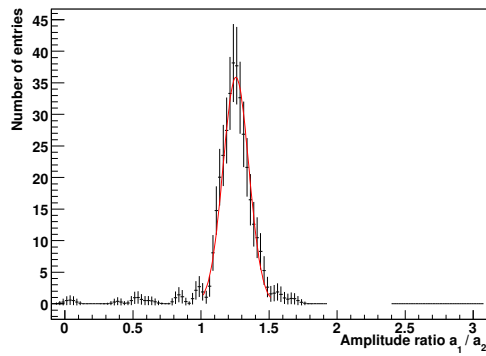


Figure 4.9: The amplitude ratio distribution for a particular time bin of 0.5 ns is fitted by a Gaussian function.

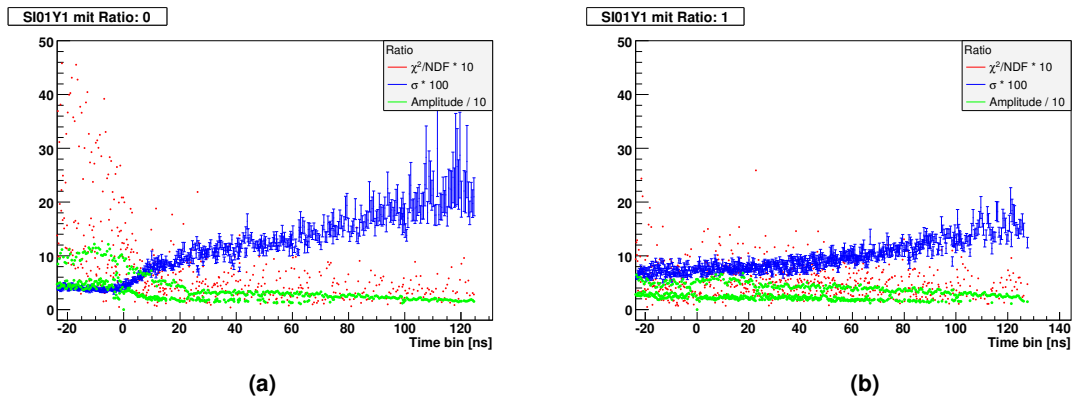


Figure 4.10: Stability of Gauss fits can be checked by looking at the amplitude of the fit in green, the σ in blue and the χ^2/ndf in red for signal amplitude ratio r_{02} (a) and for r_{12} (b). (Note that all values are scaled.) The region of r_{02} with bad χ^2 ($t < 10$ ns) contains no real detector signals since the time slice of a_0 lies before the signal.

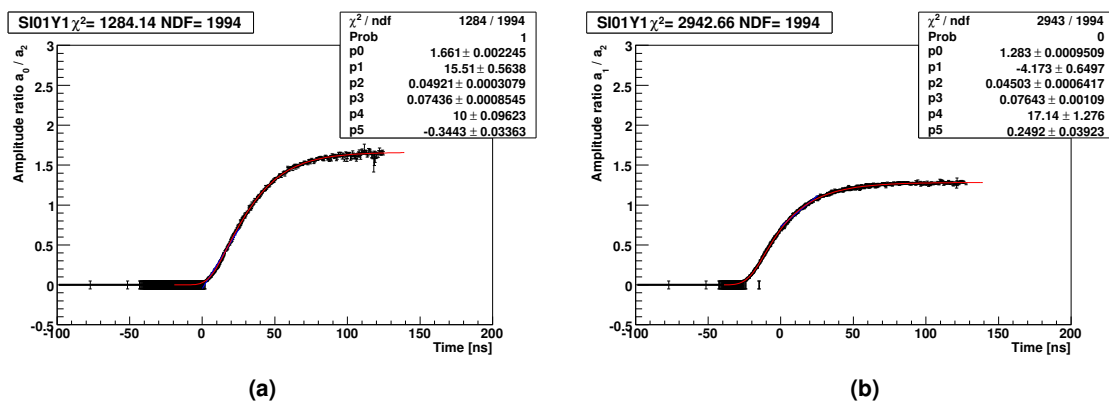


Figure 4.11: An example timing-fit on the signal amplitude ratio distribution $r_{02}(t)$ on the left hand and on the right hand for $r_{12}(t)$ of the silicon plane SI01Y for muon run 2006. The red curve is the theoretical function eq. (4.5) with the fitted parameters.

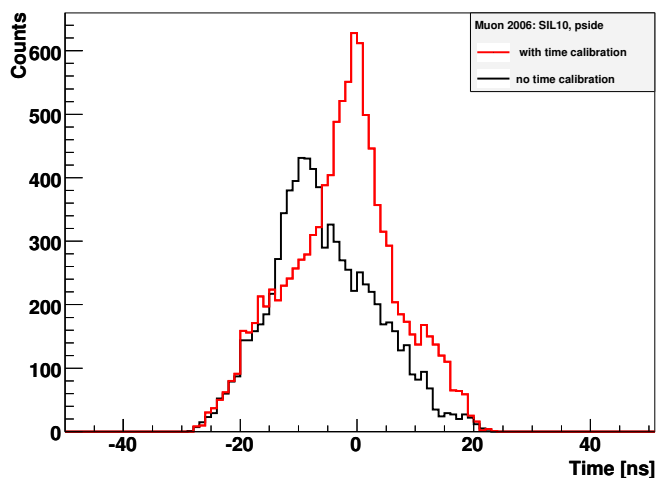


Figure 4.12: This histogram shows the hit time distribution for SI01Y before (black) and after the time calibration (red) for 10000 events of run 47799.

the fit errors of all Gauss fits including the modification for small ratios are filled in one graph, as it is shown in Fig. 4.11. This graph is fitted by the analytical function eq. (4.5). The function with the fitted parameters is indicated by the red curve in Fig. 4.11. The good χ^2/ndf values indicated that model eq. (4.5) is correct.

The parameters of this so-called *timing-fit* are stored in a file which has to be transferred to the COMPASS calibration database which stores all constants and calibrations parameters of the detectors and provides access to all software packages of COMPASS. The time calibration was performed for each silicon projection for the years 2004 to 2006. In appendix D.1 more technical details can be found about the whole time calibration procedure. The values of the timing reconstruction function eq. (4.6) for the hadron setup 2004 are given as an example in appendix D.1.2 and Table D.3.

Fig. 4.12 shows the strip time distribution for the silicon plane SI01Y (SIL10 p-side) before and after the time calibration, generated with COOOL. Hits are only filled, when they are within a certain time window. Clearly the shift of the peak distributed around time zero can be seen which refers to the expected signal time. About a factor of 1.3 more hits are stored after applying the new time calibration. The events which are in correlation with the trigger time are on top of a broad background due to noise and beam halo.

4.5 Clustering

A particle traversing the silicon detector creates a tube of electron-hole pairs of about $1 \mu\text{m}$ (neglecting δ -electrons³) around the track [Pei92]. The charge drifts due to the elec-

³ δ -electrons, also called knock-on-electrons: The number of electron-hole pairs generated by a traversing charged particle is statistically distributed and follows a Landau-distribution with a long tail to high values.

tric field of the applied bias voltage. The electrons and holes are diffusing by multiple collisions, and the transverse diffusion of the drift within a 300 μm thick silicon detector has a typical full width of half maximum of 6 - 10 μm , depending on the applied bias voltage. A higher bias voltage reduces the diffusion. If the charge is shared between adjacent strips, this entails an improvement of the localisation precision of the impact point of the particle. The spread of the charge is predominantly influenced by the wafer design as it is the case for the COMPASS silicon detector. On the p-side of the wafer, intermediate strips enhance the charge sharing via capacitive coupling, see subsection 3.2.2.

The next section describes the cluster finding algorithm by using the strip time information followed by a discussion on the cluster localisation, see subsection 4.5.2.

4.5.1 Cluster Finding

The algorithm starts searching for all adjacent channels, so called *cluster candidates*, with a signal higher than the zero suppression cut for the particular triggered event. Normally, several cluster candidates are found. In the next step, the strip times are compared in order to distinguish between accidental and real clusters.

There are different scenarios resulting in cluster candidates. Clusters are unambiguous, if they are caused by two particles crossing the detector in a distance sufficiently far from each other such that their hit strips are not adjacent. In case the particles passed the detector so close to each other that they hit adjacent strips, then they can be separated due to the inconsistency of their strip time assuming they are related to different incoming beam particles. This can be done for cluster candidates composed of a particle signal and a noisy channel as well. Two tracks hitting adjacent strips can not be distinguished if their timing is the same. A further scenario are overlapping tracks, so their signals pile up. Since the time reconstruction relies on the signal shape, those pile-up events would have different timing for the two signal ratios of the strips.

Strips are combined to a cluster, if they fulfil a *consistency* criterion Y to proof if the strip times agree within their errors. The consistency Y depends on the time difference of the strip times, weighted by their errors σ_1 and σ_2

$$(4.18) \quad Y = \frac{t_2 - t_1}{\sqrt{\sigma_1^2 + \sigma_2^2}} < 3.5.$$

From the asymmetric error $\sigma_{t_1}^+$ and $\sigma_{t_1}^-$ of each strip time t_1 , those error contribution is chosen which points to the direction of t_2 which is meant here with σ_1 and vice versa for choosing the error σ_2 of the second strip time t_2 . The combined cluster time t_{cl} and

The mean energy loss of a traversing charged particle in a 280 μm thick silicon detector corresponds to $2 \cdot 10^4 - 3 \cdot 10^4$ electron-hole pairs just above ionisation threshold. However (rarely) also very high energy electrons are created. Those high energy electrons can traverse several mm mostly transverse to the impact particle along the silicon wafer [Pei92].

its asymmetric errors σ_{cl} are calculated analogue to eq. (4.15) and eq. (4.16), see subsection 4.6.1 for the results. For cluster candidates with more than two strips, this consistency check is performed iteratively. Each strip is successively added to the consistency check and a new cluster time with errors is calculated. The clustering algorithm is not limited on the cluster size. Small clusters like one and two are dominating. Nearby clusters with the same timing are combined to one big cluster which is a limitation of the current treatment. But bigger clusters are mainly generated by high energy electrons which can traverse longer distances along the wafer causing signals in several adjacent strips.

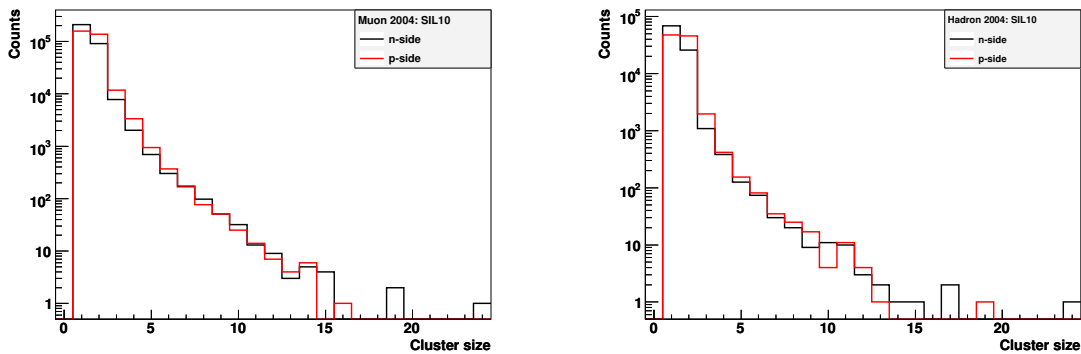


Figure 4.13: Silicon cluster size distribution for muon run 36926 on the left and hadron run 43220 on the right of beam time 2004, both for the p-side (red) and n-side (black) of the detector module SIL10.

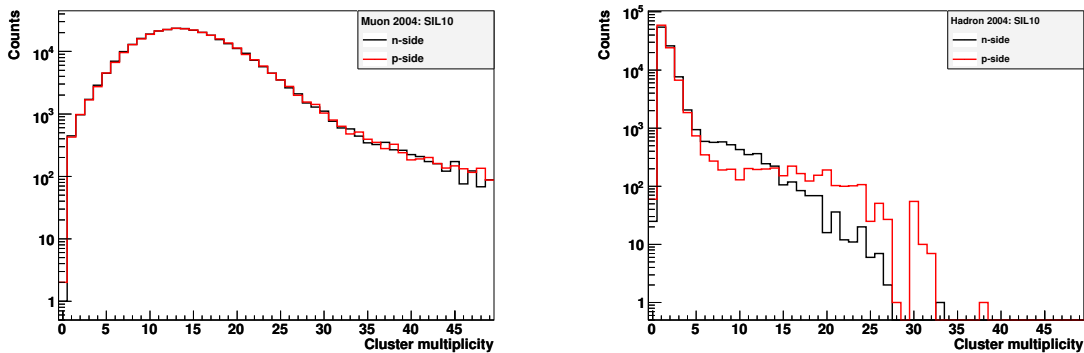


Figure 4.14: Number of clusters per event of the p-side (red) and n-side (black) of the silicon module SIL10 for a chunk of the high intensity muon run 36926 on the left and a chunk of the low intensity hadron run 43220 on the right of the beam time 2004. The large difference between the distributions of the two histograms comes from the different beam intensities of about a factor 100 between muon and hadron run.

Fig. 4.13 shows the cluster size distributions for the COMPASS silicon micro-strip detector with double-sided readout for both muon and hadron run of run time 2004. The majority of the particles traversing the detector lead to a cluster of one or two strips. The

reason for the difference between the p- and the n-side is due to the wafer design. On the p-side intermediate strips enhance charge sharing between the two adjacent strips. So, the number of cluster size one events is nearly equal to cluster size two events. For the n-side of the detector, about two thirds of the detected particles leave a signal only at one strip above the ADC threshold. A tail up to cluster size 20 can be seen, caused by high energy electrons. Apart from the beam particle, the largest difference between muon and hadron run is the beam intensity which was for muons $2 \cdot 10^8$ per SPS cycle and hadrons $5 \cdot 10^6$ per SPS cycle respectively. This has a great impact on the cluster multiplicity per event which is shown in Fig. 4.14. For the high intensity muon run the cluster multiplicity has a peak of 15 clusters per event, but for the low intensity hadron run there are mainly 1 - 3 clusters per event. The signal amplitude distribution is shown in Fig. 4.15, also separate for different cluster sizes. A higher cluster size correlates with a higher amplitude, coming from a high energy electron which can traverse longer distances along the wafer causing signals in several adjacent strips. The corresponding residual distributions show a significant offset as it will be discussed later, see Fig. 4.23.

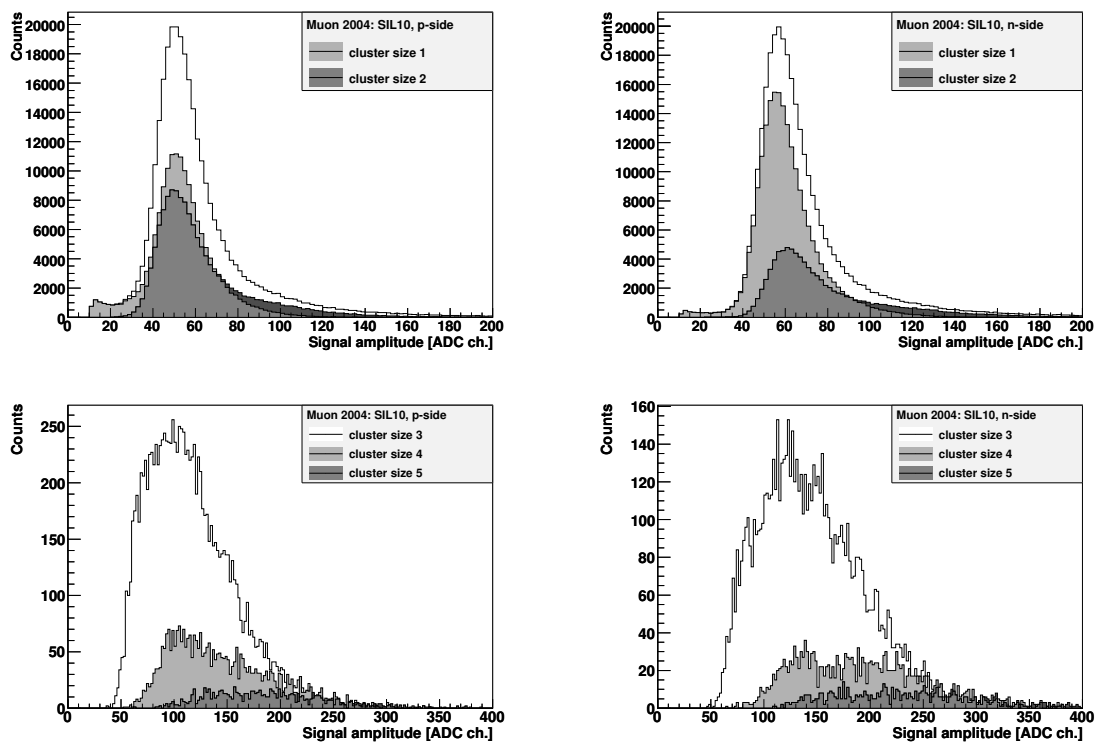


Figure 4.15: Signal amplitude for n- and p- side of silicon module SIL10 (SI01X, SI01Y) of muon run 36926 of beam time 2004, on the upper row for 1 - 2 strips per cluster and 3 - 5 strips per cluster on the lower row (Note the different scaling).

The time resolution and resulting track time achieved with this clustering algorithm is discussed in subsection 4.6.1 including the analysis routine and event selection. The track time resolution is strongly correlated with the signal amplitude, as depicted in Fig. 4.16:

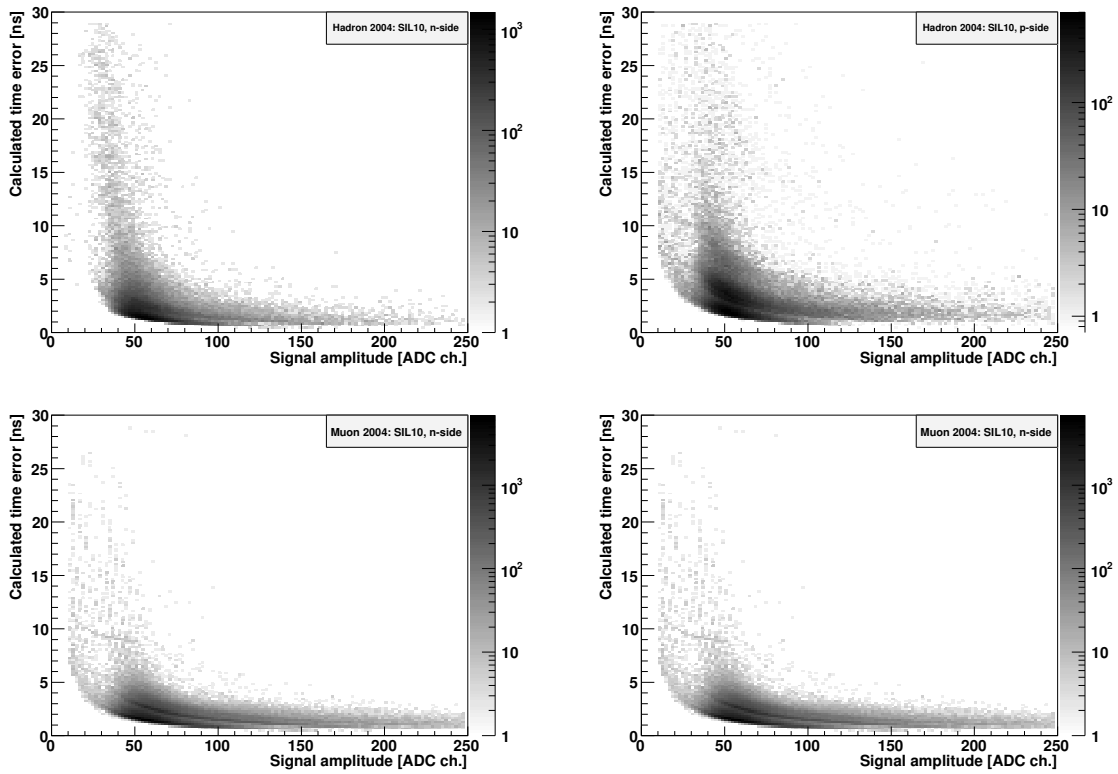


Figure 4.16: Correlation of the signal amplitude and calculated time error for the silicon module SIL10, both n- and p-side (left, right) for muon run 36926 (SI01X, SI01Y) in the upper row and hadron run 43220 (SI04X, SI04Y) in the lower row, respectively. The different visible structures refer to different cluster sizes.

The higher the signal amplitude, the smaller is the error on the time information. The error reaches values smaller than 1 ns for larger signal amplitudes. The different visible structures refer to different cluster sizes.

4.5.2 Determination of Cluster Position

After extracting clusters out of all hit strips for one trigger signal with the help of the time information of the strip, the next step is to determine the cluster position.

The wafer design predominantly influences the spread of the charge [Pei92]. The particle impact can be localised more precisely if the charge is spread over two strips n and $n + 1$. A simple approach to determine the cluster position is to calculate the weighted mean of the adjacent strip amplitudes. If the expected charge distribution is taken into account, a better precision can be achieved. The charge distribution can be studied by the quantity η , defined as the fractional charge seen on the strip $n + 1$, where $a_{2,n}$ and $a_{2,n+1}$ are the signal amplitudes, see section 4.2, of the two strips:

$$(4.19) \quad \eta = \frac{a_{2,n+1}}{a_{2,n} + a_{2,n+1}}$$

Fig. 4.17 shows the η -distributions for a chunk of the pion run 43220 (upper row) and for muon run 36926 (lower row) for cluster size two. The association of the cluster with a track is ensured by matching the cluster and the track time within a time window of ± 1 ns. The p-side shows a peak around $\eta = 0.5$: Nearly all charge of the cluster is collected by the intermediate strip. Via capacitive coupling both neighbouring strips see an equal amount of the charge. Since the n-side has no intermediate strips, the centre of the charge is not located between the strips but concentrated more on one strip. This can be seen in the increase of the distribution for η -values 0.15 and 0.8. There, a much higher rise of η is expected but events with stronger asymmetries of the charge distribution are not reconstructed as events of cluster size 2: Due to the zero suppression algorithm of the readout electronics, only values above a certain noise threshold are recorded. Events with only a very small fraction of the charge on the adjacent strip end up as a single strip cluster.

As seen in Fig. 4.18, it is not optimal to determine the cluster position by only calculating the weighted mean for two cluster strips. There, the residuum p , the difference between track position and cluster position calculated by the weighted mean method is shown versus η . By analysing the residual p for different η -bins, an empirical parameterisation for a position correction to the calculated cluster position o_p and o_n is obtained. The cluster position h in case of two strip events for the simple weighted mean approach is the product of the fractional charge η , the strip pitch d of the detector and n the strip

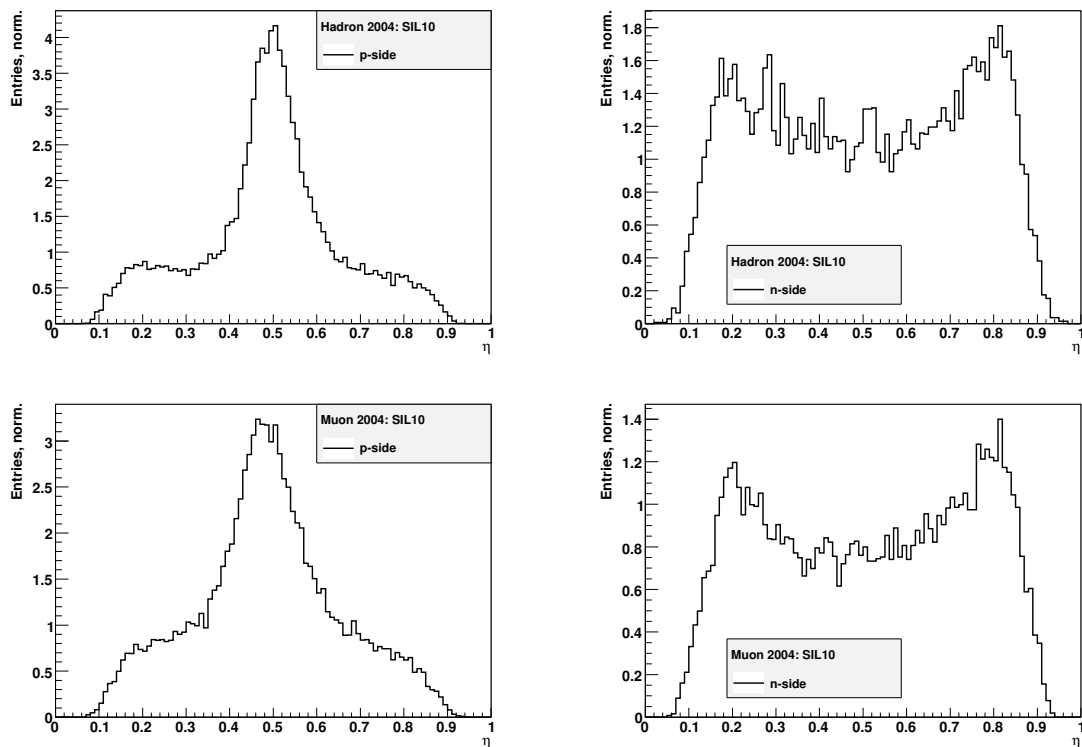


Figure 4.17: Charge distribution η between strips on the p-side (left) and n-side (right), extracted from a chunk of the hadron run hadron 43220 and muon run 36926 of beam time 2004. Only clusters of cluster size two are shown. On the left η is depicted for the p-side with intermediate strips, and on the right for the n-side without intermediate strips. The histograms are normalised so that the integral is equal to 100. Numerical artifacts are avoided by blurring the discrete signal amplitudes $a_{2,n}$ and $a_{2,n+1}$ with random values between -0.5 and 0.5.

number

$$(4.20) \quad p = \sum_n \eta \cdot n \cdot d.$$

The empirically determined offsets o_p and o_n for the n- and p-side are

$$(4.21) \quad \Delta o_n = (7.3 + 40.37 \cdot h - 199.04 \cdot h^2 + 184.67 \cdot h^3 - 49.10 \cdot h^4) \cdot 10^{-3};$$

$$(4.22) \quad \Delta o_p = (-24.39 + 378.91 \cdot h - 2126.23 \cdot h^2 + 5512.19 \cdot h^3 - 7113.01 \cdot h^4 + 4360.25 \cdot h^5 - 981.77 \cdot h^6) \cdot 10^{-3}.$$

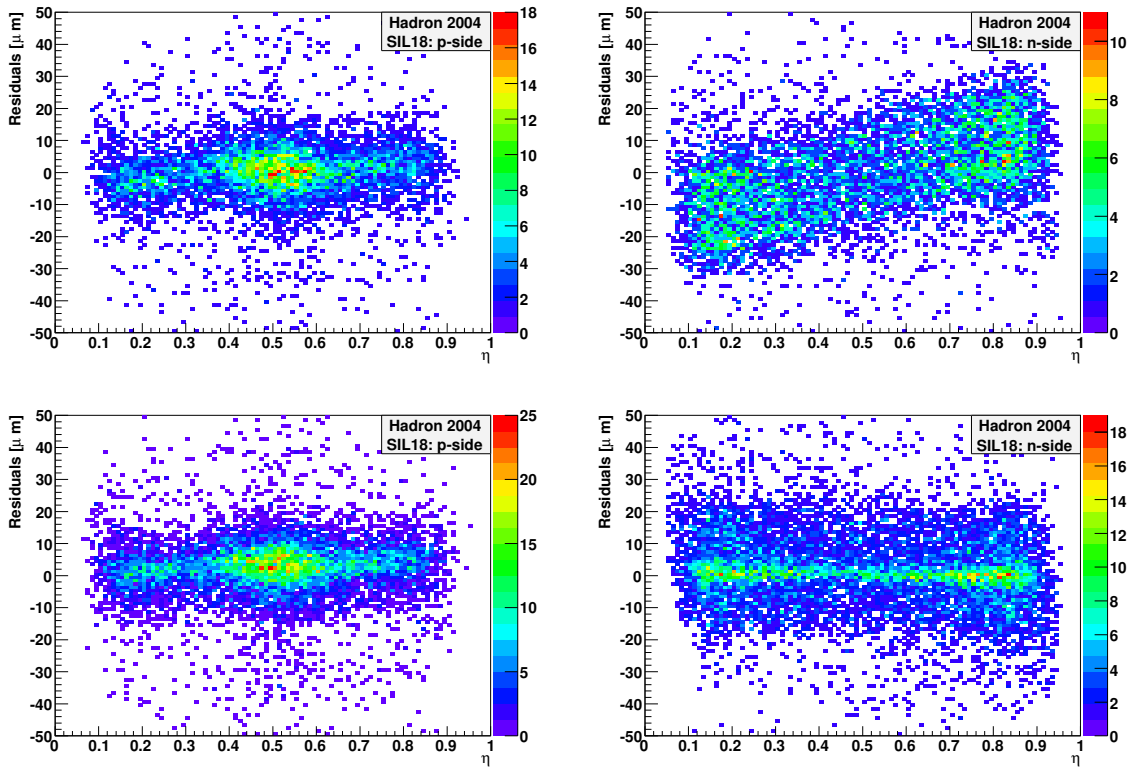


Figure 4.18: The η -distribution versus the residuum of the track position for the n- and p-plane (SI01X, SI01Y) of the silicon module SIL18 for a chunk of hadron run 42324, the upper row without and the lower row with the empirically determined corrections eq.(4.23) on the cluster position.

The effect of the correction can be seen in Fig. 4.18. The offset o_n deviates up to 10 μm , o_p about 2 μm . Especially visible is the improvement for the n-plane of the silicon detector. The result of the spatial resolution of the silicon detectors and its analysis is discussed in subsection 4.6.2.

4.6 Results

In order to study the silicon detector performance, the COMPASS analysis chain was used, see section 2.3. COMPASS raw data are processed with CORAL such that the raw information of the detector, e.g. signal amplitudes, are stored as GigaDST data. Within this work, the above described timing and clustering method of the online filter was integrated to CORAL, as well as the revised determination of the cluster position.

The analysis is focused on the silicon telescope and the preceding and following scintillating fibre (SciFi) stations, as depicted for the muon run in Fig. 3.7 on page 31 and for the hadron run on Fig. 3.8. CORAL is configured such that only the silicon telescope including the SciFi stations are considered by its tracking algorithm. A list with special CORAL options is explained in section D.2.2. The produced GigaDST data are analysed with PHAST. The `UserEvent`-function associates the clusters with the position of the track extrapolated to the corresponding detector plane. For such clusters the time, position and all raw signal amplitudes etc. are stored in a `ROOT-TTree`.

In the following subsections, detector planes are called *passive* if they were intentionally not considered by the tracking algorithm, otherwise they are *active* detector planes. This will become important for determining the spatial resolution of the detectors.

4.6.1 Time Resolution

Fig. 4.19 displays the signal time distributions and Fig. 4.20 the corresponding time error distribution for a typical high intensity muon (36926) and a nominal low intensity hadron run (43220) of the beam time in 2004. These distributions are the results of the cluster finding algorithm as described in 4.5.1 which requires a time calibration and the calculation of the cluster time t_{cl} with its asymmetric errors σ_{cl}^+ and σ_{cl}^- . These histograms also show the particular contributions for events with one or two strips hit. The signal time distributions were fitted with a simple Gaussian. The Gaussian sigma of the time distribution for the hadron run is about 3.0 ns for the p-side of the detector and 2.0 ns for the n-side. For the muon run, the sigma values are about 1 ns broader compared to hadron run. For the p-side of the detector, the sigma is 4.0 ns and for the n-side 2.8 ns. The main difference between hadron and muon run comes from a difference in beam intensity by a factor of 40 and its impact on the cluster multiplicity of the detector plane, see Fig. 4.14. Since the time information is retrieved from the ratio of the signal amplitudes r_{02} and r_{12} , *pile-up* (signal tail of the previous particle is seen), will lead to a shift of the time information.

The Gaussian means of the n- and p-side of the detector differ about 1 ns for both, muon and hadron run. This is due to a systematic offset between the time of a single hit and the cluster time combined with two strip times. This is visible for both, muon and hadron run, and it is not a specific feature of e.g. detector SIL10. The effect is in the order of 1 ns for the n-side of the detector and much more distinctive for the p-side with a difference of 2.5 ns. This observation suggests to correct the time information, depending whether

it stems from 1 strip- or 2 strip clusters on the p- or n-side. For the p-side, a significant improvement from 3.0 ns to 2.6 ns can be expected.

For events with cluster size 2, the calculated time error is much larger than for single strip events, see Fig. 4.20. This was also visible as a double band structure in Fig. 4.16, where the signal amplitude is plotted against the calculated time error.

After the single plane analysis, the time information of all silicon projections is combined in order to obtain the track time. For a track, reconstructed by CORAL, all associated hits n with its time information of the various silicon projections are determined. From the asymmetric errors $\sigma_{cl_i}^+$ and $\sigma_{cl_i}^-$ of each cluster i belonging to the track of each cluster time t_{cl_i} , those error contributions are chosen pointing to the direction of the meantime of the track \hat{t}_{track} computed by CORAL. The track time t_{track} is now calculated by weighting the sum of the errors σ_{cl_i} of each silicon cluster time t_{cl_i}

$$(4.23) \quad t_{track} = \frac{\sum_{i=1}^n \frac{t_{cl_i}}{\sigma_{cl_i}^2}}{\sum_{i=1}^n \frac{1}{\sigma_{cl_i}^2}}, \quad \sigma_{track} = \sqrt{\sum_{i=1}^n \frac{1}{\sigma_{cl_i}^2}}$$

Fig. 4.21 shows on the left the time distribution for a single silicon projection (dark grey, SIL22 SI02U) and the calculated track time t_{track} (light grey) of hadron run 43220. For the analysis, only tracks were chosen which were reconstructed due to the information of at least 10 silicon projections. Since the various triggers of the hadron run have offsets of up to 2.5 ns, only events with a ‘‘Primakoff-2 trigger’’, see subsection 2.2.4 and Fig. 5.5, were considered in this analysis. On the right of Fig. 4.21, the error distributions of a single silicon plane σ_{cl_i} and of the track error σ_{track} are shown. When the timings from all hits of a track in the silicon telescope are combined, the propagated error on the track timing σ_{track} is much narrower compared to the time distribution of a single plane. The reason is, that the single Landau fluctuations average out and virtually always a big amplitude appears contributing with big weight a precise timing information. The most probable track time error is found to be about 530 ps, and the complete distribution is contained in the interval up to 1 ns. This value differs from the $\sigma_{track} = 0.87$ ns, where the latter also contains the trigger-time width which is found to be the deconvolution of uncertainties of the trigger and silicon time:

$$(4.24) \quad \sigma_{trigger} = \sqrt{\sigma_{track}^2 - \sigma_{si-track}^2} = \sqrt{0.87^2 - 0.53^2} \text{ ns} = 0.69 \text{ ns}$$

4.6.2 Spatial Resolution

The distribution of spatial residuals for the p- and n-side of a detector plane are displayed in Fig. 4.22 and Fig. 4.23 for the high intensity muon and low intensity hadron run. The analysis required a particle track with hits in 10 silicon projections and the cluster multiplicity for each particular plane was restricted to values smaller than 25 hits per

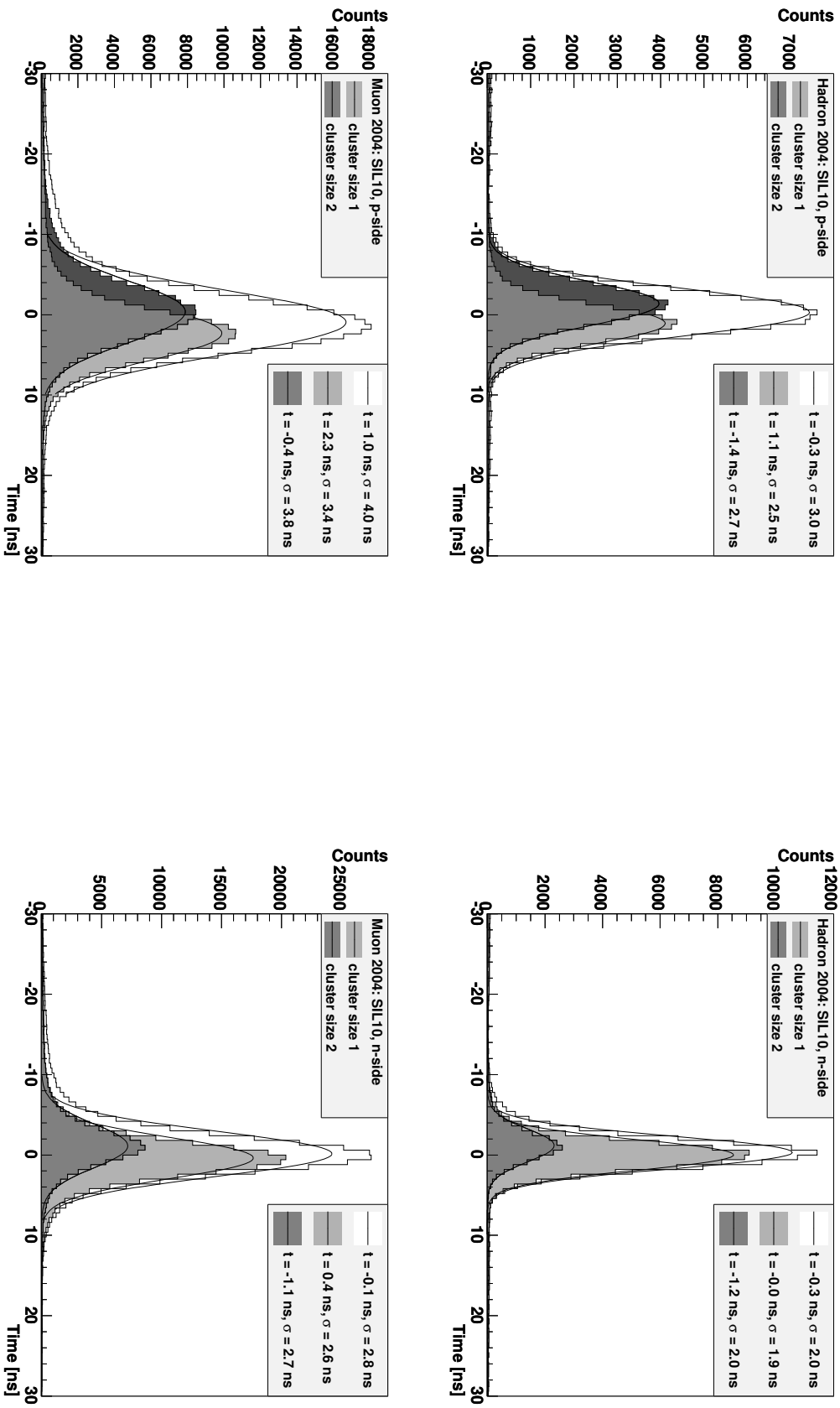


Figure 4.19: Signal time distribution for the (left) p- and (right) n-side of silicon module SIL10 for muon run 36926 (SI01X, SI01Y) and hadron run 43220 (SI04X, SI04Y) of beam time 2004. The Gaussian mean and the sigma of the time distribution are listed in the legend.

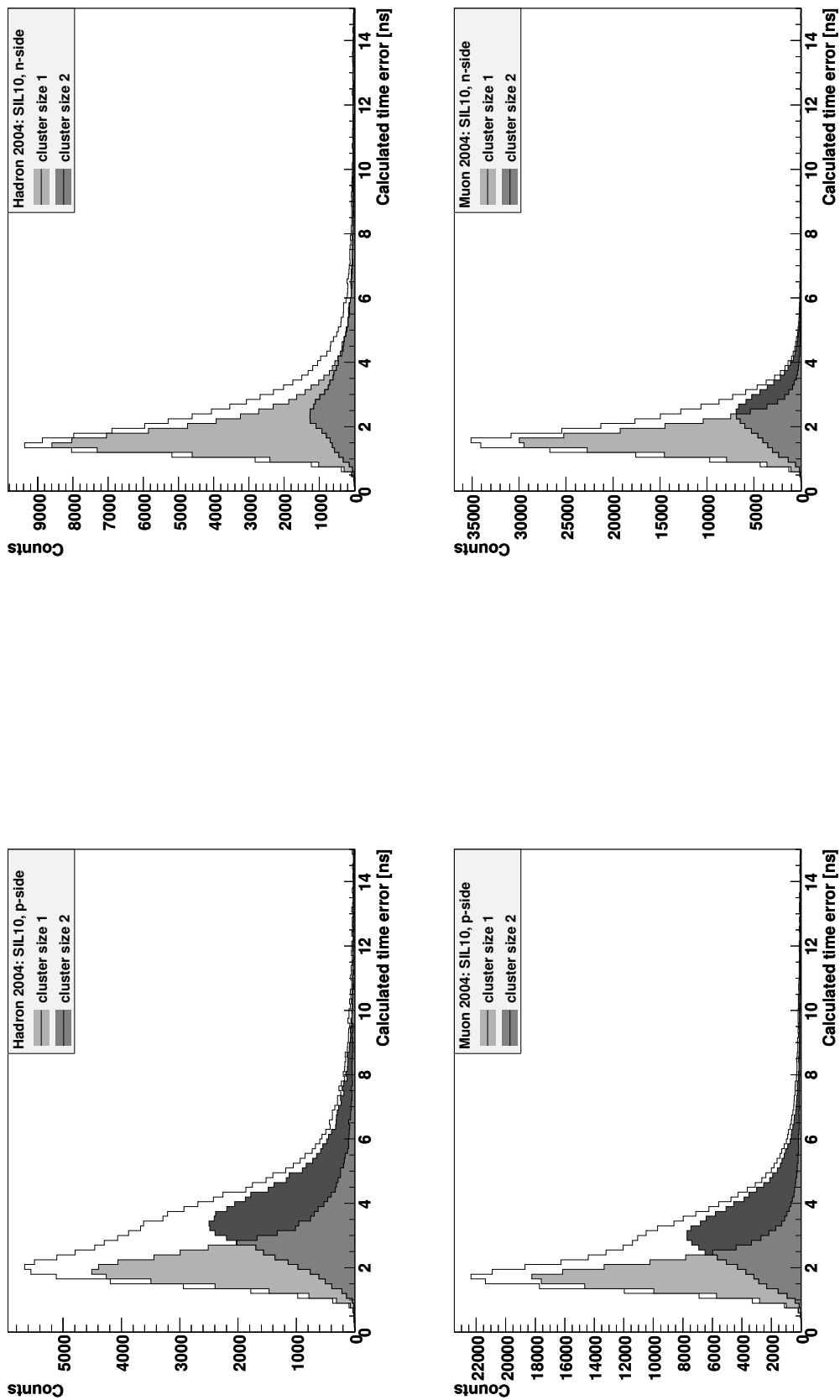


Figure 4.20: Distribution of the calculated time error of the (left) p- and (right) n-side of the silicon module SIL10 for muon run 36926 (SI01X, SI01Y) and hadron run 43220 (SI04X, SI04Y) of beam time 2004.

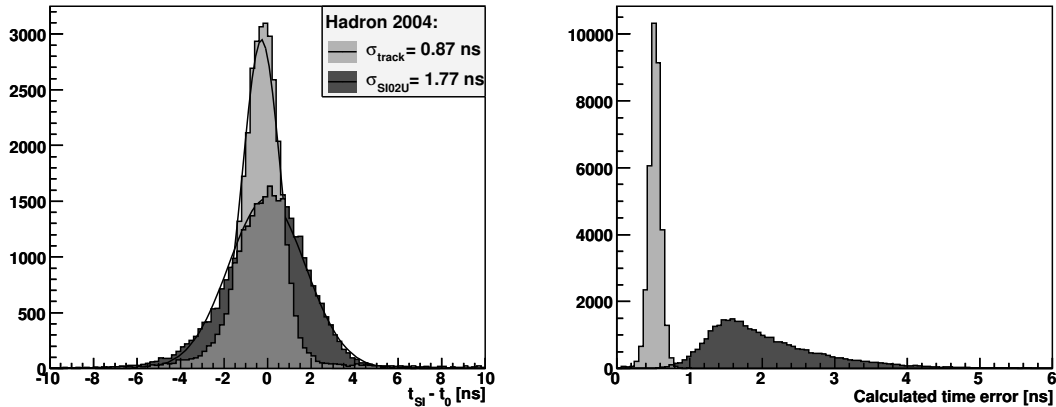


Figure 4.21: Timing (left) and error distribution (right) of a single silicon projection SI02U (SIL22) (dark grey) for run 43220. The calculated track time and its error of the silicon telescope with 10 projections are shown in light grey.

projection. The residual distributions were determined for a silicon projection which was passive in the event reconstruction process which means its hits were not considered by the tracking algorithm of CORAL.

The distribution for cluster size 1 and cluster size 2 are shown in Fig. 4.22 and for cluster size 3, 4, and 5 in Fig. 4.23. For cluster size 2, the spatial resolution can be better determined than for cluster size 1. The more cluster size 2 “events” are generated, the better is the whole spatial resolution of the plane. The resolution differs between the p-side and n-side of the detector, due to intermediate strips on the p-side. After deconvoluting the track error on the particular planes, for cluster size 1 events on the n-side 14 μ m resolution in space are observed and 9 μ m on the p-side. For cluster size 2, the charge cloud is not shared linearly by the contributing strips. This is corrected in order to calculate the precise cluster position, see subsection 4.5.2. In the current status of the analysis, the achieved resolution for cluster size 2 on the n-side is 6 μ m and on the p-side 5 μ m.

The correlation of the residual with the signal amplitude for different cluster sizes is shown in Fig. 4.24 of muon run 2004 which points also to a difference between the p- and n- side. For events with cluster size 1 and small signal amplitudes below 60 ADC units, the distribution gets broader and splits into two sections. This indicates that those events actually hit two strips, but one was rejected due to the zero suppression cut. The effect is more pronounced for the n-side. The picture of this correlation is similar for the hadron run.

A higher cluster size correlates as expected with a higher signal amplitude, see also Fig. 4.15. A high energy electron which traverses longer distances along the wafer causes signals in several adjacent strips. For cluster sizes > 2 the spatial resolution gets worse, according to Fig. 4.23 and Fig. 4.24. The residual distribution splits into two peaks. The

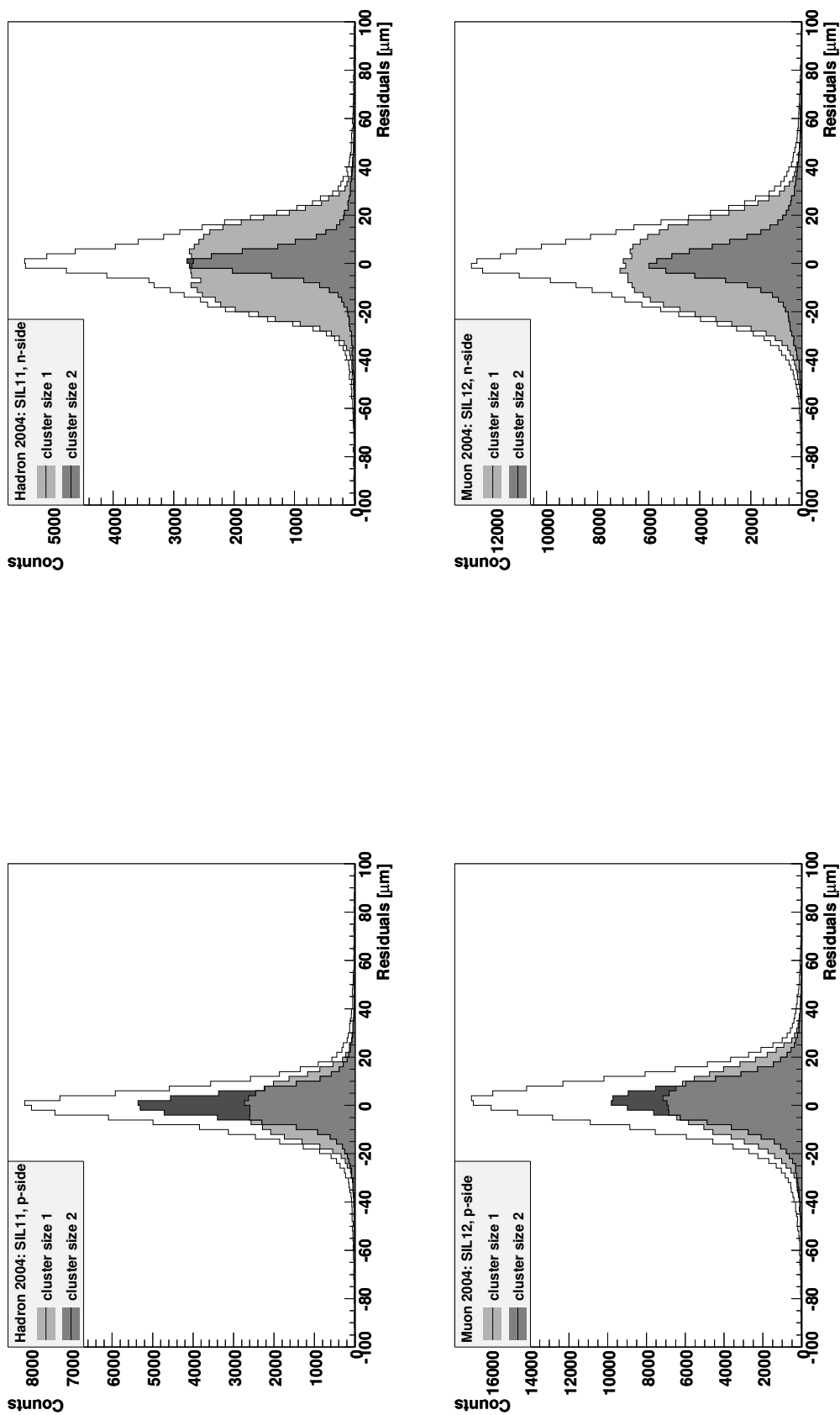


Figure 4.22: Residuals for (left) p- and (right) n-side (SI02X, SI02Y) of silicon module SIL12 in muon run 36926 and silicon module SIL11 (SI04U, SI04V) of hadron run 43220 of beam time 2004.

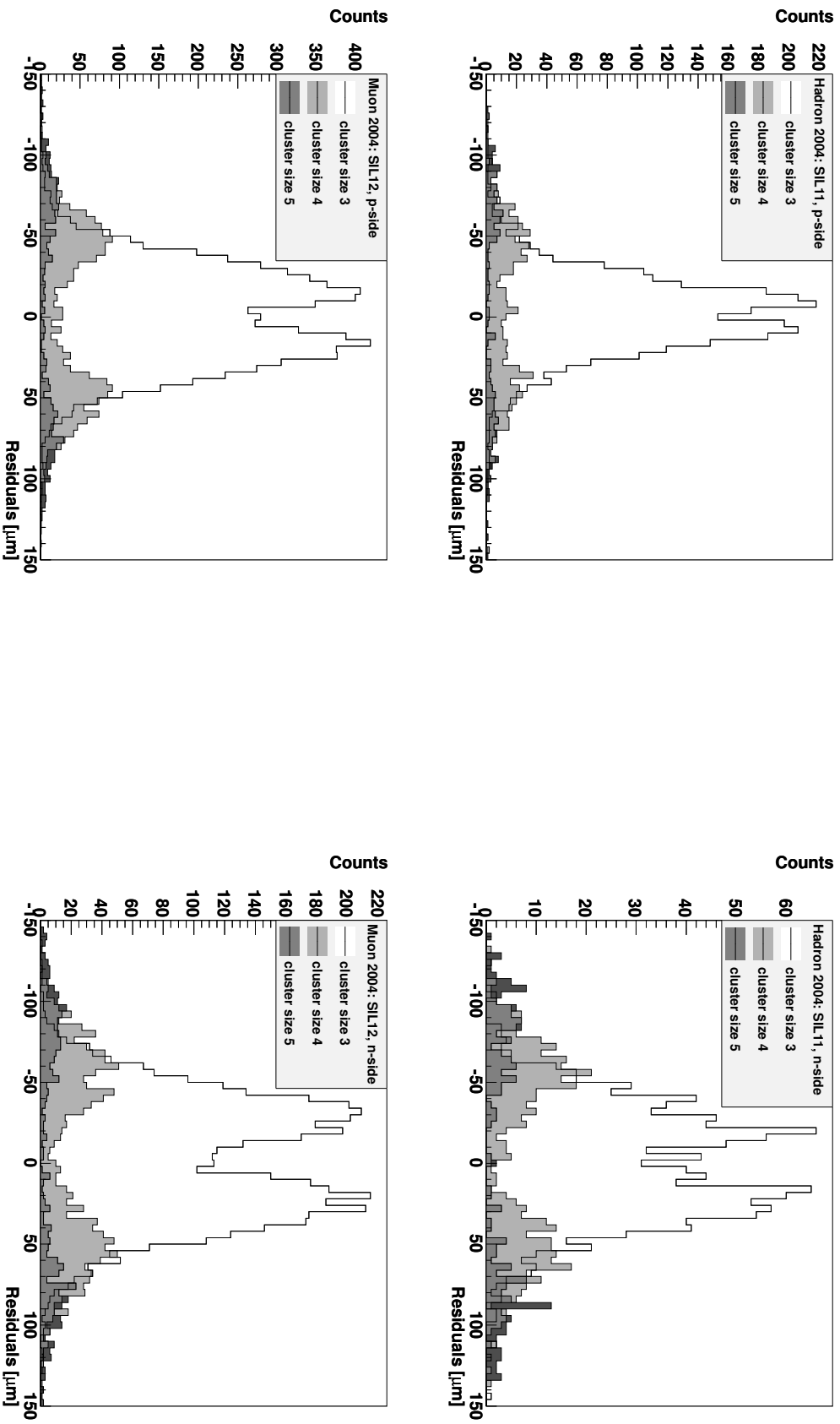


Figure 4.23: Residuals for (left) p- and (right) n-side (SI02X, SI02Y) of silicon module SIL12 in muon run 36926 and silicon module SIL11 (SI04U, SI04V) of hadron run 43220 of beam time 2004 for cluster sizes 3–5.

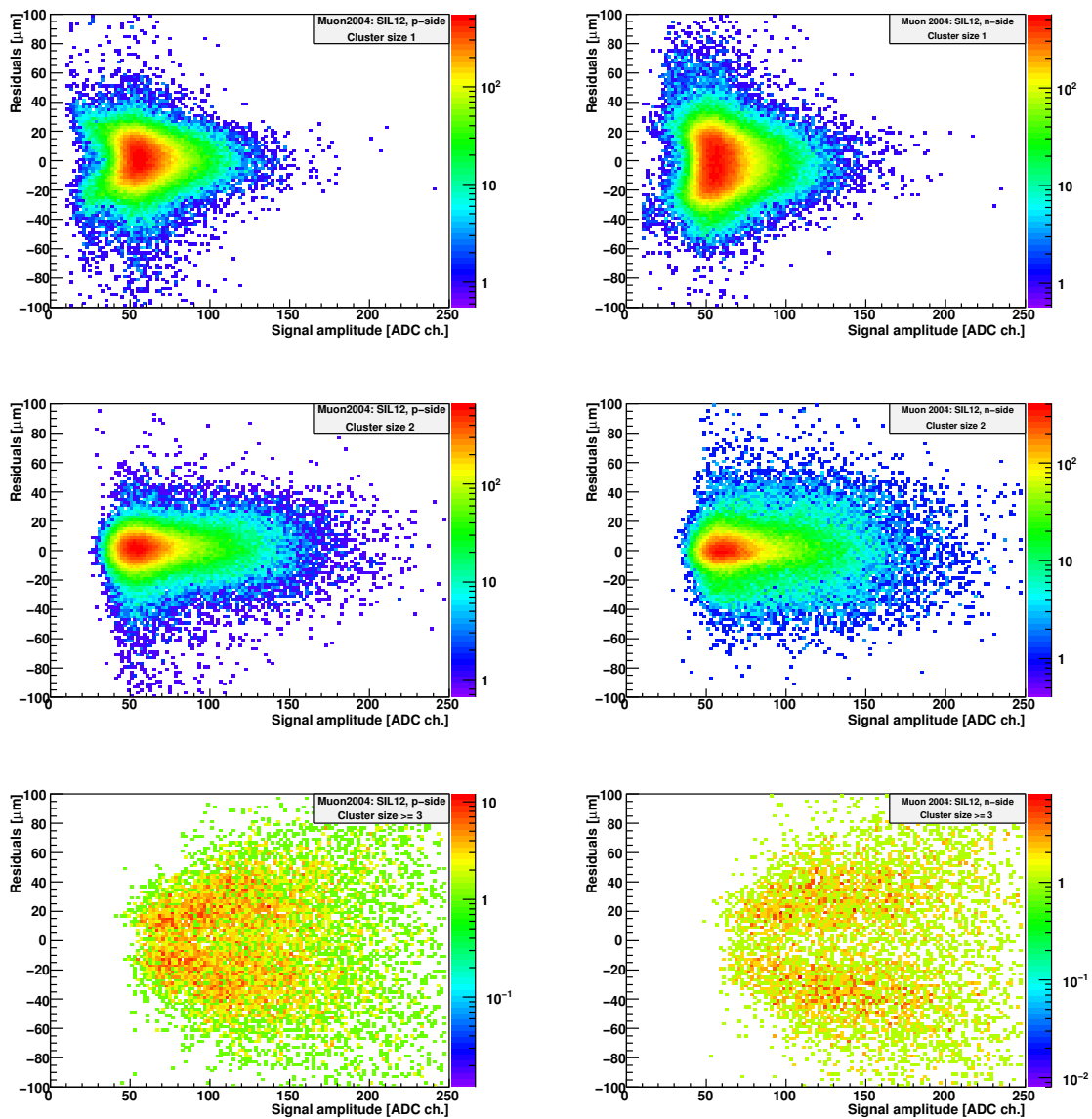


Figure 4.24: Correlation between the signal amplitude and spatial resolution, for (left) p- and (right) n-side (SI02X, SI02Y) of silicon module SIL12 in muon run 36926 of the beam time 2004, on the top row for cluster size 1, in the middle for cluster size 2 and on the bottom for cluster size ≥ 3 . The correlation is similar for the hadron run.

distance between the two peak positions increases about the strip pitch for rising cluster sizes. This finding came in the last editing phase of this work. It suggests to enhance the cluster position determination by splitting large clusters into two, positioned at the corners of the original large cluster. Since the wrong-sided "ghost cluster" will be ruled out in the tracking stage, the overall performance of the silicon telescope would profit from such a modification in the range of several percent.

4.7 Summary

From the amplitude signal of a particle trajectory traversing the detector, the time and its error can be reconstructed. Therefore, certain parameters have to be determined by a dedicated calibration procedure as presented above. This time information is needed by the clustering process. The timing and clustering method was implemented for the first time in the online filter [Nag05] and was integrated within this work to CORAL as well as the revised determination of the cluster position.

The Gaussian sigma of the time distribution for the hadron run is about 3.0 ns for the p-side of the detector and 2.0 ns for the n-side. For the muon run, the sigma values are about 4 ns and 2.8 ns on the p- and n-side, respectively. This difference between hadron and muon data can be explained by different beam intensities. Besides the time distribution, also the corresponding calculated time error is presented. For the p-side, an improvement of the sigma value of about 0.6 ns can be expected if the time information is corrected depending, whether it stems from 1 strip or 2 strip cluster.

When the timings from all hits of a track in the silicon telescope are combined considering the individual time errors, the most probable track time error is found to be about 530 ps. The complete track error distribution is contained in the interval up to 1 ns.

The achieved resolution in space for cluster size 1 on the n-side is 14 μm and on the p-side 9 μm , for cluster size 2 it is 6 μm on the n-side and 5 μm on the p-side. The resolution differs between the p-side and n-side of the detector, due to intermediate strips on the p-side. Since the charge cloud is not shared linearly by the contributing strips a correction is applied to cluster size 2 events.

Detector Plane	1-strip	2-strip	
n-side	$\Delta X = 14 \mu\text{m}$	$\Delta X = 6 \mu\text{m}$	$\Delta t = 2.0 \text{ ns}$
p-side	$\Delta Y = 9 \mu\text{m}$	$\Delta Y = 5 \mu\text{m}$	$\Delta t = 3.0 \text{ ns}$

Table 4.1: Spatial and time resolution of the COMPASS silicon detectors.

Chapter 5

Silicon Detectors in Hadron Run 2004

In autumn 2004, five silicon stations were installed for the COMPASS pilot hadron run, two stations for beam definition and three downstream the target for reconstruction of the trajectories of outgoing charged particles. In Fig. 3.8 on page 31, a photograph of the target region has been already presented, showing the whole silicon telescope and including a schematic drawing of this setup. Within this chapter, specific silicon detector concerns of the pilot hadron run are discussed. This includes detector quality and operation as well as their alignment. The naming conventions used in this chapter are as introduced and explained in chapter 3.

5.1 Operation

Besides the detector stations available from the previous muon runs, see Table 3.1, two more detector stations were built for the hadron pilot run in 2004. This included the production of four new detector modules plus one spare detector (SIL18-SIL22). The detector modules were assembled by a commercial company. The production of the silicon modules was delayed and the last two detector modules (SIL21 and 22) were picked up two weeks before the start of the hadron run. In addition, the whole production batch suffered damage due to lack of care at the side of the manufacturer¹, the damages are summarised in Table 5.1. The aluminium layer of the pitch adapter (Fig. 3.3) used for the silicon module SIL21 was oxidised and not all channels could be bonded. Due to the same problem, also bonds on SIL18 for channels 490-505 were loose in the centre of the detector. On SIL22, the first APV fronted chip is not connected because this chip wafer was wrongly cut. Since the hadron beam (Gaussian $\sigma = 3.4 \times 2.8 \text{ mm}^2$) is more focused than the muon beam ($\sigma = 10 \times 8 \text{ mm}^2$), all four new detectors with their local damages could be arranged such that the beam only passed good regions. These detectors were placed at the beam telescope and not, as it was planned, after the target. This was

¹As result of this negative experience, the manufacturer was changed. Now Hightec MC AG in Lenzburg, Switzerland, assembles the silicon detector modules.

the reason why the silicon modules were completely reshuffled for the hadron run, and same silicon projection names for muon and hadron run mean different silicon detector modules, see e.g. Table C.1 or Table 5.2.

Plane	Module	Damage
SI01Y	SIL18	broken bonds at channels 490–505
SI02U	SIL22	broken APV chip no. 1, chip wrongly cut
SI02XY	SIL21	on both sides many unconnected bonds due to oxidised pitch adapter

Table 5.1: Production problems of the new silicon detectors for hadron run.

Fig. 5.1 illustrates the hardware performance of the detectors during the hadron pilot run. Each of the five green bars indicates a detector station with the four projections (U, V, X, Y), when it was operating without significant errors. The periods of a detector plane with readout errors, noise and missing planes are marked in red as well as the periods in grey where no physics data was taken. For the detector stations SI01 and SI02, a new generation of ADC cards in the prototype stage were used which lost their settings from time to time. This error could only be recognised by monitoring the online histograms. Problems with noise which appeared occasionally, especially at projection SI03V, could be traced back to corroded power connectors on the repeater and ADC cards.

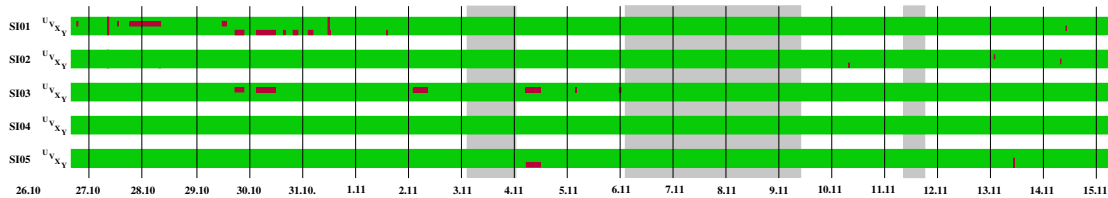


Figure 5.1: Silicon performance in hadron run 2004. Each bar indicates a detector station. The period of detector planes, where problems occurred, are marked in red (including readout errors, noise and missing planes). The dark grey areas indicate the time where no physics data were taken.

The central regions of the detectors were irradiated by $8 \cdot 10^{11}$ pions/cm² in hadron run 2004. Due to an increase of the noise distribution of several silicon detectors during this time, it became necessary to raise the bias voltage of the silicon detectors. In average, the bias voltage was increased by 20 V. In Table 5.2, the bias voltage settings are listed of all silicon detectors, the settings during muon run and the various settings during hadron run. Fig. 5.2 displays a typical trending of the leakage current of a silicon detector, here of SIL08 which is in use since 2002. On the bottom the temperature trending in the experimental area is shown. The leakage current follows to a large extent the temperature, as expected. The effect on the leakage current of the high intensity muon and hadron beam can be clearly seen.

Bias Voltage Settings 2004						
Plane	Module	Muon Run	Hadron Run			
		01.10.04	19.10.04	01.11.04	03.11.04	11.11.04
SI01UV	SIL20		60V			70V
SI01XY	SIL18		60V			70V
SI02UV	SIL22		90V			100V
SI02XY	SIL21		90V			100V
SI03UV	SIL16	70V	130V	140V	150V	160V
SI03XY	SIL13	60V	140V	150V		160V
SI04UV	SIL11	110V	140V			160V
SI04XY	SIL10	130V	160V			180V
SI05UV	SIL08	90V	130V			140V
SI05XY	SIL12	120V	120V			130V

Table 5.2: High voltage settings at the end of the muon run and the different settings during the hadron run 2004. Note, that SI03 - SI05 in hadron run are the renamed stations SI05, SI01, SI02 of muon run 2004, see Table 3.1 and Table 3.2.

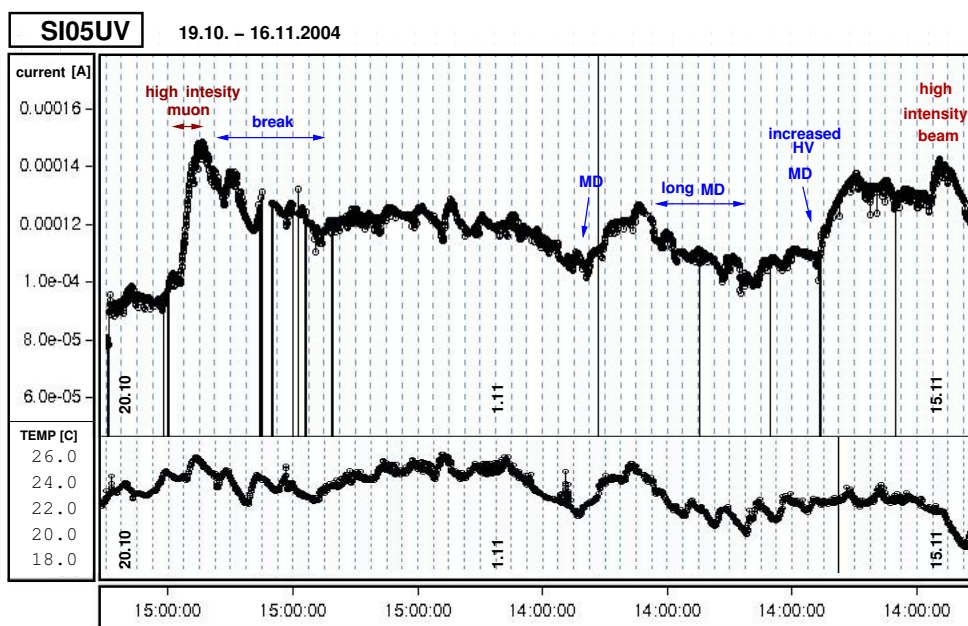
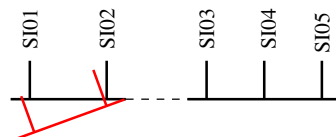


Figure 5.2: Leakage current trending of SI05UV (SIL08), on the bottom the temperature trending of the experimental area is displayed. The periods where no physics data was taken, are marked in blue, particularly “MD” stands for Machine Development (i.e. the shutdown of the accelerator for maintenance).

In the upper plot of Fig. 5.4, the residual distribution is shown for all silicon projections as a function of time. For 264 runs these residuals were determined. The beam telescope containing the detector stations SI01 and SI02 moves significantly with respect to the telescope after the target (SI03, SI04 and SI05). The displacement is in the order of 30 μm during the first 10 days of beam time, and after the two-days break (7.-8.11.2004) up to 250 μm for SI01Y and V and about 100 μm for SI02Y and V projections. This corresponds to a tilt of about 0.1 mrad.

Visualisation of the effect: Due to the method, it can not be distinguished whether beam or spectrometer telescope moved, only the relative effect is clarified here. The full alignment problems of the 2004 hadron run were never fully worked out.



The correction values for the detector position based on this analysis were made available for CORAL. On the second plot at Fig. 5.4 the effect of the correction is shown. The position of the residuals remains mainly constant over time, and the displacement is mostly within the resolution of the silicon detectors.

The coordinates of the detector signals are available in the wire reference system², where the measured coordinate u_X is perpendicular to the strips. To get a space point $P(x,y)$, the u_X value for SI03X and u_Y of SI03Y have to be combined. With respect to the main reference system, both systems are tilted by an angle α for the X and β for the Y case, see Fig. 5.3 which should be equal since the strips on the two sides of a detector form exactly an angle of 90° . In case one knows the position of the hit along coordinates d_X and d_Y , respectively, the space point $P(x,y)$ can be calculated in two ways:

$$(5.1) \quad \begin{pmatrix} x \\ y \end{pmatrix} = \begin{pmatrix} \cos \beta & -\sin \beta \\ \sin \beta & \cos \beta \end{pmatrix} \cdot \begin{pmatrix} u_Y \\ d_Y \end{pmatrix} = \begin{pmatrix} \cos \alpha & -\sin \alpha \\ \sin \alpha & \cos \alpha \end{pmatrix} \cdot \begin{pmatrix} u_X \\ d_X \end{pmatrix}$$

The angles α and β are known from the COMPASS alignment and they take uncertainties due to the detector production, assembly and setup into account. This system of equations can be solved in different ways, but in comparison with other solutions the following turned out to be numerically the most stable one

$$(5.2) \quad d_X = \frac{u_X(\cos \alpha \cos \beta + \sin \alpha \sin \beta) - u_Y}{\sin \alpha \cos \beta - \cos \alpha \sin \beta}.$$

After the rotation from the wire to the main reference system, the slope of the track in X and Y is calculated and the point of the line is SI03XY which is necessary to define a track within a method of PHAST, see [PHA].

²The definitions of the various coordinate systems used in COMPASS are explained in appendix A.

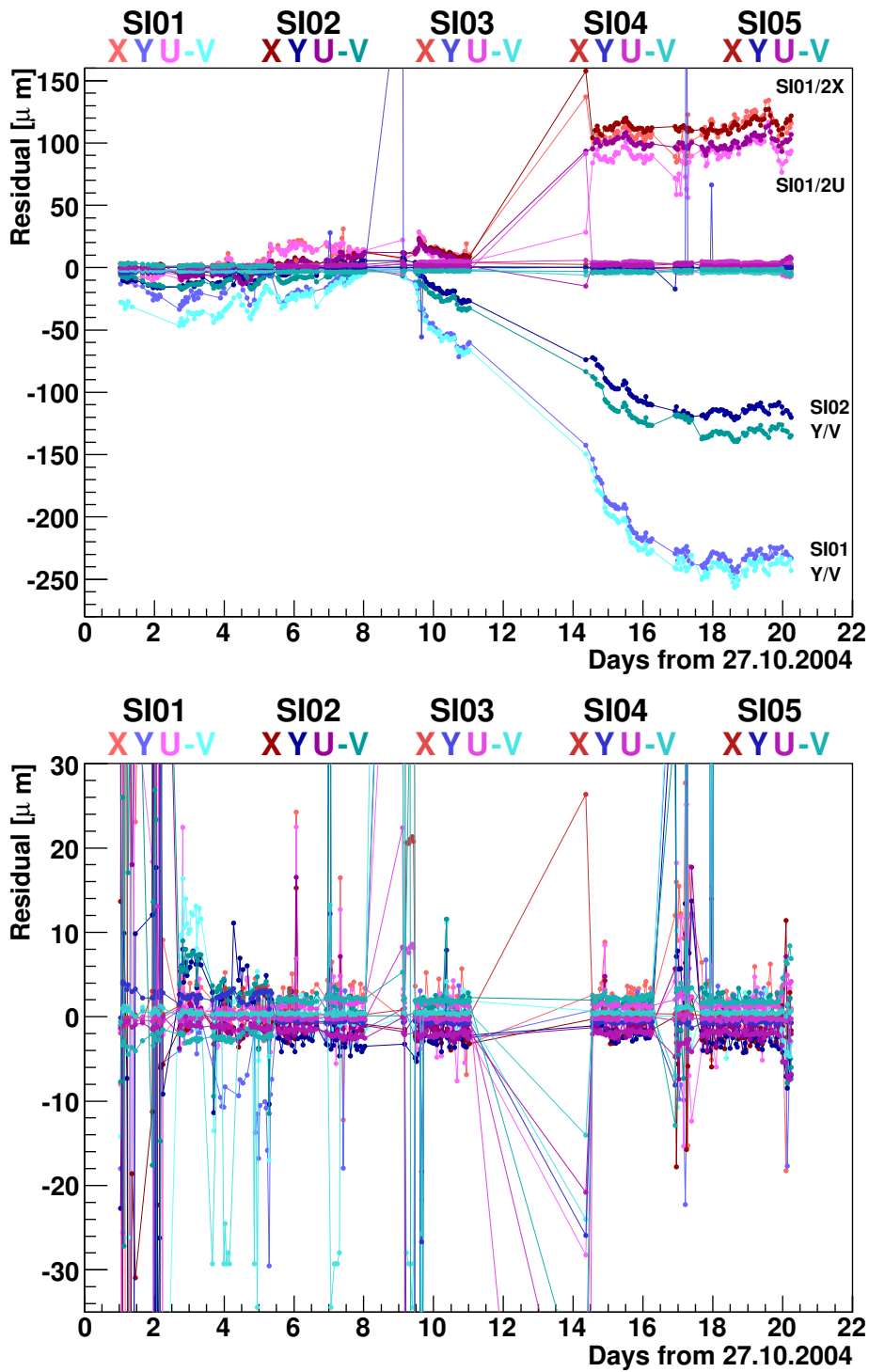


Figure 5.4: Residual position of the silicon planes before (on top) and after the alignment correction (bottom). Note the different scale on the y-axis.

5.3 Trending of Silicon Time

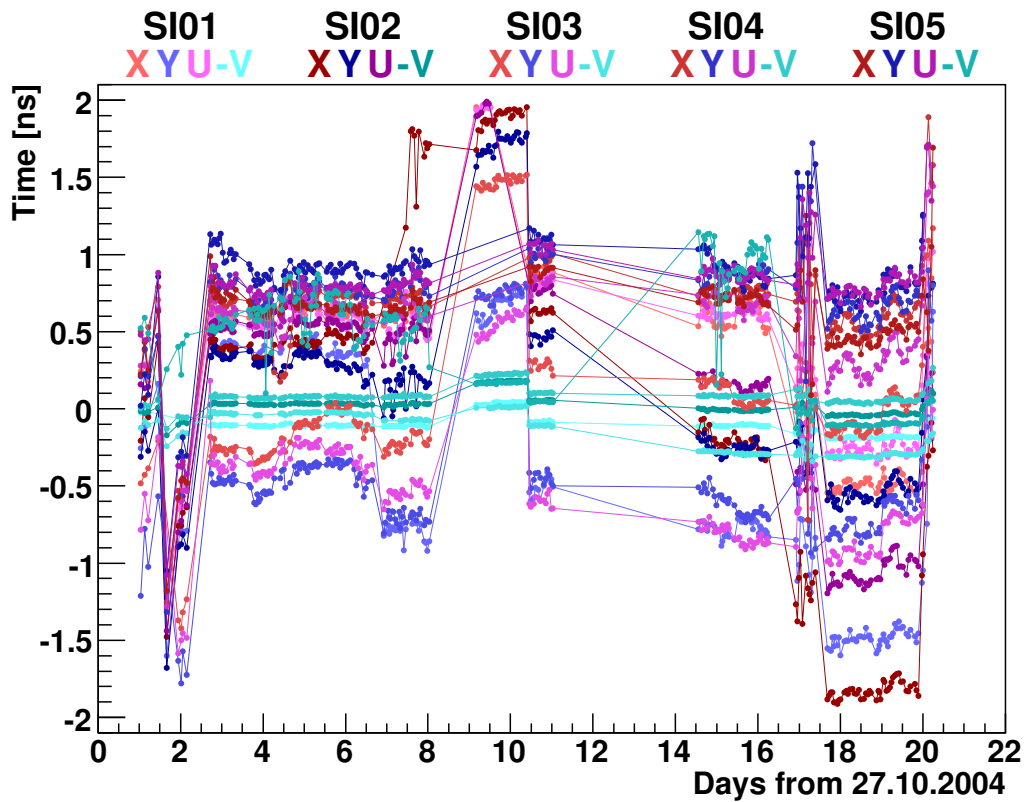


Figure 5.5: The time trending for all silicon planes during the hadron run in 2004.

A check of the stability with time of the time calibration is shown in Fig. 5.5, see section 4.4. For chunks of 242 runs the time distributions of all 20 silicon projections were analysed. The signal time distributions, as shown in Fig. 4.19 on page 56, were fitted by a Gaussian and the mean values, the peak positions of the signal time distributions are plotted in Fig. 5.5. The maximum movement of a single plane is in the order of 1.5 ns.

It is very conspicuous that all X, Y and U projections have a very similar movement in the same order, but the V projections remain much more stable. It appears that the V projection does not really measure its timing but produces always a value (peak) close to zero. This may happen due to the indirect method of reconstructing the time signal, where a broad peak close to zero can be artificially produced, especially if the slope parameters a and c , c.f. eq. (4.5), are chosen too steep (from the common trigger time jump on 4./5.11.2004, one conducts a factor ~ 7).

In Fig. 5.5, there are some jumps followed by all projections. This is a hint for an external reason, e.g. jump of the trigger time, but it is not an instability of the time calibration. The smaller movements are caused by fluctuations of the temperature in the experimental area.

5.4 Performance Test with COOOL

The online monitoring software COOOL is suitable for an almost-online analysis of the silicon tracking telescope, very soon after the commissioning of the experiment. It needed the implementation of a new functionality which provides a simple vertexing, avoiding the complex reconstruction software CORAL and the dependence on the official alignment and various detector calibrations.

For the primary vertex finding, only the silicon telescope has to be internally aligned and the time calibrations of the silicon detectors and the scintillating fibre stations have to be available. A fast alignment procedure performed with COOOL for the silicon telescope is described in appendix D.1 and section 4.4.

In the new `TwoTrackCDA` method of COOOL, the tracking is executed for each event of the detector sets upstream the target (SI01 and SI02) and therefore independent of the silicon stations downstream the target (SI03-SI05). For each track, the tracking package of COOOL provides the tracking parameters, a point $\vec{P}(X, Y, Z)$ and the slopes $\vec{S}(dX, dY, dZ)$.

The closest distance of approach (CDA) between the track of the beam particle (\vec{P}_1, \vec{S}_1) and the scattered particle (\vec{P}_2, \vec{S}_2) can be calculated using the formula:

$$(5.3) \quad d_{CDA} = \frac{\overrightarrow{P_1 P_2} \cdot (\vec{S}_1 \times \vec{S}_2)}{\vec{S}_1 \times \vec{S}_2}$$

The angle between these two tracks is determined by the cross product of the slopes \vec{S}_1 and \vec{S}_2 . The positions in X, Y and Z are also calculated for the CDA. All values are stored in a `TTree` for analysing the combinations of the two outgoing tracks.

This procedure made available a comparison of runs with and without the lead target already during the hadron beam time. The effect of multiple scattering on the angular resolution could be shown to be $\sigma_\theta = 57 \mu\text{rad}$, see Fig. 5.6, consistent with the 3 mm lead (50% r.l.) target. The z-position of the reconstructed vertices shows a second structure around -400 cm nearly as large as the lead target, see Fig. 5.7. This peak is associated with the multiplicity counter right after the target, see Fig. 3.8 on page 31. This result was already available on 2.11.04 and as a consequence, the beam counter between SI02 and the target was moved more upstream between FI01 and the inner veto, see hadron history Table B.1 on page 165.

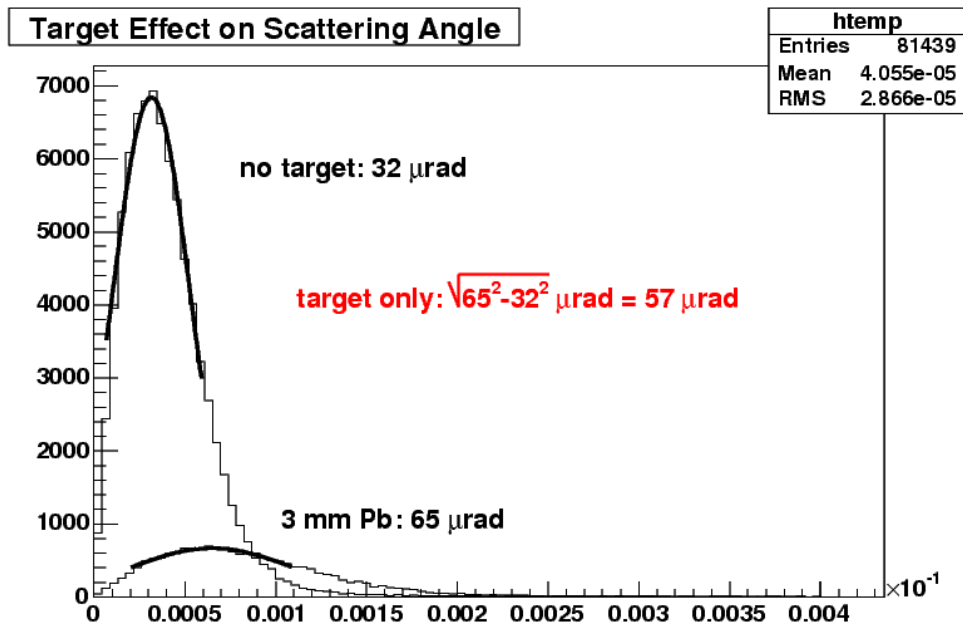


Figure 5.6: Target effect on the pion scattering angle (in rad) analysed with COOL. The original plot submitted to the COMPASS online logbook on 2.11.04 is shown. For this plot chunks of run 42322 (empty target) and 42324 (3 mm lead target) were analysed.

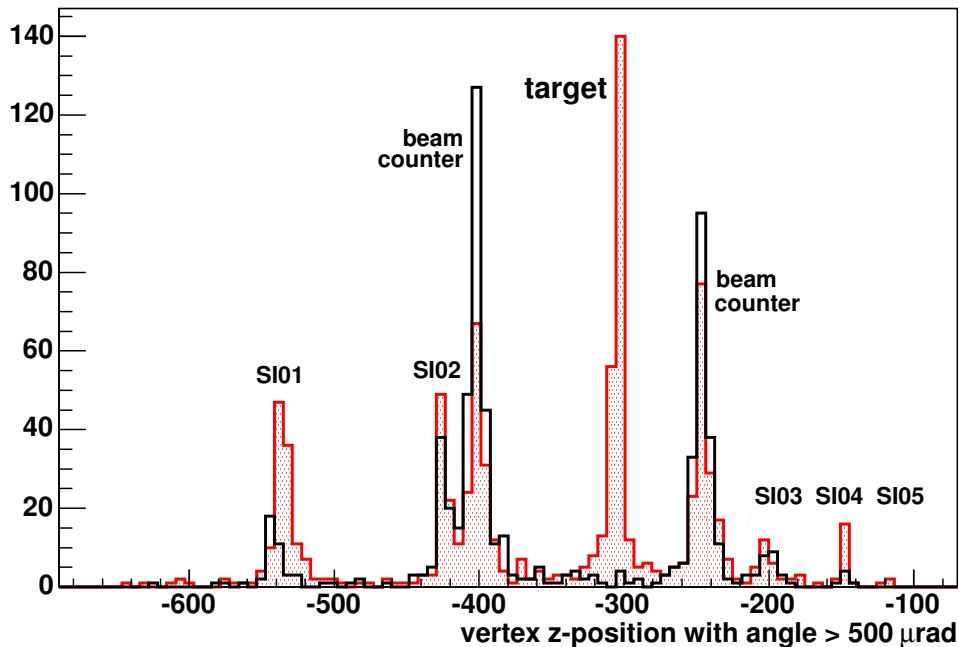


Figure 5.7: Vertex position (in cm) generated with the silicon telescope only by the online monitoring program COOL for run 42322 (empty target) and 42324 (3 mm lead target). The effect of the lead target and the influence of the beam counter can be clearly seen. These plots were submitted to the COMPASS online logbook on 2.11.04, and as a consequence the first beam counter at -400 cm was removed for the remaining beam time.

5.5 Summary

After a challenging setup phase for the hadron run 2004, five silicon detector stations were operated in the COMPASS experiment most of the time in stable conditions. The alignment of the detectors was significantly improved from tilts of about 0.1 mrad between the beam telescope and the silicon telescope after the target, such that the remaining shifts are within the spatial resolution of the detectors. In CORAL, the corrections of the silicon detector positions for hadron run 2004 were implemented. It was also presented that the parameters of the time calibration were stable within the hadron beam time.

The realisation of a simple vertexing algorithm in COOL lead to a very fast analysis of the target region during the hadron run 2004. As a consequence, the setup could be optimised for the desired measurement programme, aiming at the reactions with extremely small scattering angles.

This work on the alignment corrections, the results of the analysis of the spatial resolution, the clustering algorithm and time calibration was implemented in CORAL. This was used for the hadron data productions.

Chapter 6

Calibration of the Electromagnetic Calorimeter

6.1 Motivation

For the observation of Primakoff events, aiming e.g. at the extraction of the electromagnetic pion polarisabilities, it is important to get a precise knowledge of the performance of the calorimeter ECAL2, since the effect of the polarisabilities is small, in the order of a few percent on the production cross section for single photons measured in ECAL2, as described in section 7.2.

Fig. 6.1 shows the reconstructed energy sum of the scattered pion and the produced photon which should correspond to the beam energy of about 190 GeV for the exclusive reaction $\pi + Pb \rightarrow \pi' + \gamma + Pb$ since the energy transfer to the nucleus is negligible. This exclusivity peak reflects by its position and width the quality of different ECAL2 calibration sets for determining the photon energy. For the broad distribution peaking around 207 GeV, the primary ECAL2 calibration used also for the mDST production, was employed. The ECAL2 detector group provided in 2006 a second set of calibration values which could also be applied on the already processed mDST data sets, see section 6.4. The improvement of the second calibration is demonstrated by the blue distribution of Fig. 6.1.

A different type of events depicts Fig. 6.2, where the energy difference calculated from track momenta and their associated signals in ECAL2 are plotted, the peak at zero stemming mostly from electrons and positrons. The curves show the distribution using the primary calibration for two different runs, 42800 and 43280. The significant difference between these two runs is caused by a readjustment of the amplification of the calorimeter cells. This gave the reason that the second calibration, unlike the primary calibration, contains two calibration sets, one for the period from runs 42321 to 42840 (based on runs 42650–42665). The other set is for the period from runs 43034 to 43348 (based on runs 43220–43247) [Kol06]. This poses the question for the following work, presented in this

chapter, whether two new calibration sets are enough, or if there are more larger fluctuations with time so that a time-dependent calibration is necessary.

In this chapter, the method for a time-dependent calibration developed within this work is presented, including a short detector description of ECAL2. The stability of single channel amplification is studied, and a new fitting procedure on the cluster is considered. The outcome of this calibration and fitting procedure are discussed and concludes with a discussion on the performance during hadron run 2004.

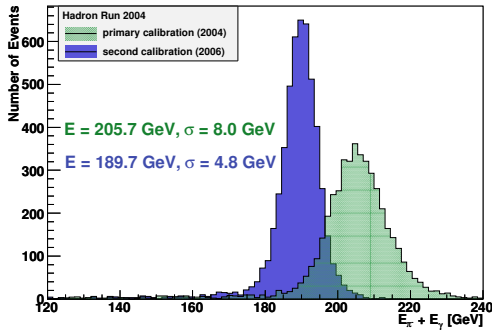


Figure 6.1: Primakoff signal with the primary calibration and the second calibration set for part of the runs of 43200-43320.

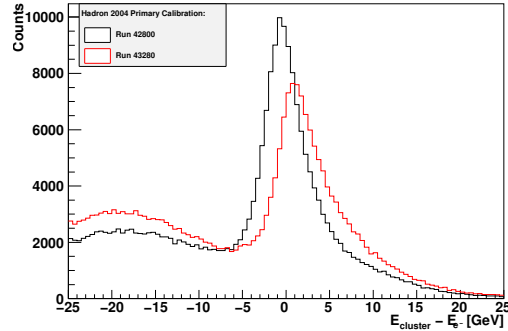


Figure 6.2: Energy difference of the electron track and its ECAL2 cluster for run 42800 in black and run 43280 in red, both with primary calibration.

6.2 Operation Principle of an Electromagnetic Calorimeter

The electromagnetic calorimeter is optimised to measure the electromagnetic shower component of impinging particles, i.e. the total energy of high-energetic electrons, positrons and photons. In matter, e.g. lead glass, the electromagnetic radiation initialises an electromagnetic cascade where photons and e^+e^- -pairs with lower energy per particle are produced by bremsstrahlung and pair production. This process of a leptonic shower is finally taken over by ionisation energy loss which dominates below the critical energy E_c for electrons at energies of a few MeV for high-Z materials. Here the energy loss due to ionisation or excitation is in the same order like the loss due to bremsstrahlung:

$$(6.1) \quad \left(\frac{dE}{dx}\right)_{\text{ion}} \approx \left(\frac{dE}{dx}\right)_{\text{brems}}$$

The energy where these loss rates are equal is called critical energy E_c . In order to describe the shower behaviour, it is convenient to introduce the scale factors

$$(6.2) \quad t = x/X_0 \quad y = E/E_c$$

where t is the distance in units of radiation length X_0 ([Tsa74],[PDG06]) and y the energy in units of the critical energy. The mean longitudinal profile of the energy deposition of

the cascade can be described by a Γ -distribution [PDG06], [Ros65],

$$(6.3) \quad \frac{dE}{dt} = E_0 b \frac{(bt)^{a-1} e^{-bt}}{\Gamma(a)}.$$

The longitudinal shower profile peaks at t_{\max} which has a weak energy dependence

$$(6.4) \quad t_{\max} = (a - 1)/b = 1.0 \times (\ln y + C_j), \quad j = e, \gamma$$

where $C_e = -0.5$ for electron-induced and $C_\gamma = 0.5$ for photon induced cascades. The parameter b is a Z - and energy dependent scale factor for energy deposition profiles obtained by simulations. For many purposes like for the COMPASS electron calorimeter, it is sufficient to set $b \approx 0.5$ [PDG06], then a can be determined with eq. (6.2) and eq. (6.4).

The transversal distribution of the shower is mainly defined by multiple scattering of the recoiling, mostly low-energetic electrons. The radial decay of the profile is described as a superposition of two exponentials, one describing the core and the other the surrounding halo [Gri90]. It is nearly matter independent in units of the Molière radii R_M which is defined as [Bat70], [Nel66],

$$(6.5) \quad R_M = E_s \cdot \frac{X_0}{E_c},$$

where $E_s = \sqrt{4\pi/\alpha} \cdot m_e c^2 \approx 21 \text{ MeV}$ is the energy scale. Measurements show that 90% of the shower energy lies within this radius and $3.5 R_M$ contain 99% [Nel66], [Bat70]. In Table 6.1 the values of the Molière radii and the critical energy E_c are listed for lead glass. The knowledge about the radial shower form is important to estimate the possible resolution in space for a given granularity of the calorimeter. A calorimeter is designed such that a shower is distributed over several detector cells.

Charged particles moving with high-relativistic speed can pass the material faster than light ($v > c_{\text{medium}}$) and Cherenkov light is emitted under a specific angle Θ_{Ch} . For electrons, this is true to energies of a few MeV, so that practically all electrons forming the shower emit Cherenkov light. The expected number of Cherenkov photons created by the charged particles of an electromagnetic shower, is estimated by [Rud92]

$$(6.6) \quad N = 2\pi\alpha \cdot L \int_{\lambda_1}^{\lambda_2} \sin^2 \Theta_{\text{Ch}} \frac{1}{\lambda^2} d\lambda$$

where L is the path length. The number of photons is limited by the optical acceptance of wave lengths λ_1 to λ_2 for a given detector. These Cherenkov photons are detected by Photo Multiplier Tubes (PMT) in order to determine the energy and the position of the incident particle.

Physical parameters	TF1	Chemical composition	TF1-000	TF101
Density ρ	3.86 g/cm ³	PbO	51.2%	51.2%
Radiation length X_0	2.8 cm	SiO ₂	41.3%	41.5%
Interaction length	38.0 cm	K ₂ O	7.0%	7.0%
Moliere radius R_M	3.68 cm	As ₂ O ₃	0.5%	-
Refractive index n_e	1.65	CeO ₂	-	0.2%
Total internal reflection angle	36°			
Critical energy E_c	16 MeV			

Table 6.1: Chemical composition of the lead glass types TF1 and TF101 and their physical parameters [Evd05], [Dav03].

The energy resolution is usually parameterised [PDG06],

$$(6.7) \quad \frac{\sigma_E}{E} = \frac{a}{\sqrt{E}} \oplus b \oplus \frac{c}{E} = \sqrt{\frac{a^2}{E} + b^2 + \frac{c^2}{E^2}}$$

so \oplus stands for summation in quadrature and E in units of GeV. The parameter a is a stochastic term and reflects the uncertainty due to the fluctuations of the individual shower profiles, leading to a spread in the (Cherenkov) energy deposition for a given incident energy E , as well as detector specific components like passive material in front of the calorimeter. The constant parameter b specifies mainly the uncertainty of the calibration and the third parameter c takes contributions due to electronic noise into account. An equivalent parametrisation as eq. (6.7) is also sufficient without the third term, for the resolution in space with a a parameter in the order of several mm and b , dependent on the detector design, being of the order 6 mm and 0.5 mm for the COMPASS calorimeter ECAL2 [COM07a].

6.3 The COMPASS Electromagnetic Calorimeter

6.3.1 The Detector Setup

The electromagnetic calorimeter ECAL2 is located in the second part of the COMPASS spectrometer SAS, in front of the hadron calorimeter and the muon filter 2, see Fig. 2.2 on page 8. It consists of 3068 lead glass blocks, where each one has the size $38.3 \times 38.3 \times 450 \text{ mm}^3$, arranged in a matrix of 64×48 blocks and numbered from 0 to 3067. The block length corresponds to 16 radiation lengths. Beam particles which did not undergo a hard reaction in the target region or in the spectrometer, pass the spectrometer on the beam line which is bended due to the spectrometer magnets. Therefore, the ECAL2 is equipped with a hole of at least 2×2 blocks¹. In the inner region of ECAL2, about 800 radiation-hardened lead glass blocks of the type TF101 are used, and the outer

¹This size is specific for the hadron beam time. The hole is enlarged for muon run, see subsection 2.2.5.

region is covered by TF1 blocks, see Fig. E.1 on page 179. The properties of these lead glass types are given in Table 6.1.

Electrons and photons induce an electromagnetic shower in the lead glass. The Cherenkov light of the shower, in good approximation proportional to the total shower energy, is collected for each cell by a photo multiplier PMT (FEU-84-3 PMT with tri-alkaline photo-cathode S-20 type) of 34 mm diameter which is mounted at the end of each block. The optical contact between the PMT and the lead glass block is established by a layer of silicon grease. Special high voltage dividers are designed to operate the PMTs in a maximum range of linearity. At the front of each lead glass block, a gain monitoring system is attached, where light pulses of a Light Emitting Diode (LED) radiate the lead glass block which is performed between the SPS cycles². The whole lead glass block is wrapped in aluminised mylar foil. The modules used in ECAL2 were already in use in the former experiment GAMS-4000 [Ald86], [Ald85], [Bin81].

Fast Integration ADCs (FIADC) measure the PMT anode signals of 2048 ECAL2 modules in the central part. If a trigger signal arrives, the charge on the PMT anode is integrated over a time frame of 100 - 250 ns by a charge sensitive integrator. This integrator converts the charge into a voltage value which is digitised by an ADC chip to a 12 bit word. In the FPGA chip the pedestal values which are determined at the beginning of each run, are subtracted from the digitised information. If the digitised information is about 5 ADC counts above the pedestal value, it is combined with the digital signals of the other ECAL2 modules and sent as a data-block to the DAQ system. The other 1024 ECAL2 modules, located in the outer region, are connected to the Sampling ADC (SADC) which is the successor of the FIADC. The SADC allows a direct measurement of the signal shape. The ADC chip samples continuously the analogue signal, and each digitised value represents the anode value at a certain time. The sampling rate is 77.76 MHz, and the values are stored in a buffer. If a trigger signal arrives, 30 consecutive samples are readout matched with the trigger latency settings. The signals which are above the threshold are combined to a data-block and send to the DAQ. More detailed information on the FIADC and SADC can be found in [COM07a].

6.3.2 A Glimpse on the Shower Reconstruction

The framework of CORAL, see subsection 2.3.5, includes a package for reconstruction of the energy and position of electromagnetic showers. From the energy deposited in neighbouring lead glass blocks which will be called *cells* in the following sections, the shower parameters are obtained assuming a certain average of the shower profile.

For each event (section 2.3), the algorithm searches for cells with an energy deposit above a predefined threshold defining the local maximum. In case two local maxima are neighbouring cells, those are not separated. The energy and position of the local maximum cell serve as start values for the shower reconstruction. Further cells belonging to the shower

²see section 2.2 on page 6 for more details.

are searched within an area of 3×3 or 5×5 cells around the local maximum cell, depending on the estimated shower energy. The energy deposit of the surrounding cells can be shared between several showers, but not the local maximum cell. The initial values of the local maximum cell are used for estimating the energy deposit of the surrounding cells. This is performed for each shower, then the relative energy contributions of cells shared by two or more showers can be determined. The shower energy or cluster energy itself is calculated as the sum of contributing cell energies, where cell sharing in case of overlapping showers is taken into account. The summed energy is corrected by a factor of 1.06 to compensate for energy leaks outside the cluster [Kol06]. The position of the shower is determined by an inverse 1D-cumulative shower profile function [Led95]. The information of this subsection is taken from [COM07a].

6.4 Calibration Method

The spatial dimensions of the electromagnetic shower in ECAL2 caused by a photon, electron or positron, respectively, changes depending on the energy of the particle. From one single block up to 25 lead glass blocks can be affected by the shower. An algorithm is needed which combines these blocks, respectively cells, to a cluster. The aim of the calibration is to receive as precisely as possible the relation between the ADC-signal of each cell and the energy deposited in it. This section presents a calibration method which is based on processed data (mDSTs), where a cluster-finding and shower-reconstruction algorithm in the frame work of CORAL has already been applied, see subsection 6.3.2. In these mDSTs, the raw energy information in units of ADC-channels for cells of a cluster E_{cADCraw} is not available, but with the COMPASS analysis software PHAST one has access to the particular cell energies E_{cell} . By dividing the cell energy E_{cell} with the primary calibration value a_{cell} used in the mDST production (see section 6.1), it is possible to reconstruct a quasi ADC-information E_{cADC} :

$$(6.8) \quad E_{\text{cADC}} = E_{\text{cell}} / a_{\text{cell}}$$

For the local maximum cell of a cluster, E_{cADC} corresponds to the original ADC-signal of this cell. In case of surrounding cells the energy can occasionally be shared amongst showers.

Prior to the calibration procedure presented here, the two sets of the second calibration provided by the ECAL2 detector group were available, one valid for all runs from 42324 to 42840, and the other for runs 43034 to 43348. This second calibration does not necessarily deliver event by event the best result, but every known systematic effect has to be revised in average because a new calibration will again contain all systematic deviations. In order to use the calibration values of the second calibration, the cell energy has to be divided by the old primary calibration value and multiplied with the value of the second calibration [Kol06]:

$$(6.9) \quad E_{\text{cellSecondCalib}} = E_{\text{cellPrimary}} / a_{\text{cellPrimary}} \cdot a_{\text{cellSecondCalibration}}$$

The values of the second calibration contain an unspecified systematic error [Kol09]. This error was compensated in the $a_{\text{cellPrimary}}$ values. This means calculating back to ADC values does not deliver integer values as expected. The calibration constants derived within this thesis have to be used in combination with this special primary calibration set.

For the new calibration of ECAL2, electrons and positrons are used which originate from background reactions of hadron run 2004. Electrons reach the experiment as part of the hadron beam, and electron-positron pairs are created by gamma conversion $\gamma \rightarrow e^- + e^+$, where the photons are also produced in many hadronic decays, e.g. $\pi^0 \rightarrow \gamma\gamma$.

Electrons and positrons have the advantage, that in case they have passed at least SM2, their momentum is known as well as their impact position in the calorimeter. On account of this, the cluster energy can be compared with the energy of the electron track³. With a description of the electromagnetic shower, the expected energy deposit in each cell of such a cluster can be predicted in average and the calibration values of each cell can be determined.

6.4.1 Event Selection

A particle is identified as electron or positron candidate, respectively, if the following selection criteria are fulfilled.

The electron track candidate has to have its first measured point at least before SM2 to ensure a momentum measurement. The last measured point of the electron track has to be before the muon wall MW2, otherwise the track originates from a muon. According to the kinematic range of the e^\pm and the acceptance of the SAS⁴, only tracks with momenta above 10 GeV/c and below 180 GeV/c are extrapolated to the z-position of ECAL2 at 3327.5 cm (see chapter A for coordinate definition).

An ECAL2 cluster is associated with the track if the distance between the cluster position and the predicted track position matches within a radius of 2 cm, see Fig. 6.3. In case more electron candidates are found in one event, they are only accepted if the associated ECAL2 clusters have a distance of at least 12 cm to avoid overlapping of clusters. The sample is cleaned from hadron tracks by requiring an energy deposit in the corresponding HCAL2 region less than 5% of the ECAL2 cluster energy E_{cls} (here the second calibration set is applied). The energy difference of the cluster E_{cls} and the track E_{e^-} has to be smaller than 8 GeV, see Fig. 6.3.

If an electron candidate passed all selection criteria, the relevant ECAL2 information is stored in a μ DST. These μ DSTs are produced with PHAST for each run and serve as basic data sample for the extraction of the shower model presented in the following. In section 6.7 will be described, that several cells were in saturation during the hadron run

³Unless otherwise mentioned, if it is written electrons then also positrons are meant in the following.

⁴see subsection 2.2.1 on page 7 for more details.

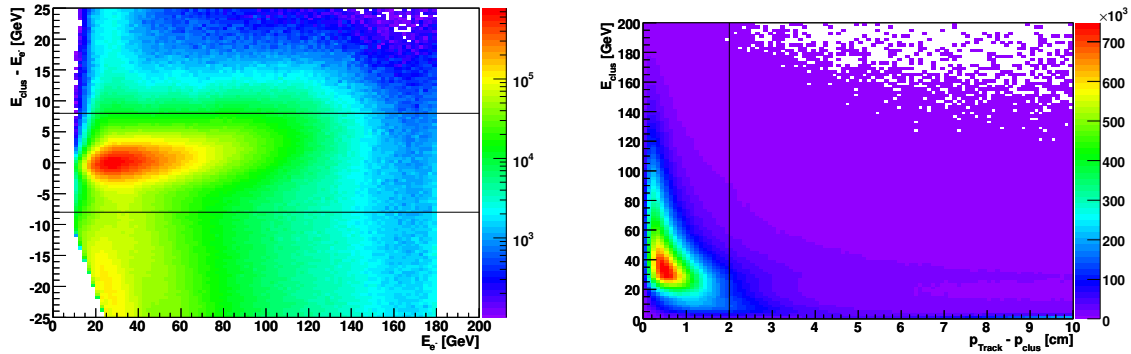


Figure 6.3: Both histograms illustrate the cuts used to study the shower shapes. On the left plot, the energy difference of the electron and the ECAL2 cluster (here the second calibration set is applied) is displayed versus the electron energy for 86 runs of hadron run 2004. On the right, the cluster energy distribution is shown dependent on the distance between the cluster position and the impact point of the extrapolated electron track.

2004. In order to prevent artifacts due to saturating cells, only hits with corresponding cell energies $E_{\text{CADC}} < 3500$ or below their specific saturation threshold, were stored in the μDST .

6.4.2 Shower Model

A shower model is developed for two reasons. It has been found (c.f. section 6.7) that several cells were dead, unstable or saturated during all or part of the hadron run 2004. A shower fit algorithm, see section 6.5, based on a data-driven shower model should recover clusters which were affected by such cells. Secondly for a run-dependent calibration of the cells, the prediction of the shower model for all the cells of a cluster turned out to be useful.

The data-driven shower model is derived from the electron preselection where all showers initiated by the electrons are superposed. Since the electron energy E_{e^-} is known from the track momentum reconstruction, the energy ratio of the measured cell energy E_{cell} and the electron energy E_{e^-} can be calculated. Due to the strong variation of this energy ratio, it is convenient to consider the logarithm in the following:

$$(6.10) \quad r = \log_{10} \frac{E_{\text{cell}}}{E_{e^-}}$$

The energy ratio r depends obviously on the distance d of the cell centre $(x_{\text{cell}}, y_{\text{cell}})$ and the centre of the shower which is assumed to be at the impact point of the track $(x_{\text{tr}}, y_{\text{tr}})$

$$(6.11) \quad d = \sqrt{(x_{\text{tr}} - x_{\text{cell}})^2 + (y_{\text{tr}} - y_{\text{cell}})^2}.$$

Fig. 6.4 depicts a theoretical shower distribution, where some possible positions of cells

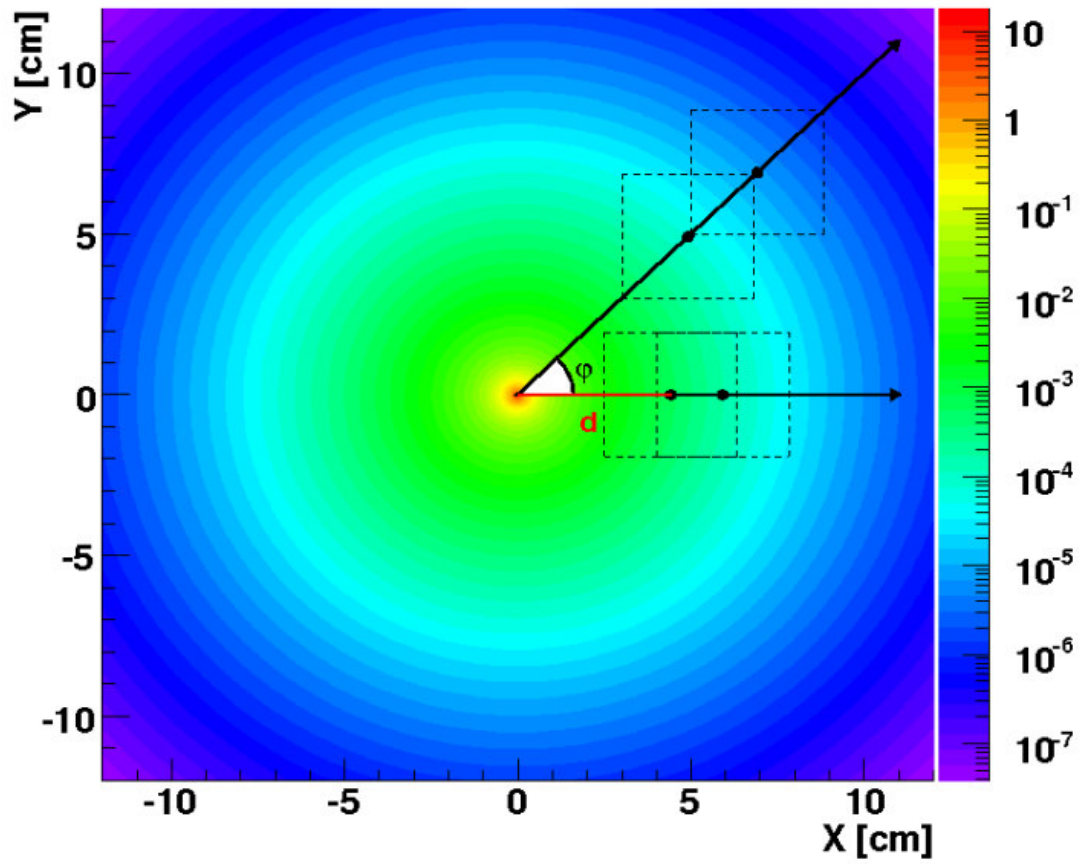


Figure 6.4: Simplified distribution of an electromagnetic shower (z -axis in units of GeV). The black squares illustrate possible cell positions and distances d from the shower centre. The integrated energy collected by one cell depends on the position of the cell which strongly decreases with larger d .

are indicated by the black squares. The expected energy collected by a single cell is given by the respective integral of the theoretical shower prediction. In the data, the shower centres are distributed randomly with respect to the cells. The shower is a radially symmetric distribution, but not the integrated energy per cell, as it can be seen in Fig. 6.8 (a). It makes a difference for the integrated energy, if cells are horizontally or diagonally at a distance d from the shower centre, see black squares in Fig. 6.4. This means the distribution of the ratio r versus the distance d varies with the angle φ

$$(6.12) \quad \varphi = \arctan \left(\frac{x_{\text{tr}} - x_{\text{cell}}}{y_{\text{tr}} - y_{\text{cell}}} \right).$$

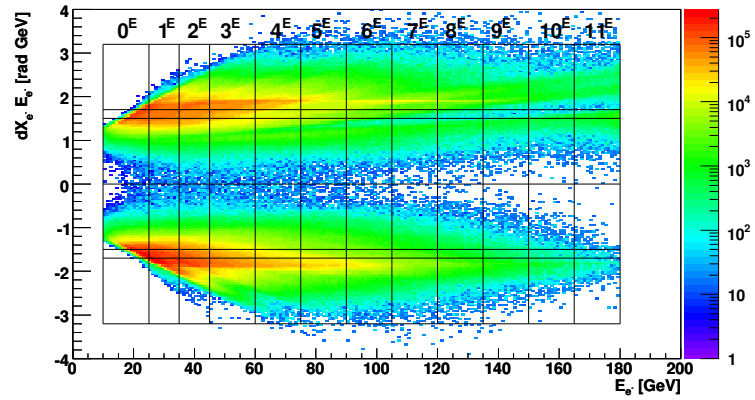
One approach within this thesis pursued the strategy of determining empirically a description of the shower energy distribution as a function of $r(d, \varphi)$. But this ansatz was dismissed at the stage of checking its feasibility, because it did not incorporate all physical effects in the energy conversion properties of the cells.

The idea of the second approach was to investigate the distributions $r(x, y)$ extracted from the data by superposing all ECAL2 clusters from the selected electrons, as described in subsection 6.4.1. The shower distribution itself is radially symmetric around the trajectory axis, but particles are hitting ECAL2 with a certain angle. The strong correlation of the energy and the impact angle can be seen in Fig. 6.5. The electrons and positrons are bent due to the two dipole magnets SM1 and SM2 in the spectrometer, such that the product of the track angle dx_{tr} and the particle energy is roughly constant, cf. Fig. 6.5 (a). The used coordinate system is oriented such that a positive sign of the track angle means negative charge. Fig. 6.5 (b) depicts the unbent case for the angle in the vertical direction dy_{tr} . The projection of the energy-weighted angles is shown on (c). In order to take the effect of the impact angle on the shower distribution into account, the available data are divided into 2×9 angle-bins for both impact directions, see Table E.1. The angle-bins are numbered as indicated in (c) e.g. 9^{A} , in a sequence reflecting the symmetry properties used later on. The shower profile of the particular angle-bin depends also on the energy of the particle, therefore the data-set is additionally subdivided into 12 energy-intervals e.g. 4^{E} , see (a, b) and Table E.2. In total, 216 r -distributions are generated containing the shower information and will be referred as e.g. Bin $[4^{\text{E}}, 9^{\text{A}}]$ in the following.

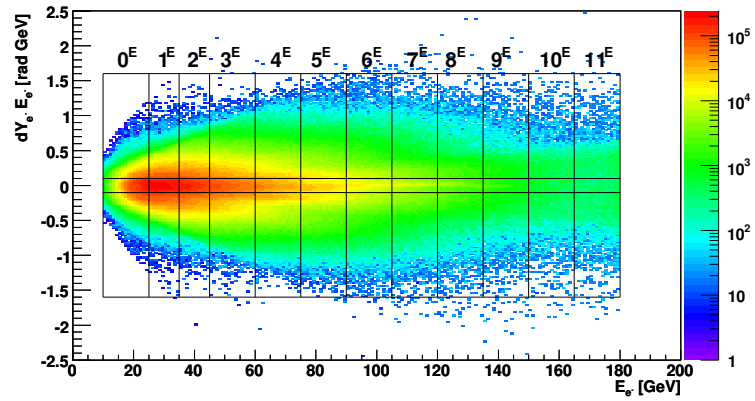
As source of the r -distributions served 85 runs (see Table E.4) because for those runs, the information of the LED signal per cell existed at the time performing this analysis. The two sets of the second calibration were corrected for the run-dependent fluctuations received from the LED information, see subsection 6.4.4. That is, the quasi-raw ADC information per cell of each ECAL2 cluster is multiplied by the LED-corrected calibration value $a_{\text{cell_LED}}$:

$$(6.13) \quad E_{\text{cell}} = a_{\text{cell_LED}} \cdot E_{\text{cADC}}$$

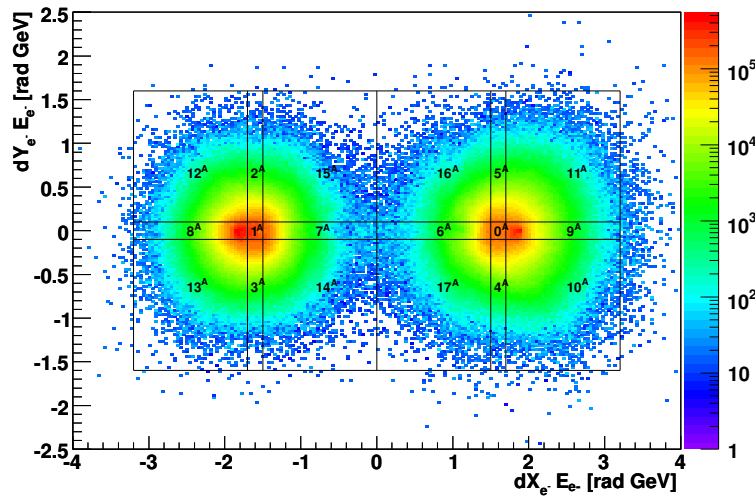
In Fig. 6.6 an example of the logarithmic 2D- r -distribution is plotted as a function of X and Y for Bin $[8^{\text{E}}, 0^{\text{A}}]$ with its typical bell-shaped form. Each single entry represents the



(a)



(b)



(c)

Figure 6.5: The correlation of the impact angle and energy of the electrons and positrons is pictured in (a) and (b). The product of the impact angle in X and Y, respectively, and the energy of the particle is displayed on (c). The black lines surround the areas of the particular angle-bins and energy intervals for which r -distributions are generated. In (c) the numbers of the particular angle bins are depicted which are listed in Table E.1. Notation, e.g. Bin $[4^E, 9^A]$.

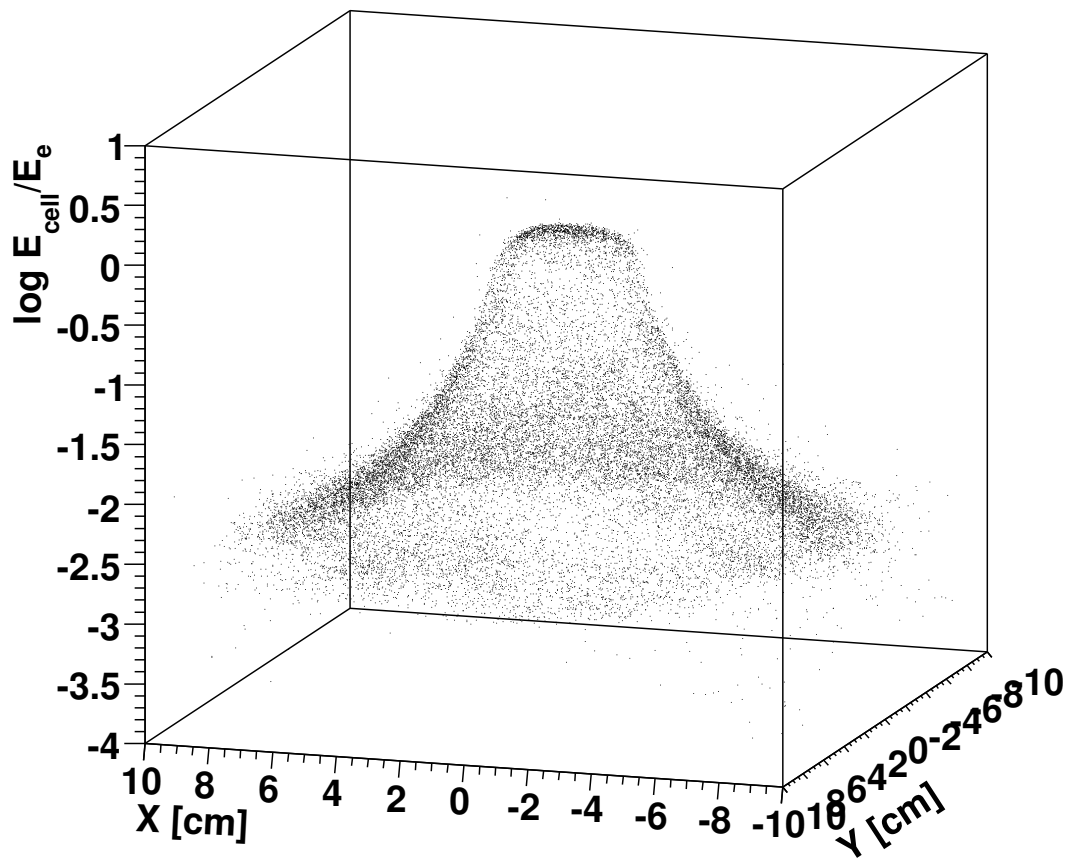


Figure 6.6: Example of an r -distribution in the 2-dimensional presentation of Bin $[8^E, 0^A]$ with its bell-shaped form.

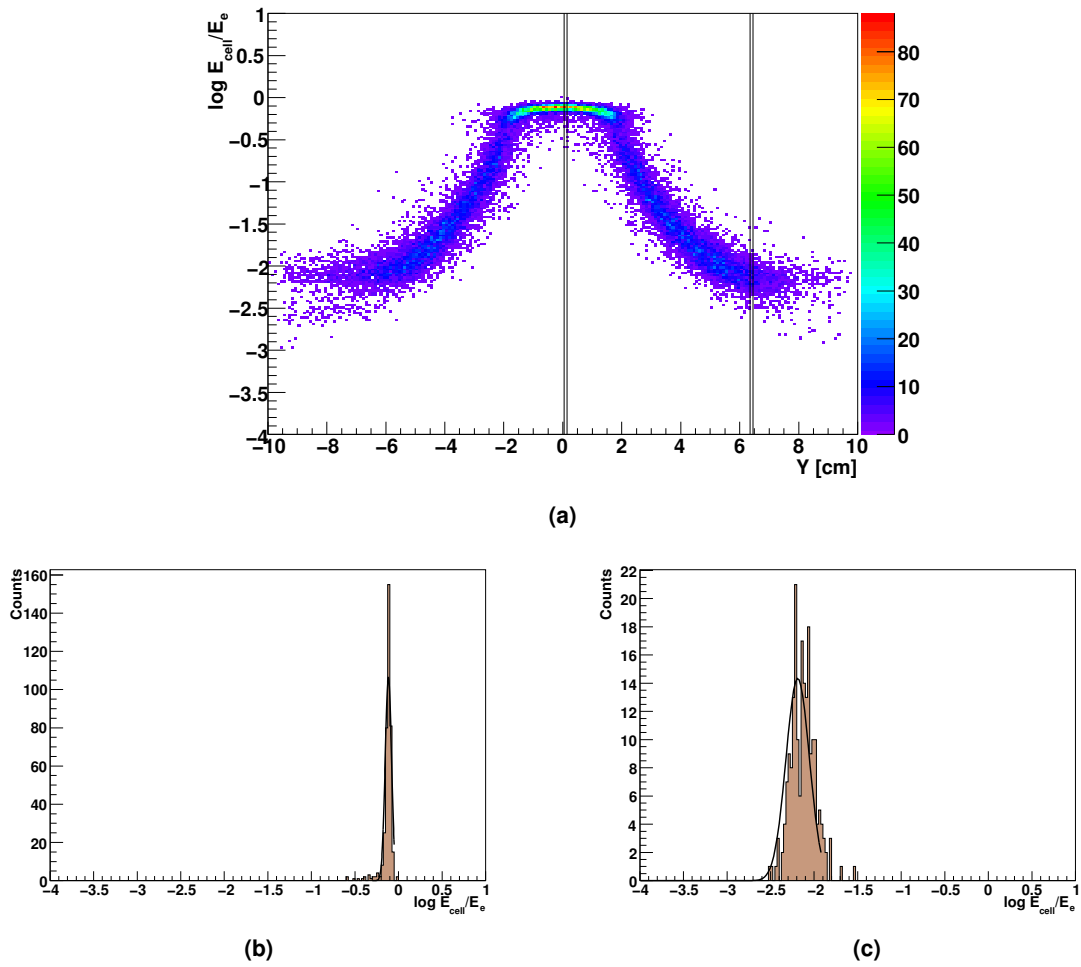


Figure 6.7: (a) shows the r -profile for Bin $[2^E, 1^A]$ along X-bin 100 of a 2D- r -plot as presented in Fig. 6.6. Figure (b) and (c) represent $r = \log E_{\text{cell}}/E_e$ at certain X and Y bins (corresponding intervals marked with black lines in (a)) fitted by a Gaussian distribution. Due to the logarithmic scale, the r -distribution at 0.1 cm in (b) is narrower compared to the outer region at 6.4 cm in (c).

logarithmic energy ratio r of the shower deposited in a single cell, decreasing with the distance to the shower centre. The goal of the following procedure is to recover this 2D- r -distribution such, that for each position of a cell within ± 10 cm in X and Y away from the shower centre, respectively, the uncertainty for r is determined by fitting each r -projection of the $200 \text{ X} \times 200 \text{ Y}$ -bins of Fig. 6.6 with a Gaussian-distribution. Such Gaussian-fits are depicted in Fig. 6.7 (b) and (c). All mean values of the Gaussian-fits build the bell-shaped shower form. This is performed for all angle and energy bins. In case a bin does not contain enough statistics, the mean value is set to a default value with a large error assigned.

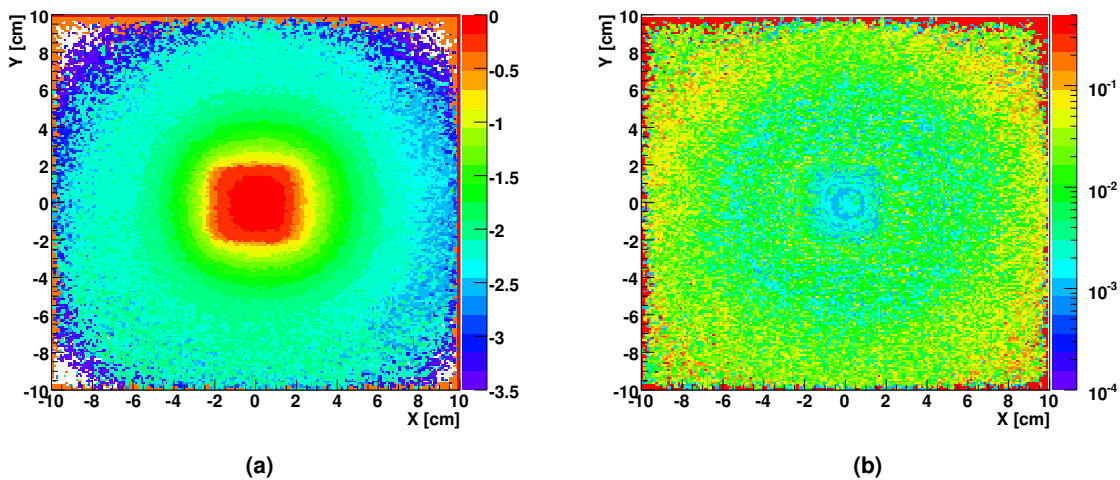


Figure 6.8: (a) depicts the r -distribution after applying the Gaussian-fitting-procedure for Bin $[2^E, 1^A]$. r is the mean value of the Gaussian fits, see e.g. Fig. 6.7. The fit error on the mean values is shown in (b).

Fig. 6.8(a) shows a typical r -distribution for Bin $[2^E, 1^A]$ as a result of the Gaussian-fitting-procedure. r is the mean value of the Gaussian fits, the error on these mean values are shown in Fig. 6.8(b). The shape of the r -distribution is not radially symmetric due to the fact that each ratio value represents the integrated energy ratio r of the calorimeter cell. The highest energy ratio of about $E_{\text{cell}}/E_{\text{cluster}} \approx 0.8$ corresponding to $r = \log_{10}(E_{\text{cell}}/E_{\text{cluster}}) \approx -0.1$ carries the central cell of a shower, thus the r -distribution has its maximum plateau in the range of the dimensions of the cell, see as an illustration Fig. 6.20 on page 101, where a cell grid is drawn in a final r -distribution.

Not for all of the 2×9 angle-bins and energy intervals, the statistics of the 2D- r -distribution is sufficient for deriving a meaningful r -distribution, as shown on Fig. 6.9 (a) for Bin $[7^E, 5^A]$. In order to compensate the missing information, it is possible to exploit symmetries of the various angle-bins. The distribution of the electromagnetic shower is assumed to have the same shape for electrons and positrons, but due to the spectrometer magnets they are bent in opposite directions. The track angles dX_{tr} of the electrons have a positive sign and positrons a negative sign which corresponds to the *right* and *left* accumulation, respectively, of Fig. 6.5 (c). Before combining the statistics, the showers

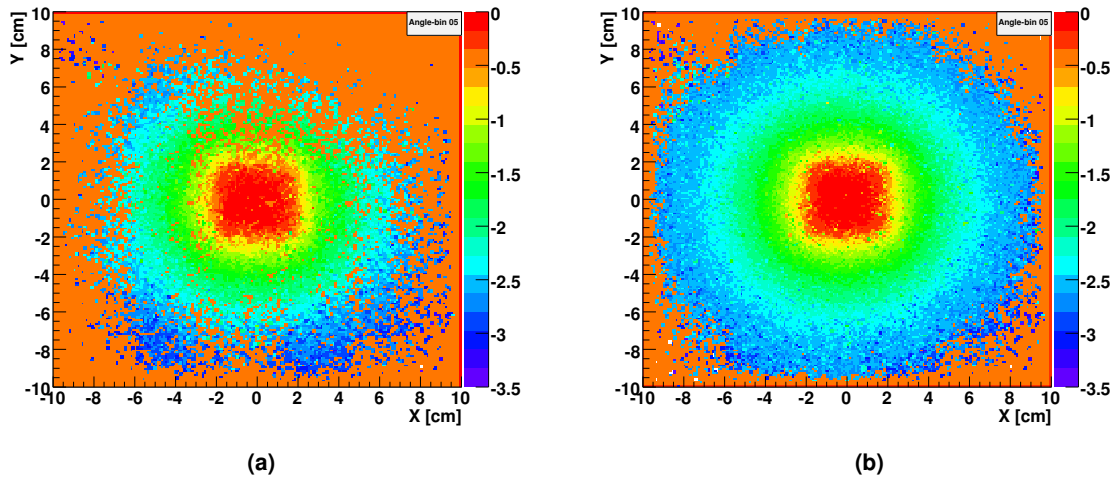


Figure 6.9: Figure (a) shows the r -distribution for Bin $[7^E, 5^A]$ before and on (b) after exploiting symmetries.

are mirrored along the X -axis. Since track angles dY_{tr} are distributed symmetrically, as shown in Fig. 6.5 (b), the *up* and *down* symmetry can be exploited by mirroring along the Y -axis. In Table 6.2 the various exploited symmetries are summarised. For example, the r -distribution for angle bin 2^A and 5^A should have the same form but mirrored along X as well as 3^A and 4^A . By mirroring 3^A and 4^A along Y , the four angle-bins can be superimposed. The new value for the energy ratio r_{new} is calculated by adding each bin content of the histogram r_i and weighted by their errors σ_i for the number of superimposed angle-bins n

$$(6.14) \quad \sigma = \sum_{i=1}^n \frac{1}{\sigma_i^2}$$

$$(6.15) \quad r_{new} = \frac{1}{\sigma} \sum_{i=1}^n \frac{r_i}{\sigma_i^2}, \quad \sigma_{new} = \frac{1}{\sqrt{\sigma}}.$$

Fig. 6.9 (b) shows the effect for a particular bin after exploiting the symmetries. For energy intervals higher than 120 GeV, the statistics for some angle-bins is not sufficient to generate a shower distribution, see Fig. 6.5 (a) and (b). In order to prepare a shower distribution for these bins, further angle-bins have to be combined which are listed in Table 6.3.

The r -distributions, even with exploiting the symmetries, are not smooth due to the binning (bin width = 0.1 cm). In order to achieve smooth distributions, each bin with its surrounding neighbourhood of up to 10 bins is fitted by a two-dimensional quadratic function:

$$(6.16) \quad r_{smooth}(\Delta x, \Delta y) = p_0 + p_1(\Delta x) + p_2(\Delta y) + p_3(\Delta x)^2 + p_4(\Delta y)^2 + p_5(\Delta x)(\Delta y)$$

Shower Symmetries							
X-axis	left		right				
Sym 1	1 ^A	- X -	0 ^A				
Sym 2	7 ^A	- X -	6 ^A				
Sym 3	8 ^A	- X -	9 ^A				
Y-axis	up		down				
X-axis	left	right	left	right			
Sym 4	2 ^A	- X -	5 ^A	- Y -	3 ^A	- X -	4 ^A
Sym 5	12 ^A	- X -	11 ^A	- Y -	13 ^A	- X -	10 ^A
Sym 6	15 ^A	- X -	16 ^A	- Y -	14 ^A	- X -	17 ^A

Table 6.2: Exploited shower symmetries, see mapping of the angle bins in Fig. 6.5 (c) and Table E.1.

Shower Symmetries				
120 - 135 GeV	4 + 5 → 0, 9	2 + 3 → 1, 8	16 + 17 → 6	15 + 14 → 7
135 - 150 GeV	11 + 10 → 0	12 + 13 → 1	11 → 5	10 → 4
	12 → 2	13 → 3	16 + 17 → 6	15 + 14 → 7
150 - 165 GeV	11 + 10 → 0, 6	12 + 13 → 1, 7	11 → 5, 16	10 → 4, 17
	12 → 2, 15	13 → 3, 14		
$E > 165$ GeV	11 + 10 → 0, 6	12 + 13 → 1, 7	11 → 5, 16	10 → 4, 17
	12 → 2, 15	13 → 3, 14		

Table 6.3: Additional shower symmetries exploited for higher energy-bins, see mapping of the angle bins in Fig. 6.5 (c) and Table E.1. For purpose of readability, the angle bin index ^A was left out.

with the fit parameters p_0 to p_5 . The fit parameters from one bin are used as start parameters of the next bin. It turns out that by fitting the bins starting from the centre of the histogram and moving spirally from the centre to the outer part of the histogram, e.g. Fig. 6.8 (a), systematic shifts of the r -distribution towards X or Y are avoided. This procedure is performed two times. One time with a fine step-size Δx and Δy of 0.05 cm which models the central region with the plateau and the falling edge, see Fig. 6.10 (b). The falling edge is a crucial region, because it is representing the energy sharing between the maximum cell and the neighbour cell. The second fitting is done with more coarse step-sizes Δx and Δy of 0.2 cm for modelling the tails of the transverse shower distribution. Fig. 6.10 displays the r -distributions for parameter p_0 for the zoomed (b) and the large case (a) for Bin $[7^E, 5^A]$. Due to a lack of statistics for the outer tail of the r -distribution, this outer region is set for radii larger than 6-7 cm to a default ratio $r = -3$ which means the collected energy by the particular cell is only a thousandth of the shower energy.

The r -distributions cover the range of the 5×5 cells which form a cluster, see Fig. 6.20. The energy sum of these 25 cells corresponds to the deposited energy of the particle. Since

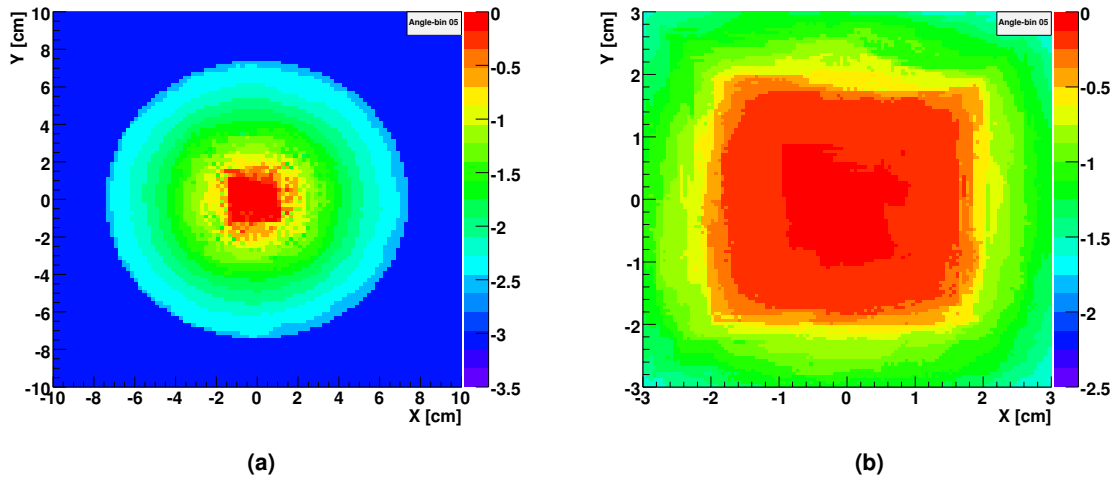


Figure 6.10: Parameter p_0 of the fit function eq. (6.16) for both cases: the coarse one for the shower tails (a), the zoomed one describing the shower centre (b).

we are looking at the logarithm of the energy ratio r_i deposited per cell i , see eq. (6.10), the sum of all cells has to fulfil the following constraint

$$(6.17) \quad R_i = 10^{r_i}, \quad R_{\text{SUM}} = \sum_{i=1}^{25} R_i = 1,$$

where r_i is calculated with eq. (6.16). In case the X and Y position of the cell i with respect to the cluster centre is smaller than 3 cm, the parameters p_0 to p_5 of the zoomed histogram are used, otherwise those from the coarse histogram. This constraint on the sum of the energy ratio is used by the smoothing step described in the following.

The 5×5 cell grid is evaluated with shifts in 480 steps along the central area of -2.2 cm to 2.2 cm in X and Y . For each point, R_{SUM} is calculated. The ratio RC of the central cell is corrected via several iterations by the missing value

$$(6.18) \quad RC_n = 10^{r_{c_n}}, \quad RC_n = RC_{n-1} - 0.35 \cdot (R_{\text{SUM}_{n-1}} - 1)$$

where n is the iteration number and 0.35 is a damping factor. The algorithm passes through $n = 10$ iterations which turned out to be sufficient. Fig. 6.11 shows the result of the summed ratio $R_{\text{SUM}_{10}}$, mainly the inner part is well corrected. The corrected ratio values are stored as a revised parameter p_0^{corr} . Fig. 6.12 pictures the r -distribution for the example plot of Bin $[7^E, 5^A]$ after this cell correction. Sharp edges on the corners of the inner cells are visible.

As last step, the new corrected r -distribution is calculated by using eq. (6.16) with the corrected parameter p_0^{corr} and the parameters $p_1 - p_5$. This calculated r -distribution is again fitted by eq. (6.16) as described above, and the final parameters are stored in histograms, see e.g. in Fig. 6.13 and Fig. 6.14 the coarse and zoomed, respectively, parameters of

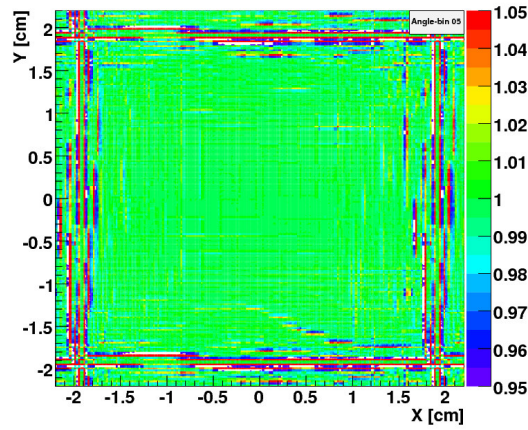


Figure 6.11: Summed energy ratio R_{SUM10} for Bin $[7^E, 5^A]$ after the correction. Only along the edge of the cell remain deviations from 1 fluctuating to positive and negative values by more than 1%.

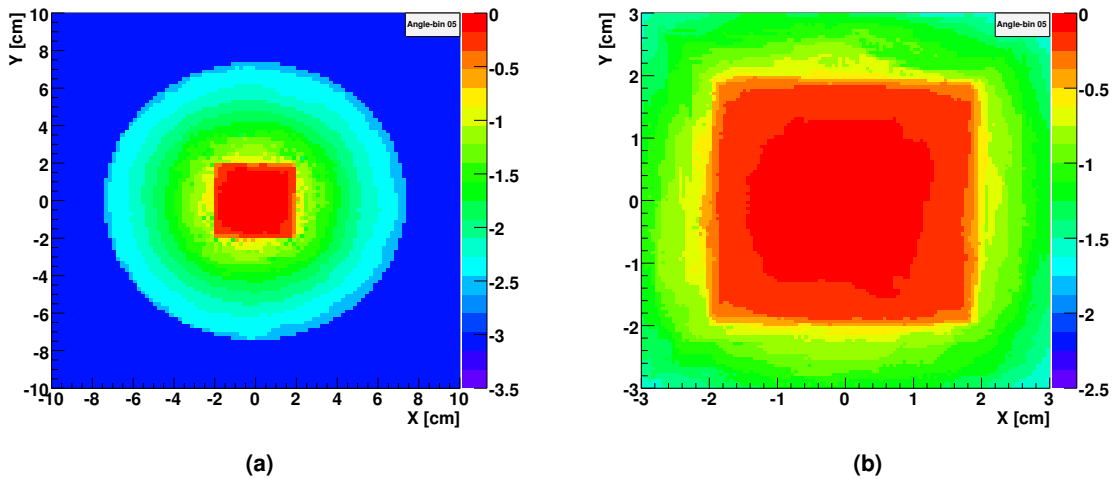


Figure 6.12: r -distributions for parameter p_0^{corr} after the energy correction for Bin $[7^E, 5^A]$.

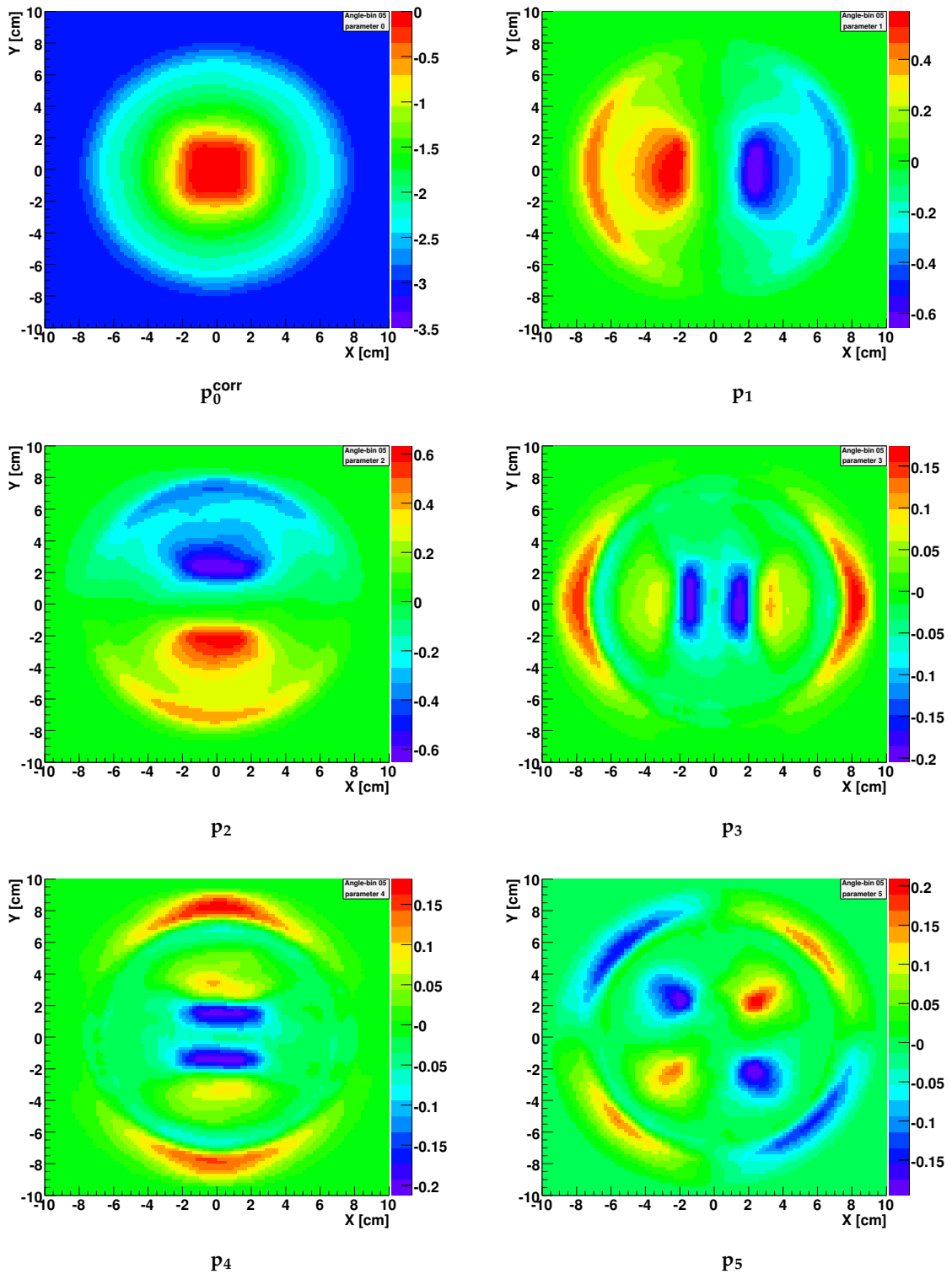


Figure 6.13: Final distribution of the six parameters storing the information of the coarse r -distribution of Bin $[7^E, 5^A]$.

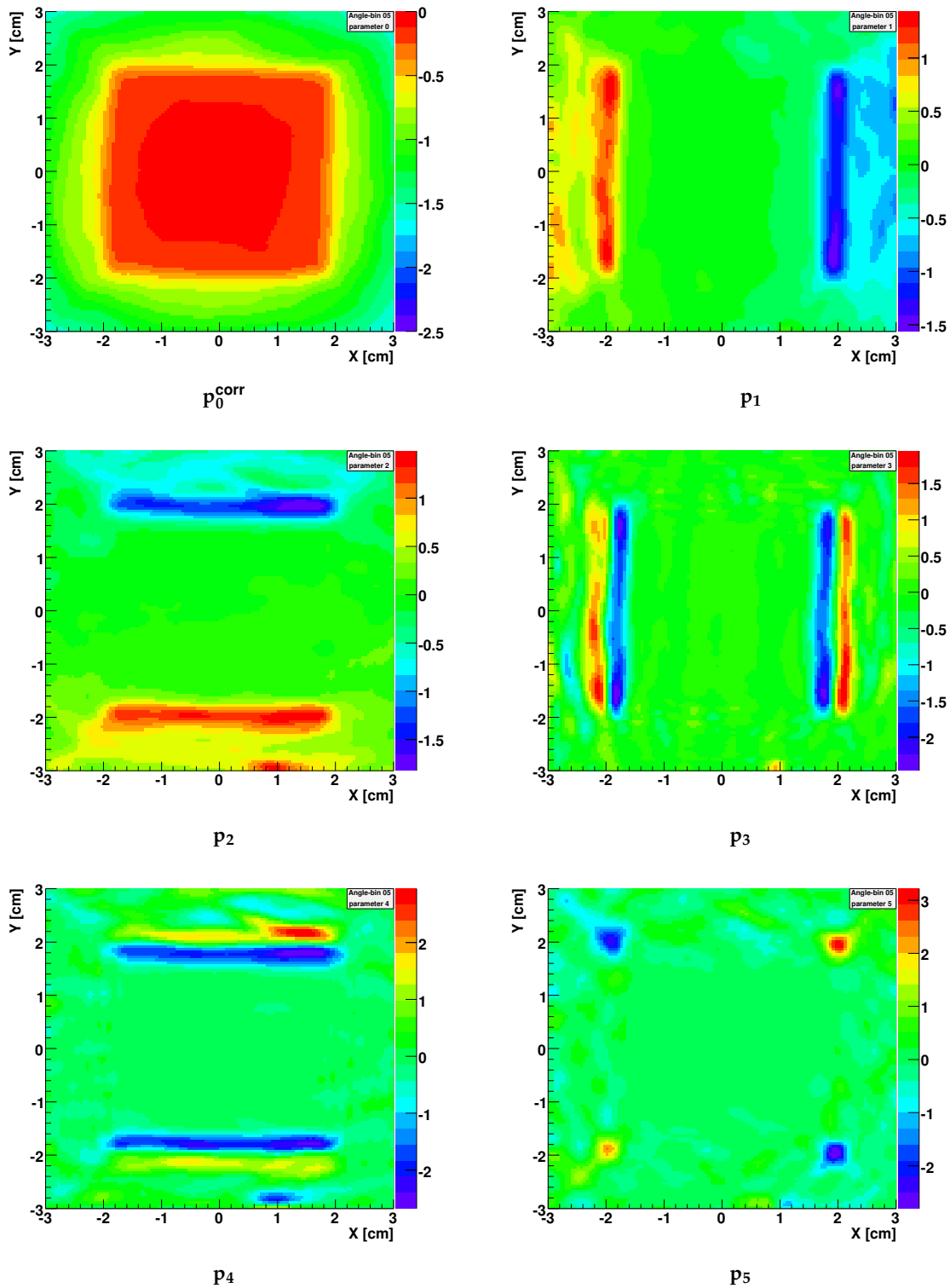


Figure 6.14: Final distribution of the six parameters storing the information of the zoomed r -distribution of Bin $[7^E, 5^A]$.

Bin $[7^E, 5^A]$. Compared to the raw 2D- r -distribution in Fig. 6.9, the final r -distribution is parametrised, and a smooth r -distribution is generated. Especially for regions with less statistics a smooth shape could be constructed. In subsection E.2.1 the macros for generating this r -distribution are listed with a short description of the functions.

With this data-driven shower model, the expected (averaged) energy deposit in each cell of a cluster can be predicted and calibration values of each cell can be determined, see 6.4.3. Based on this shower-model, a fit procedure in order to refit the clusters is developed, see 6.5. As source of the shower model served 30% of the available statistics, see Table E.4, where information of the LED signal per cell existed at the time performing this analysis. With higher statistics, the zoomed ratio distribution could be smoothed better and the outer region of the ratio distribution could be better described. This ansatz of a data-driven shower model is promising and could not be further elaborated in this work, but it should be refined in a further analysis.

6.4.3 Calibration Values from Application of the Shower Model

The previous subsection described, how the logarithmic energy ratio $r(\Delta x, \Delta y)$ can be obtained (eq. (6.10)) for a cell with a relative position $\Delta x, \Delta y$ to the shower centre. For each cell in all clusters, the expected r is calculated by using the parameter histograms with eq. (6.16). The appropriate energy interval and angle-bin is chosen by determining the electron energy and its impact angle. For all cells of a cluster in each run, the relation between the expected energy E_{exp} and r

$$(6.19) \quad E_{\text{exp}} = E_{e^-} \cdot 10^r$$

can be assumed. The expected energy E_{exp} can be correlated with the quasi-ADC-value E_{cADC} of the particular cell, see Fig. 6.15 (a) for illustration.

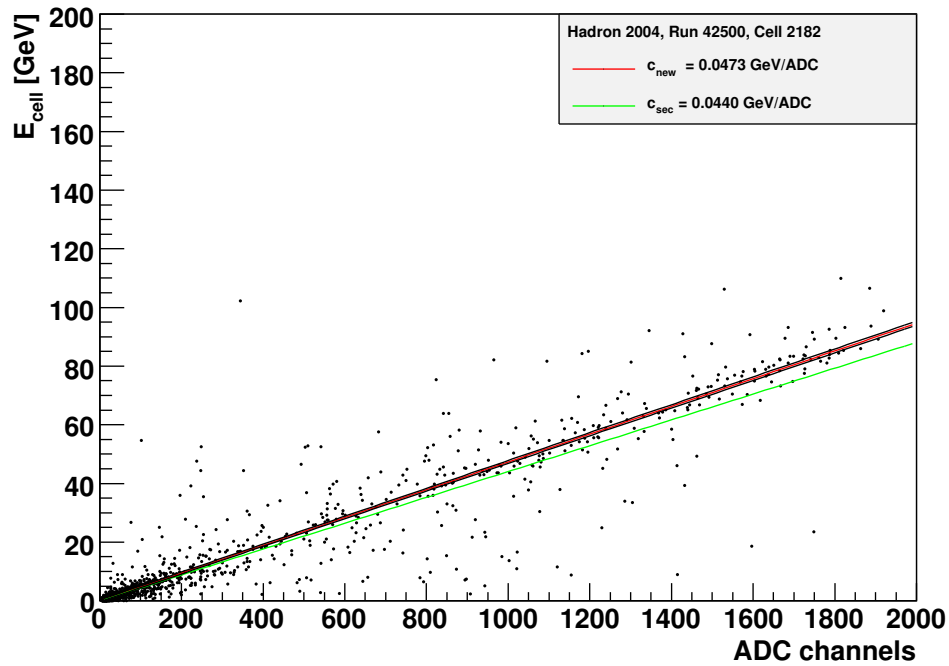
The event selection for determining the calibration values follows basically the description of 6.4.1 apart from the fact, that the constraint to the energy difference of the cluster E_{cls} and the electron E_{e^-} is changed to

$$(6.20) \quad |E_{\text{cls}} - E_{e^-}| < 5\% \cdot E_{\text{cls}}$$

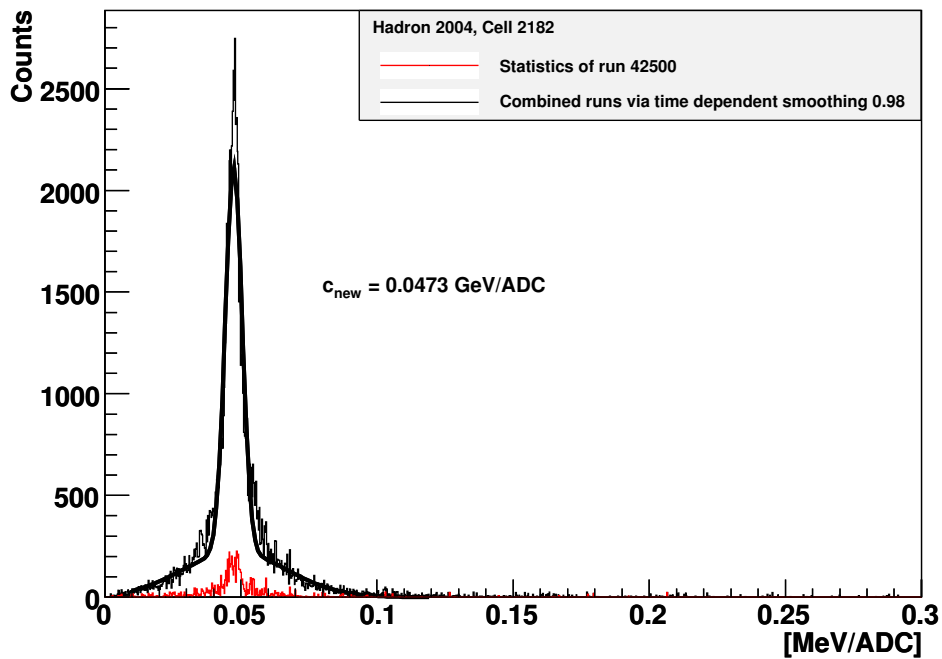
in order to further clean the data sample from background (like hadrons). The calibration value c is the ratio of the expected energy E_{exp_i} and the ADC-values E_{cADC_i} :

$$(6.21) \quad c_i = E_{\text{exp}_i} / E_{\text{cADC}_i}$$

An example of the resulting distribution is given in Fig. 6.15 (b). The selected events are weighted by the factors $\sqrt{E_{\text{exp}}}$ and $\sqrt[5]{E_{\text{ADC}}}$. These factors are introduced to approximately compensate the effect, that a cell is more often hit by the tail of a shower. For this reason, there are many entries in Fig. 6.15 (a) at small energies and ADC-values, respectively. But for determining the calibration value, especially the events with higher



(a)



(b)

Figure 6.15: (a) Expected cluster energy versus the (quasi-) ADC-value, in red the correlation value from the fit and in green the value of the second calibration for cell 2182; (b) Distribution of the new calibration values (in red) for run 42500 only and (in black) including the statistics of the neighbouring runs with the smoothing factor 0.98.

energies are important.

The calibration value is the peak position in Fig. 6.15 (b), which is found by a double Gaussian fit. The fit range is adjusted around the peak position. The fit value of the peak mean position (the calibration constant) and its error are written into a file, as well as the width of the Gaussian and its error, see Table E.3 on page 182.

The statistics for each cell varies strongly, depending mainly on the available events per run as well as the position in ECAL2. Fig. 6.16 illustrates the impact coordinates of the electrons and positrons in ECAL2 of all events of 270 runs used by the calibration. The statistics per run is not for all cells sufficient to extract calibration values. Therefore the statistics of the previous run is included using exponential smoothing which means that the calibration distributions are added up in time, but weighted by a factor

$$(6.22) \quad w = e^{S(t-t_{\text{prev}})}$$

which is dependent on the time difference between the start time t from the current run, the previous run t_{prev} and the smooth factor S . With this method also longer breaks while collecting data are taken into account in the correct way. It turned out that the smooth factor of 0.98 per hour delivers the best results in the physics analysis for cells of the Primakoff region⁵. This high smooth factor leads to over-smoothing as it can be seen in Fig. 6.17 and Fig. 6.18. A further analysis could study the optimal smoothing factor dependent on the position of the cell in ECAL2 and its run-dependent statistics in combination with the final physics analysis. Fig. E.4 and Fig. E.5 display the different statistics (raw entries, smoothing factor 0.85 and 0.98) exemplarily for a cell of the outer region and central region.

In Fig. 6.15 (b) the distribution of the calibration value is shown for cell 2182 of the central region of ECAL2 (see Fig. 6.38 for its position), with the statistics of run number 42500 and the statistics including the smoothing. The fit result with the new calibration value and the static second calibration are drawn for illustration in the correlation plot of the expected energy and the quasi-ADC-values Fig. 6.15 (a). Fig. 6.17 demonstrates the trending of the calibration value of this cell with time.

6.4.4 LED Analysis

At the front of each lead glass block of ECAL2, a gain monitoring system is attached, where light pulses of a Light Emitting Diode (LED) radiate the lead glass block which is performed between the SPS cycles. The light is collected, analogously to the Cherenkov light, and permits a relative determination of amplification changes (assuming the LED to operate with constant emission). In case the amplification has changed, e.g. the high voltage of the photo multipliers, this is seen as a change in the intensity of the pulse and in turn also the calibration value for this cell has to be adjusted. The ECAL2 detector group

⁵ see chapter 7 for introduction and chapter 8 for the physics analysis.

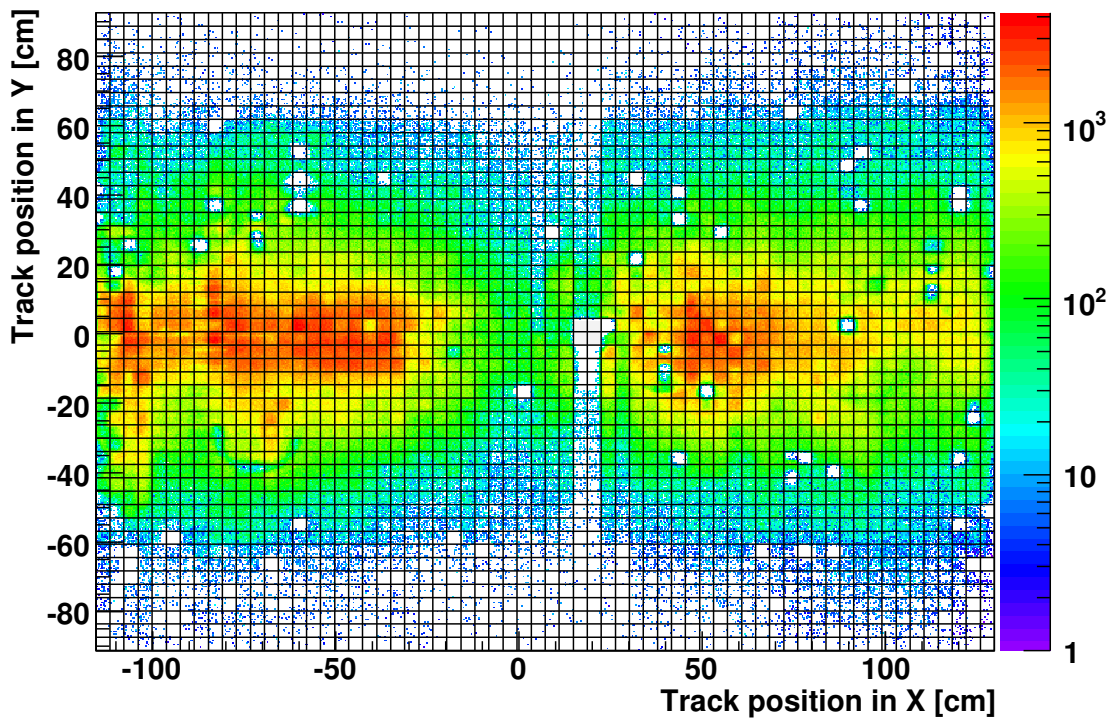


Figure 6.16: Position of tracks at ECAL2 after event selection for calibration. The column not in the trigger is visible at "+2" in X, see subsection 8.3.2 for more details.

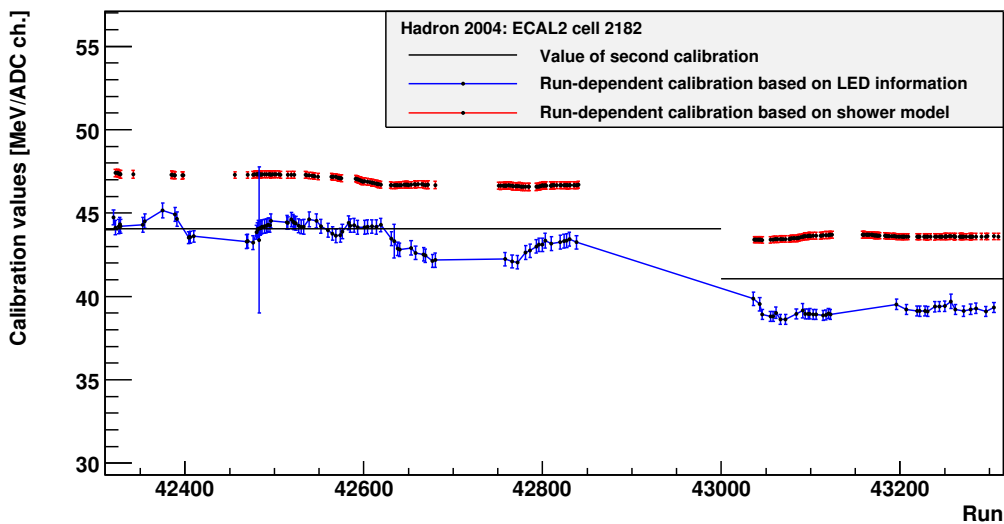


Figure 6.17: Trending of the calibration value for cell 2182 with time. The black line marks the level of the static second calibration and in red are plotted the calibration values derived with the shower model with the time smoothing factor 0.98 and in blue the values derived by the LED analysis, see subsection 6.4.4.

provided at the point of this analysis for 110 runs the mean value m_i and the sigma σ_{m_i} of the LED signal distribution (ADC values per light pulse) for all 3068 cells of ECAL2.

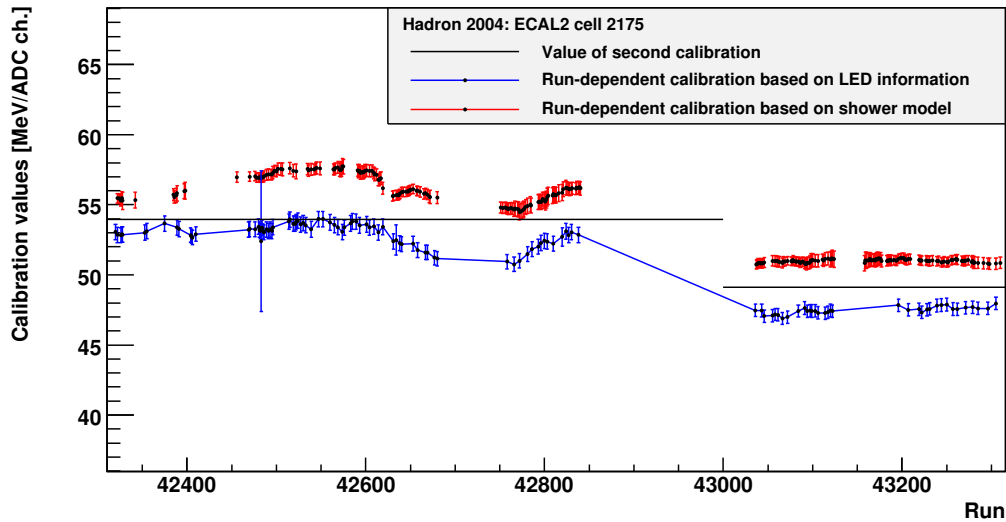
In the following analysis, the LED values are related to the static second calibration value (see 6.1). For each particular cell, the truncated mean $\bar{m}_{25\%}$ ⁶ of the LED signals m_i of all 110 runs is calculated. The conversion ratio between m_i and the corresponding calibration constant (in GeV per ADC) is unknown. For this reason the LED values are scaled according to the mean \bar{c}_{sec} of the two static values of the second calibration. The new LED based calibration value per cell c_{LED_i} for each run i and its error σ_{LED_i} are determined as follows:

$$(6.23) \quad c_{LED_i} = \frac{1}{m_i} \cdot \frac{c_{sec}}{\bar{m}_{25\%}}, \quad \sigma_{LED_i} = \frac{c_{sec}}{\bar{m}_{25\%}} \cdot \frac{1}{m_i^2} \cdot \sigma_{m_i}$$

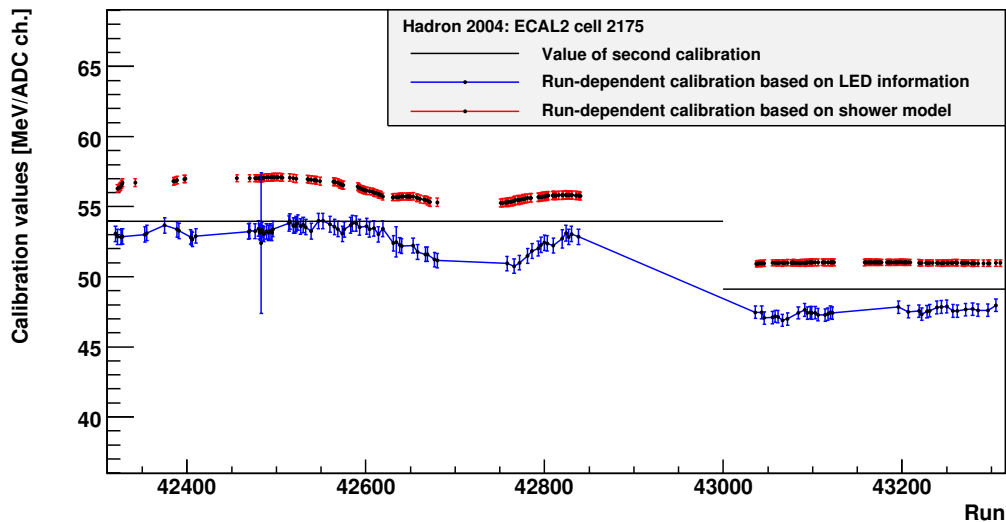
Fig. 6.18 (a) displays as an example the trending of the LED based calibration value over time for cell 2175 as well as the trending of the calibration values derived by the shower model with the time smoothing factor 0.85. The black line marks the level of the static second calibration. The LED based calibration as well as the shower model derived calibration values follow the same relative trending. Also the LED based calibration follows the jump between the two run periods before and after run 43000, since the HV on the photo multipliers was adjusted in between. The difference between the two plots is the smooth factor of the shower model based calibration, 0.85 for (a) and 0.98 for (b). The run dependent fluctuations are also revealed by the shower model based calibration, which is as expected more distinctive in (a) with the smaller smooth factor.

The difference of the cluster and the track energy for run 42781 is depicted in Fig. 6.19, for the static second calibration and the LED calibrations applied. The distributions are fitted by a double Gaussian. The signal peak for LED based calibration is narrower than the peak for the static second calibration and contains about 2.5% more events. The positive effect can be seen throughout the runs, but the relative position of the peak varies due to the fact that the LED signal values are scaled according to the static second calibration. The LED signal could be used to correct the ECAL2 cells for run dependent fluctuations, due to instabilities of the photo multipliers. It might also compensate long term variations, e.g. due to radiation damage of the lead glass cells which lose light transparency with time. But for the hadron run 2004 there was no reference system installed in order to compensate instabilities of the LED light pulse in terms of temperature variations and aging of the LEDs themselves.

⁶For calculating the truncated mean value, 25% smallest and largest values of the set of LED values are discarded.



(a)



(b)

Figure 6.18: Trending of the calibration value for cell 2175 with time. The black line marks the level of the static second calibration, in red are plotted the calibration values derived with the shower model and in blue the constants derived by the LED analysis. For (a) the smooth factor of the shower model based calibration was 0.85 and in (b) 0.98. The LED calibration values follow the same trending as the values based on the shower model.

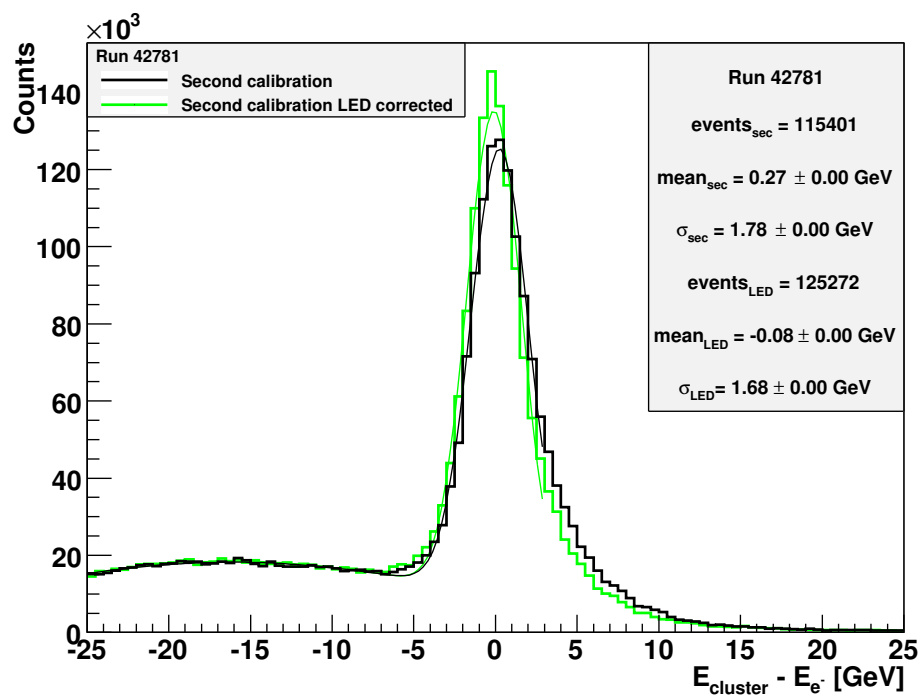


Figure 6.19: Difference of the cluster and the track energy. The black curve shows the distribution in case the second calibration was applied and for the green curve LED-based calibration values were employed.

6.5 Cluster Fit

The previous section described the development of a data driven shower model based on electron tracks. As input calibration the second calibration set was used, corrected by the results obtained from the LED data. The data-driven r -distributions which serve as shower model, are generated for 12 energy intervals and 2×9 angular sets. These distributions are prepared so that the shape of the ratio distribution is encoded by means of a two-dimensional quadratic function with six parameters $p_{0...5}$ which are stored in histograms. By applying new calibration values to the cells of an ECAL2 cluster, the centre of the cluster, to be identified with the impact position of the particle, may get shifted. Therefore the clusters must be refitted, making use of the shower distributions. A goal is also to improve the resolution on space and energy especially for special cases as e.g. clusters near dead cells, see section 6.7.

The refitting algorithm is implemented on PHAST-level which means that it will be applied to mDST data which have to contain the list of cells and their energy per ECAL2 cluster. In the following the basic steps of the algorithm are listed which are performed for clusters comprising at least two cells. A short overview of the particular functions of the code is listed in subsection E.2.4

- Apply for cells of a cluster the shower-model based calibration set with equation eq. (6.13) on page 82, and calculate the new energy sum of the cluster

$$(6.24) \quad E_{\text{cls}} = \sum_{i=1}^{25} E_{\text{cell}}$$

For some cells, e.g. at the upper and lower border of ECAL2, the statistics was not enough to determine a new calibration value. In this case the values of the second calibration are applied.

- Search for the cell with the maximum energy deposit.
- Arrange the cluster in a two dimensional 5×5 matrix according to their positions in x and y , centred around the maximum cell. An example cluster array is shown in Fig. 6.21 (b).
- Check whether there are saturated or dead cells in the matrix, see section 6.7. A tag is set for cells close to the border or beam hole of ECAL2.
- For each cell the error is set proportional to the measured energy. For the cell without a signal the energy is set to zero, and the error is set to a default value of 0.2 GeV. The particular error formulae are listed in Table 6.4, also such for the special cases like a dead cell or cluster close to the border or beam hole. In case of a saturated cell the error is asymmetric, according to the fact that the measurement represents a lower bound to the true energy. The specific functions have been fine tuned in order to correspond to pulls with unit width contributions in the χ^2 -fit.

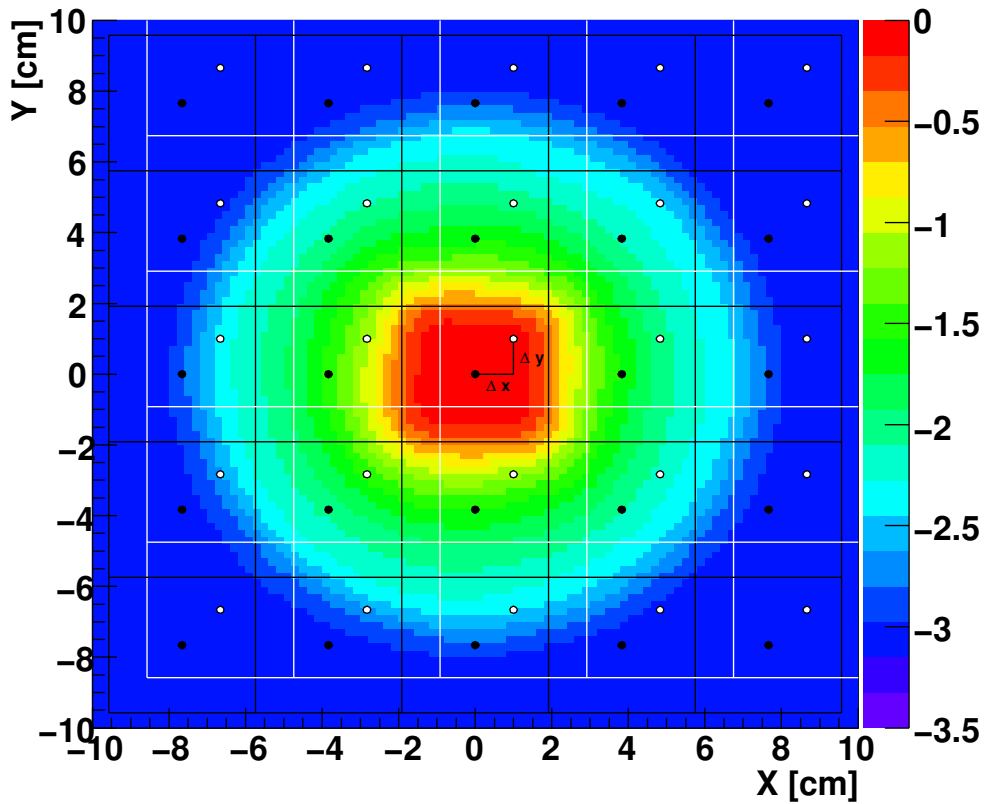


Figure 6.20: An example of a log-energy-ratio distribution. The black grid indicates the cell grid of a cluster in ECAL2 which has maximum size of 5×5 cells for the case when a cell is hit exactly in its centre. The logarithmic energy ratio r , see eq. (6.10), read off at the centre of each cell is the integrated energy ratio for the whole cell. The sum of the energies of all cells delivers the cluster energy. For a real cluster the measured energy fractions of the cells are fitted to this energy-ratio distribution. The position of the cluster is determined by the offsets Δx and Δy , as the white grid shows.

- The idea of the fit is indicated in Fig. 6.20. It shows a sample log-energy-ratio distribution. The black raster indicates the borders of cells for a cluster when the cell is hit perfectly in the centre. The cell energies E_{cell} are connected to the cluster energy E_{cls} via the log-energy-ratio, whose parameterised value of the quadratic function is stored in the histogram bins located at the centre of the cell

$$(6.25) \quad E_{\text{cell}} = E_{\text{cls}} \cdot 10^{r_{\text{smooth}}}$$

$$(6.26) \quad r_{\text{smooth}} = p_0 + p_1(x - \Delta x) + p_2(y - \Delta y) + p_3(x - \Delta x)^2 + p_4(y - \Delta y)^2 + p_5(x - \Delta x)(y - \Delta y)$$

The white raster in Fig. 6.20 indicates the position of a cluster which fits best to the r -distribution. So, Δx and Δy are the offsets of the cluster position towards the new

Error Setting		
Standard Cluster	Errors	
Cell without signal	$\sigma_{\text{cell}} = 0.2 \text{ GeV}$	
Cell with signal	$\sigma_{\text{cell}} = 0.15 \text{ GeV} + 0.03 \cdot E_{\text{cell}}$	
Standard Cluster	$\sigma_{\text{cluster}} = 0.15 \text{ GeV} + 0.025 \cdot E_{\text{cls}}$	
Special case	σ_{cell}	σ_{cluster}
Dead cell (at centre)	$1 \cdot 10^5 \text{ GeV}$	6500 GeV
Dead cell	$1 \cdot 10^5 \text{ GeV}$	$0.2 \cdot E_{\text{cell}}$
Beam hole	$2 \cdot 10^5 \text{ GeV}$	70 GeV
Border	$3 \cdot 10^5 \text{ GeV}$	70 GeV
Asymmetric error	σ^-	σ^+
Saturated cell	$0.1 \cdot E_{\text{cell}}$	$6000/E_{\text{cell}}^2 \text{ GeV} + 0.15 \text{ GeV} + 0.03 \cdot E_{\text{cell}}$
E_{cls} with saturated cell	$0.1 \cdot E_{\text{cls}}$	$6000/E_{\text{cls}}^2 \text{ GeV} + 0.15 \text{ GeV} + 0.03 \cdot E_{\text{cls}}$

Table 6.4: Errors applied on cell energies and cluster energies for the cluster refit, for standard clusters and special cases.

position. As further preparation for the fit, the angle and energy bin in order to use the correct energy-ratio distribution of the shower model has to be determined from the summed cell energy E_{cls} and the impact angle $dx_{e^-, \gamma}, dy_{e^-, \gamma}$ of the particle track. The parameters of the fit are the cluster energy E_{cls} and the offsets Δx and Δy . The fit uses the ROOT minimising package MINUIT. For this purpose, the 5×5 matrix array is rearranged in a 1D-histogram, see Fig. 6.21 (a). The bins 0 to 24 are filled with the cell energies and the last bin 25 with the summed cluster energy. The assumed error on the cluster energy is given in Table 6.4. This histogram is then fitted by the function derived from the shower model. As start parameters for the fit serve the summed cell energy E_{cls} and for Δx and Δy the mean values of the 2D-histogram of the cluster as shown in Fig. 6.21 (b). Since the fit searches for the best shower parameters which are stored in a fine binned histogram, the fit may fail due to the discrete steps of the binning. The fit converges by applying the bilinear interpolation routine from [Po92].

Fig. 6.21 shows an example of the cluster refit. The energy of the electron measured via the track momentum is 68.4 GeV. The fit reconstructs the cluster energy $69.8 \pm 1.3 \text{ GeV}$. The underlying log-energy-ratio distribution for the fit was Bin $[4^E, 9^A]$.

As described in section 6.7, the calorimeter ECAL2 was in a problematic condition. Several cells were dead and other cells had a restricted dynamical range, so starting from a certain energy deposit, they saturate. In case of a saturated or dead cell, the cluster is fitted twice. For the second iteration the cluster centre is not the cell with the maximum energy, but the saturated or dead cell. In case the χ^2 of the second fit is better, the new fit values are taken.

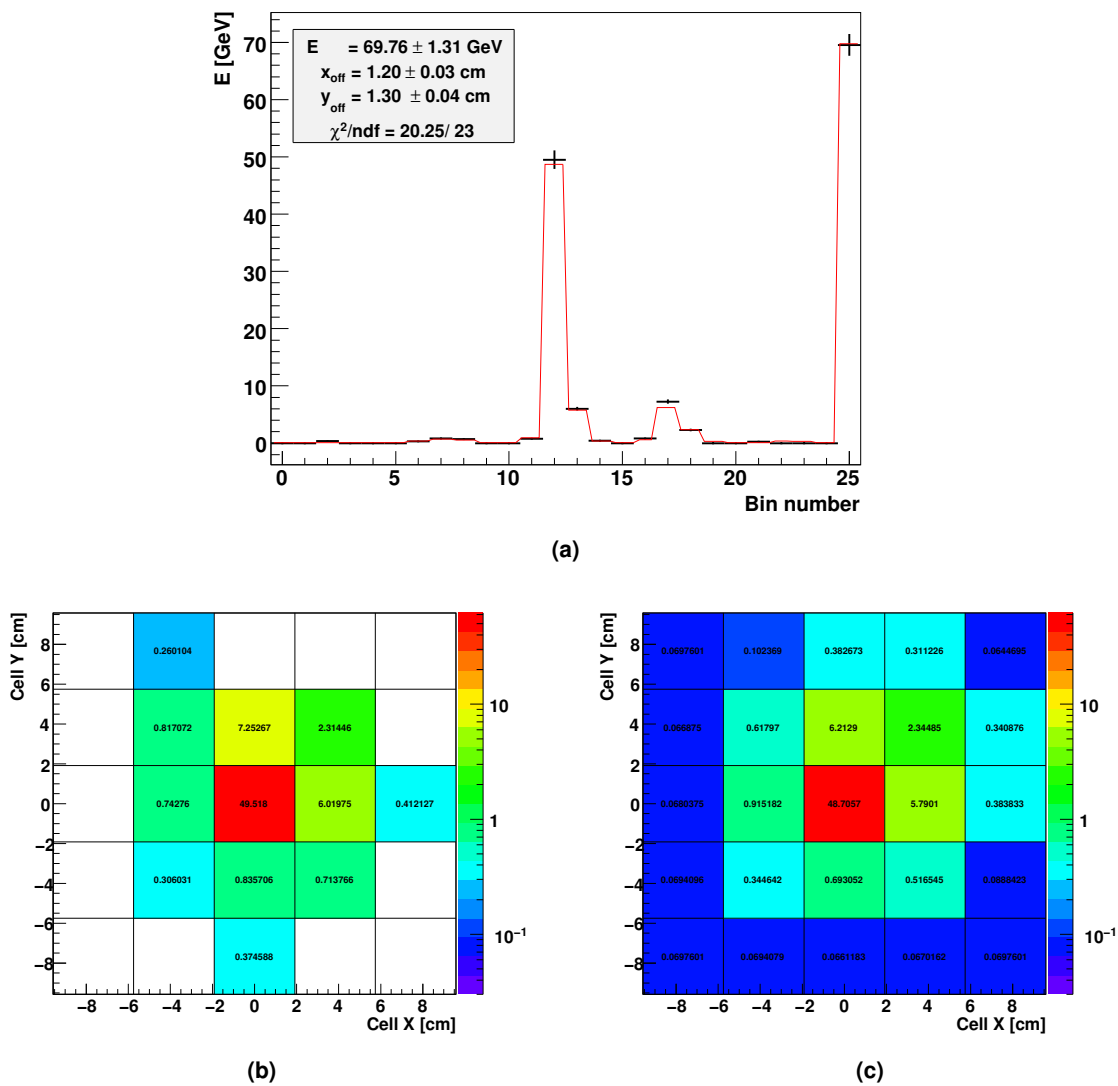


Figure 6.21: Example cluster in event 182536111133143 of run 42500. (a) the fit function, (b) the cell energies, (c) the energy values predicted by the fit function. The energy of the electron from the track momentum is 68.39 GeV and the underlying log-energy-ratio distribution for the fit was Bin $[4^E, 9^A]$.

6.6 Checking the Calibration

6.6.1 Electron Track Analysis

In this chapter, the results of the new calibration and the cluster refit compared with the second calibration are presented. A good check of the calibration is the energy residual of the cluster energy E_{cls} and the electron track energy E_{e^-} , as well as the residual of the cluster position and the impact position of the electron track at ECAL2.

The event selection for the figures in this subsection is similar as described in subsection 6.4.1, but without the cut on the energy residual, unless otherwise mentioned. In addition, the cut on the minimum distance between two clusters is changed from 12 cm to 32 cm. The data set for the following figures includes runs from 42500 - 42840. For the second beam period 43198 - 43323, the distributions give similar results for the electron track analysis.

In the following, the performance histograms, Fig. 6.22 to 6.28, of the new calibration and the cluster refit for different cluster types are discussed. Each figure contains:

- a) The energy residuals for the second calibration, for the new calibration and for refitted clusters with the new calibration values applied according to the formulae as described in section 6.4:

$$(6.27) \quad E_{\text{second}} = 1.06 \cdot \sum_{i=1}^{25} a_{i,\text{sec}} E_{\text{cADC}}, \quad E_{\text{new}} = \sum_{i=1}^{25} a_{i,\text{new}} E_{\text{cADC}} .$$

The summed cell energy E_{second} has to be corrected by a factor of 1.06 to compensate for energy leaks outside the cluster [Kol06] as mentioned in 6.3.2. Such a factor is not needed by the new calibration.

The energy residual is modelled by three Gaussian functions, two for describing the peak and one for the background:

$$(6.28) \quad \begin{aligned} f_G(x) &= \text{Gauss}[x; a_1, m_1, \sigma_1] + \text{Gauss}[x; a_2, m_2, \sigma_2] + \text{Gauss}[x; b_0, b_1, \sigma_b] \\ \text{with} \quad \text{Gauss}[x; p_0, p_1, p_2] &\equiv \frac{p_0}{\sqrt{2\pi}p_2} \cdot \exp\left[-\frac{(x-p_1)^2}{2p_2^2}\right]. \end{aligned}$$

The σ of the peak is calculated from the contributions of the two Gaussian functions as follows

$$(6.29) \quad \sigma = \sqrt{\frac{a_1\sigma_1^2 + a_2\sigma_2^2}{a_1 + a_2}} .$$

This σ and the maximum peak-position of the fit function f_G are listed in the histogram as well as the number of entries in the peak.

- b) The pull ζ of the cluster refit which is depicted for all cells close to the fitted cluster position (within a radius of 5 cm) :

$$(6.30) \quad \zeta = \frac{E_{\text{cell}} - E_{\text{refit}}}{\sigma_{\text{cell}}}$$

- c), d) The X and Y residuals for the original clusters and the refitted clusters: These distributions are fitted by eq. (6.28) which models the peak with the background. ΔX_{max} and ΔY_{max} , respectively, are the position of the maximum of the fit function, and the σ is calculated according to eq. (6.29).
- e) The χ^2 -distribution of the cluster refit.
- f) The χ^2 -probability of the cluster refit.

Standard clusters, Fig. 6.22:

The cluster fit has results comparable to those of the second calibration. The differences of the σ and the entries in the peak are at 1% level. The new calibration stand-alone leads to a 1 GeV offset of the peak position and about 3% smaller residual width compared to the second calibration. The bump to negative energy residuals can be assigned to hadrons. In order to generate the position residuals with electrons, an energy cut $|E_{\text{cluster}} - E_{e^-}| < 10 \text{ GeV}$ was applied on the data set in order to reduce hadronic background. The width of the position residual in x is improved by the cluster fit by about 8%. In y, the position residual is about 2% worse, but the peak position is improved about 0.06 cm. The pull distribution with $\sigma = 1.1$ and the χ^2 - and χ^2 -probability distributions show, that basically the underlying model and error assumptions of the cluster fit are consistent. The rise of the χ^2 -probability towards zero can be addressed to the hadronic background.

Clusters with a saturated cell in the centre, Fig. 6.23:

The energy residuals with the second calibration and new calibration show, that energy is missing due to the saturated cell which is indicated by the steep slope on the right side and the flat slope on the left side of the residual peak. The cluster fit shifts the peak position about 2 GeV with respect to the other curves towards zero with a more Gaussian shape. The pull shows a bump at -8.5 which can be traced back to a few cells mainly in the outer region. The width of the pull $\sigma = 1.2$ points to a reasonable error assumption. The cluster refit improves the peak position in x-direction by about 0.09 cm, but loses in y about 0.11 cm. The location of the saturated cells in ECAL2 are visualised in Fig. 6.38 and in the appendix Fig. E.2 (c).

Clusters contain a dead cell, Fig. 6.24:

The cluster refit recovers the energy for clusters which have a dead cell close by the central cell. About 50% more entries in the signal can be found with the cluster refit which come from events shifted from the hadronic background (position at negative residual values). The fit enhances the precision of the cluster position. The σ in x is improved by about 4.3% and 0.07 cm in the offset. In y, the residual width is improved by 12.5%.

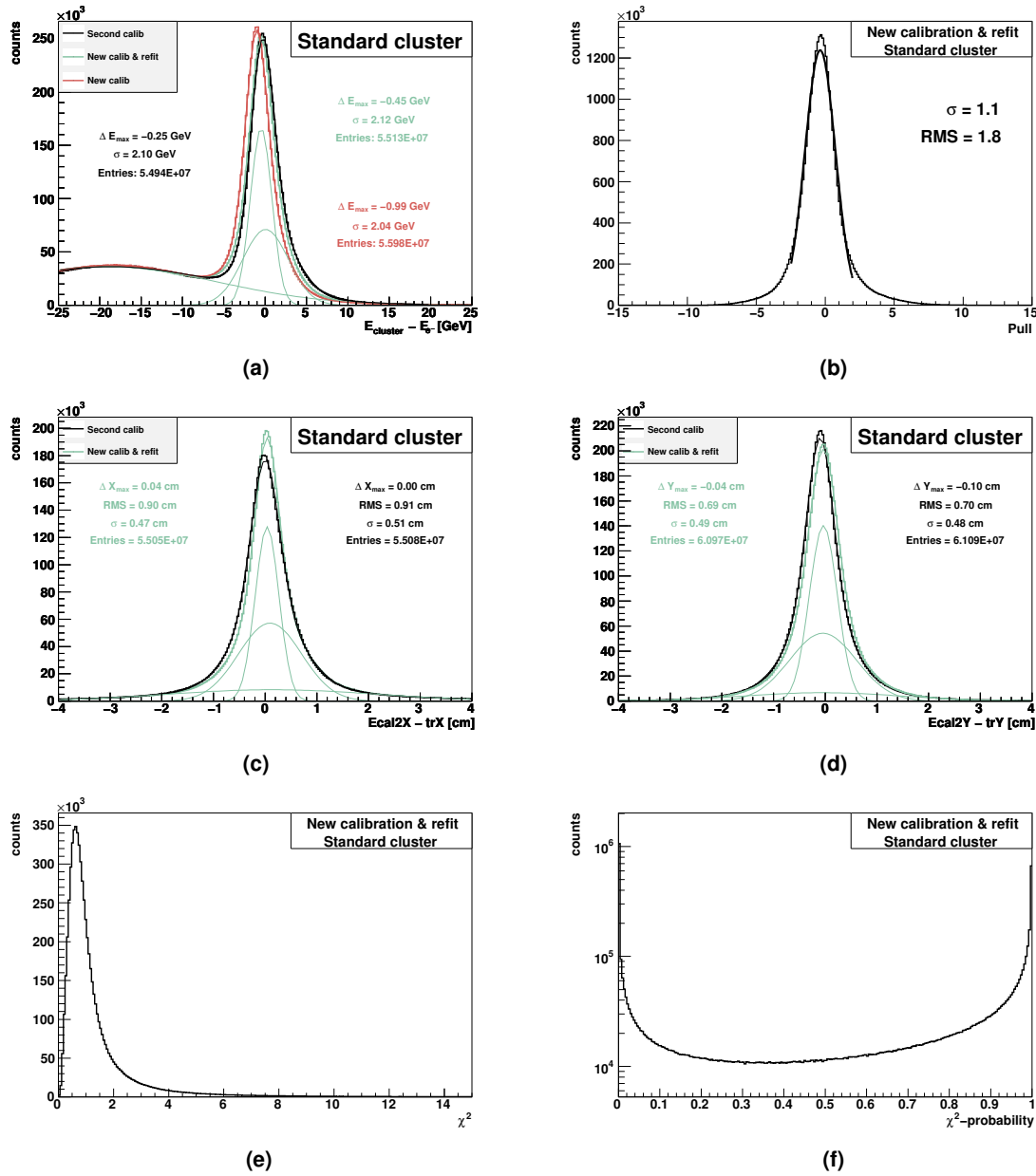


Figure 6.22: The cluster fit has results which are comparable to those of the second calibration. The differences of the σ and the entries in the peak are at 1% level. The new calibration stand-alone leads to a 1 GeV offset of the peak position and about 3% smaller residual width compared to the second calibration. The bump to negative energy residuals can be assigned to hadrons. In order to generate the position residuals with electrons, an energy cut $|E_{\text{cluster}} - E_e| < 10 \text{ GeV}$ was applied on the data set. The width of the position residual in x is improved by the cluster fit by about 8%. In y, the position residual is about 2% worse, but the peak position is improved about 0.06 cm. The pull distribution with $\sigma = 1.1$ and the χ^2 - and χ^2 -probability distributions show, that basically the underlying model and error assumptions of the cluster fit are consistent. The rise of the χ^2 -probability towards zero can be addressed to the hadronic background.

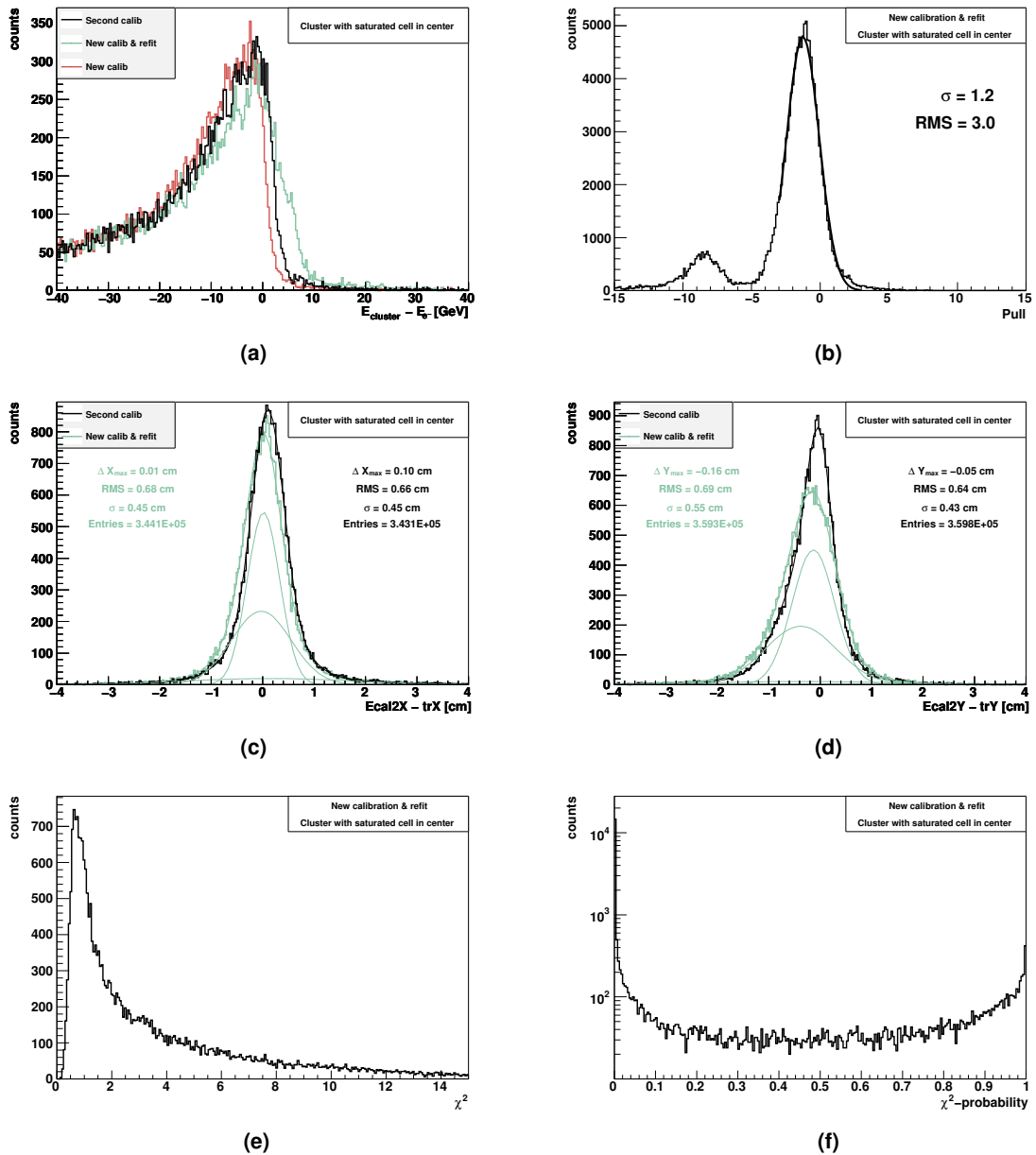


Figure 6.23: The energy residuals with the second calibration and new calibration show, that energy is missing due to the saturated cell which is indicated by the steep slope on the right side and the flat slope on the left side of the residual peak. The cluster fit shifts the peak position about 2 GeV with respect to the other curves towards zero with a more Gaussian shape. The pull shows a bump at -8.5 which can be traced back to a few cells mainly in the outer region of ECAL2. The width of the pull with $\sigma = 1.2$ points to a reasonable error assumption. The cluster refit improves the peak position in x-direction about 0.09 cm, but loses in y about 0.11 cm. The location of the saturated cells in ECAL2 are visualised in Fig. 6.38 and in the appendix Fig. E.2 (c).

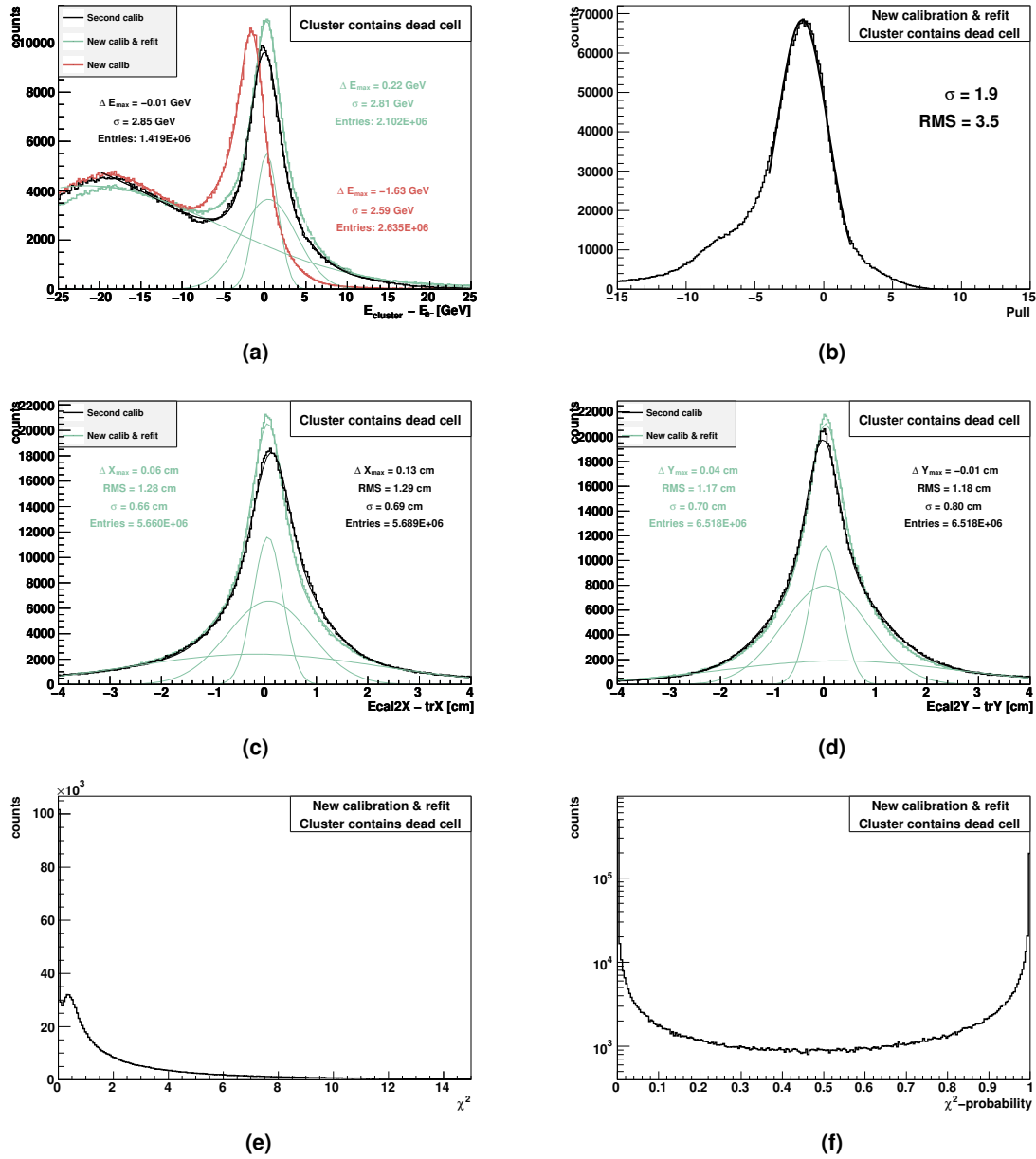


Figure 6.24: The cluster refit recovers the energy for clusters which have a dead cell close by the central cell. About 50% more entries in the signal can be found with the cluster refit which come from events shifted from the hadronic background (the position at negative residual values). The fit enhances the precision of the cluster position. The σ in x is improved by about 4.3% and 0.07 cm in the offset. In y , the residual width is improved by 12.5%.

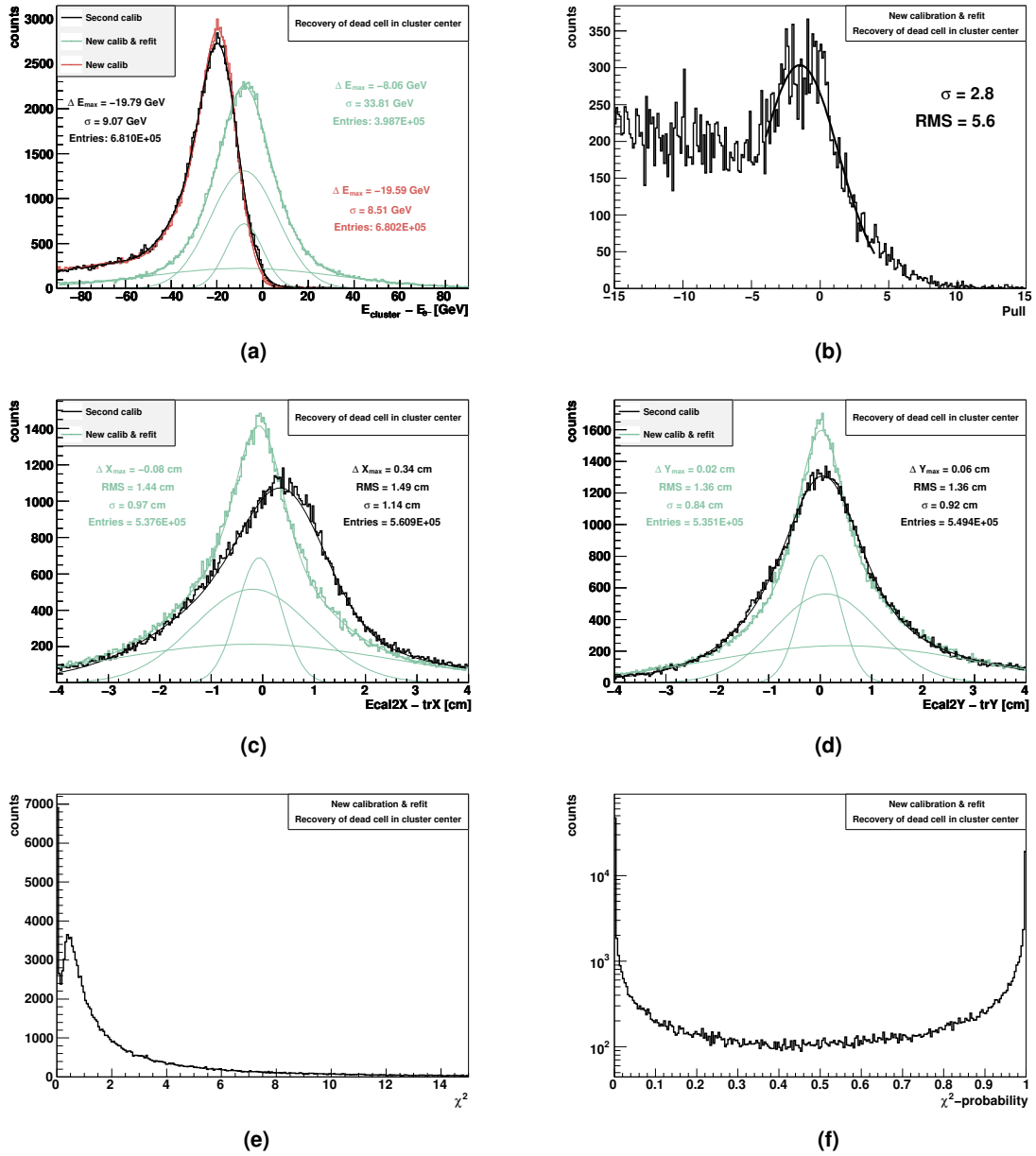


Figure 6.25: The cluster refit checks the hypothesis whether the dead cell originally was the centre of the cluster. These histograms show events, in case the cluster refit has better result in assuming the dead cell as the new cluster centre. The cluster fit recovers in the mean about 11 GeV of the missing energy. The σ position residual in x is improved by about 15% and in y about 8%. The peak position in x is corrected by about 0.26 cm.

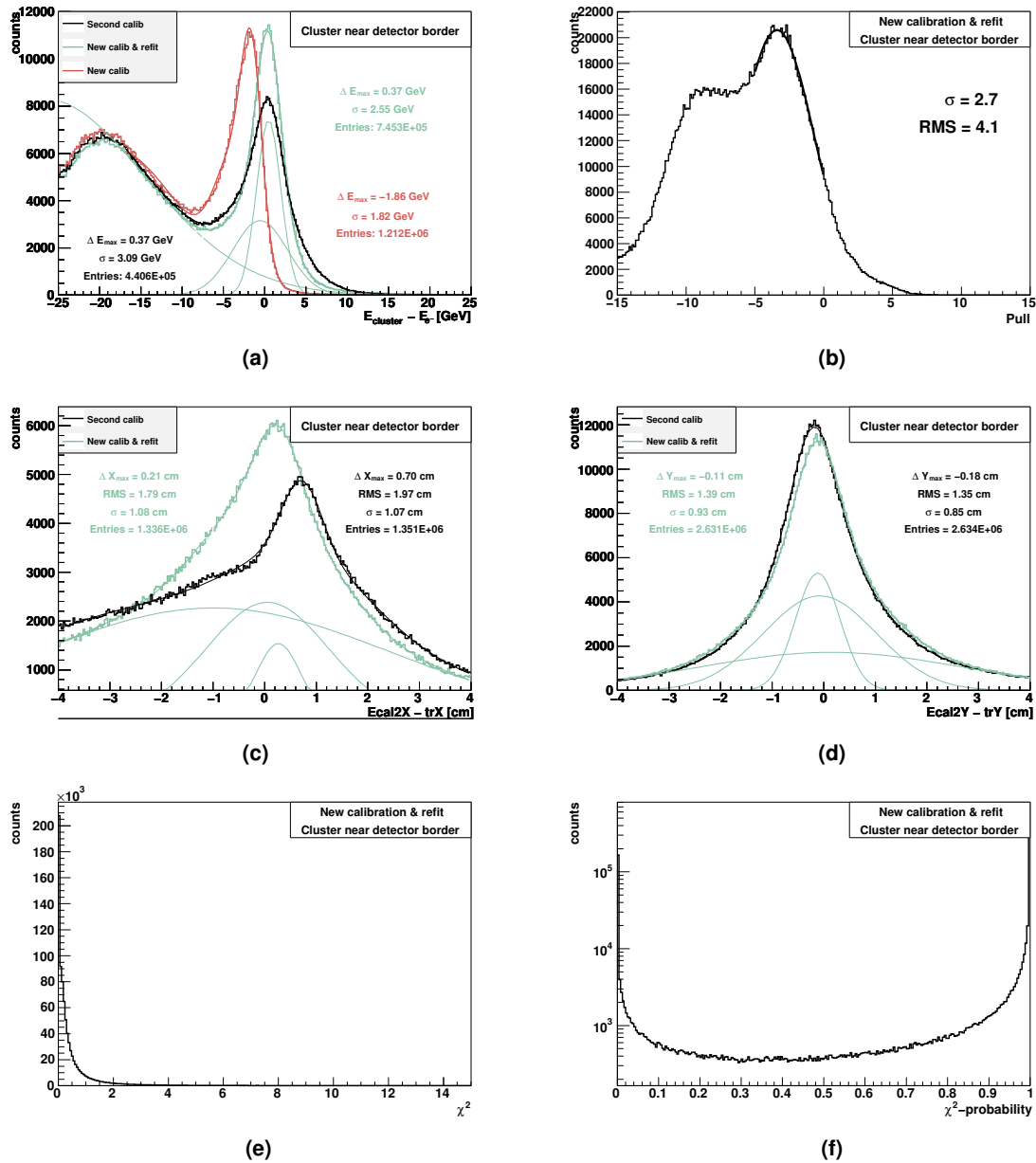


Figure 6.26: Clusters close to the border are treated similar by the refit like clusters with dead cells, since part of the information is missing. The refit recovers those clusters. The peak of the energy residual contains about 69% more entries compared to the distribution of the second calibration and has an improved σ of about 17%. Basically, the new calibration in combination with the refit leads to this observed improvement. The position residual in x is improved by the fit of about 0.49 cm and 0.07 cm in y.

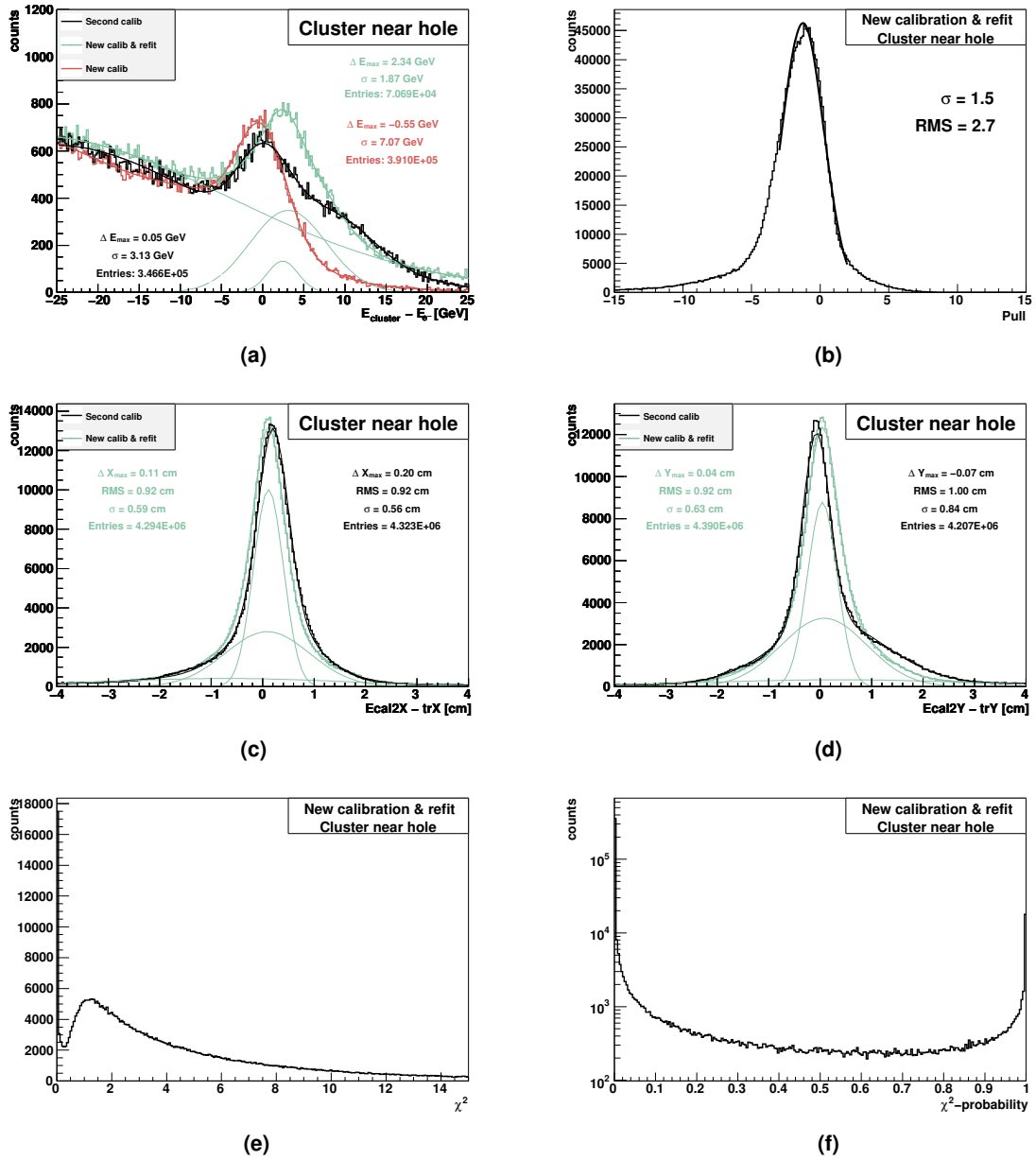


Figure 6.27: Clusters near the beam hole of ECAL2 are truncated. The new calibration and the fit lead to an improvement, the distributions are highly dominated by the background. The cluster refit improves the peak position of the position residual about 0.09 cm in x and the σ about 25% in y which can be mainly addressed to a change in the broader component of the peak.

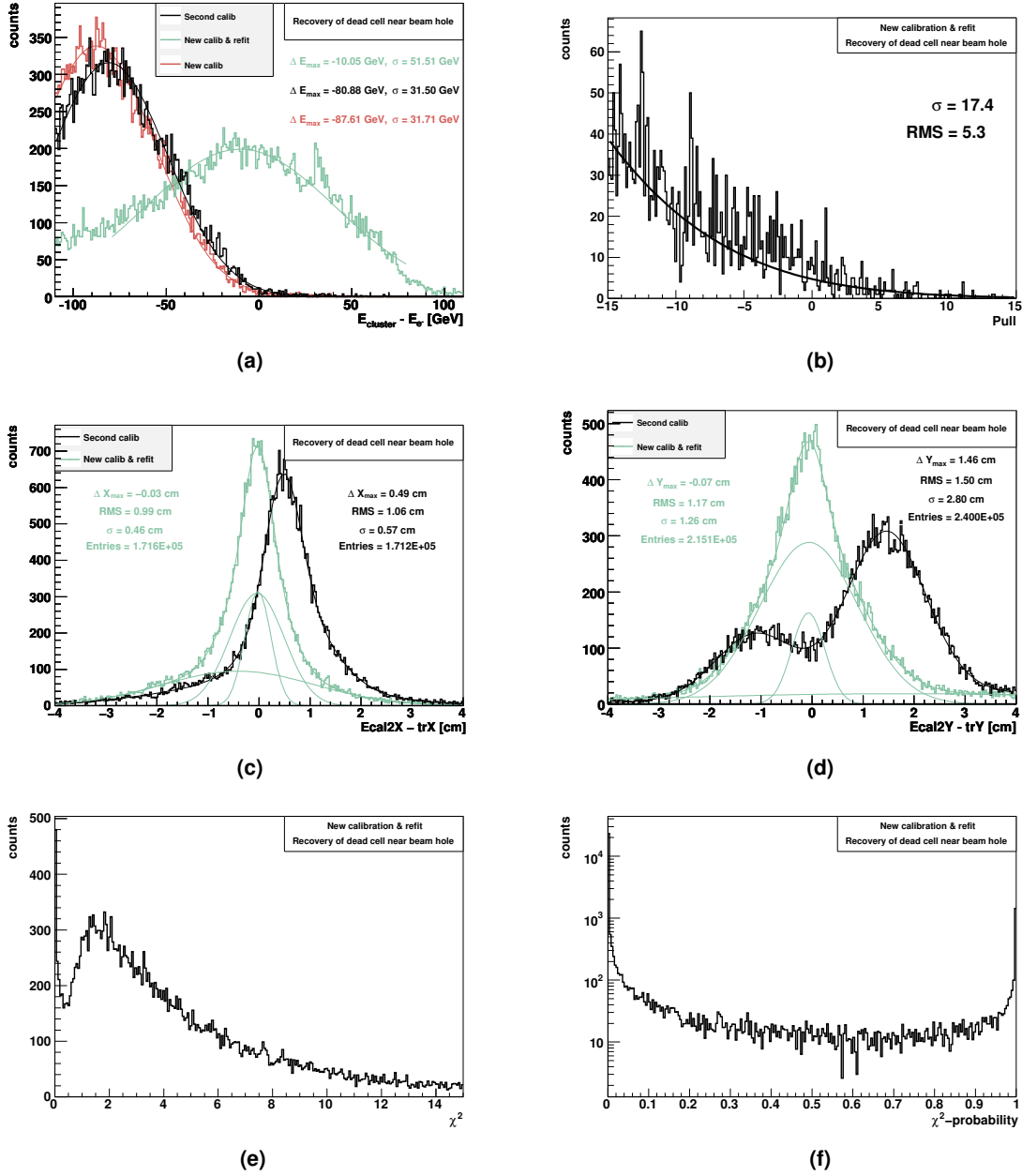


Figure 6.28: A dead cell is located close near the beam hole. Here, the energy information of the cluster is nearly lost, but the refit can give a vague trend and in average about 60 - 70 GeV can be recovered. Nevertheless the cluster position can be better estimated, and the peak position in x is improved by 0.46 cm and in y by more than 1 cm.

Cluster fit recovers dead cell in the centre, Fig. 6.25:

The cluster refit checks the hypothesis whether the dead cell originally was the centre of the cluster. These histograms show events in case the cluster refit has better results when assuming the dead cell as the new cluster centre. The cluster fit recovers on average about 11 GeV of the missing energy. The σ position residual in x is improved by about 15% and in y about 8%. The peak position in x is corrected by about 0.26 cm.

Clusters near the detector border, Fig. 6.26:

Clusters close to the border are treated similar by the refit like clusters with dead cells, since part of the information is missing. The refit recovers those clusters. The peak of the energy residual contains about 69% more entries compared to the distribution of the second calibration and has an improved σ of about 17%. Basically, the new calibration in combination with the refit leads to this observed improvement. The position residual in x is improved by the fit of about 0.49 cm and 0.07 cm in y.

Clusters located near the beam hole, Fig. 6.27:

Clusters near the beam hole of ECAL2 are truncated. Fig. 6.27 shows the results for clusters close to the beam hole. The new calibration and the fit lead to an improvement, the distributions are highly dominated by the background. The cluster refit improves the peak position of the position residual about 0.09 cm in x and the σ about 25% in y which can be mainly addressed to a change in the broader component of the peak.

Cluster fit recovers the dead cell near the beam hole, Fig. 6.28:

A dead cell is located close near the beam hole. Here, the energy information of the cluster is nearly lost, but the refit can give a vague trend and in average about 60 - 70 GeV can be recovered. Nevertheless the cluster position can be better estimated, and the peak position in x is improved by 0.46 cm and in y by more than 1 cm.

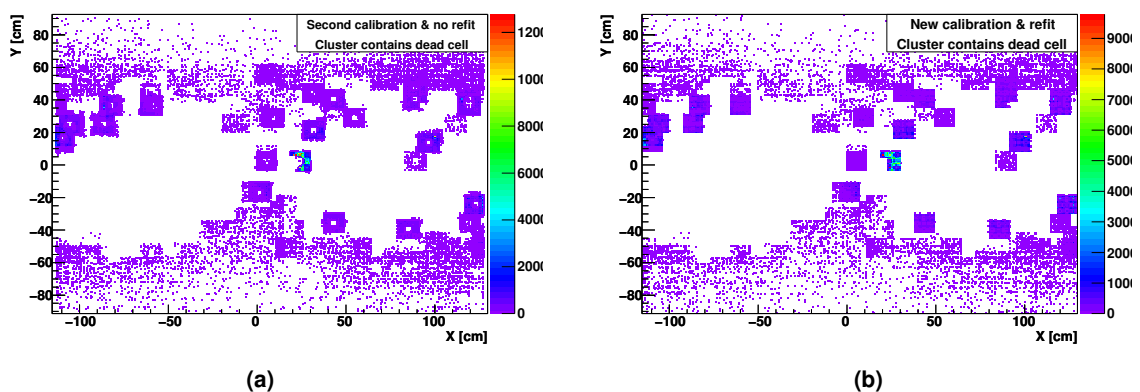


Figure 6.29: Clusters containing a dead cell: (a) with original cluster position, (b) new position after refit.

In case the refit of the cluster recovers a dead cell, the cluster position is improved. This is illustrated in Fig. 6.29, where in (a) the original cluster positions for clusters containing

a dead cell are shown. The cluster centres lie annular around the dead cell. This structure vanishes by applying the cluster refit (b) which can recover the missing energy of a dead cell. Fig. E.2 and Fig. E.3 in the appendix show the position in ECAL2 before and after the cluster refit for each cluster type mentioned above.

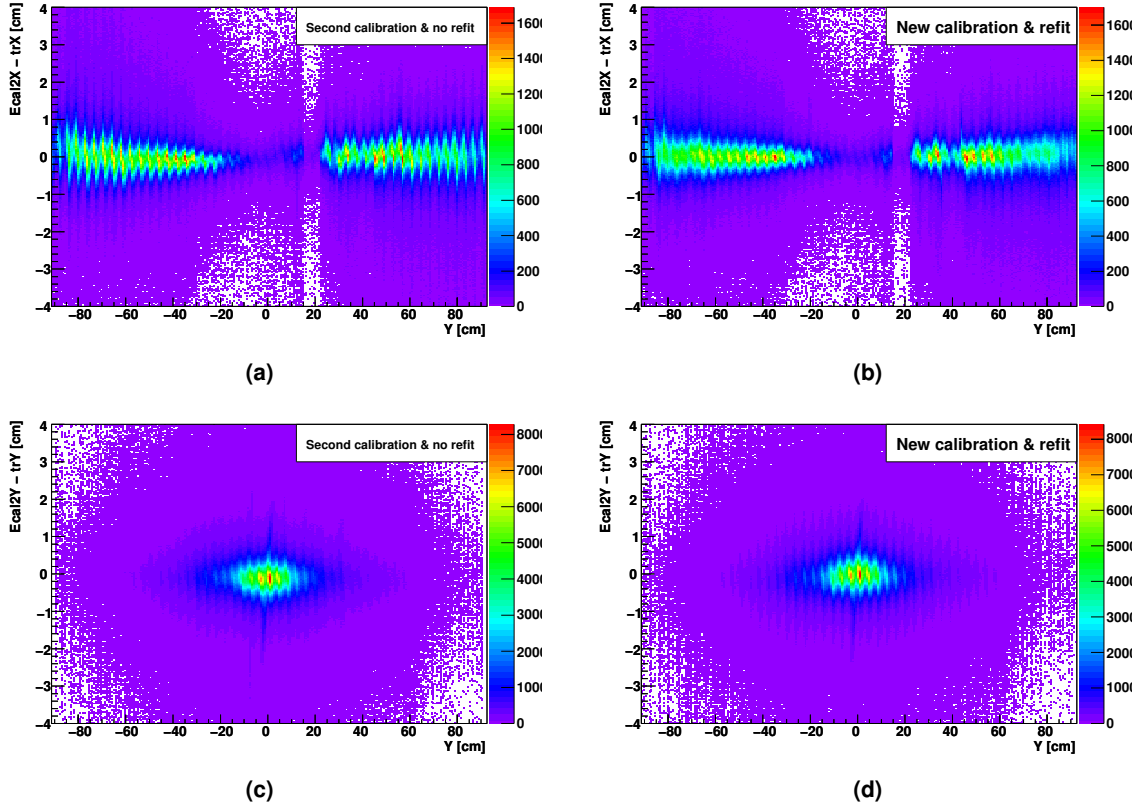


Figure 6.30: Correlation between the residual of the cluster position and the ECAL2 position of the cluster in x and y, respectively, of the electrons. On the left side for the original clusters and on the right with the new calibration applied and refitted. The zigzag structure which marks the cell structure of the calorimeter, is less distinctive after refitting the cluster (right), especially in the outer regions of the X projection.

The dependence of the position residual (including all cluster types) can be seen in Fig. 6.30, in (a) and (c) for x and y of the original electron cluster position and in (b) and (d) for refitted clusters. In both cases, the cell structure is seen, but more distinctive for the original cluster position. Depending on the impact of the electron, there is no systematic shift of the cluster position residual in both cases.

6.6.2 Primakoff Compton Analysis

The initial motivation for the investigations of this chapter is their application to Primakoff Compton events, in order to reach the best efficiency and purity for them. The new calibration values and cluster refit is applied on Primakoff Compton candidates. The

event selection in order to extract Primakoff Compton events from the data set of hadron run 2004 is described in section 8.1.

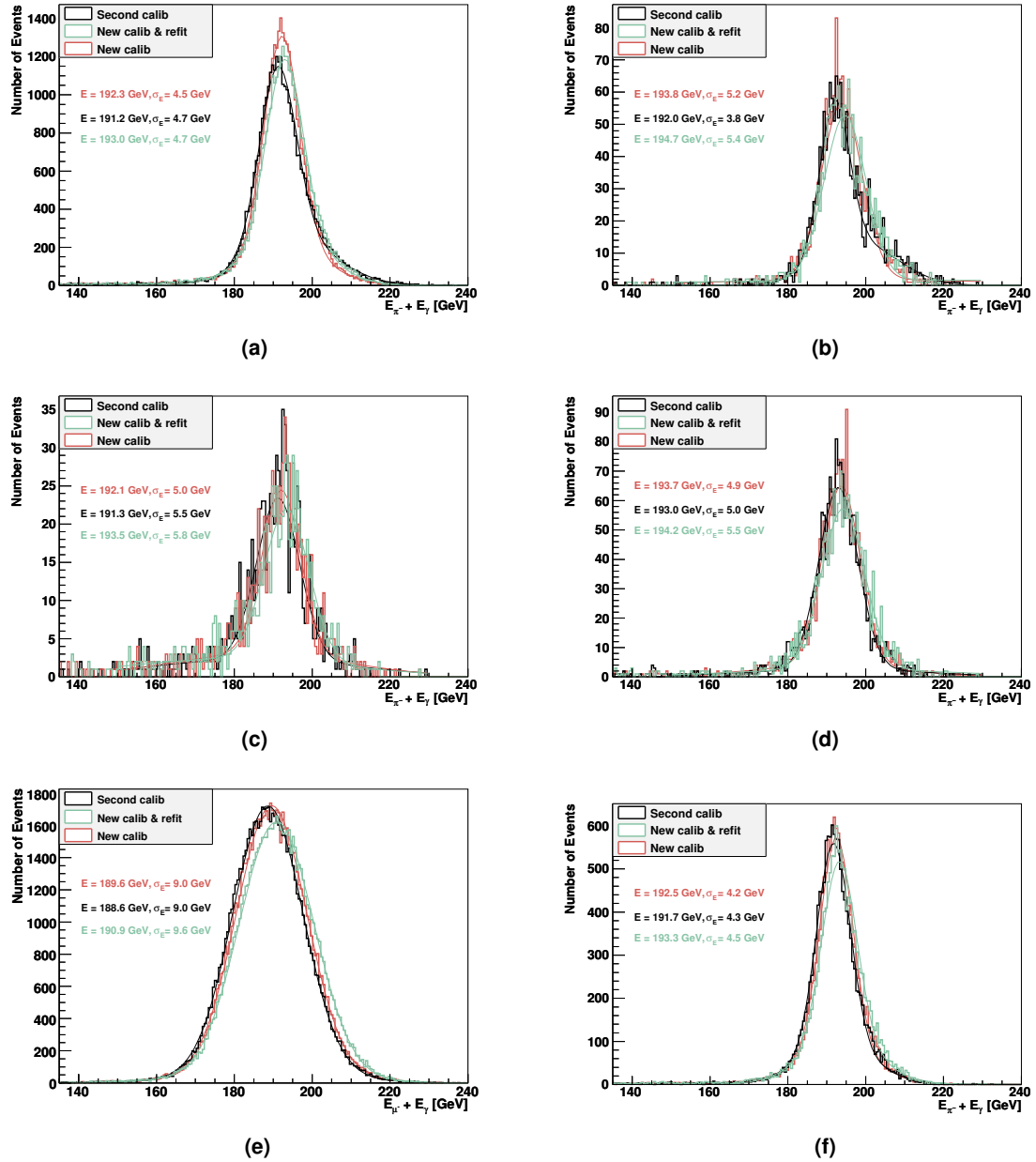


Figure 6.31: Primakoff exclusivity peak for the different target configurations of hadron run 2004, (a) Pb 3 mm, (b) Pb 1.6 mm, (c) C, (d) Cu, (f) 2-1 mm Pb, and for the muon scattering in the segmented lead target (e).

In Fig. 6.31, the distributions of the reconstructed beam energy of the reaction $\pi^- Z \rightarrow \pi^- Z \gamma$ are presented. They are called “exclusivity distribution” and are reconstructed as explained in section 8.1. The sum of the scattered pion and photon energy is expected to be equal to the nominal beam energy of about 190 GeV, since the recoil energy can be

neglected. The plots (a) - (f) show the exclusivity distributions for the different target configurations of hadron run 2004, see 2.2.4 and section B.1. The exclusivity peak for muon scattering on lead target is depicted in (e). Especially in the 3 mm Pb-target period, the new calibration leads to a narrower exclusivity peak with more Primakoff events than the second calibration, see Table 6.5. The effect on the width is in the order of 2%. For the 3 mm and 1.6 mm Pb-target periods more Primakoff events are found with the new calibration compared to the second calibration about 4.7% and 8.1%, respectively. The cluster refit delivers on the level of 1% and 5.0% more events for the 3 mm and 1.6 mm Pb-target periods. For the muon data sample the new calibration has 8.9% more Primakoff events but the cluster refit about 1.6% less. For the segmented Pb-target, copper and carbon period, the new calibration has within $\pm 1\%$ level the same number of events than the second calibration. The cluster refit finds about 2% less events. On the whole, the performance of the cluster refit is not as good as just applying the new calibration. A reason could be, that the underlying shower profile (r -distributions) for high photon energies may have not enough statistics as discussed in 6.4.2 where certain shower profiles had to be added in order to increase the statistics. So, the empirically derived shower model for high energies may have introduced new uncertainties, and the cluster refit is sensitive to them. In general, the exclusivity distributions with the new calibration has comparable, and in some cases better results than the second calibration. This is a difference compared to the electron track analysis, where the new calibration alone does not deliver better results but in combination with the cluster refit.

Fig. 6.32 shows the exclusivity peak for events, where the cluster refit recovered the energy of a dead cell, but without applying the Primakoff cuts. The peak at 190 GeV indicates that events are recovered which fulfil the exclusivity criteria. But these events do not pass the selection criteria of the Primakoff Compton analysis presumably because the spatial resolution is not sufficient to resolve the small Q^2 . In Table 6.5, the number of Primakoff events for the different target configurations including the fraction of events containing cluster types like a dead or a saturated cell are given. The fraction of events affected by non standard clusters is well below $< 0.4\%$.

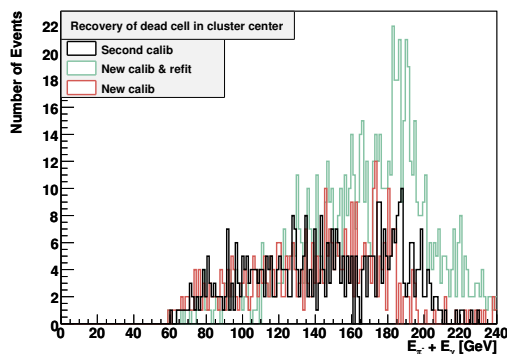


Figure 6.32: $E_\pi + E_\gamma$ for clusters with a dead cell in the cluster center of the 3 mm Pb-target period.

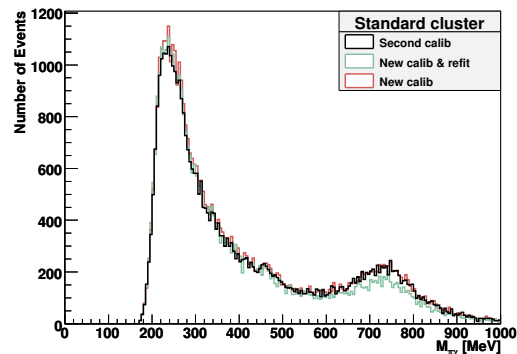


Figure 6.33: Primakoff $\pi\gamma$ -invariant mass spectrum of the 3 mm Pb-target period.

Data set	Second calibration	Cluster refit	New calibration
Pb target 3 mm			
Full statistic	30857	31178	32302
Standard cluster	30750	31067	32182
Saturated cell in centre	2	2	2
Cluster near hole	14	15	18
Cluster contains dead cell	91	94	100
Dead cell in cluster centre	2	1	2
Pb target 1.6 mm			
Full statistic	1376	1446	1487
Standard cluster	1373	1445	1484
Saturated cell in centre	0	0	0
Cluster near hole	0	0	0
Cluster contains dead cell	3	1	3
Dead cell in cluster centre	0	0	0
C target			
Full statistic	746	699	737
Standard cluster	734	686	725
Saturated cell in centre	0	0	0
Cluster near hole	2	1	2
Cluster contains dead cell	10	12	10
Dead cell in cluster centre	0	2	0
Cu target			
Full statistic	1660	1611	1660
Standard cluster	1648	1599	1647
Saturated cell in centre	0	0	0
Cluster near hole	3	3	3
Cluster contains dead cell	9	9	10
Dead cell in cluster centre	0	0	0
Pb target 2 +1 mm, Muon			
Full statistic	67471	65974	67964
Standard cluster	67355	65862	67832
Saturated cell in centre	50	50	51
Cluster near hole	5	7	7
Cluster contains dead cell	61	55	74
Dead cell in cluster centre	0	0	0
Pb target 2 +1 mm, Pion			
Full statistic	13160	12822	13160
Standard cluster	13116	12780	13110
Saturated cell in centre	4	4	4
Cluster near hole	3	2	2
Cluster contains dead cell	37	36	44
Dead cell in cluster centre	0	0	0

Table 6.5: Number of Primakoff events for all different beam time periods of hadron run 2004 in comparison between the second calibration, the new calibration and the cluster refit.

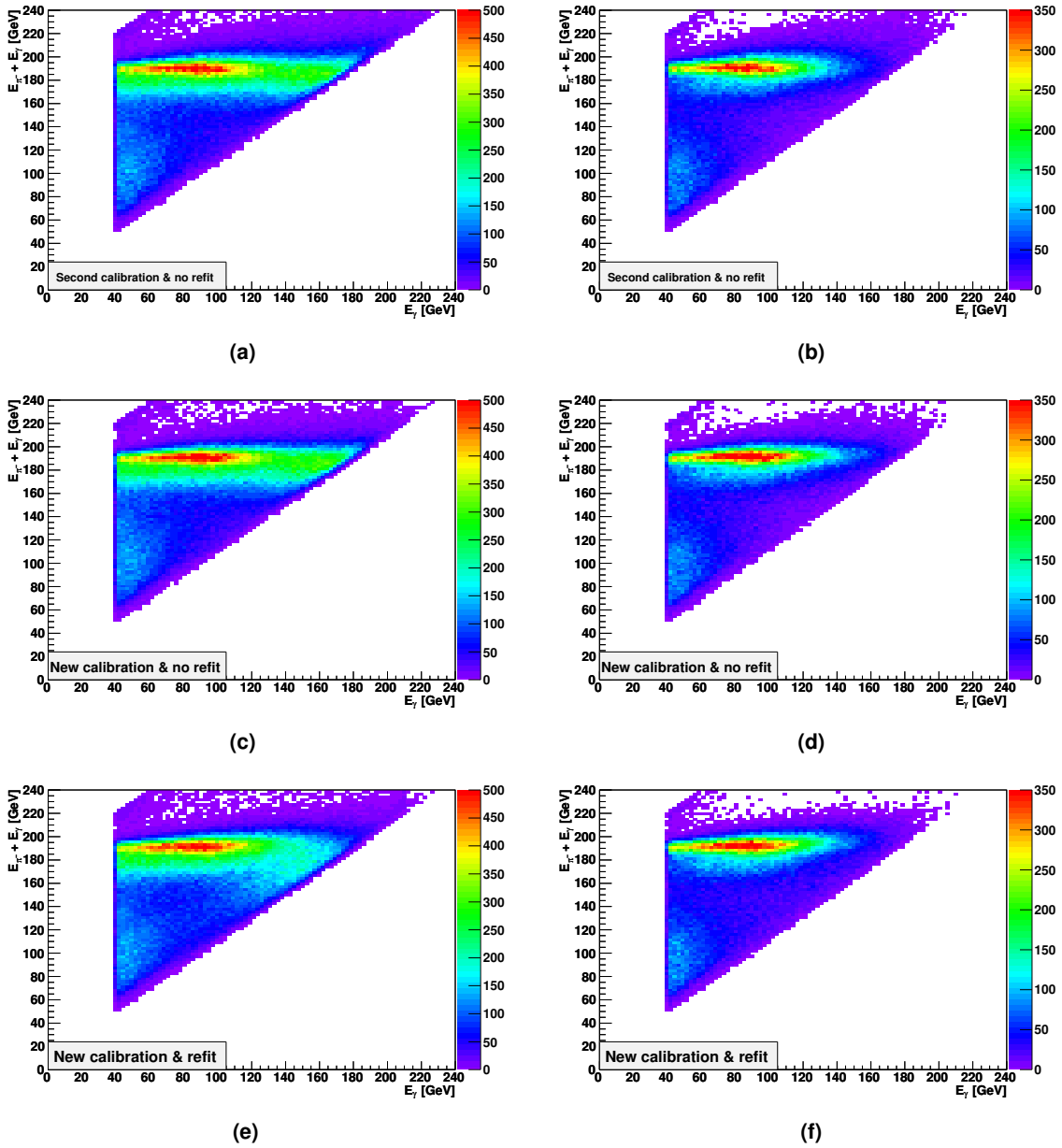


Figure 6.34: Dependence of the reconstructed beam energy on the photon energy, without a cut on the invariant $\pi\gamma$ -mass (left) and with $m_{\pi\gamma} < 3.87 m_{\pi}$ (right). The data are from the Pb 3 mm target period and the photon energy determined with the second calibration is shown in (a, b), with the new calibration (c, d) and the cluster refit with new calibration (e, f). The cluster refit (e) shows less events for high energies, compared to the distribution (a) and (c). Due to the fact that $E_{\gamma} > 140$ GeV are reduced by the cut on the invariant mass (right), this indicates that the cluster refit reduces the $\pi^0 \rightarrow \gamma\gamma$ background. For this histograms, the Primakoff cuts except the exclusivity cuts were applied to the data, see section 8.1 for explanation.

Fig. 6.34 displays the dependence of the reconstructed beam energy of Primakoff candidates on the photon energy determined with the second calibration (a, b), the new calibration (c, d) and the cluster refit (e, f) with new calibration. The right figures show the Primakoff candidates with a cut on the invariant $\pi\gamma$ -mass ($m_{\pi\gamma} < 3.87 m_\pi$) and on the left side without this cut. No obvious dependence on the cluster energy can be obtained. The distribution (e) with refitted clusters contains less events of high energy photons compared to the second (a) and new calibration (c). This difference vanishes by applying the cut on the invariant mass, see (a, d, f). A possible explanation might be the signal of a $\pi^0 \rightarrow \gamma\gamma$ decay. For high energies the angle between the two photons in the laboratory frame lead to an impact position at ECAL2 very close to each other such that the clustering algorithm will not separate them. Since the r -distribution underlies the shower distribution of single events, the cluster refit will not work for a two photon shower. Such an indication shows the $\pi\gamma$ -invariant mass spectrum for the 3 mm Pb-target period, see Fig. 6.33. In the region of the ρ -resonance at 770 MeV ($\rho \rightarrow \pi\pi^0 \rightarrow \pi\gamma\gamma$), there are less entries for the cluster refit compared to the distribution of the second calibration, while for lower masses this effect vanishes.

The photons of the Primakoff reaction hit ECAL2 mainly in the centre. In Fig. 6.35 and Fig. 6.36, the cluster positions of the photon of Primakoff candidates are shown, without (left) and with (right) the Primakoff exclusivity cuts applied, see section 8.1 for cut definition. Fig. 6.35 shows the cluster position as originally determined by CORAL and Fig. 6.36 as determined by the cluster refit. In each case the Figures (a) and (b) contain all events, (c) and (d) display only clusters with a saturated cell, (e) and (f) clusters containing a dead cell. Like in the electron case, the cluster refit can recover the cluster position for dead cells. But the dead cells are (fortunately) out of the Primakoff or on the verge of the Primakoff region. There are clusters with a cell in saturation, but even with the cluster refit no event remains after the kinematic cuts. The halo structure in Figures (a) at $R = 17$ cm comes from photon losses due to the He-gas pipe of RICH, see subsection 8.3.1. After applying all Primakoff selection cuts on the data, compared to other cells, there are significantly less events for clusters $x \approx 5$ cm and $y > 3$ cm. This comes from a trigger inefficiency, cf. subsection 8.3.2.

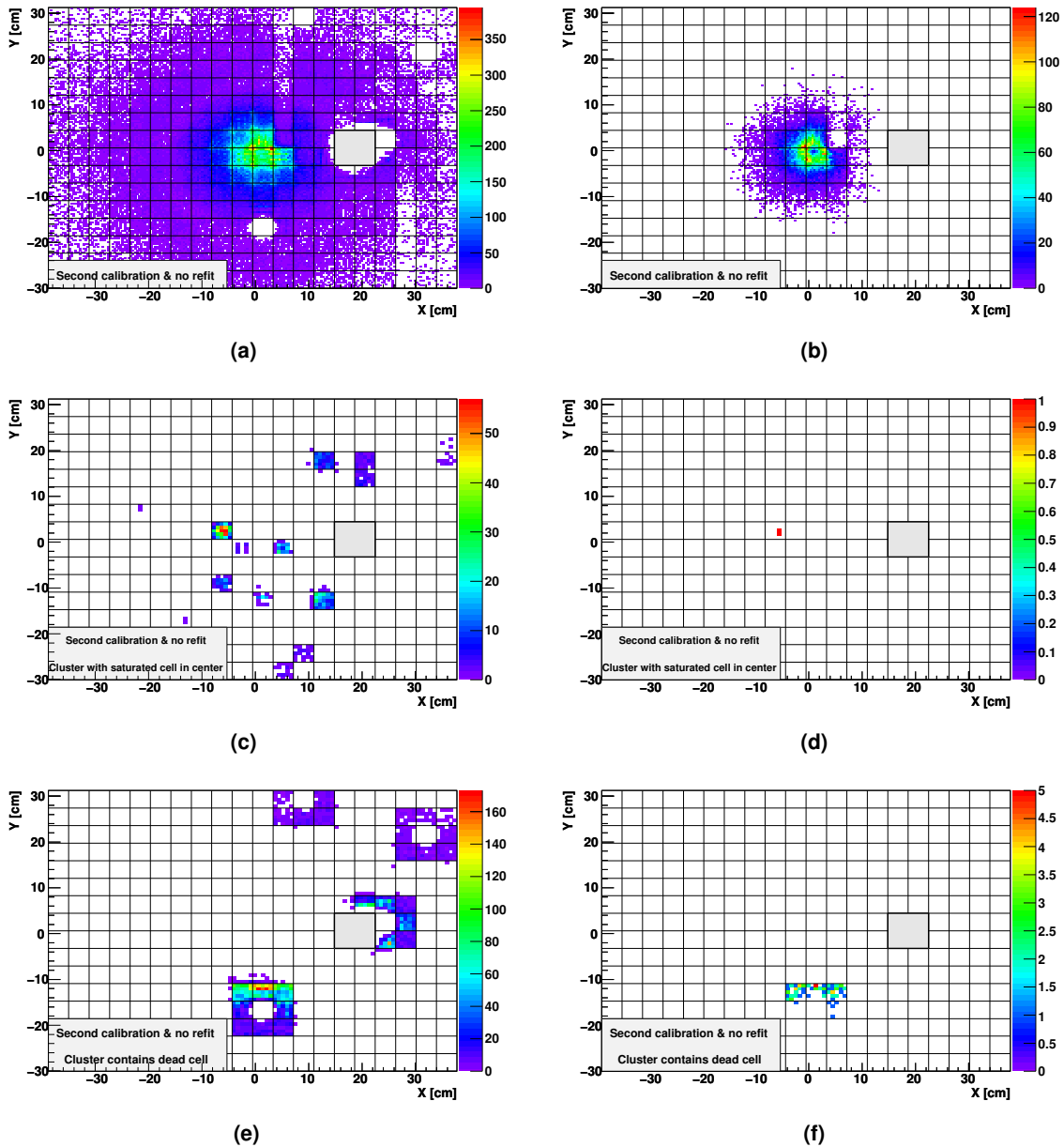


Figure 6.35: Cluster position originally determined by CORAL for Primakoff candidates, on the left without and on the right with the exclusivity cut set applied, see section 8.1. Picture (a) and (b) contains the full statistics, (c) and (d) display only clusters with a saturated cell (e) and (f) those with a dead cell, for 3 mm Pb-target period.

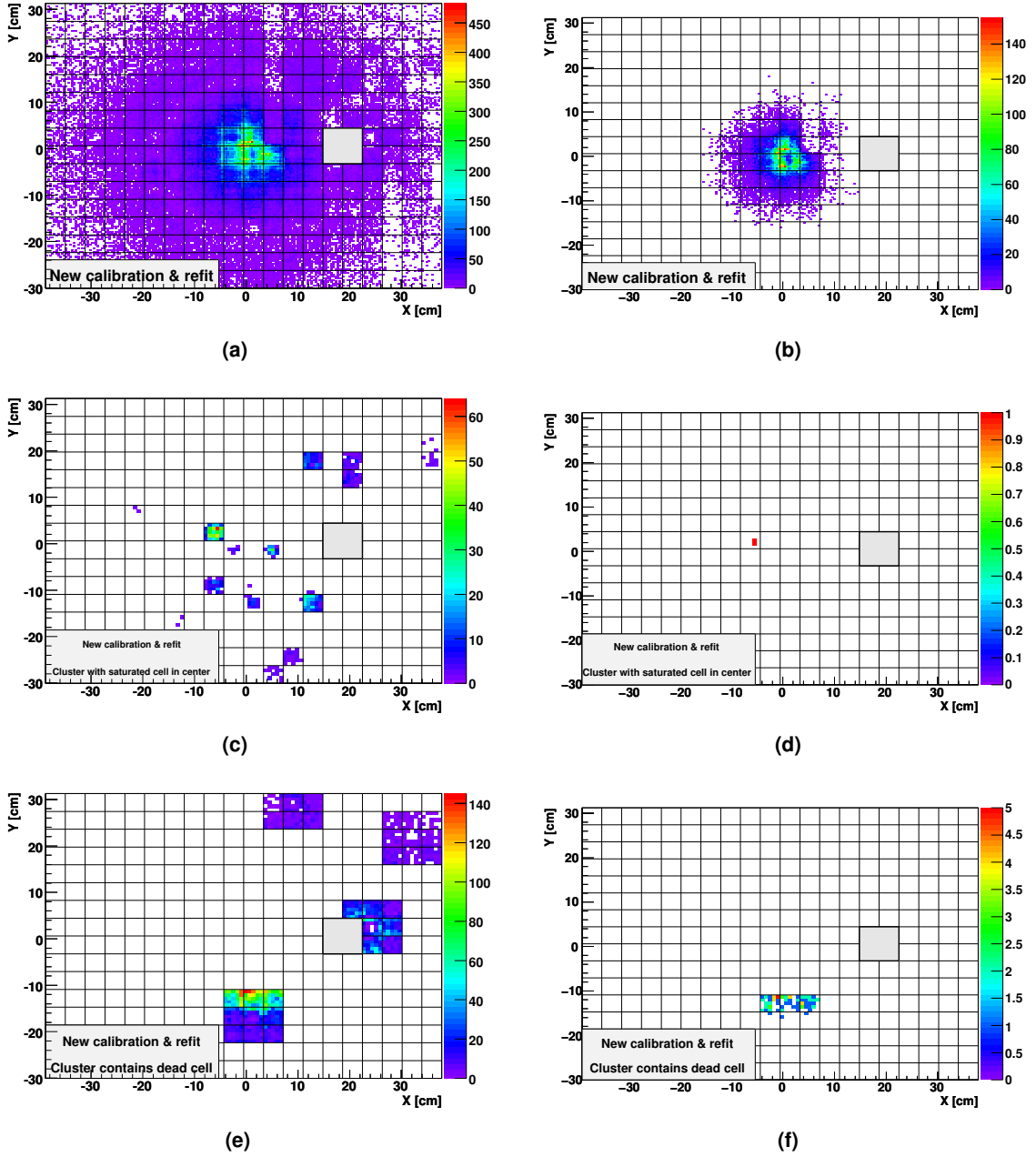


Figure 6.36: Cluster position after refit for Primakoff candidates, on the left without and on the right with the exclusivity cut set applied, see section 8.1. Picture (a) and (b) contains the full statistics, (c) and (d) display only clusters with a saturated cell (e) and (f) those with a dead cell, for 3 mm Pb-target period.

6.7 Performance of ECAL2 in Hadron Run 2004

6.7.1 Problematic Cells

In the hadron period in 2004, the high voltage dividers of the PMTs were adjusted out of their dynamic range and ran into saturation for several cells. Fig. 6.37 shows the ADC-spectrum of cell 2057 which is located in the region where also the photons of the Primakoff reaction enter the detector, see Fig. 6.38. So, ADC-values corresponding to energies above 3500 are not correctly detected. In order to derive the saturation values for all ECAL2 cells, the ECAL2 clusters of 269 runs of the hadron period in 2004 were analysed cell by cell, see Table E.5. In case of saturation, an algorithm detects the peak at the end of the ADC-spectrum. The value of this peak, subtracted by a safety margin of ten ADC-values, is stored in the calibration file.

For the physics analysis, the performance of the cells which are hit by the photons of the Primakoff reaction are of interest. The cell numbers in this particular region are depicted in Fig. 6.38. Within this region, 14 cells were in saturation over the whole hadron run period and 17 turned out having been unstable for a significant amount of runs. For most of these cells, the saturation threshold is in the order of 3000 ADC-values which corresponds to energies of 50 GeV up to 180 GeV depending on the calibration factor of the particular cell. As an example of unstable cells, the calibration values dependent on the run number for the cell 2191 and 2117 are depicted in Fig. 6.39 and Fig. 6.40, respectively. Especially the analysis of the LED data shows large variations of the calibration values within short time. The calibration based on the electron data is not sensitive to such fluctuations due to the calibration method as described in the previous sections. Some of the cells in ECAL2 were dead during the hadron run 2004. In the centre of ECAL2 the cells 2020, 2430, 814 and near the beam hole 672 were affected.

6.7.2 Energy and Spatial Resolution

Fig. 6.42 to 6.47 display the normalised energy resolution $\sigma(\Delta E)/E$ and the spatial resolution $\sigma(\Delta X)$ and $\sigma(\Delta Y)$ as a function of the electron energy for the clusters with the second calibration and for the cluster refit, respectively. Each energy interval (width 10 GeV) is fitted by eq. (6.31) which models the background by a Gaussian function and the peak position with two Gaussians:

$$(6.31) \quad f_G(x) = \underbrace{\text{Gauss}[x; a_1, m_1, \sigma_1]}_{\text{Background}} + \underbrace{\text{Gauss}[x; a_2, m_2, \sigma_2] + \text{Gauss}[x; a_3, m_3, \sigma_3]}_{\text{Signal}}$$

with $\text{Gauss}[x; p_0, p_1, p_2] \equiv \frac{p_0}{\sqrt{2\pi}p_2} \cdot \exp\left[-\frac{(x-p_1)^2}{2p_2^2}\right]$.

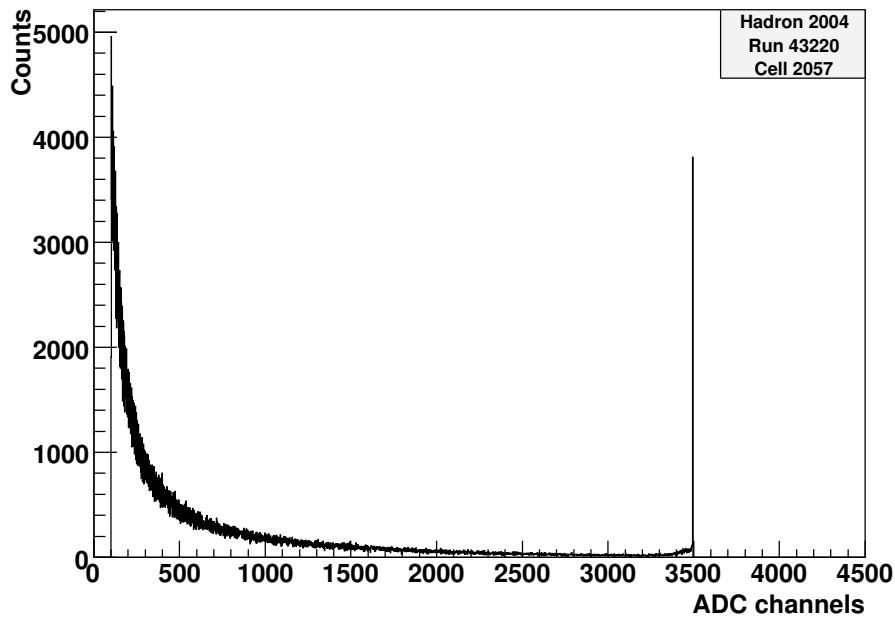


Figure 6.37: The energy distribution in values of ADC channels for cell 2057 of run 43220 which saturates for energies higher than corresponding 3500 ADC-values. The data were filtered so that ADC values below 100 were not stored in the analysis tree in order to reduce the size of the TTree.

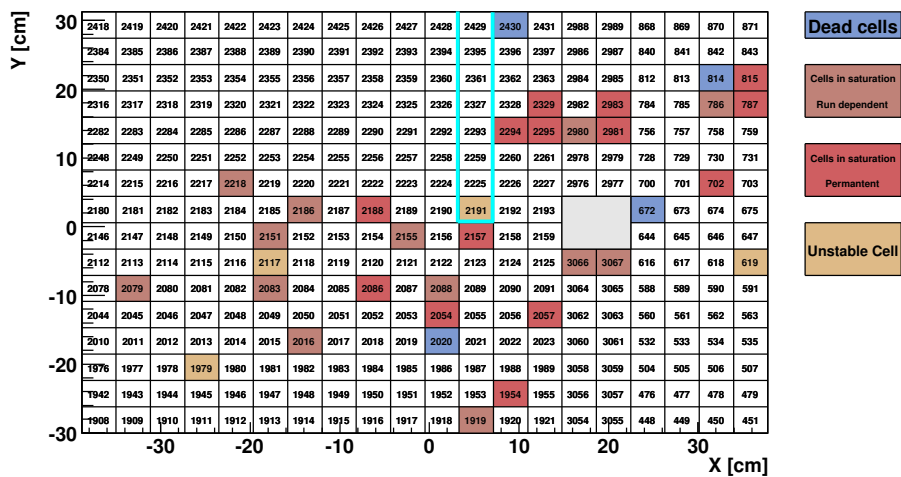


Figure 6.38: Cells of the central part of ECAL2, where the scattered photons of the Primakoff reaction hit the detector. The grey shaded region indicates the position of the hole. Cells which were in saturation or dead during the hadron run 2004, are coloured. The turquoise bordered region mark the cells erratically not connected to the trigger logic, see subsection 8.3.2.

6 CALIBRATION OF THE ELECTROMAGNETIC CALORIMETER

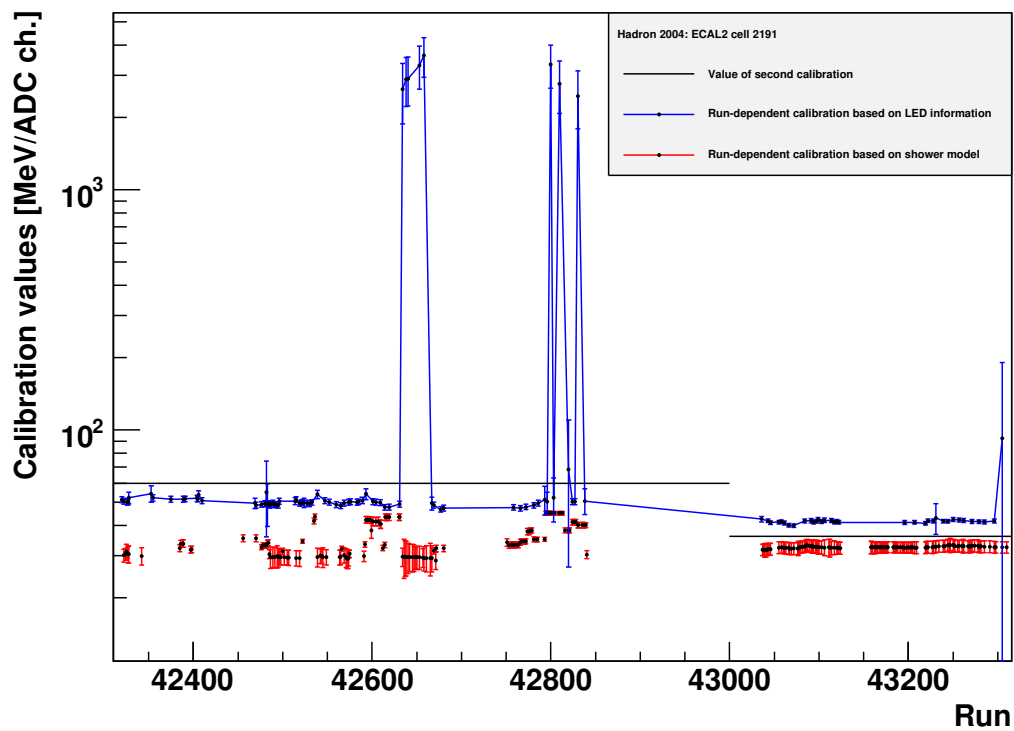


Figure 6.39: Calibration trending over time of calibration values for unstable cell 2191.

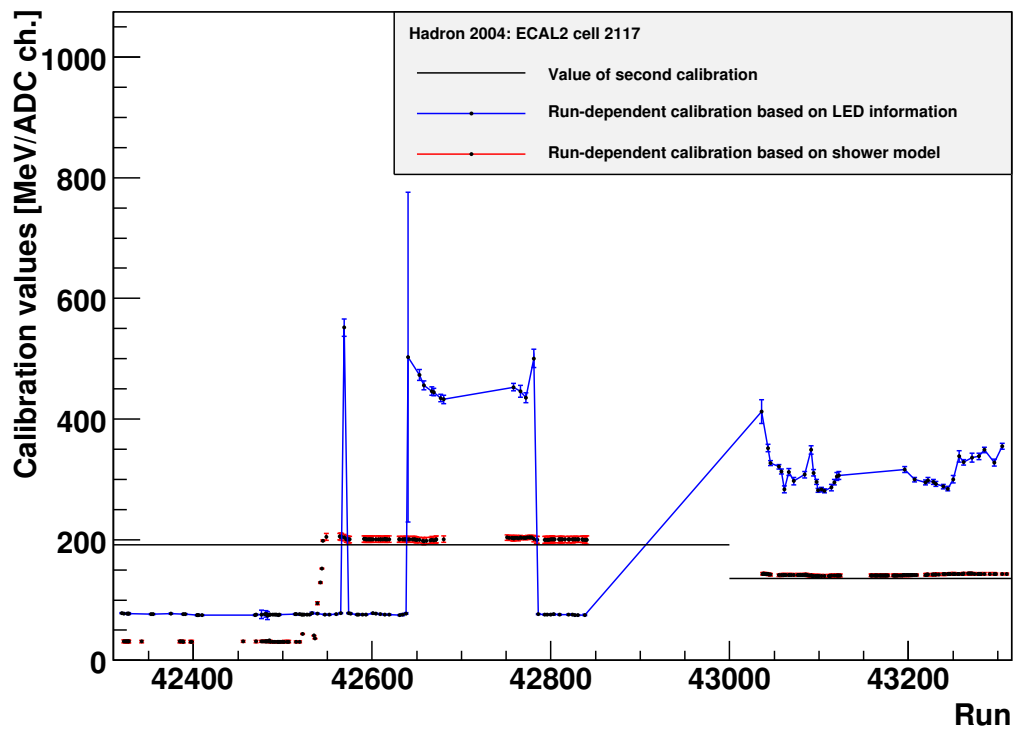


Figure 6.40: Calibration trending over time of calibration values for unstable cell 2117.

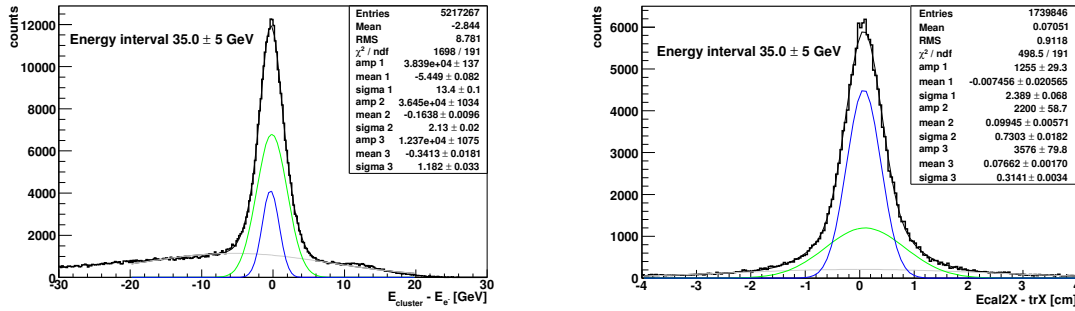


Figure 6.41: Example fit of eq. (6.31) for a energy residual (left) and a spatial residual in X (right). The background Gaussian 1 is coloured grey and the signal is described by Gaussian 2 in green and Gaussian 3 in blue.

The σ_{23} of the peak is calculated from the contributions of the two Gaussian functions as follows

$$(6.32) \quad \sigma_{23} = \sqrt{\frac{a_2\sigma_2^2 + a_3\sigma_3^2}{a_2 + a_3}}.$$

An example of the fit for determining the energy and position resolution is given in Fig. 6.41. The sigma values, the mean of the three Gaussian function and their relative contributions are shown in Fig. 6.42 to 6.47. In order to get the energy dependent energy and spatial resolution, the σ_{23} of the peak is fitted in the range from 10 GeV - 120 GeV by the usual parametrisation of the energy and spatial resolution, see eq. (6.7) on page 76. The results of the fit are summarised in Table 6.6. The cluster refit improves the spatial resolution about 2.2% in X and loses about 4.4% in Y compared to the position originally determined by CORAL. The overall spatial resolution is in the order of 3.0-3.2 cm/ \sqrt{E} , which is about a factor 5 larger than the published value [COM07a] for parameter a . The result of the energy resolution depends on the treatment of the parameter c , which takes the contribution due to electronic noise into account, see section 6.2. In Fig. 6.42 and Fig. 6.43 two fit curves are displayed. In one case, the parameter was fixed to zero and in the other case c was fitted. The published parameters a for ECAL2 [COM07a] which do not consider parameter c are about a factor 6 smaller than determined by this analysis. Leaving c as a fit parameter, the contributions of parameter a vanishes and c converges to a value of about 1.5 GeV/ E . For the second calibration and cluster refit, there is a systematic drift towards higher cluster energies of about 5% and 4.5%, respectively, in this analysis based on electrons. This effect is not seen in Fig. 6.34 where the showers are initiated by photons.

6 CALIBRATION OF THE ELECTROMAGNETIC CALORIMETER

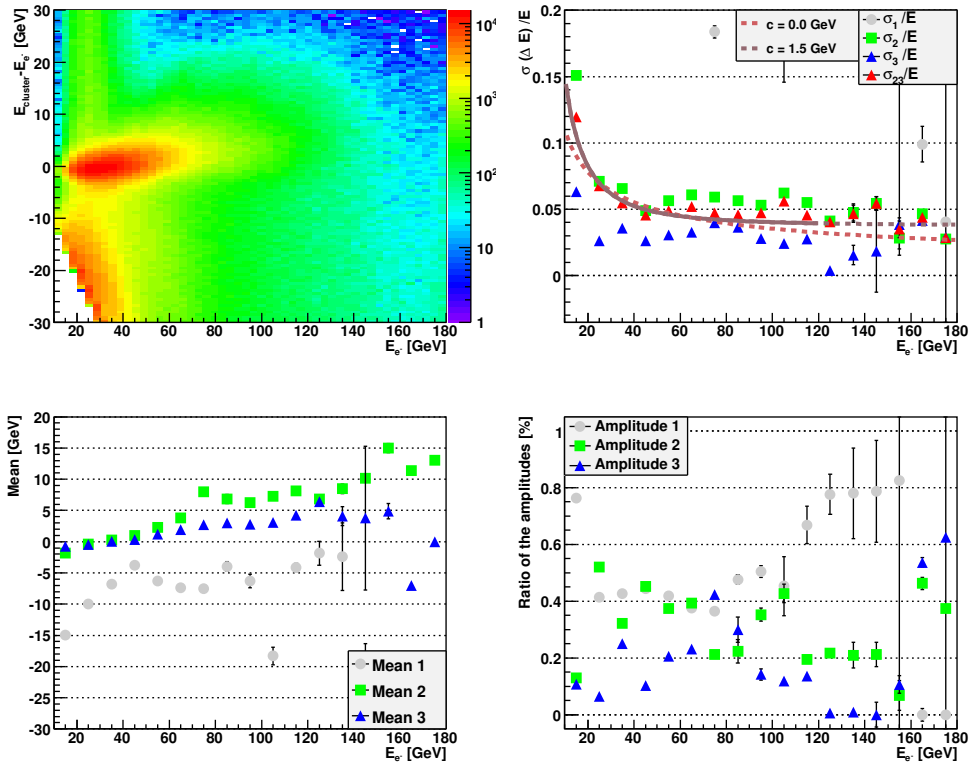


Figure 6.42: Energy resolution for cluster with second calibration values applied.

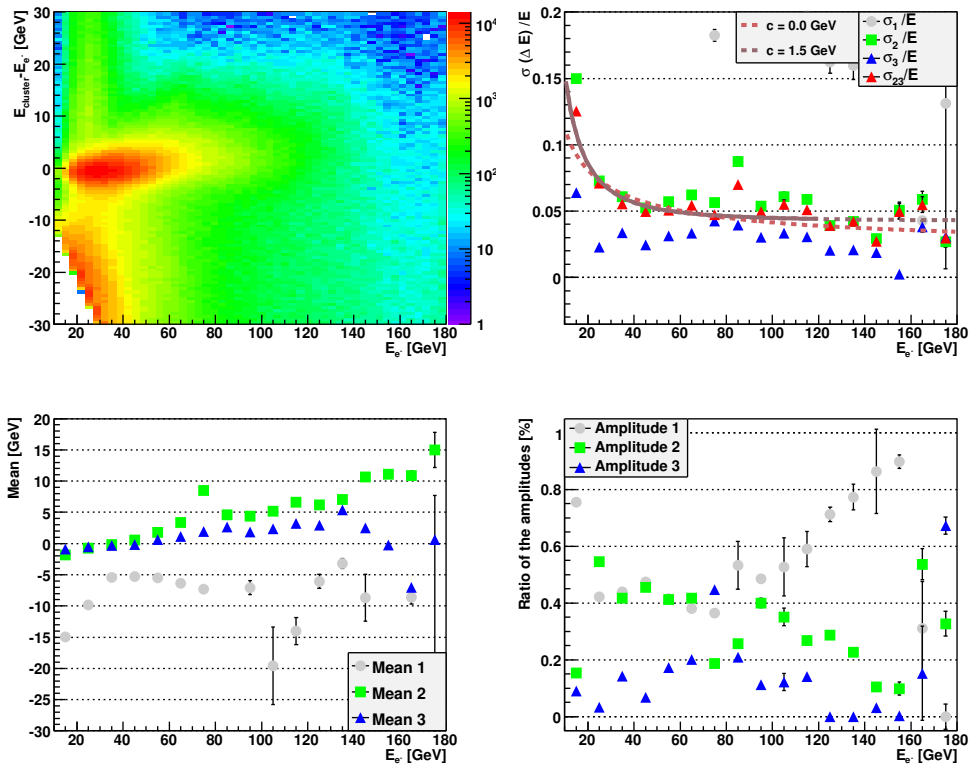


Figure 6.43: Energy resolution for refitted clusters and new calibration values applied.

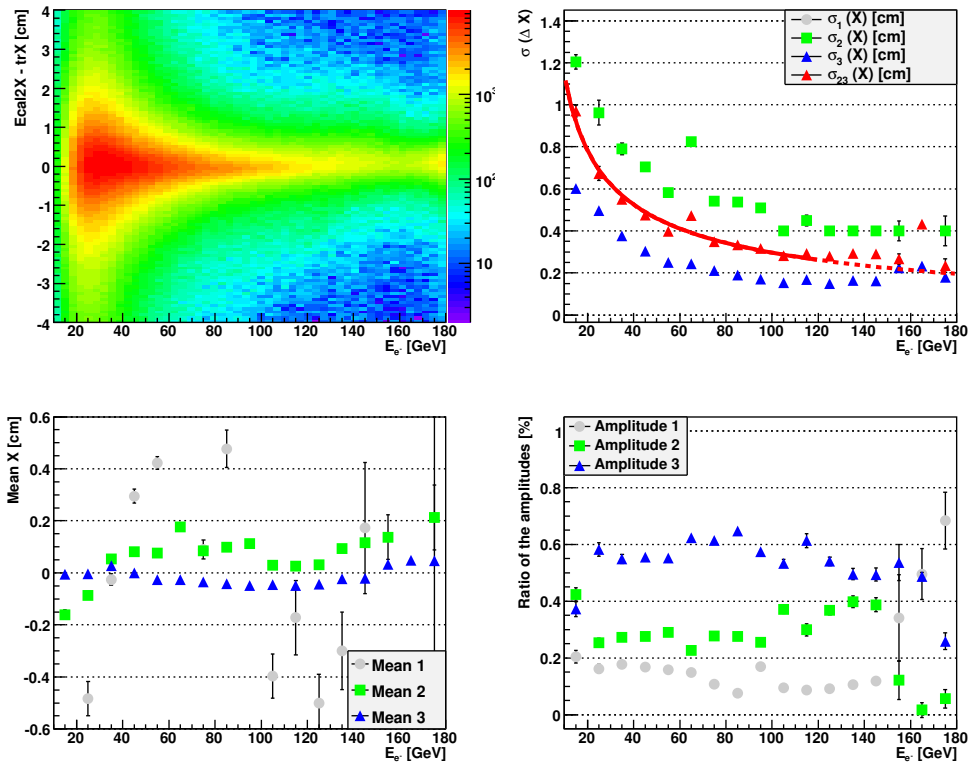


Figure 6.44: Spatial resolution in X for original cluster position determined by CORAL.

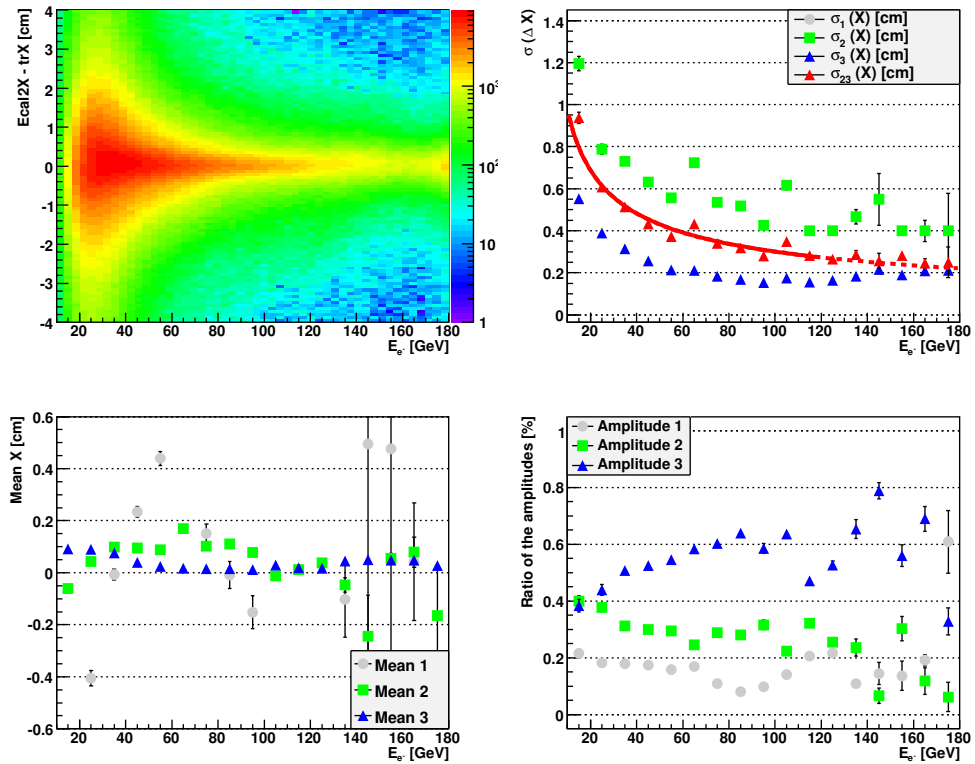


Figure 6.45: Spatial resolution in X after cluster refit.

6 CALIBRATION OF THE ELECTROMAGNETIC CALORIMETER

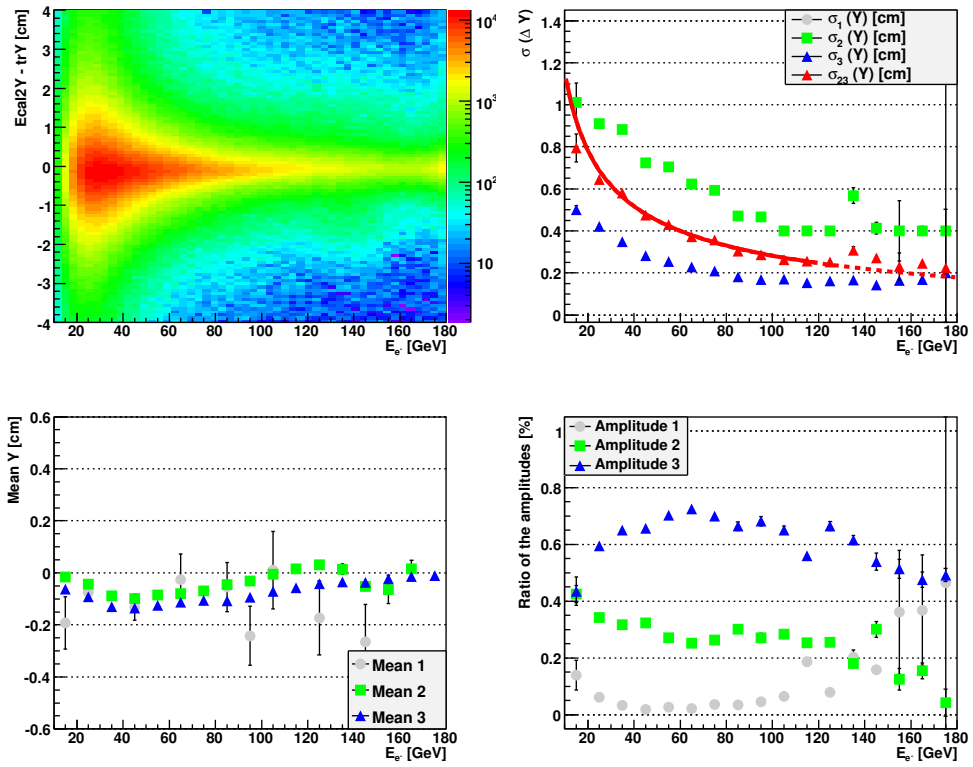


Figure 6.46: Spatial resolution in Y for original cluster position determined by CORAL.

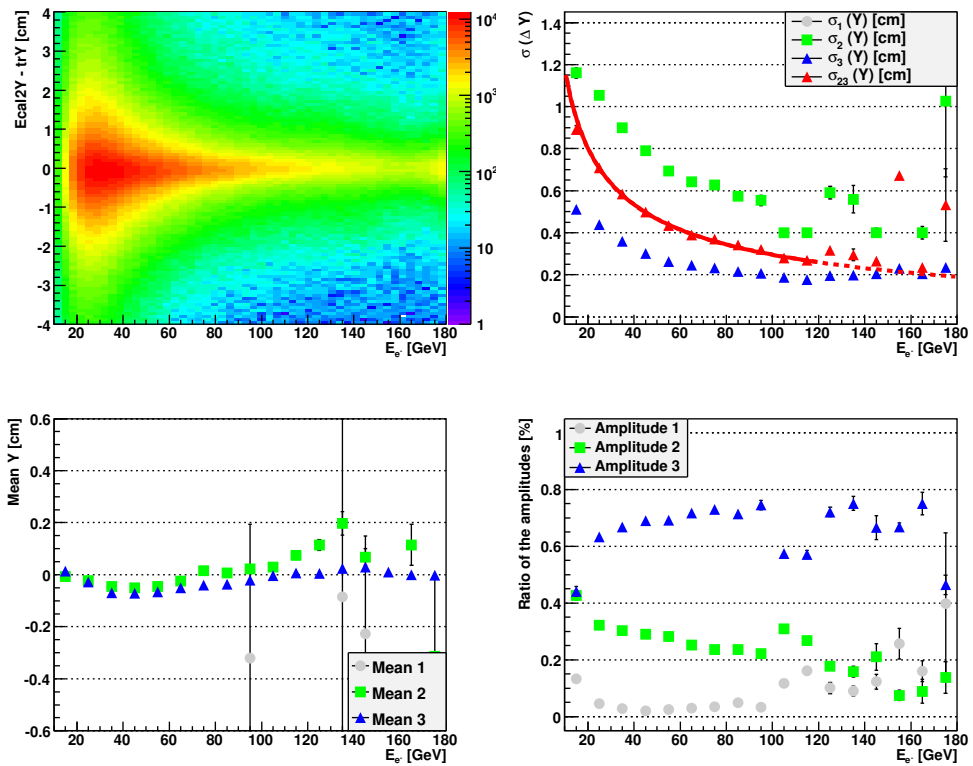


Figure 6.47: Spatial resolution in Y after cluster refit.

Energy Resolution: $\sigma(E)/(E) = a/\sqrt{E} \oplus b \oplus c/E$	a [$\sqrt{\text{GeV}}$]	b	c [GeV]
Published values [COM07a]	5.5%	1.5%	$c == 0$
Second calibration	34.8%	0.7%	$c == 0$
New calibration & cluster refit	34.7%	2.3 %	$c == 0$
Second calibration	26.8%	2.5%	$c == 0.9$
New calibration & cluster refit	26.9%	3.3%	$c == 0.9$
Second calibration	18.3%	3.3%	$c == 1.2$
New calibration & cluster refit	18.8%	3.9%	$c == 1.2$
Second calibration	4.5%	3.9%	$c == 1.4$
New calibration & cluster refit	6.9%	4.3%	$c == 1.4$
Second calibration	0.0%	3.7%	1.47
New calibration & cluster refit	0.0%	4.2%	1.50

Resolution: $\sigma(\Delta X/Y) = a/\sqrt{E} \oplus b$	a [cm]	b [cm]
Published values [COM07a]	0.6	0.05
Second calibration X	3.10	0.00
New calibration & cluster refit X	3.03	0.00
Second calibration Y	3.07	0.00
New calibration & cluster refit Y	3.21	0.00

Table 6.6: Energy and spatial resolution of ECAL2 with the electron track analysis.

6.8 Summary and Conclusion

The investigation of this chapter pointed to their application to Primakoff Compton events, in order to reach the best efficiency and purity for them. A method to recalibrate run-dependent ECAL2 with already processed data was presented. For this purpose, the electrons and positrons of background reactions like photon conversion $\gamma \rightarrow e^+e^-$ were proven to be useful.

The new calibration is based on a data-driven shower model. The r -distributions are extracted by superposing all ECAL2 clusters. These distributions contain the ratios of the measured cell energies and the electron energies as a function of the distance of the cells from the cluster centre. The r -distributions are generated for 18 angle- \times 12 energy-bins. Beside the new calibration, also a fit procedure was developed based on this shower model, in order to refit the ECAL2 clusters. The motivation was to recover clusters containing dead or unstable cells, e.g. in the Primakoff region 4 dead cells, 17 unstable and 14 cells in saturation were observed.

For electron tracks with energies $> 10 \text{ GeV}$, the new calibration leads to an improvement of the energy resolution in the order of 1-3%, with a systematic offset in the or-

der of 1 GeV. In combination with the cluster refit, this offset vanishes and the result is comparable with the second calibration for standard clusters. For Primakoff events, the new calibration improves the exclusivity peak in 1 - 2% level, especially for the 3 mm-Pb period about 4.7% more Primakoff events were found. The cluster refit decreases the resolution of the Primakoff exclusivity peak about 2% compared to the second calibration. But in this case, the photon energies are well above 80 GeV and π^0 -background ($\pi^0 \rightarrow \gamma\gamma$) occurs, where the two photons are falsely identified as one cluster. Due to the underlying shower model, the cluster fit is sensitive to this π^0 -background, which is a success of the cluster refit.

The cluster fit treats truncated clusters, e.g. clusters with dead cells, close to the border or near the beam hole in a better way. It enhances the position of these clusters and recovers their energies, e.g. 50% more entries are found in the energy residual peak for clusters containing a dead cell and their spatial residual is improved up to 12%. Yet, the resolution is not sufficient to fully recover the events for the desired physics analysis. In case of the Primakoff reaction, it turned out that less than 0.4% of the events are affected by such cells.

These studies confirm that in general, the two sets of the second calibration for ECAL2 have lead to a big improvement compared to the primary calibration. As a result of this work, it turned out for most of the ECAL2 cells, the step between the two periods 42321 – 42840 and 43034 – 43348 covered by the two sets of the second calibration is the biggest effect. The new calibrations led to a small improvement because the statistics to generate the calibration values was limited. The available statistics is dependent on the length of a run and the position of the cell at ECAL2. Especially in the centre, less electron events for the calibration were available. The statistics per run is shown for the central cell 2219 in Fig. E.4 which is for many runs below 100. For comparison, Fig. E.5 shows cell 2171 of the outer region, where for most of the runs more than 1000 events were available. In order to overcome this statistics problem the smoothing factor of the exponential smoothing is set to 0.98 (eq. (6.22)) which delivered the best results so far for the Primakoff Compton analysis. But, this high smoothing factor equalises the fluctuations of the calibration values. From the analysis of the LED signals, it is known that quite many cells show fluctuations. A further analysis could study individual smoothing factors depending on the available statistics for the cells. The limited statistics concerns also the cluster refit which depends on the r -distributions. Only 30% of the total statistics was used, where the LED information was available at the time of this work. The LED based calibration was the best starting point for generating the r -distributions, since the run-dependent fluctuations were minimised. In a further analysis, it would be best to get the LED information for all runs so that the shower profiles can be improved with more statistics and in addition the process of generating such shower profiles could be refined.

Chapter 7

Compton Scattering and Pion Polarisability

7.1 Motivation and Cross Section

Strong interaction phenomena involving quarks and gluons are very well described by QCD, a gauge theory based on SU(3) colour symmetry. It makes up one of the cornerstones of the standard model of particle physics. QCD is characterised by *asymptotic freedom* meaning quarks to move almost freely at small distances or high energies and *confinement* reflecting quarks and gluons to only live in bound states of finite size (scale parameter about 1fm). The key parameter is the coupling constant $\alpha_s(Q^2)$ which varies considerably in the momentum range of 1-100 GeV/c². QCD is directly applicable as long as processes are short-distance interactions, so that $\alpha_s(Q^2)$ is small and perturbative methods in the framework of an SU(3) gauge theory are valid. Of importance is the concept of asymptotic freedom, referring to the fact that the coupling strength decreases for increasing momentum transfer (from [Sch03]). At present, QCD is compatible with all empirical phenomena of the strong interactions in the asymptotic (high energy) region. Low energy problems, as the description of bound states like mesons or nucleons, can therefore not be described in perturbation theory as they live in a strong coupling regime. Such low energetic processes (large distance phenomena) cannot be perturbatively calculated in α_s , because at small momenta the coupling $\alpha_s(Q^2)$ becomes too large. In order to describe these processes, a low energy effective theory has been constructed, namely Chiral Perturbation Theory (ChPT), using the left right symmetry (chiral symmetry) inherent in QCD. It systematically provides corrections to the soft-pion predictions based on symmetry properties of QCD Greens functions (transition amplitudes at low energy). ChPT describes the dynamics of Goldstone bosons in the framework of an effective field theory. Such a theory allows for a perturbative treatment in terms of a small momentum expansion. The basis of ChPT is the global SU(3)_L × SU(3)_R × U(1)_V symmetry of the QCD Lagrangian in the limit of massless *u*, *d* and *s* quarks. According to the Goldstone theorem, the spontaneous breaking of the chiral symmetry in the QCD-vacuum mani-

feats itself in the occurrence of (almost) massless pseudoscalar Nambu-Goldstone bosons ([COM10]). The light pseudoscalar octet mesons (π , K , η) are regarded as the Goldstone bosons of the spontaneous chiral symmetry breaking. They are not massless, because the chiral symmetry is further more explicitly broken by the non-vanishing masses of the light quarks u , d and s . However, their masses are significantly smaller than typical hadronic scales. Gasser and Leutwyler [GL84] systematically developed ChPT and presented the general chiral Lagrangian up to $\mathcal{O}(p^4)$. Besides the well-known physical parameters like the pion mass $m_\pi = 139$ MeV and the pion decay constant $f_\pi = 94$ MeV, these contain new low energy constants $\bar{l}_i (i = 1, 2, 3, 4, 5, 6)$. These additional parameters may be fixed phenomenologically by comparison with experimental low energy data. For example processes like $\pi\pi$ -scattering, the pion scalar and vector form-factors allow to extract values \bar{l}_1 up to \bar{l}_6 and with these, one can make predictions to other processes.

A complementary question is the way, how hadrons (pions) react to external forces. For the case of electromagnetic fields, this response of a composite particle is encoded in the electric α and magnetic β polarisabilities. In external electric and magnetic fields, electric and magnetic dipole moments are induced in the first order which are characterised by the polarisabilities α and β , respectively. In the classical picture, see Fig. 7.1, the electric dipole moment is proportional to the external electric field, with the polarisability α being the proportionality constant ($\vec{d}_e = \alpha \vec{E}$). In the same way β is the proportionality constant between the induced magnetic dipole moment and external magnetic field ($\vec{\mu}_m = \beta \vec{B}$). This intuitive classical picture can not be directly carried over to composite particles like the pion with a $\bar{q}q$ content, but electric α and magnetic β polarisabilities are properly defined in terms of the Compton scattering amplitudes.

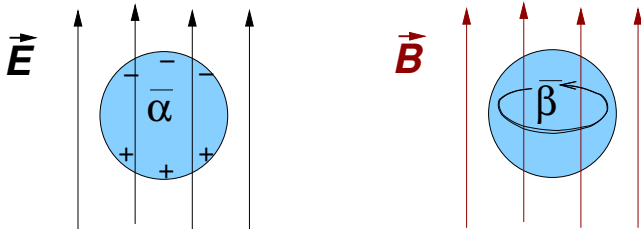


Figure 7.1: Classical analogon of a polarisability: in an external electromagnetic field the charge separates and in an external magnetic fields a current is induced.

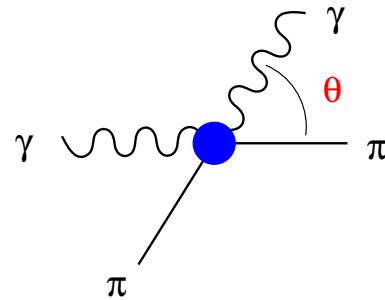


Figure 7.2: Pion Compton scattering in the centre-of-mass system.

ChPT gives accurate predictions for strong interaction dynamics of Goldstone bosons at low energies in particular for the pion electromagnetic polarisabilities α_π and β_π . The polarisability difference $\alpha_\pi - \beta_\pi$ of the charged pion is directly related (through chiral symmetry) to the radiative pion decay $\pi^+ \rightarrow e^+ \nu_e \gamma$ from which the relevant energy constant $\bar{l}_6 - \bar{l}_5$ are known. The crucial question is the accuracy of the relation $\alpha_\pi - \beta_\pi$ and $\bar{l}_6 - \bar{l}_5$. This has been addressed within a complete 2-loop calculation by Bürgi [Bur96a], Gasser and Ivanov [GIS06], which leads to the following precise predictions for the pion

polarisability difference

$$(\alpha - \beta)_\pi = (5.7 \pm 1.0) \cdot 10^{-4} \text{fm}^3.$$

at the same time a small value

$$(\alpha + \beta)_\pi = (0.16 \pm 0.1) \cdot 10^{-4} \text{fm}^3$$

has been found for the sum of the polarisability.

Besides ChPT also other approaches give predictions for the pion polarisabilities, see Table 7.1. The quark confinement model of Efimov, Ivanov and Mizutani [GVE93] [IM92] treats quark loop terms as well as meson exchange contributions and the obtained values for the pion polarisabilities are

$$\alpha_\pi = 3.64 \cdot 10^{-4} \text{fm}^3, \beta_\pi = -3.41 \cdot 10^{-4} \text{fm}^3.$$

Another ansatz for estimating the pion polarisabilities is based on dispersion relations for the helicity amplitudes of the process $\gamma\gamma \rightarrow \pi^+\pi^-$. The dispersion sum rules [AG68], [FK06] obtain these values

$$\begin{aligned} (\alpha - \beta)_\pi &= (13.60 \pm 2.15) \cdot 10^{-4} \text{fm}^3 \\ (\alpha + \beta)_\pi &= (0.166 \pm 0.024) \cdot 10^{-4} \text{fm}^3. \end{aligned}$$

However, Bürgi [Bur96b] has concluded that using the $\gamma\gamma \rightarrow \pi^+\pi^-$ amplitude as an interpolation, the statistical error in present low energy data and uncertainties in the low energy constants do not allow to pin down $(\alpha + \beta)_\pi$ to reasonable accuracy.

In order to study experimentally the polarisabilities of hadrons, like pions and kaons, the Compton effect (elastic scattering of photons) is used. Deviations of the measured cross section from that of a point-like particle give a signature of the polarisabilities α and β . For a point-like particle with spin 0, the Compton cross section for a spin-0 particle is completely determined by the scalar QED and given by an expression analogous to the Klein-Nishina formula for spin-1/2 particles. For a point-like target the Compton scattering process is completely determined by QED.

The polarisabilities are defined through an expansion of the Compton amplitudes at low energies. When using the reduced (Born terms subtracted) spin-flip and spin-nonflip helicity amplitudes H_\pm , one obtains according to [GIS06]

$$(7.1) \quad \frac{\alpha}{m_\pi} H_\pm(s = m_\pi^2, t) = (\alpha_1 \pm \beta_1) + \frac{t}{12} (\alpha_2 \pm \beta_2) + \mathcal{O}(t^2)$$

where s and t are the standard Mandelstam variables of the $\pi\gamma$ -system and (α_1, β_1) are the dipole and (α_2, β_2) the quadrupole polarisabilities, respectively. This leads to a modification in the real Compton cross section which can be written in the centre-of-mass

Experiment	Reaction	$(\alpha - \beta)_\pi$ [10^{-4}fm^3]
Serpukov	$\pi^- Z \rightarrow \pi^- Z \gamma$	$15.6 \pm 6.4 \pm 4.4$
Mami A2	$\gamma p \rightarrow \gamma \pi^+ n$	$11.6 \pm 1.5 \pm 3.0$
Lebedev Inst.	$\gamma p \rightarrow \gamma \pi^+ n$	40 ± 24
Mark II	$\gamma\gamma \rightarrow \pi^- \pi^+$	4.4 ± 3.2
PLUTO	$\gamma\gamma \rightarrow \pi^- \pi^+$	$38.2 \pm 49.6 \pm 11.4$
DM1	$\gamma\gamma \rightarrow \pi^- \pi^+$	34.4 ± 9.2
DM2	$\gamma\gamma \rightarrow \pi^- \pi^+$	52.6 ± 14.8
Theory		[10^{-4}fm^3]
χ PT (Gasser)	$(\alpha - \beta)_\pi$	5.7 ± 1.0
	$(\alpha + \beta)_\pi$	0.16 ± 0.1
QCM	$(\alpha - \beta)_\pi$	7.05
	$(\alpha + \beta)_\pi$	0.23
Dispersion sum rules	$(\alpha - \beta)_\pi$	13.60 ± 2.15
	$(\alpha + \beta)_\pi$	0.166 ± 0.024

Table 7.1: Experimental and predicted values for the pion polarisabilities $(\alpha - \beta)_\pi$ [GIS06] and [Gus10] and references therein.

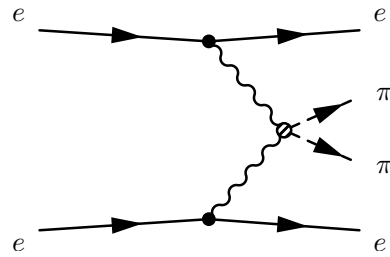
system, see Fig. 7.2, as

$$\begin{aligned}
 \frac{d\sigma_{\pi\gamma}}{d\Omega_{cm}} &= \frac{d\sigma_{\pi\gamma}^{(\text{pt})}}{d\Omega_{cm}} + \frac{d\sigma_{\pi\gamma}^{(\text{pol})}}{d\Omega_{cm}} + \dots \\
 (7.2) \quad &= \frac{\alpha^2(s^2 z_+^2 + m_\pi^4 z_-^2)}{s(sz_+ + m_\pi^2 z_-)^2} - \frac{\alpha m_\pi^3 (s - m_\pi^2)^2 \left[z_-^2 (\alpha_\pi - \beta_\pi) + \frac{s^2}{m_\pi^4} z_+^2 (\alpha_\pi + \beta_\pi) \right]}{4s^2 (sz_+ + m_\pi^2 z_-)} + \dots
 \end{aligned}$$

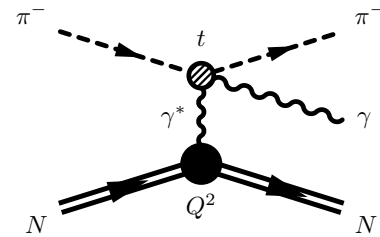
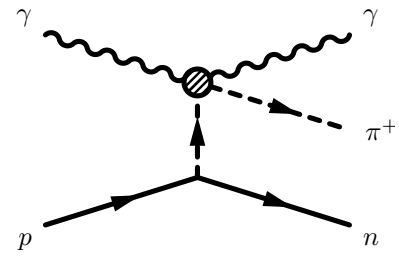
with $z_\pm = 1 \pm \cos \theta_{cm}$ related to the scattering angle θ_{cm} of the outgoing $\pi\gamma$ -pair and \sqrt{s} the total centre-of-mass energy. The quadratic terms in α_π and β_π are neglected here as well as the contributions from the quadrupole polarisabilities and chiral loops [KF08a], [GIS06].

However, real pion Compton scattering cannot be performed directly, since pions are not stable, and there exists neither a pion target nor a real photon target. The pion polarisabilities can be experimentally accessed via different processes involving virtual particles:

- $e^+e^- \rightarrow e^+e^- \pi^+ \pi^-$ ($\gamma\gamma \rightarrow \pi^+ \pi^-$) which tests the pion polarisabilities in the production process.



- $\gamma p \rightarrow \gamma n \pi^+$ radiative pion photoproduction off the proton.
- $\pi + {}^A Z \rightarrow \pi' + {}^A Z' + \gamma$ high-energy pion-nucleus bremsstrahlung, where the ultra-relativistic pion beam (quasi-stable) scatters off in the Coulomb field of a heavy nucleus (in the region of sufficiently small photon virtualities) and a hard photon is emitted. This is called *Primakoff effect*.



When considering the results of various experiments, see Table 7.1, there is no coherent picture of the pion polarisabilities yet. These experiments measured the pion polarisabilities via different processes featuring different systematics. The prediction of ChPT is in conflict with the Serpukov experiment and the Mami (Mainz) results which amount to values more than twice as large. The result from the Mark II data is consistent with the prediction, but the corresponding low-energy cross sections for $\gamma\gamma \rightarrow \pi^+\pi^-$ are rather insensitive to even sizable changes of the pion polarisabilities [KF08a].

The COMPASS experiment follows the approach of measuring the pion polarisabilities α_π and β_π via the Primakoff effect, namely pions scattering off quasi-real photons in the Coulomb field of a heavy nucleus (high-energy pion-nucleus bremsstrahlung). The production of real photons in this bremsstrahlung process corresponds to pion Compton scattering in inverse kinematics which is sensitive to the pion polarisabilities α_π and β_π . In practice, one preferably analyses the spectrum of bremsstrahlung photons produced in the reaction $\pi Z \rightarrow \pi Z \gamma$ in the so-called Coulomb peak. This kinematical regime is characterised by very small momentum transfers $\sqrt{Q^2} \ll m_\pi$ such that virtual pion Compton scattering $\pi^-\gamma^* \rightarrow \pi^-\gamma$ occurs as the dominant sub process (from [KF09]). This Primakoff reaction was firstly measured at Serpukov using a 40 GeV pion beam [Ant83] and [Ant85].

The measured quantities in Primakoff scattering are the following four-momentum vectors:

$$(7.3) \quad p^\mu = (E, \vec{p}) \quad \text{beam pion,}$$

$$(7.4) \quad p_\pi^\mu = (E_\pi, \vec{p}_\pi) \quad \text{scattered pion,}$$

$$(7.5) \quad p_\gamma^\mu = (E_\gamma, \vec{p}_\gamma) \quad \text{emitted photon.}$$

The Lorentz-invariant Mandelstam variables of the pion-photon sub-system, $\pi^-\gamma^* \rightarrow$

$\pi^- \gamma$ are

$$(7.6) \quad s = (p_\pi^\mu + p_\gamma^\mu)^2 \quad \text{and} \quad t = (p^\mu - p_\pi^\mu)^2.$$

For all Mandelstam variables, an expression can be found which depends only on measurable quantities of the experiment. An exhaustive discussion in the description of the kinematics is given in [Fri10]. The kinematics of the Primakoff Compton scattering process requires a minimum momentum transfer Q_{\min} to the nucleus in the laboratory frame which is given to good approximation by

$$(7.7) \quad Q_{\min} = \frac{s - m_\pi^2}{2p}$$

with $p = |\vec{p}|$ the beam momentum. In the centre-of-momentum frame, see Fig. 7.2, the scattering angle θ_{cm} is given in terms of the Mandelstam variables in the approximation of small Q^2 , valid in the range of interest here,

$$(7.8) \quad \cos \theta_{\text{cm}} = 1 + \frac{2st}{(s - m_\pi^2)^2}.$$

This is a consequence of expressing the photon energy p_γ in the same approximation [Fri10] as

$$(7.9) \quad p_\gamma \approx p \frac{-t}{s - m_\pi^2},$$

since the laboratory photon energy is, for larger s (cf. Fig. 7.4), a measure of the scattering angle θ_{cm} .

To the level of precision needed in the following, the differential cross section of the Primakoff Compton scattering can be described by the equivalent photon approximation, which relates Primakoff Compton scattering to real Compton scattering in the following way

$$(7.10) \quad \frac{d\sigma}{ds dt dQ^2} = \frac{\alpha}{\pi(s - m_\pi^2)} \cdot F_Z^2(Q^2) \cdot \frac{Q^2 - Q_{\min}^2}{Q^4} \cdot \frac{d\sigma_{\pi\gamma}}{dt}$$

$d\sigma_{\pi\gamma}/dt$ determined by eq. (7.8) and eq. (7.2). In addition the electromagnetic form factor $F_Z(Q^2)$ is the charge form factor of the heavy nucleus as well as the Mandelstam variables s and t refer to the $\pi\gamma$ -system, as noted above. Due to the small momentum transfer of $Q \approx 0$, the form factor can be approximated by $F_Z(Q^2) \approx Z$ [KF08a].

7.2 Effect of Pion Polarisabilities

In order to extract the cross section of the pion polarisabilities from the pion-nucleus bremsstrahlung $\pi^- Z \rightarrow \pi^- Z \gamma$, the subprocess of virtual pion Compton scattering

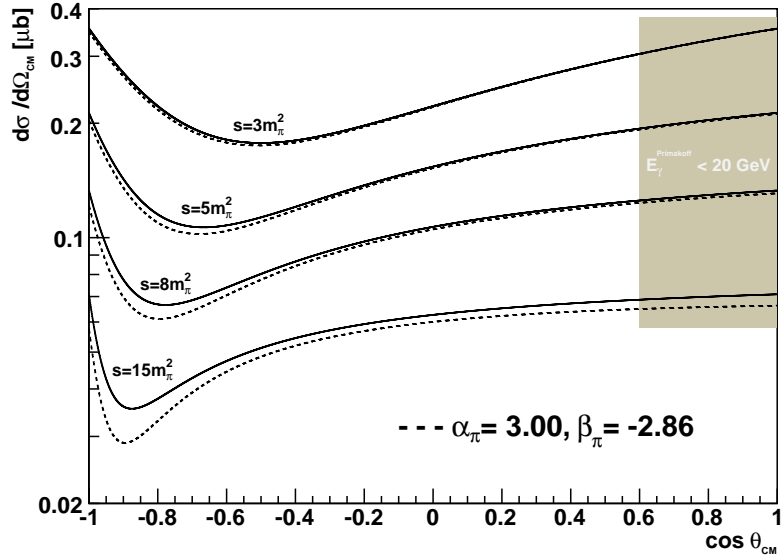


Figure 7.3: Angular dependence of the differential cross section for charged Compton scattering in the centre-of-mass system. The dashed curves are the predictions of the chiral perturbation theory with polarisabilities, $(\alpha_\pi = 3.0, \beta_\pi = -2.86) \cdot 10^{-4} \text{ fm}^3$, the full curves represent the point-like case. The region of the cross section belonging to scattered photon energies $< 20 \text{ GeV}$ is highlighted in grey [Fri10].

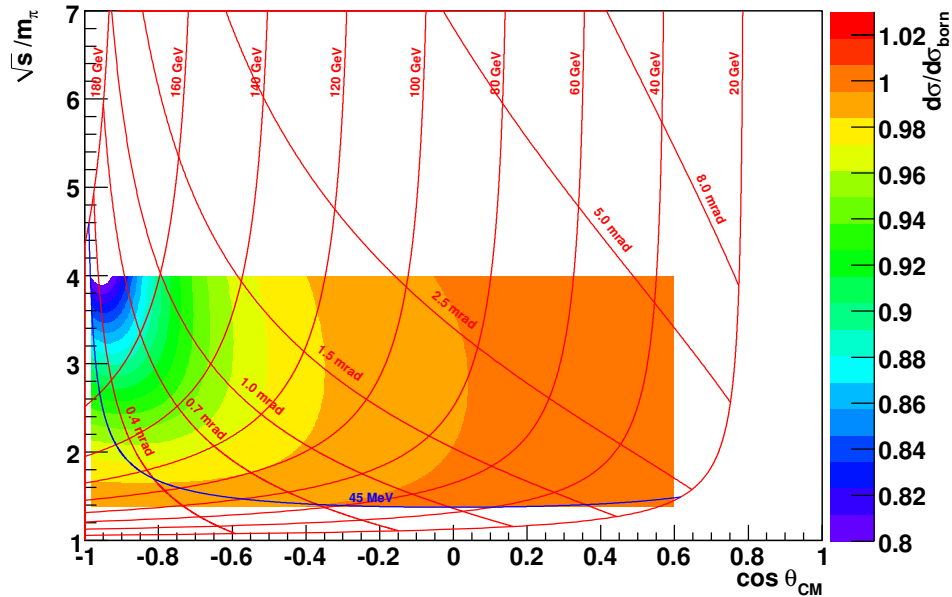


Figure 7.4: The relative effect of polarisabilities (ChPT values) on the pion Compton scattering cross section is visualised by the colour code. The experimentally motivated cut on $p_{\pi\perp} > 45 \text{ MeV}/c$ is marked in blue which suppresses multiple scattering effects, see 8.1. The energy and the production angle of the scattered photon in the laboratory frame is displayed by the red grid [Fri10].

$\pi^- \gamma^* \rightarrow \pi^- \gamma$ (in the Coulomb peak) has to be isolated from the strong interacting background. The signature of those reactions are very small momentum transfers to the nucleus $Q \rightarrow 0$ which can be treated as the limit in real pion Compton scattering $\pi^- \gamma \rightarrow \pi^- \gamma$. The measured deviations of the cross sections from that of a point-like particle is attributed to the low-energy structure of the pion as characterised by its electric and magnetic polarisabilities α_π and β_π .

Fig. 7.3 visualises the effect of the electric and magnetic pion polarisabilities in the angular dependence $\cos \theta_{\text{cm}} = z$ of the differential cross section $d\sigma/d\Omega_{\text{cm}}$ for the Compton scattering in the centre-of-mass frame. The differential cross sections are calculated for four different centre-of-mass energies, $s = (3, 5, 8, 15) m_\pi^2$. The dashed curves show the cross section calculated with assumed polarisabilities ($\alpha_\pi = 3.0 \cdot 10^{-4} \text{ fm}^3$, $\beta_\pi = -2.86 \cdot 10^{-4} \text{ fm}^3$), whereas the full curves represent only the Born approximation for a point-like spin-0 particle. This figure demonstrates, that the effect of the polarisabilities is significant particularly in backward direction in the centre-of-mass system. However, there the Compton cross section is rather small. This means, the low-energy structure of the pion as represented by the polarisabilities α_π and β_π has only a small effect on the angular dependence of the differential cross section and a measurement has therefore to be performed with high accuracy.

Fig. 7.4 shows the cross section of pion Compton scattering as a function of the centre-of-mass energy \sqrt{s} and the scattering angle θ_{cm} . The effect of the pion polarisability is visualised by the ratio $d\sigma/d\sigma_{\text{born}}$ of the differential cross sections $d\sigma$ including the pion polarisabilities and $d\sigma_{\text{born}}$ the point-like pion. With increasing centre-of-mass energies \sqrt{s} the effect of the polarisabilities increases, and for $\sqrt{s} = 4 m_\pi$ it reduces the backward cross section by about 20%. The relations to the scattered photon kinematics is shown in Fig. 7.4 showing that the physically interesting region includes photons in the energy range 20 GeV - 180 GeV and scattering angles in the laboratory up to 8 mrad with respect to the incoming beam pion direction. At higher centre-of-mass energies the pion Compton scattering is accompanied by the excitation of the broad $\rho(770)$ -resonance ($m_\rho \simeq 5.5 m_\pi$) not included by the calculation, which is the reason why higher centre-of-mass energies are not considered.

7.3 Radiative Corrections

Since the measurable effect of the pion polarisabilities is small, it is necessary to estimate the size of other processes like radiative corrections to the cross section. The papers [KF09], [KF08a] and [KF08b] cover this topic. The authors have calculated all contributions of one-photon loop diagrams for radiative corrections to pion-nucleus bremsstrahlung $\pi^- Z \rightarrow \pi^- Z \gamma$ for small momentum transfer, where the sub-process of quasi-real Compton scattering $\pi^- \gamma^{(*)} \rightarrow \pi^- \gamma$ dominates.

Chapter 8

Data Analysis

8.1 Event Selection

The events of the exclusive reaction $\pi^- + \text{Pb} \rightarrow \pi^{-'} + \text{Pb} + \gamma$ of Primakoff Compton scattering (see chapter 7) have to be extracted from the data sample. The experimental setup including the trigger specifications is described in subsection 2.2.4. The following analysis is performed with PHAST.7.062 and ROOT_v5.20.00. All events are accepted for which at least one of the two Primakoff triggers has fired, see 2.2.4.3. Several selection criteria are worked out and discussed in the following.

Track selection: An event is only accepted if there is one primary vertex with one single outgoing track. This track has to have negative charge. The first measured position of the track must lie downstream of the target. It turned out that background is sufficiently suppressed if a track leaves 10 hits in the silicon telescope downstream of the target. Events are not further analysed in case the track energy is above 180 GeV. This reduces background due to non interacting beam particles. In order to identify the scattered π^- , its track has to end upstream of the muon wall and pass the magnet SM1 to guarantee a momentum measurement. If an additional track is found which may falsely not be attached to the primary vertex, then this event is rejected. A track segment is considered as additional track, if it has a momentum assigned or 10 hits in the silicon telescope.

Vertex selection: The target disks¹ were positioned at $Z = -309.5$ cm for the single lead target and at -304.6 cm and -314.5 cm, respectively, for the segmented target. Since the disk has a radius of 1.5 cm, the XY-plane of the primary vertex should lie within the radius of 1.4 cm. Fig. 8.1 shows the z-position of the primary vertex as a function of the pion scattering angle for the data set of the 3 mm Pb-target. The target can clearly be identified, but interactions are also seen in the multiplicity counters at -250 cm and -410 cm. The multiplicity counter in front of the target was removed within the beam time, see Table B.1 on page 165 for details. Events at -200 cm result from interactions in the silicon detector station SI03. The cuts on the primary vertex are motivated empirically by

¹see Table 2.2 on page 13 for target materials and their dimensions and section B.1 for hadron run history.

Fig. 8.1 and the vertex resolution, since for smaller scattering angles the vertex resolution deteriorates. For Primakoff candidates, the primary vertex should lie in the interval $\Delta z = \pm 4$ cm within the physical target for scattering angles (> 1 mrad) and in $\Delta z = \pm 30$ cm around the target for smaller scattering angles ($0.2 \text{ mrad} < \theta < 1 \text{ mrad}$). In case of the segmented target, this cut is adapted accordingly. The resolution of the primary vertex in the target as a function of the scattering angle of the pion is shown in Fig. 8.2. In a further analysis, the vertex cut should be adapted according to a mathematically better described vertex resolution.

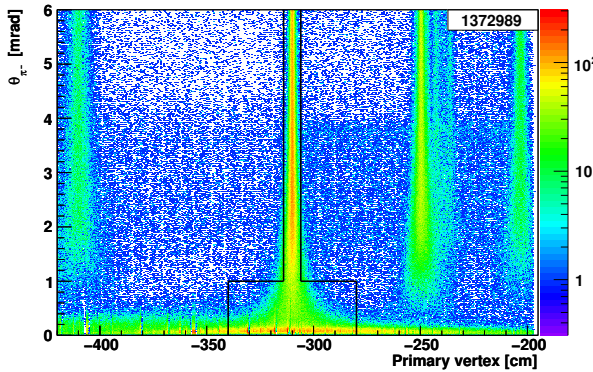


Figure 8.1: Distribution of the primary vertex as function of the pion scattering angle for the 3 mm Pb-target.

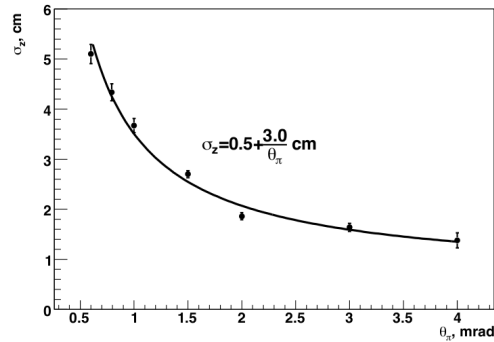


Figure 8.2: Primary vertex resolution in the target as a function of the pion scattering angle, from [Gus10].

Photon selection:

Clusters in ECAL2 are ignored if they can be associated with the scattered pion, since there is a probability for pions to interact in ECAL2 and initialise a shower above 7 GeV. If a pion track extrapolated to ECAL2 and a corresponding cluster lie within a radius of 5 cm, this cluster is rejected as photon candidate.

If more than one cluster per event in ECAL2 remain as possible photon candidates then this event is discarded.

Muon rejection:

The π^- -beam is contaminated with muons up to 3%, see Table 2.1 on page 12. The reaction $\mu + \text{Pb} \rightarrow \mu' + \text{Pb} + \gamma$ could lead to a similar event signature. Such events have to be rejected. Therefore the PHAST function for particle identification is used as selection criteria, using the information from the muon walls and the trigger system.

Multiple scattering and electron rejection:

The vertex resolution decreases for very small scattering angles and interactions, e.g the multiplicity counter and Pb-target can not be resolved, see Fig. 8.1. This necessitates a cut on the minimum scattering angle θ_{π^-} of the pion. This angle has to be significantly larger than the mean multiple scattering in the target. The radiation length of the 3 mm lead target is $0.5X_0$ and the mean multiple Coulomb scattering angle is in the order of

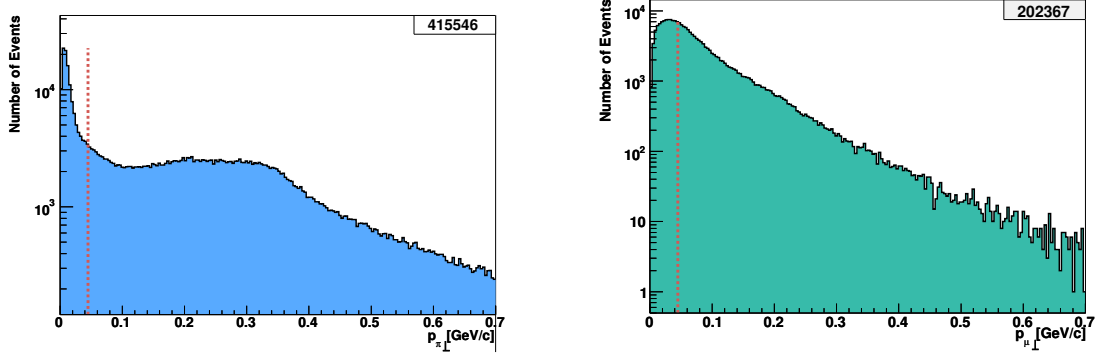


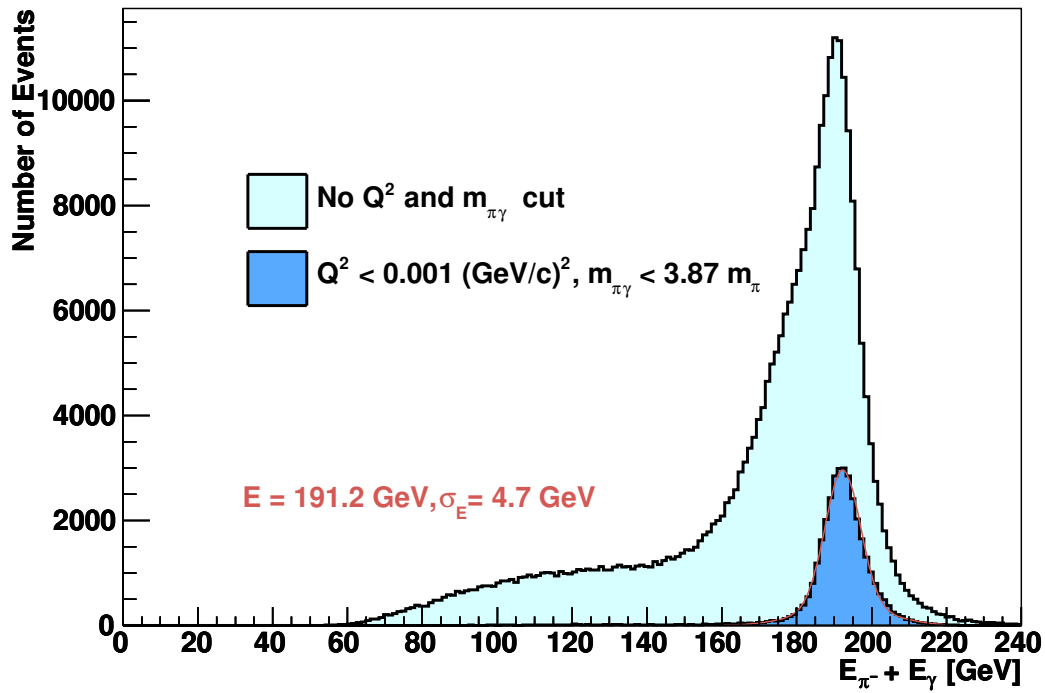
Figure 8.3: p_{\perp} -distribution without the Primakoff selection cuts for the pion Pb-target period (left) and muon period (right). The red dashed line marks the specific cut on p_{\perp} .

Primakoff Selection Cuts	
p_{\perp} -cut	$p_{\perp} > 45 \text{ MeV}/c$
Minimum photon energy	$E_{\gamma} > 40 \text{ GeV}$
Exclusivity cut	$ E_{\gamma} + E_{\pi} - 190 < 15 \text{ GeV}$
Low mass region	$m_{\pi\gamma} < 3.87 m_{\pi}$
Low Q^2	$< 0.001 (\text{GeV}/c)^2$

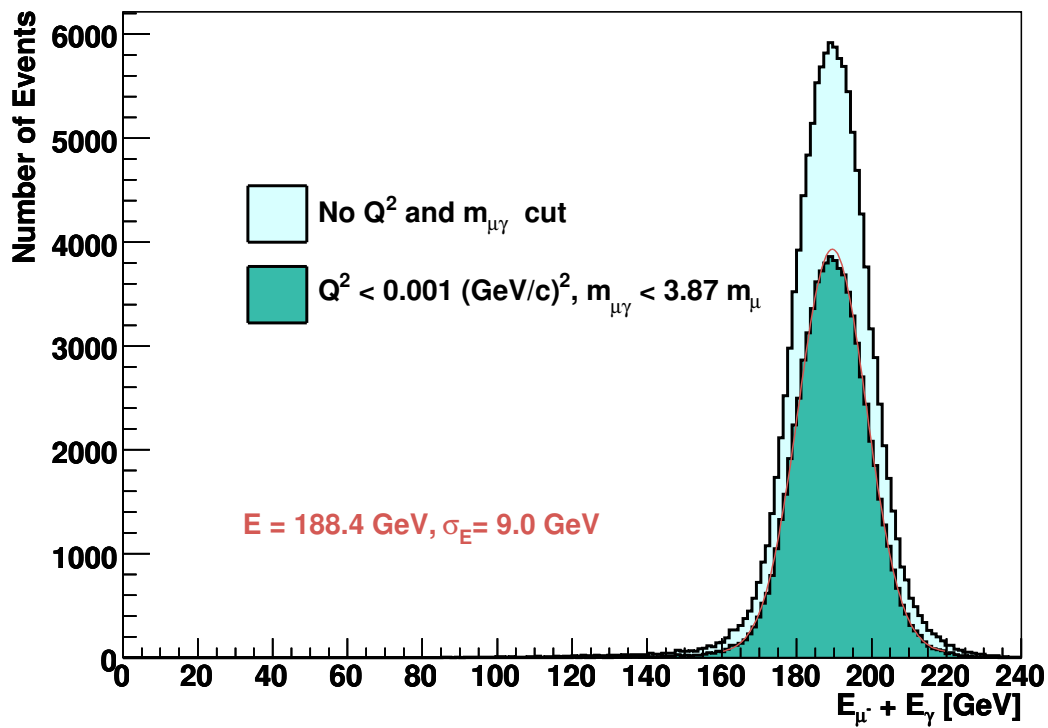
Table 8.1: Primakoff selection cuts.

$\theta_0 = 0.05 \text{ mrad}$, see Table 2.2 on page 13. This corresponds to a minimum transverse pion momentum $p_{\perp} > 15 \text{ MeV}/c$. Fig. 8.3 shows the distribution of p_{\perp} with the selection criteria as described above for the 3 mm Pb-target period. The effect of multiple scattering is significantly suppressed with $p_{\perp} > 45 \text{ MeV}/c$. This is an efficient cut to reduce also background from $e^{-} + \text{Pb} \rightarrow e^{-'} + \text{Pb} + \gamma$, since the beam also contains electrons besides the pions. Due to their small mass, electrons radiate with much higher cross section.

Primakoff selection cuts: The reconstructed beam energy E_B is equal to be the sum of the scattered pion and photon, $E_{\pi'} + E_{\gamma}$. Since in the Primakoff reactions the energy transfer to the nucleus is negligible. The nominal beam energy E_B^0 is 190 GeV. The distribution of E_B , displayed in Fig. 8.4, is a measure of the exclusivity of the Primakoff reaction. The light blue distribution shows the reconstructed beam energy E_B with all cuts as described above. The dark blue distribution also includes a cut on the $\pi\gamma$ -invariant mass of $< 3.87 m_{\pi}$ and on the momentum transfer squared $Q^2 < 0.001 (\text{GeV}/c)^2$. This dark blue exclusivity peak in E_B has a width of $\sigma_{E_B} = 4.7 \text{ GeV}$ and is limited by the energy resolution of ECAL2. All events with the E_B in the range of $|E_B - E_B^0| < 15 \text{ GeV}$ are accepted as Primakoff candidates. The kinematic distributions of these Primakoff candidates are displayed in Fig. 8.5.



(a)



(b)

Figure 8.4: Total energy distribution E_B of the $\pi\gamma$ -system (a) and $\mu\gamma$ -system (b).

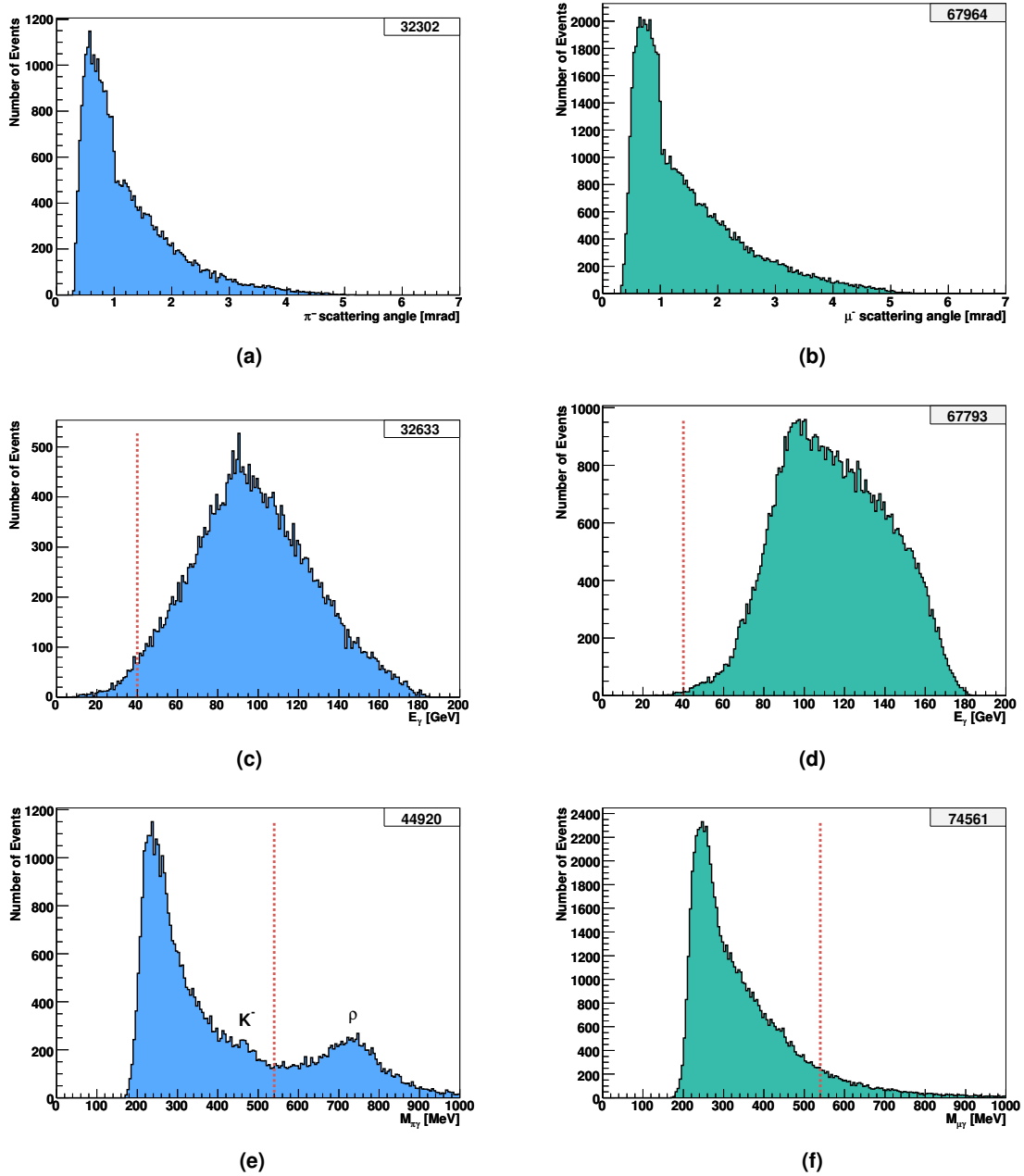


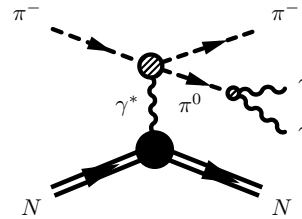
Figure 8.5: Kinematic distributions for the pion 3 mm Pb-target period (left) and muon period (right). Angle of scattered π/μ in (a, b), energy distribution E_γ in (c, d), and invariant mass spectrum of the $\pi\gamma$ - and $\mu\gamma$ -system in (e, f). For each distribution, the complete cut set of Table 8.1 has been applied, except on the quantity shown. (Muon data are scaled to the pion mass).

8.2 Background Reactions

The sample of extracted events, supposed to stem exclusively from the Primakoff Compton scattering $\pi^- + \text{Pb} \rightarrow \pi^- + \text{Pb} + \gamma$ of Primakoff Compton scattering is contaminated by different background reactions. These background reactions lead to a similar event topology:

- The beam is contaminated by kaons, electrons and muons etc., see (Table 2.1), which could be mistaken as being an incoming pion. Electrons and muons are efficiently reduced by the cuts described above.
- Events from the diffractive process $\pi^- + \text{Pb} \xrightarrow{\text{"strong"}} \pi^- + \text{Pb} + \gamma$ are predominantly rejected by the Q^2 -cut. However, the interference of the Primakoff and diffractive amplitudes for $Q^2 < 0.001 (\text{GeV}/c)^2$ has to be theoretically understood [FT07]. An estimate for the size of this background can be obtained from comparison with μ -scattering data, since for muon Compton scattering a hadronic background does not appear.
- Several reactions contain in their final state a $\pi^0 \rightarrow \gamma\gamma$, and thus can mimic the $\pi^- \gamma$ topology, if one photon of the π^0 -decay is lost or two photons were falsely combined in one cluster in ECAL2:

- Primakoff diffractive production of a neutral π^0 :
 $\pi^- + \text{Pb} \rightarrow \text{Pb} + \pi^- + \pi^0$



- The $\rho(770)$ -resonance: $\pi^- + \text{Pb} \rightarrow \text{Pb} + \rho \rightarrow \text{Pb} + \pi^- + \pi^0$
- Hadronic decay of (beam)-kaons (BR $\sim 21\%$): $K^- \rightarrow \pi^- + \pi^0$
- Kaon scattering: $K^- + \text{Pb} \rightarrow K^*(892) + \text{Pb} \rightarrow \text{Pb} + K^- + \pi^0$

The invariant mass spectrum of the $\pi\gamma$ -system is displayed in Fig. 8.5 (e). The bump in the region of 770 MeV corresponds to the ρ -resonance. On account of this, the cut on the invariant $\pi\gamma$ -mass for the Primakoff Compton candidates is set to $< 3.87 m_\pi$. The hadronic decay of (beam)-kaons lead to a peak at 480 MeV. These peaks from the ρ and K are shifted towards smaller masses, since one (the softer) photon was possibly lost. The two high energetic photons which could not be resolved by the clustering process of ECAL2 lead to a different shower distribution in ECAL2 than a high energetic cluster of a single photon. The cluster refit presented in subsection 6.6.2 is sensitive to the shower distribution, see invariant mass distribution in Fig. 6.33, so a future application lies in enhancing the suppression of background from the double-clusters from π^0 decays.

8.3 Simulation and Acceptance

The Serpukov experiment measured the pion polarisabilities by the Primakoff Compton scattering for the first time [Ant83], [Ant85]. The pion polarisabilities were extracted in the Serpukov experiment by analysing the ratio R of the measured differential cross section $d\sigma/dx_\gamma$ for the pion and the differential cross section for a point-like pion under the assumption $\alpha_\pi + \beta_\pi = 0$. This ratio R can be approximated by [Ant86]

$$(8.1) \quad R(x_\gamma) = \frac{d\sigma(\beta \neq 0)}{d\sigma(\beta = 0)} \approx 1 - \frac{2}{3} \cdot \frac{m_\pi^3}{\alpha_{e.m.}} \cdot \frac{x_\gamma^2}{1 - x_\gamma} \cdot \beta_\pi$$

with $\alpha_{e.m.}$ being the fine structure constant, m_π the pion mass and x_γ defined as the relative energy of the emitted photon in the laboratory system

$$(8.2) \quad x_\gamma = E_\gamma/E_B.$$

In an experiment the cross section $d\sigma_{\text{observed}}$ is obtained from the number of Primakoff events N_{prim} in bins of x_γ , corrected by the acceptance $a(x_\gamma)$ and normalised to the flux. The acceptance function can be emulated by a Monte Carlo (MC) simulation using the Primakoff cross section for a point-like pion. The number of simulated events N_{MC} for point-like particles as a function of x_γ can be compared to the number of events observed N_{observed} and for $R(x_\gamma)$ as follows

$$(8.3) \quad R(x_\gamma) = \frac{d\sigma_{\text{observed}}/dx_\gamma}{d\sigma_{\text{point-like}}/dx_\gamma} = \frac{N_{\text{prim}}(x_\gamma)}{a(x_\gamma) \cdot \sigma_{\text{point-like}}/dx_\gamma} = \frac{N_{\text{observed}}(x_\gamma) - B(x_\gamma)}{N_{\text{MC}}(x_\gamma)}.$$

The observed events have to be corrected for the background $B(x_\gamma)$ which has to be subtracted. The factor $a(x_\gamma)$ multiplied by $d\sigma_{\text{point-like}}$ is exactly the number of events found in the Monte Carlo simulation in a particular bin of x_γ . The number of Primakoff events is obtained by subtracting the background $B(x_{\gamma_i})$ from the total number of events $N_{\text{observed}}(x_{\gamma_i})$ found in this bin i . Fig. 8.6 shows the $R(x_\gamma)$ -distribution obtained by the Serpukov experiment. The result of a fit using the equation (8.1) to the data is $\alpha_\pi = (6.8 \pm 1.4 \pm 1.2) \cdot 10^{-4} \text{ fm}^3$.

In COMPASS Monte Carlo studies were performed in preparation of the measurement of the pion polarisabilities with a schematic approximation of the spectrometer [Kuh01], [Col05]. The true conditions of the measurement of the pion polarisabilities in 2004 were included in COMgeant (see subsection 2.3.4) [Gus10]. The muon Compton scattering on Pb-target was performed as a control measurement, in order to compare the simulated cross sections with point-like pions and study systematic effects. Therefore, the same analysis done for the pions was performed on the muon data, see Fig. 8.3 to 8.5. The acceptance function $a(x_\gamma)$ determined for pion and muon Compton scattering, respectively, follows a similar shape, see Fig. 8.7 [Gus10]. This indicates that the acceptance of the spectrometer is understood along general lines. However, Fig. 8.8 displays the cluster position of the emitted photons of the Primakoff reaction at ECAL2. A ring-like shadow

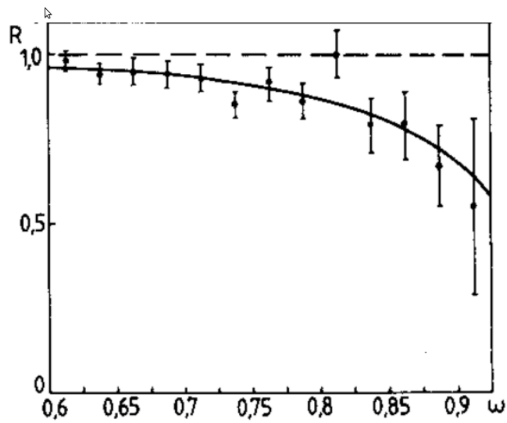


Figure 8.6: $R(x_\gamma)$ obtained by the Serpukov experiment with $\alpha_\pi = (6.8 \pm 1.4 \pm 1.2) \cdot 10^{-4} \text{ fm}^3$ under the assumption $\alpha_\pi + \beta_\pi = 0$.

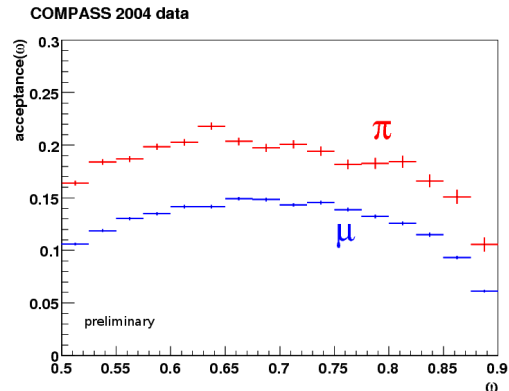


Figure 8.7: Acceptance function $a(x_\gamma)$ for 2 + 1 mm Pb-target, from [Gus10].

as well as missing events in a row of ECAL2 cells can be seen. The origin of these effects (He-gas pipe in the RICH and a trigger inefficiency) is discussed in the next subsections as well as their impact to Primakoff events and the Monte Carlo description .

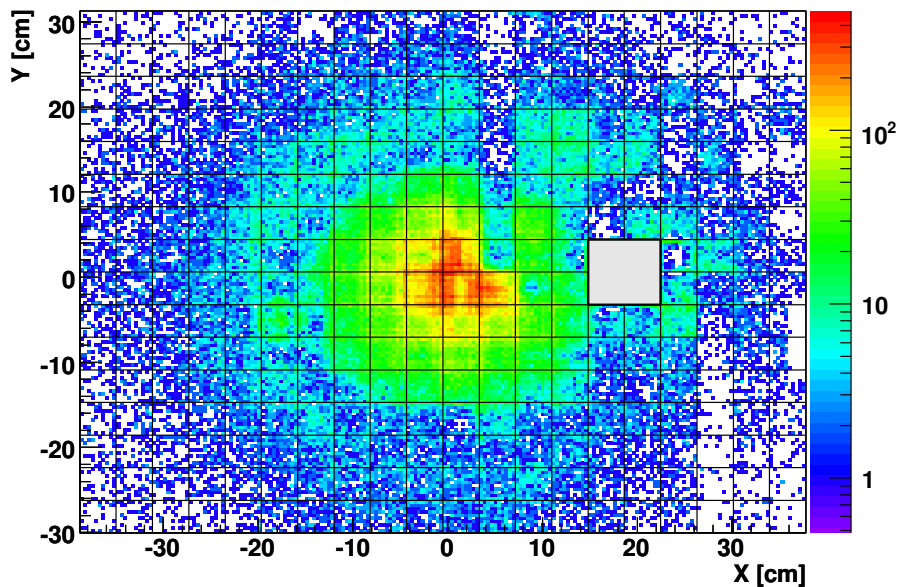


Figure 8.8: Cluster position of photons at ECAL2 for Primakoff candidates (no Primakoff selection cuts). The effect of the He-gas pipe on Primakoff candidates is seen in the halo structure at $R \approx 17 \text{ cm}$. Missing events for $x \approx 5 \text{ cm}$ and $y > 3 \text{ cm}$ come from a inefficiency of the Primakoff trigger. The beam hole is shaded in grey at $x \sim 20 \text{ cm}$.

8.3.1 He-Gas Pipe of the RICH

In the Primakoff reaction, a photon is generated which may convert via pair production $\gamma \rightarrow e^+e^-$ to e^+e^- -pairs on its way to ECAL2. The probability scales with $\Delta X/X_0$ (thickness of the scattering medium in radiation length X_0) of the materials crossed on its path. The design goal of COMPASS is the minimisation of materials in terms of radiation length X_0 . Regions with high material budget can be made visible by analysing the position of conversion vertices creating positrons or electrons. Therefore, the data-set of ECAL2 calibration can be used since it consists of identified electrons with their conversion (secondary) vertices. Fig. 8.9 shows the distribution of the conversion vertices with an emerging electron (positron) versus the distance $R = \sqrt{x^2 + y^2}$ of the vertex xy -position as a function of the beam direction z . A cylindrical structure is observed in the region from $z = 620$ cm - 880 cm, the position of the RICH detector. This detector contains a He-gas pipe made of steel, shielding Cherenkov photons generated by the beam passing through the RICH. It has a cylindrical shape with a diameter of 10 cm, a wall thickness of 0.15 mm and a length of 314 cm. The gas pipe is filled with Helium to reduce beam interactions inside the RICH. The end-caps have a thickness of 0.1 mm. The position of the cylinder axis coincides with the axis of the undeflected beam [RIC]. A cross-section of the cylindrical structure is displayed in Fig. 8.10. For comparison, the xy -plane in the interval $|z - 400 \text{ cm}| < 100 \text{ cm}$ is shown in Fig. 8.11, where the interactions along the beam axis dominate. Events in the centre come from beam particles interacting with air. In Fig. 8.10, the cross-section of the gas pipe with a radius of 5 cm and centred about $\Delta x = 0.1$ cm and $\Delta y = -0.55$ cm off the beam axis can be seen. The distances R of the conversion vertices in Fig. 8.9 are corrected by this offset. In this gas pipe, photons convert into electron-positron pairs which are generated e.g. in the Primakoff reaction. The “missing” photons can be seen in Fig. 8.8 depicting the γ -impacts in ECAL2 as a ring-like shadow (halo). This enlarged shadow of the He-gas pipe, see Fig. 8.12, matches with photons coming from the target under an angle of 5 mrad up to 7 mrad.

Besides photons also pions interact crossing the He-gas pipe under different angles, see Fig. 8.12. The xy -plane at $z = 750$ cm of scattered pions is displayed in Fig. 8.13 (a) for Primakoff candidates (no Primakoff selection cut applied) with energies < 70 GeV. The red circles indicates the region of the RICH gas pipe. The $R = \sqrt{x^2 + y^2}$ distribution depicts a dip due to interactions of pions in the pipe at $R \approx 5$ cm (Fig. 8.13 (b)). This causes a loss of pions with small energies below 70 GeV. They reflect missing Primakoff events with photon energies > 110 GeV and small photon scattering angles. This effect is not seen for muons from the data with 2 + 1 mm Pb-target, see Fig. 8.13 (c, d).

These studies demonstrated that, falsely, aluminium instead of steel was used in the MC description for the He-gas pipe. A discussion about these effects on the measured Primakoff cross section is given in section 8.4.

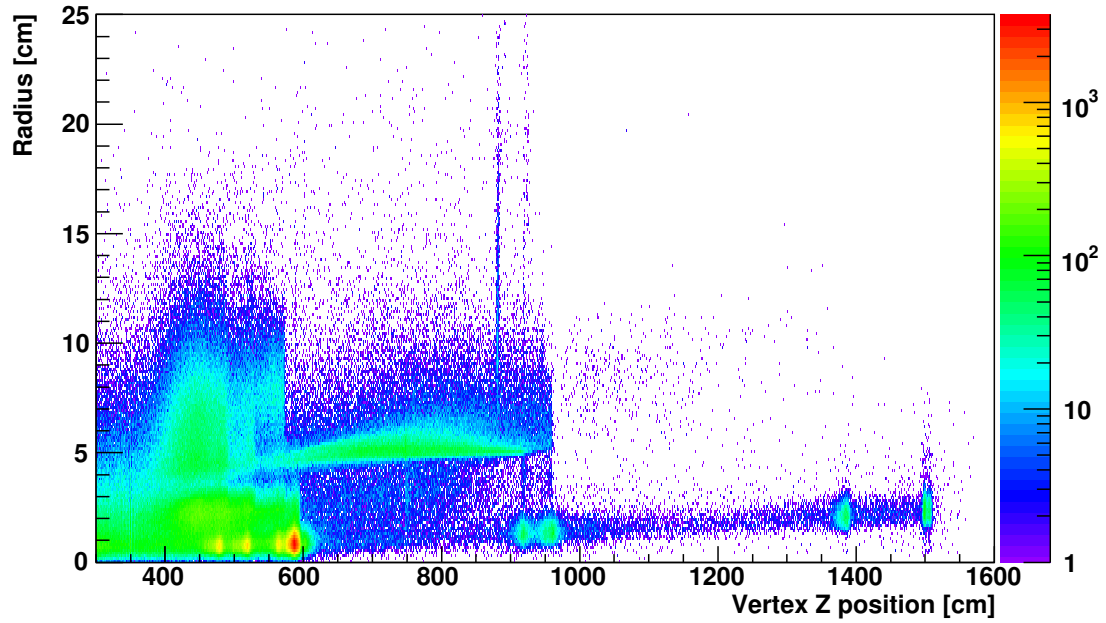


Figure 8.9: Secondary vertex distributions containing electrons (positrons) along the spectrometer as a function of the distance $R = \sqrt{x^2 + y^2}$ from the central axis in the xy -plane.

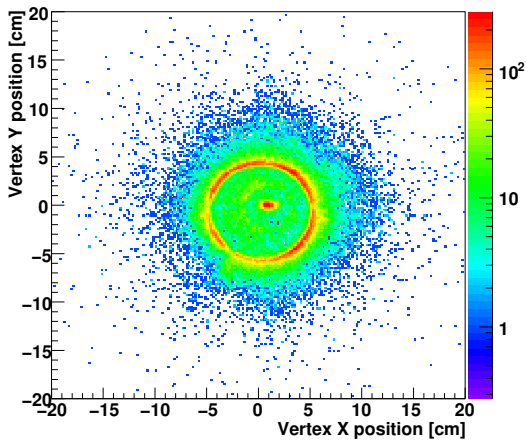


Figure 8.10: Secondary vertices in the xy -plane for the RICH region at $z = 750$ cm.

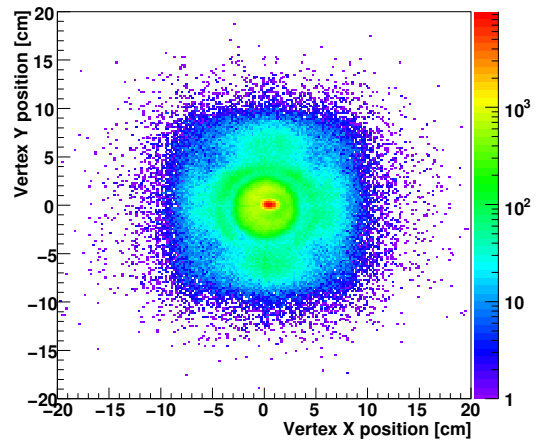


Figure 8.11: Secondary vertices in the xy -plane for the region in front of the RICH at $z = 470$ cm.

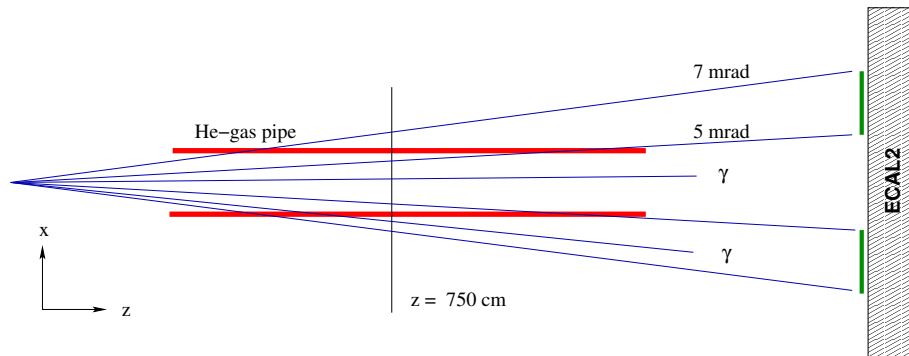


Figure 8.12: Sketch (not to scale) of particles like π and μ crossing the He-gas pipe of the RICH. The shadow of missing photons in ECAL2, see Fig. 8.8, is marked by the green bars.

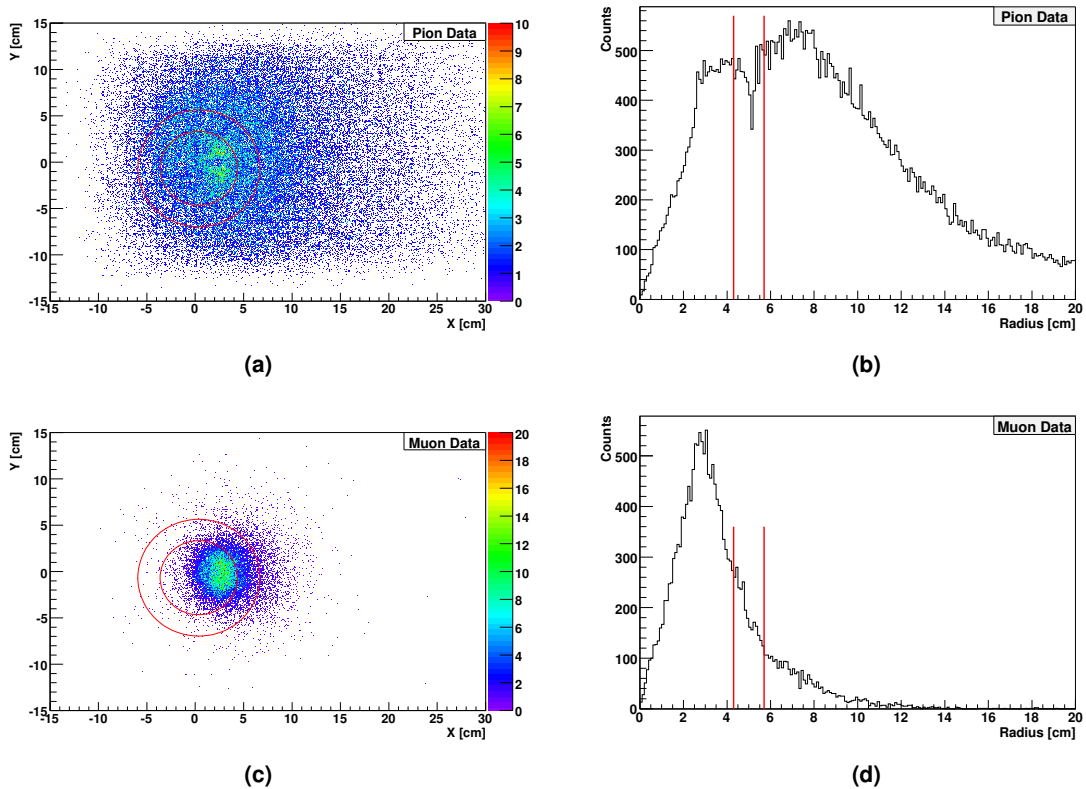
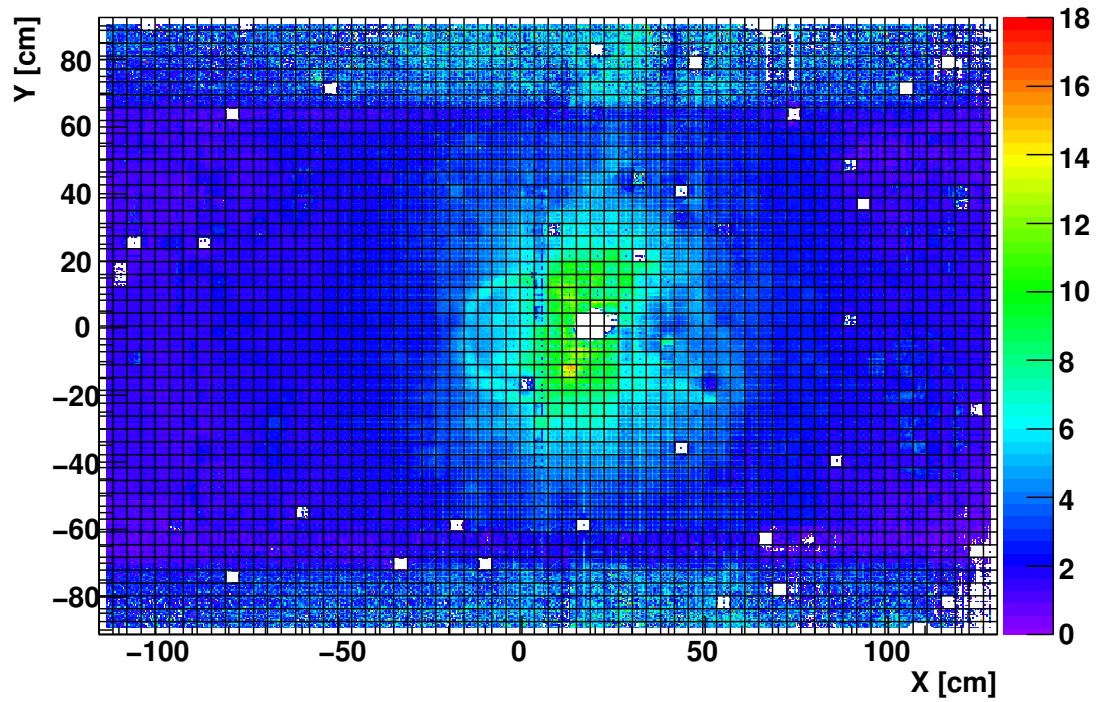
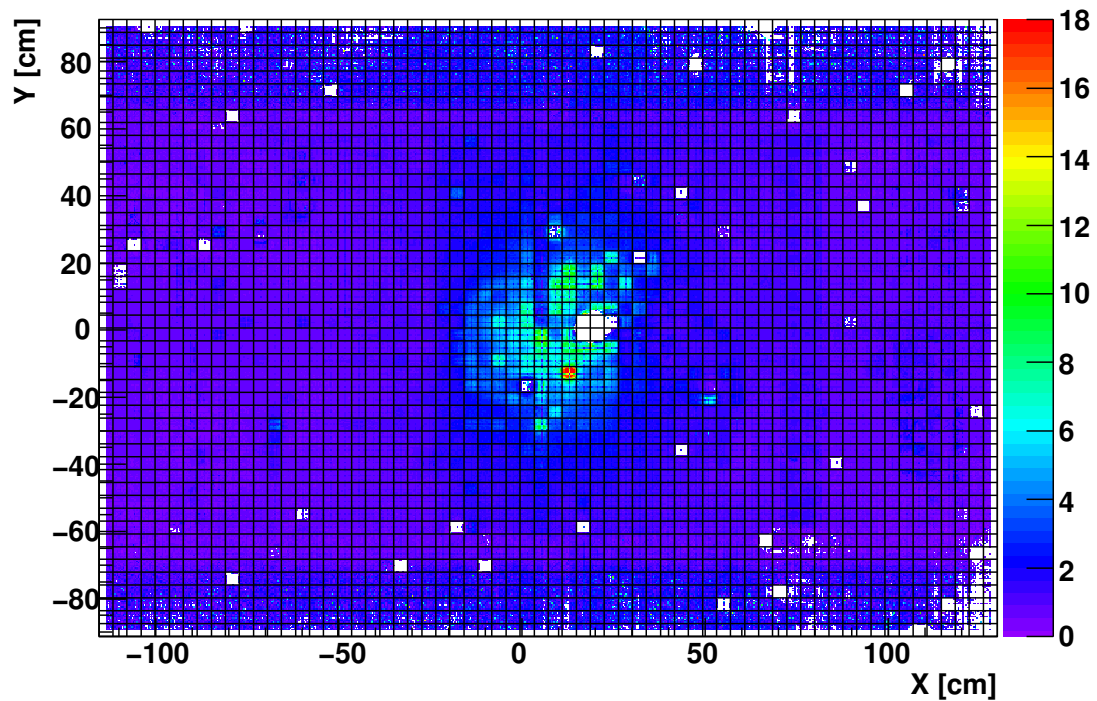


Figure 8.13: (a, c): xy -position of all particle tracks at $z=750$ cm (centre of the RICH and reconstructed also in SM2), in the upper row for pion data and lower row for muon data. The red circle indicates the position of the He-gas pipe of the RICH according to Fig. 8.12. (b, d): Distance $R = \sqrt{x^2 + y^2}$ from the beam centre in the xy -plane. In the pion case a dip at $R = 5$ cm can be seen which stems from pions lost due to secondary interactions in the pipe. No such dip is seen for the muon data (d).



(a)



(b)

Figure 8.14: ECAL2 response for Primakoff triggers normalised to the ECAL2 response for diffractive triggers, in (a) for PRIM1 and in (b) for PRIM2. In (b) the cells of column $x \approx 5$ cm and $y > 3$ cm were not included in the PRIM2 trigger, see 2.2.4.3 for trigger definition.

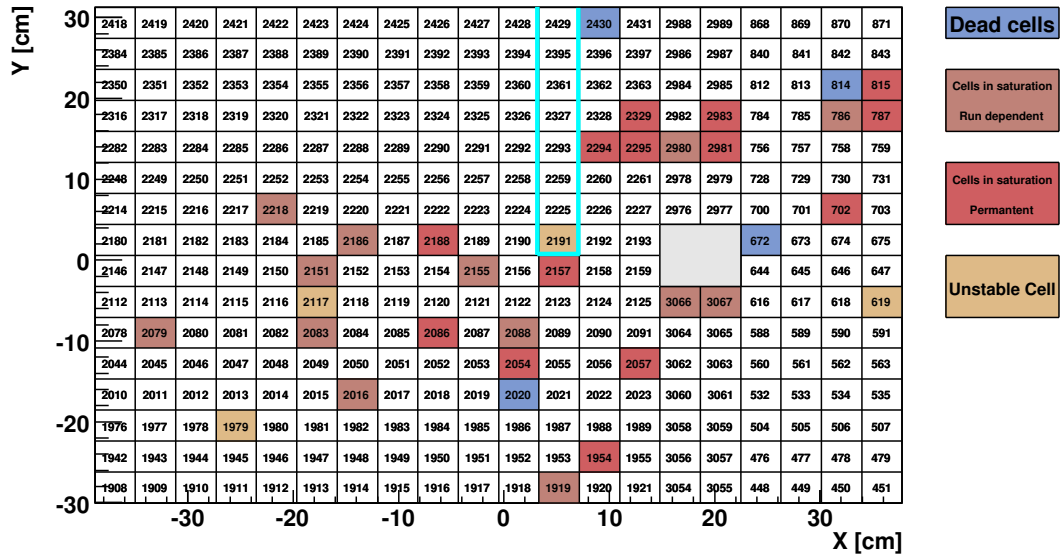


Figure 8.15: Cells of the central part of ECAL2, where the scattered photons of the Primakoff reaction hit the detector. The grey shaded region indicates the position of the hole. Coloured cells were in saturation or passive in hadron run 2004. The turquoise bordered region mark the cells erratically not connected to the PRIM2 trigger logic.

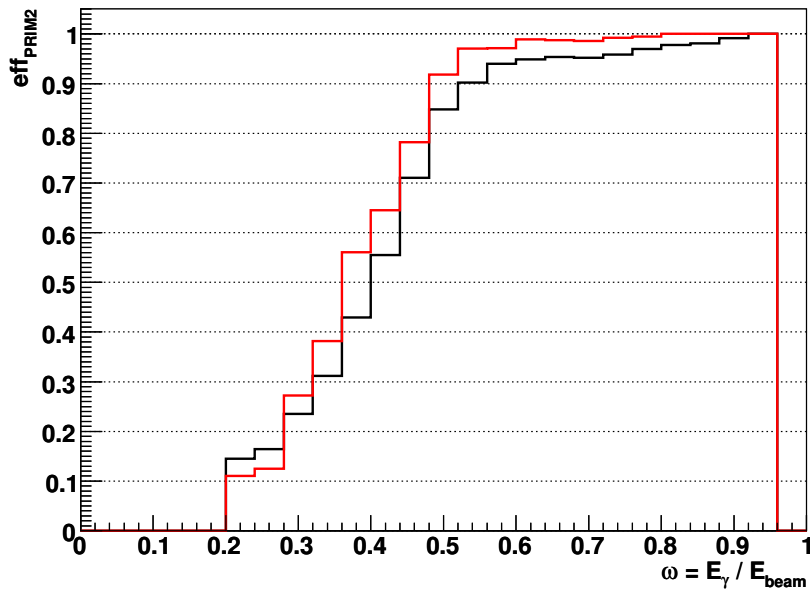


Figure 8.16: Efficiency of PRIM2 trigger using the events with PRIM1 trigger for data of the 2 + 1 mm Pb-target. Red histogram: Events with all Primakoff selection cuts applied. Black histogram: Primakoff candidates without the low mass cut and Q^2 cut.

8.3.2 Trigger Efficiency

Fig. 8.14 shows the ECAL2 response for the Primakoff triggers PRIM1 and PRIM2 normalised to the ECAL2 response for diffractive triggers (see 2.2.4.3 for trigger definition). Events of PRIM2 trigger are missing in the central region of ECAL2 (column $x \approx 5$ cm and $y > 3$ cm), see Fig. 8.8 and Fig. 8.14 (b). The PRIM2 trigger covers the region for high energy photons. The energy detection threshold for PRIM2 was set to 90 GeV for the summed energy deposited in ECAL2. Its cells 2191, 2225, 2259, 2293, 2327, 2361, 2395, 2429 ... at $x \approx 5$ cm (column number 31) were not connected to the PRIM2 trigger logic. This caused a loss of events in the interesting kinematic region. Fig. 8.15 summarises the performance of the ECAL2 cells in the central region. In particular, cell 2191, not connected to the trigger, was noisy and unstable, see Fig. 6.39.

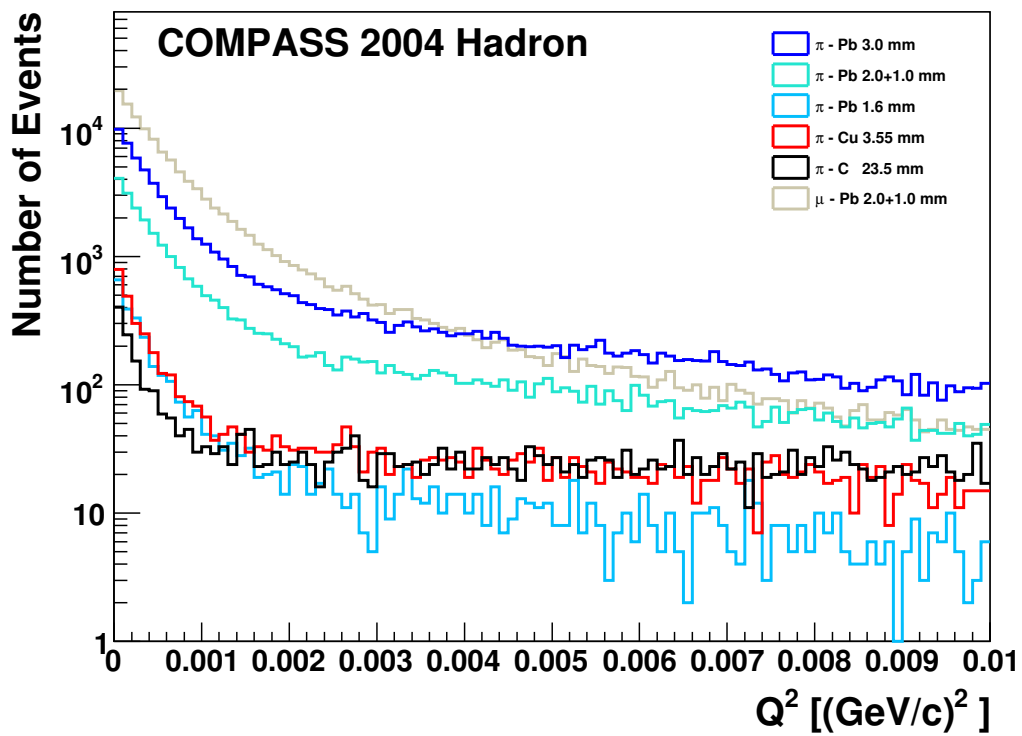
This inefficiency of the PRIM2 trigger causes sever difficulties to develop a realistic Monte Carlo description of the experiment for the Primakoff reaction. For this purpose, the response of ECAL2 for a shower of a high energy photon has to be known precisely. If a photon hits a cell not connected to the trigger, this event is only triggered by PRIM1, if the deposited energy of the neighbouring cells is larger than 40 GeV (PRIM1 trigger condition). Typically, the photon energy detected by the central cell carries about 60% to 70% of the photon energy (strongly depending on the impact position in the cell) and the remaining energy is distributed around the surrounding cells. Fig. 8.16 shows the efficiency of PRIM2 trigger under the assumption of a constant efficiency for PRIM1 trigger for Primakoff candidates of the 2 + 1 mm Pb-target:

$$(8.4) \quad \text{eff}_{\text{PRIM2}} = (\text{PRIM1} + \text{PRIM2})/\text{PRIM1}$$

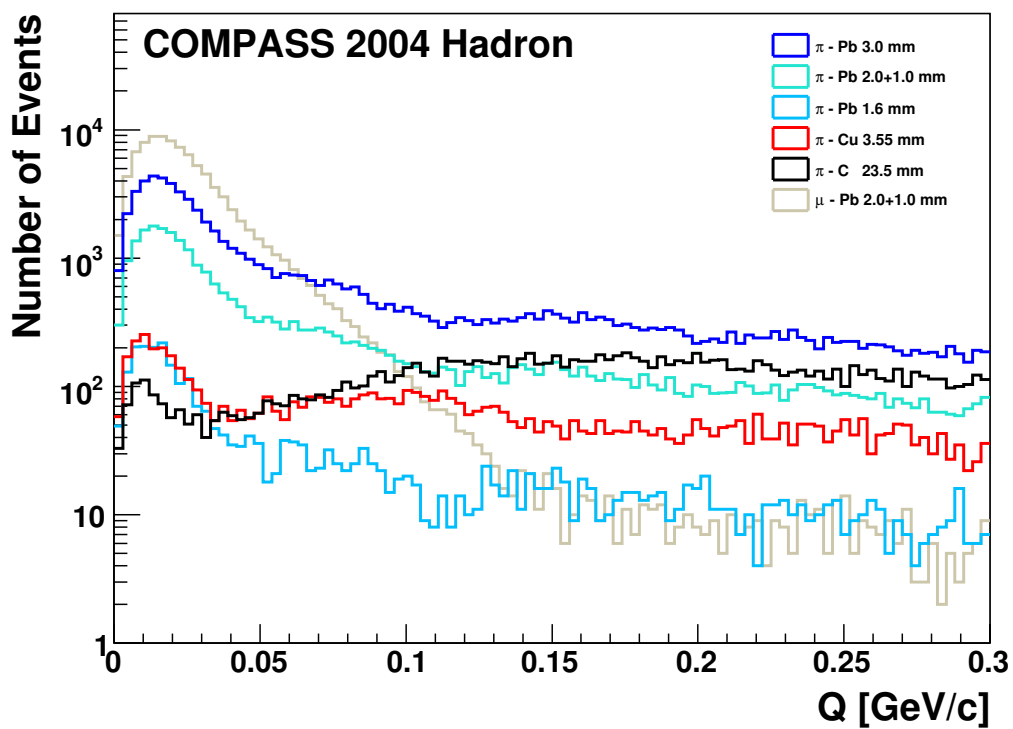
The remaining few percent uncertainty for $x_\gamma > 0.5$ would directly be misinterpreted as polarisability contribution, c.f. eq. (8.1).

8.4 Discussion

In 2004 COMPASS studied Primakoff reactions using a 190 GeV pion and muon beam impinging on solid Pb targets (3mm and 2 + 1 mm). In order to check the Z^2 dependence of the Primakoff cross section, see eq. (7.10), additional samples with Cu and C targets were collected. Fig. 8.17 (a) and (b) show their momentum transfers Q^2 - and Q , respectively, to the nucleus for Primakoff events. The majority of the Primakoff events are located in the steep rise for $Q^2 < 0.001$ (GeV/c)² (Primakoff peak), where the very small momentum transfers to the nucleus $Q \rightarrow 0$ can be treated as the limit in real pion Compton scattering $\pi^- \gamma \rightarrow \pi^- \gamma$, see section 7.2. For larger Q^2 -values the distributions turn more flat and are dominated by the diffractive background where Coulomb and nuclear amplitudes interfere. In Fig. 8.17 (b) the diffraction pattern for scattering on a Pb-target can be seen at higher Q -values. For muons scattering on Pb, the Q^2 - and Q distributions show the contributions of Primakoff Compton scattering only, since the



(a)



(b)

Figure 8.17: Q^2 and Q -distribution for different targets. The Primakoff peak at $Q \rightarrow 0$ can be clearly seen.

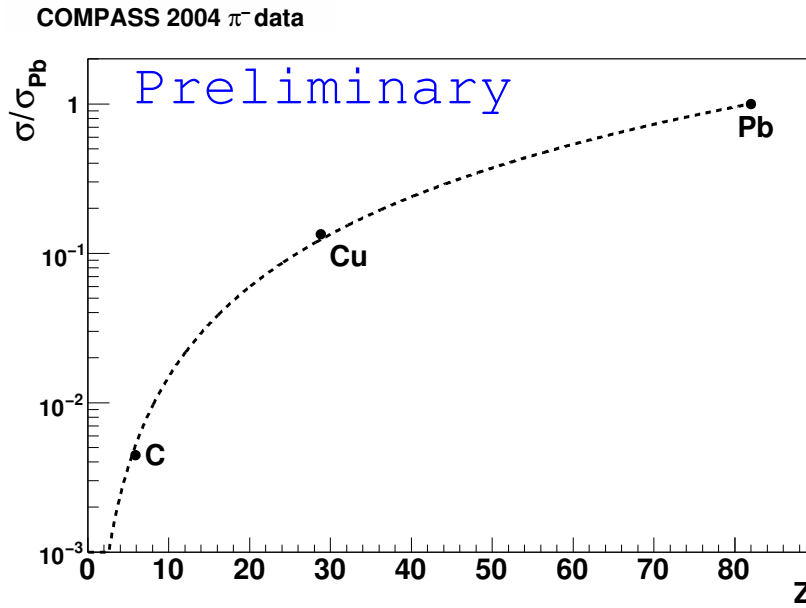
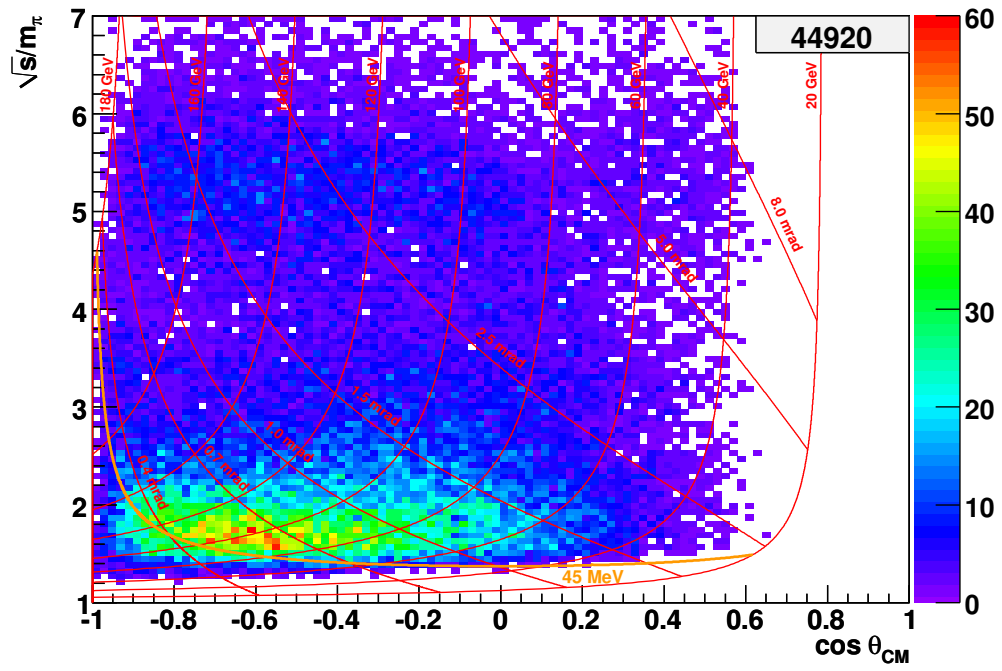


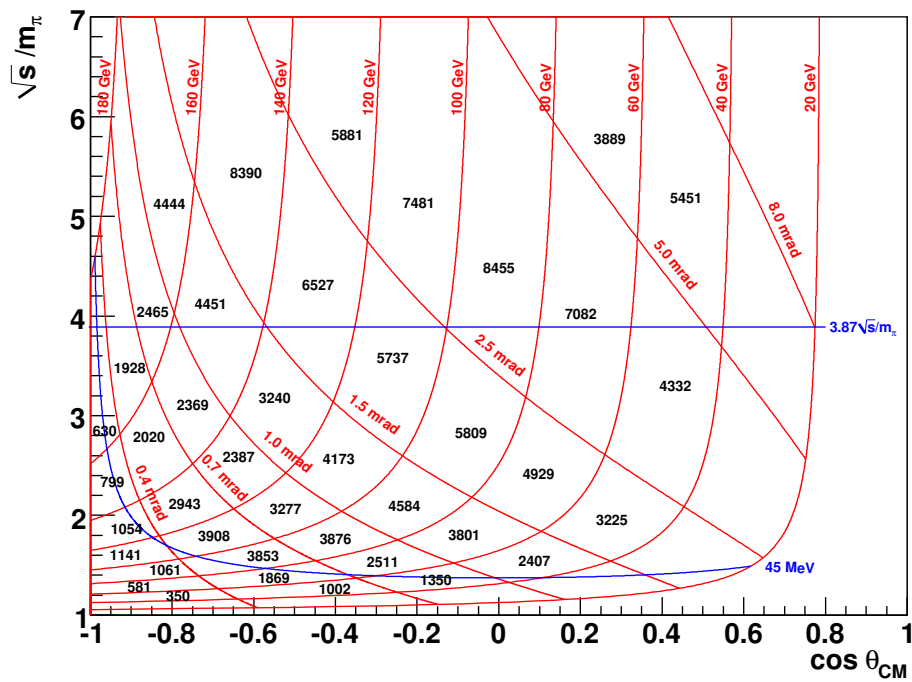
Figure 8.18: Z^2 dependence of the Primakoff cross section, from [Gus10].

muon does not interact strongly. Fig. 8.18 shows the Primakoff cross sections for different target materials normalised to the cross section for lead. It demonstrates that the Z^2 dependence of the Primakoff peak follows the theoretical prediction. This proves an effective selection of Primakoff reactions as exclusive $\pi\gamma$ -events identifying the Primakoff peak and the diffractive background in the Q^2 -distribution. The collected statistics of all Primakoff events (in the Primakoff peak) is about 45000 for the Pb targets and about 68000 for muons, see Table 6.5 and Table F.1. COMPASS collected about seven times more Primakoff events in 2004 compared to the Serpukov experiment with 6000 events [Ant83], [Ant85]. However, various detector uncertainties comprising geometrical constraints, performance problems of ECAL2, detector materials and an inefficient trigger as described above, introduce additional systematic uncertainties which do not allow to extract a reliable values for the pion polarisabilities from the 2004 data.

In the following, the measured Primakoff cross section for pions and muons are discussed as well as the impact of the He-gas pipe of the RICH and the trigger inefficiency on the Primakoff cross section. In the previous chapter, the effect of the pion polarisabilities by the ratio $d\sigma_{\text{pol}}/d\sigma_{\text{point-like}}$ (see Fig. 7.4) was introduced as a function of \sqrt{s}/m_π the centre-of-mass energy and $\cos\theta_{\text{cm}}$ the angle of the emitted photon. The relative effect of the pion polarisabilities increases with increasing \sqrt{s} and reduces the backward cross section (by about 20% for $\sqrt{s} = 4m_\pi$). The measured pion Compton cross section is shown in Fig. 8.19 (a) and the muon Compton cross section in Fig. 8.20 (a), both as a function of \sqrt{s}/m_π and $\cos\theta_{\text{cm}}$. The corresponding energies E_γ and angles θ_{lab} of the emitted photon in the laboratory frame are indicated by the red grid. For each cell of this grid the number of Primakoff events is determined, see Fig. 8.19 (b) and Fig. 8.20 (b). Experimentally, the main statistics is located at centre-of-mass energies $s = 1.8 m_\pi^2$ and at photon scattering

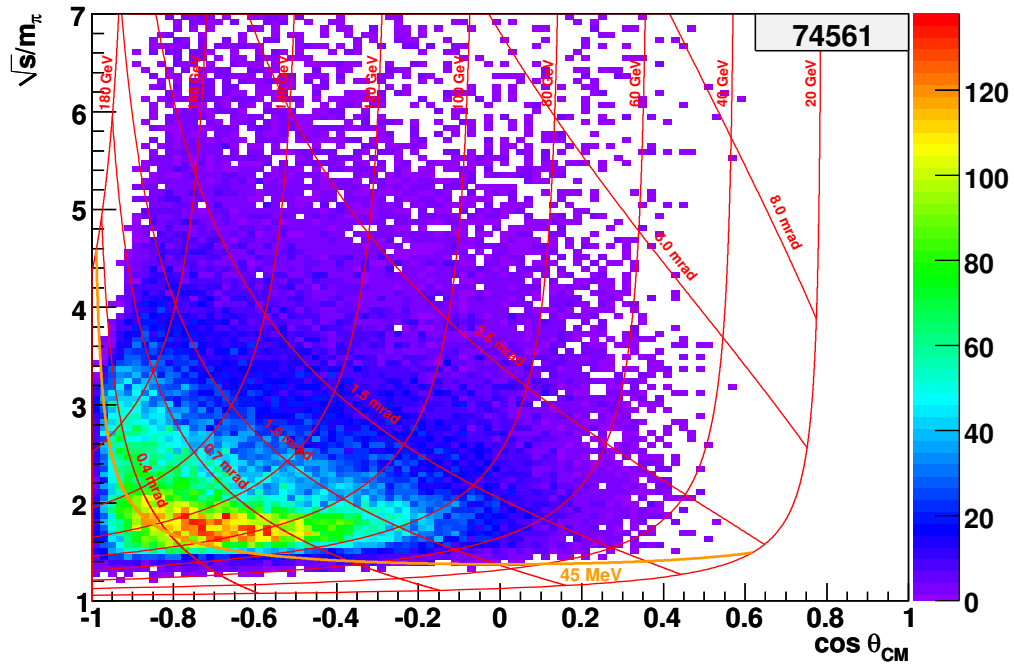


(a)

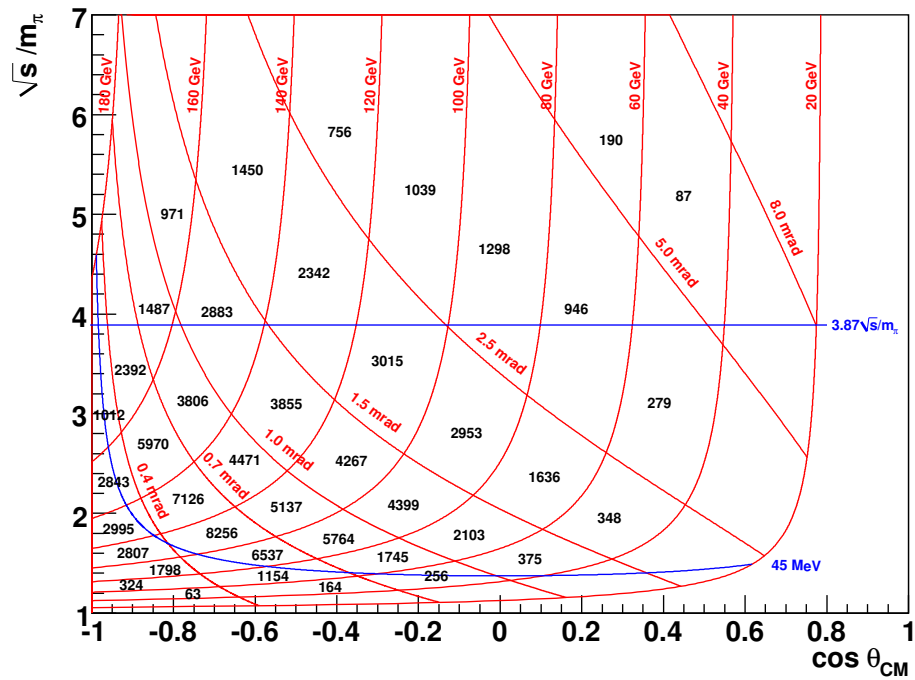


(b)

Figure 8.19: Pion Compton scattering cross section. The energy and the production angle of the scattered photon in the laboratory frame is displayed in the red grid, the cut on $p_{\perp} > 45$ in orange and of the $\pi\gamma$ -invariant mass in blue. The numbers are the events per cell of the red grid.



(a)



(b)

Figure 8.20: Muon Compton scattering cross section. The energy and the production angle of the scattered photon in the laboratory frame is displayed in the red grid, the cut on $p_{\perp} > 45$ in orange and of the $\pi\gamma$ -invariant mass in blue. The numbers are the events per cell of the red grid. (Muon data are scaled to the pion mass).

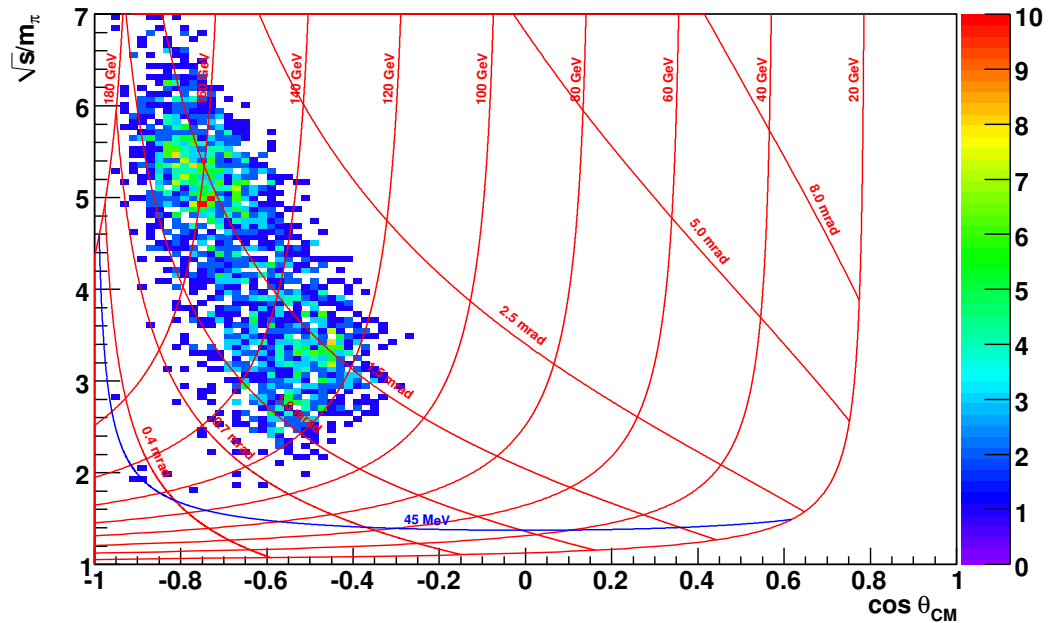


Figure 8.21: Primakoff events containing only pions passing the RICH pipe (events within the red circles of Fig. 8.13 and $E_\pi < 70$ GeV).

angles θ_{lab} from 0.3 mrad up to 1.5 mrad. In this region, the expected relative effect of the pion polarisability is in the order of 2% according to Fig. 7.4. For $\theta_{lab} < 1.2$ mrad and $E_\gamma > 140$ GeV (corresponding to $\sqrt{s}/m_\pi \approx 3.5$ and $\cos \theta_{cm} < -0.8$ in the centre-of-mass frame), the relative effect of the pion polarisabilities is maximal (10% up to 20%). However, in this most sensitive region also the cross section decreases as it is displayed in Fig. 7.3. This means also the number of collected Primakoff events decreases. Exactly in this region (at $\sqrt{s}/m_\pi \approx 3.5$) most sensitive to the pion polarisabilities, lies the kaon background. This background can be statistically subtracted, see discussion above. A future measurement of the pion polarisabilities should focus on a reliable identification of the beam particle. The contributions at $\sqrt{s}/m_\pi \approx 5.5$ in Fig. 8.19 (a) can be addressed to the π^0 s of the ρ -resonance. Since muons do not interact strongly the kaon background and the ρ -resonance are missing in Fig. 8.20 (a).

He-gas pipe of the RICH: As mentioned above, emitted photons (from the Primakoff reaction) with angles $\theta_{lab} > 5$ mrad may convert ($\gamma \rightarrow e^+e^-$) in the He-gas pipe of the RICH. These photons are missing in the measured cross section, but they lie not in the kinematical region relevant for the Primakoff analysis. Of eminent importance is the understanding of the scattered pions in this gas pipe, because it affects the Primakoff cross section in the backward scattering, where the cross section is small and the effect of the polarisabilities is about 10%. Fig. 8.21 shows Primakoff events of pions with $E_\pi < 70$ GeV (compared to $E_\gamma > 110$ GeV) passing the region of the gas pipe of the RICH (events within the red circles of Fig. 8.13). A Monte Carlo simulation has to describe this

part of the spectrometer very accurate, otherwise the missing pions would lead to a fake polarisation.

Trigger inefficiency: This affects the Primakoff cross section in a region most sensitive to the relative effect of the pion polarisabilities, namely for photon energies larger 90 GeV. A Monte Carlo description of the trigger would be based on a model of the response of ECAL2 for a shower of a high energy photon. Such a model would introduce a new systematic uncertainty directly to the pion polarisability measurement.

8.5 Conclusion

This work showed how Primakoff events are extracted from the data, and the available statistics for pion Compton scattering cross section is presented. However, geometrical constraints, performance problems of ECAL2, detector materials and an inefficient trigger lead to distortions of the differential $\pi\gamma$ count rates, from which α_π and β_π will have to be extracted.

- In the He-gas pipe of the RICH, potential Primakoff events are lost due to photon conversion which then are missing in the measured cross section. Also scattered pions interact with this pipe especially affecting pions with energies < 70 GeV. The effect addresses the region of the Compton cross section most sensitive to the pion polarisabilities. A precise Monte Carlo description of the experimental setup including a correct beam description is necessary.
- The event selection is contaminated by background reactions containing $\pi^0 \rightarrow \gamma\gamma$ which have the selected event signature if one low energetic photon is lost or the two photons are falsely combined to one cluster. The cluster refit method presented in subsection 6.6.2 showed a sensitivity to such events. The Monte Carlo simulation needs a realistic description of the calorimeter including these effects of the clustering in order to determine reliable results on the pion polarisabilities, which was not the case at the stage of this thesis. Very recently, the Monte Carlo description of ECAL2 is completely revised.
- For the determination of the pion polarisabilities, the trigger description has to be correctly implemented into the Monte Carlo simulation. For some calorimeter cells in the central part of ECAL2, the energy thresholds were erratically not connected to the trigger logic. They are geometrically located in the acceptance of the Primakoff events. Reproducing the behaviour of the trigger related to the calorimeter part is practically impossible.

In 2009 a new Primakoff measurement was performed which took more emphasise on the stability of the spectrometer. The measurement of the pion polarisabilities is an important ingredient for the understanding of QCD at low energies. For the clarification of the

presently inconsistent picture of the experimental results obtained so far, a full beam time will be dedicated to the measurement of the pion polarisabilities at COMPASS in 2012. This new measurement is also aiming for an independent determination of α_π and β_π on a new level of precision (measuring the deviation of the polarisability sum $(\alpha + \beta)_\pi$ from zero) [COM10].

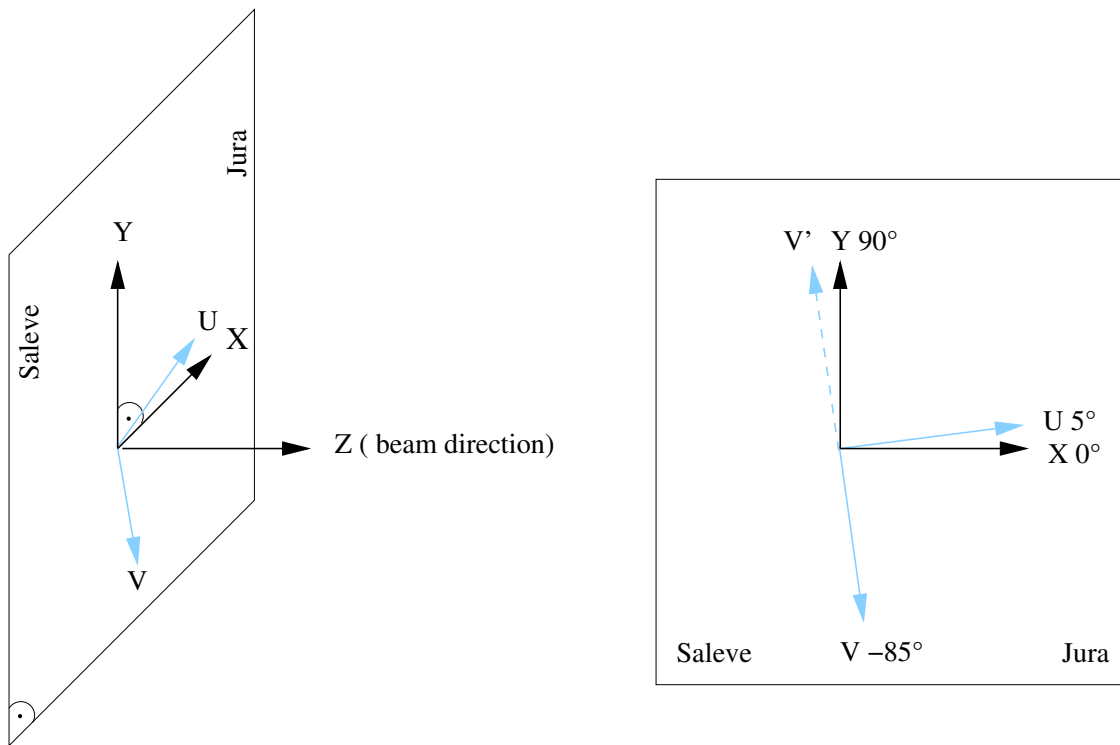
Appendix A

Coordinate Systems

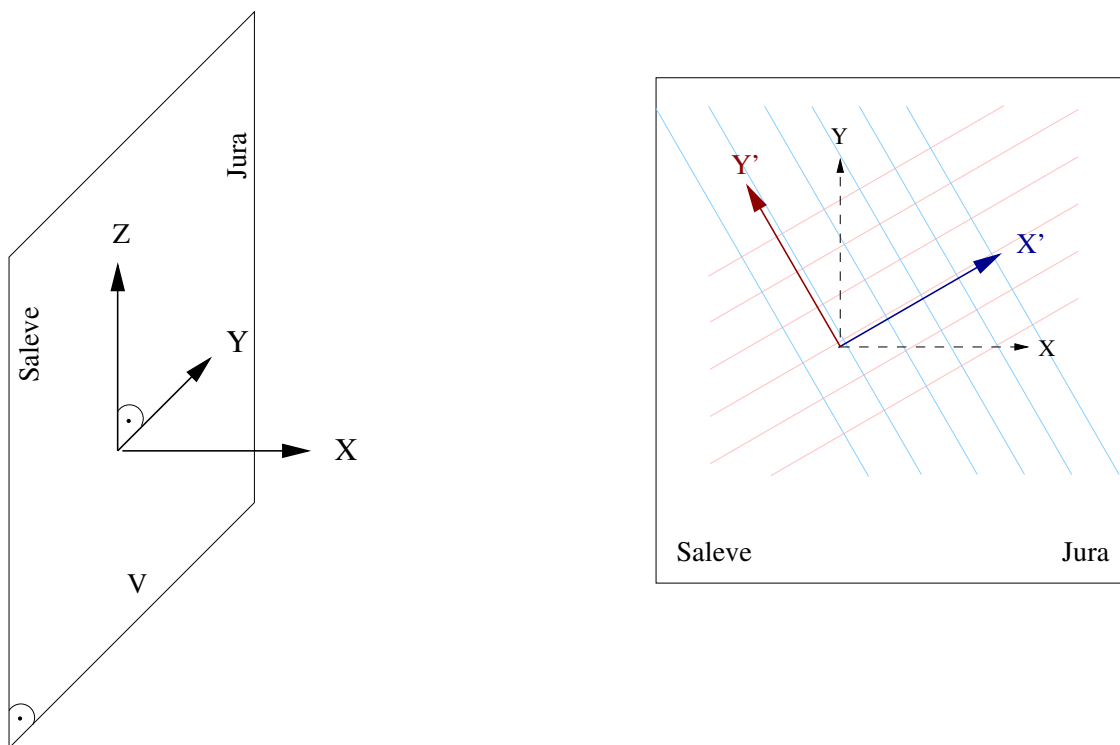
Fig. A.1 illustrates the different coordinate systems, which are used in COMPASS. All systems have their origin in the centre of the polarised target.

- **Main reference system (mrs)** used by CORAL and PHAST.
- **Wire reference system (wrs)** which is rotated around the Z-axis such that X and Y are perpendicular to the wires, e.g. hits in detectors are stored in this coordinate system.
- A **general coordinate system** is used by the surveying measurement of the detectors, by the tracking of COOOL and by COMgeant.

A COORDINATE SYSTEMS



COMPASS main reference system used by CORAL and PHAST



general coordinate system

wire reference system

Figure A.1: The different coordinate systems used in COMPASS.

Appendix B

Hadron Run 2004

B.1 History of Hadron Run 2004

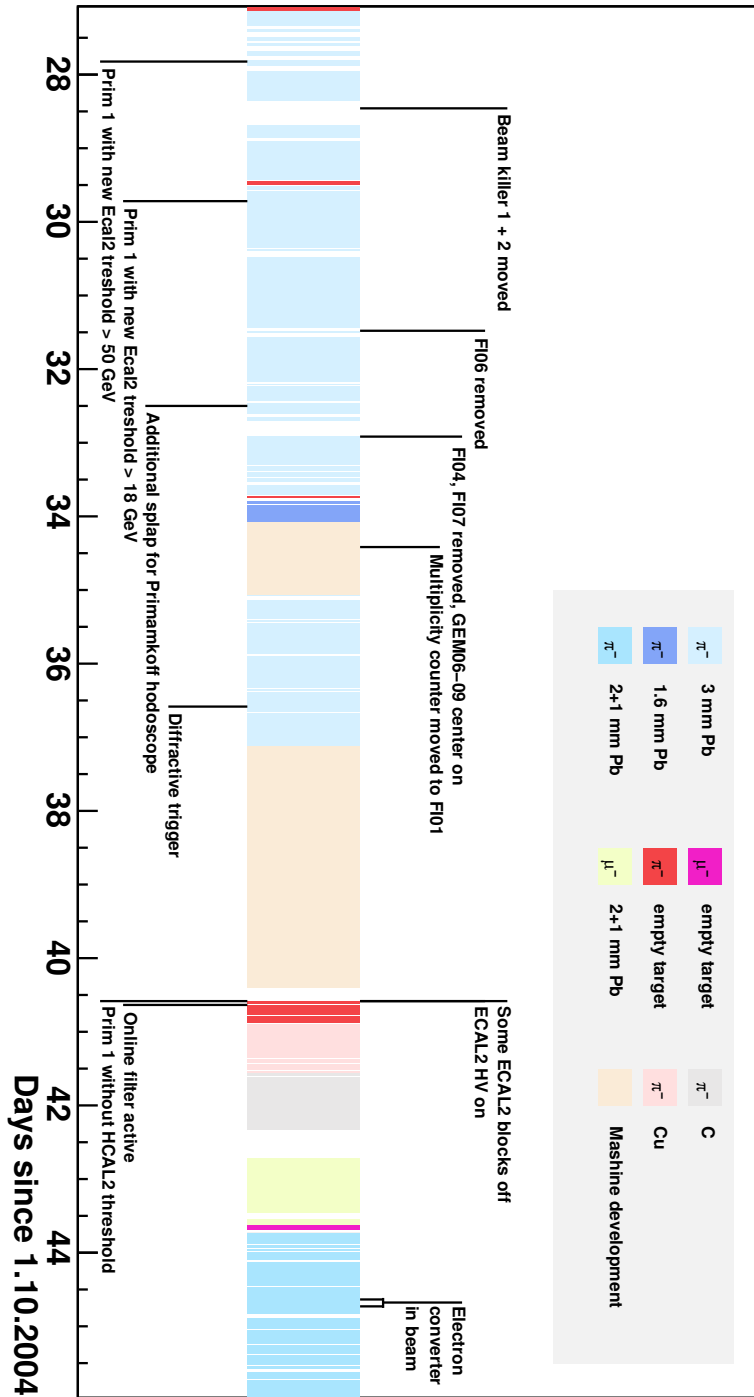


Figure B.1: History of hadron run 2004.

Date	Time	Run No.	Comment
03.10.2004	21:23	41382	Last muon physics run
04.10. - 27.10.2004			Rebuilding the spectrometer for hadron run and commissioning
27.10.2004	03:28	42324	Start of 3 mm Pb-target
27.10.2004	12:05	42353	New Primakoff settings
27.10.2004	19:56	42387	Primakoff trigger with new ECAL2 threshold > 50 GeV
28.10.2004	11:00	42421	X position of beam killer 1 (+ 5 cm) and 2 (+12 cm) moved towards Jura
29.10.2004	17:19	42514	First run with charge exchange trigger
30.10.2004	17:14	42547	First run Primakoff trigger 1 with HCAL2 threshold > 18 GeV
31.10.2004	11:31	42579	First run after FI06 moved 30 cm out of the spectrometer
01.11.2004	11:59	42615	First run with additional slab for Primakoff hodoscope (now 20 slabs)
01.11.2004	22:09	42630	First run FI04, FI07 removed, centres of GEM06XY, GEM07XY, GEM09XY active
02.11.2004	17:09	42661	End of 3 mm Pb-target
02.11.2004	19:13	42667	Start of 1.6 mm Pb-target, change in trigger
03.11.2004	02:06	42680	End of 1.6 mm Pb-target
03.11.2004	02:06	42680	Start of SPS machine development (MD)
			Multiplicity counter between SI02 and veto box moved to FI01 and inner veto
04.11.2004	01:49	42745	End of SPS machine development (MD)
04.11.2004	01:49	42745	Start 3 mm Pb-target
05.11.2004	14:01	42820	Diffraction trigger included
06.11.2004	02:47	42840	End of 3 mm Pb-target
06.11.2004	02:47	42840	Start long SPS machine development (MD)
09.11.2004	09:47	43023	End of long SPS machine development (MD)
09.11.2004	14:00	43036	Start of empty target with π^- -beam
			ECAL2 modules X=55 Y=19-22, X=56 Y=17-20, X=57 Y=17-23 HV off
09.11.2004	15:24	43037	First run with online-filter active
09.11.2004	21:10	43046	End of empty target with π^- -beam
09.11.2004	21:38	43052	Start of Cu-target
10.11.2004	13:19	43085	End of Cu-target
10.11.2004	13:40	43086	Start of 23.5 mm C-target
11.11.2004	08:03	43124	End of 23.5 mm C-target
11.11.2004	17:15	43158	Start of 2 + 1 mm Pb-target with μ^- -beam,
			HV of ECAL2 modules on, Primakoff trigger 1 without HCAL2 threshold
12.11.2004	14:18	43184	End of 2 + 1 mm Pb-target with μ^- -beam
12.11.2004	15:15	43185	Start of empty target with μ^- -beam
12.11.2004	16:28	43188	End of empty target with μ^- -beam
12.11.2004	17:14	43191	Start of 2 + 1 mm Pb-target, Primakoff trigger 1 with HCAL2 threshold >18 GeV
13.11.2004	03:02	43219	Trigger normal again
13.11.2004	15:21	43247	Electron converter in beam
13.11.2004	17:33	43251	First run without electron converter
14.11.2004	23:07	43323	End of 2 + 1 mm Pb-target
14.11.2004	23:40	43324	High intensity 10^8 hadrons/spill trigger rate 20-30 kHz
15.11.2004	08:00	43348	End of high intensity, end of beam time

Table B.1: A selection of important actions and measurement configurations taken during hadron run 2004.

Table B.2: From [COM07a]: Overview of detectors used in COMPASS, together with their respective main parameters, grouped according to their geometrical positions along the beam line and functions in the spectrometer. The first column shows the naming convention for the respective stations. The second column gives the number of detectors making up these stations, while the third column specifies the coordinates measured by the detectors. Here, e.g. XY means that both projections are measured by each detector, while X/Y means that only one of two coordinates X or Y is measured by one of the detectors. Typical values for resolutions of one detector at standard COMPASS muon beam conditions are given in the next column. These numbers correspond to an average over all detectors of this kind in the experiment, and hence may include contributions from pile-up, magnetic fringe fields, or reconstruction inefficiencies. Here, σ_s denotes the r.m.s. spatial resolution along one coordinate, σ_t the r.m.s. time resolution, σ_{ph} the single photon resolution, σ_{ring} the ring resolution. Detectors which were moved out (see Table B.1) during hadron run 2004 are marked in type-writer font.

Station	# of dets.	Planes per det.	# of ch. per det.	Active area $X \times Y$ (cm ²)	Resolution
Beam detectors					
SciFi 1	2	XY	192	3.9×3.9	$\sigma_s = 130 \mu\text{m}, \sigma_t = 0.4 \text{ ns}$
SI01, SI02	2	$XYUV$	2304	5×7	$\sigma_s = 8 - 11 \mu\text{m}, \sigma_t = 2.5 \text{ ns}$
Large angle spectrometer					
SI03, SI04, SI05	2	$XYUV$	2304	5×7	$\sigma_s = 8 - 11 \mu\text{m}, \sigma_t = 2.5 \text{ ns}$
SciFi 3, [4]	2	XYU	384	5.3×5.3	$\sigma_s = 130 \mu\text{m}, \sigma_t = 0.4 \text{ ns}$
Micromegas	12	$X/Y/U/V$	1024	40×40	$\sigma_s = 90 \mu\text{m}, \sigma_t = 9 \text{ ns}$
DC	3	$XYUV$	1408	180×127	$\sigma_s^x = 106 \mu\text{m}, \sigma_s^y = 160 \mu\text{m}^a$
Straw	6	$X/Y/U/V$	892	412×357	$\sigma_s = 190 \mu\text{m}^b$
GEM 1-4	8	XY/UV	1536	31×31	$\sigma_s = 70 \mu\text{m}, \sigma_t = 12 \text{ ns}$
SciFi 5	1	XY	340	8.4×8.4	$\sigma_s = 170 \mu\text{m}, \sigma_t = 0.4 \text{ ns}$
RICH-1	8	1 (pads)	10386	60×120	$\sigma_{\text{ph}} = 1.2 \text{ mrad}$ $\sigma_{\text{ring}} = 0.55 \text{ mrad (for } \beta = 1)$
MWPC A*	1	$XUVY$	2768	178×120	$\sigma_s = 1.6 \text{ mm}$
Straw	9	$X/Y/U/V$	892	412×357	$\sigma_s = 190 \mu\text{m}$
HCAL 1	1	1	480	420×300	$\Delta E/E = 0.59/\sqrt{E/\text{GeV}} \oplus 0.08$
MW 1	8	X/Y	1056	480×410	$\sigma_s = 3 \text{ mm}$
Small angle spectrometer					
GEM 5-10	14	XY/UV	1536	31×31	$\sigma_s = 70 \mu\text{m}, \sigma_t = 12 \text{ ns}$
MWPC A	7	XUV	2256	178×120	$\sigma_s = 1.6 \text{ mm}$
SciFi 6	1	XYU	462	10×10	$\sigma_s = 210 \mu\text{m}, \sigma_t = 0.4 \text{ ns}$
SciFi 7	1	XY	286	10×10	$\sigma_s = 210 \mu\text{m}, \sigma_t = 0.4 \text{ ns}$
SciFi 8	1	XY	352	12.3×12.3	$\sigma_s = 210 \mu\text{m}, \sigma_t = 0.4 \text{ ns}$
Large area DC	6	$XY/XU/XV$	500	500×250	$\sigma_s = 0.5 \text{ mm}$
ECAL 2	1	1	2972	245×184	$\Delta E/E = 0.06/\sqrt{E/\text{GeV}} \oplus 0.02$
HCAL 2	1	1	216	440×200	$\Delta E/E = 0.66/\sqrt{E/\text{GeV}} \oplus 0.05$
MWPC B	6	XU/XV	1504	178×90	$\sigma_s = 1.6 \text{ mm}$
MW 2	2	XYV	840	470×220	$\sigma_s = 0.6 - 0.9 \text{ mm}$

^aResolutions in x and y coordinates including contributions of the tilted planes.

^bResolution measured for 6 mm straw tubes only.

Appendix C

Silicon Detectors in COMPASS

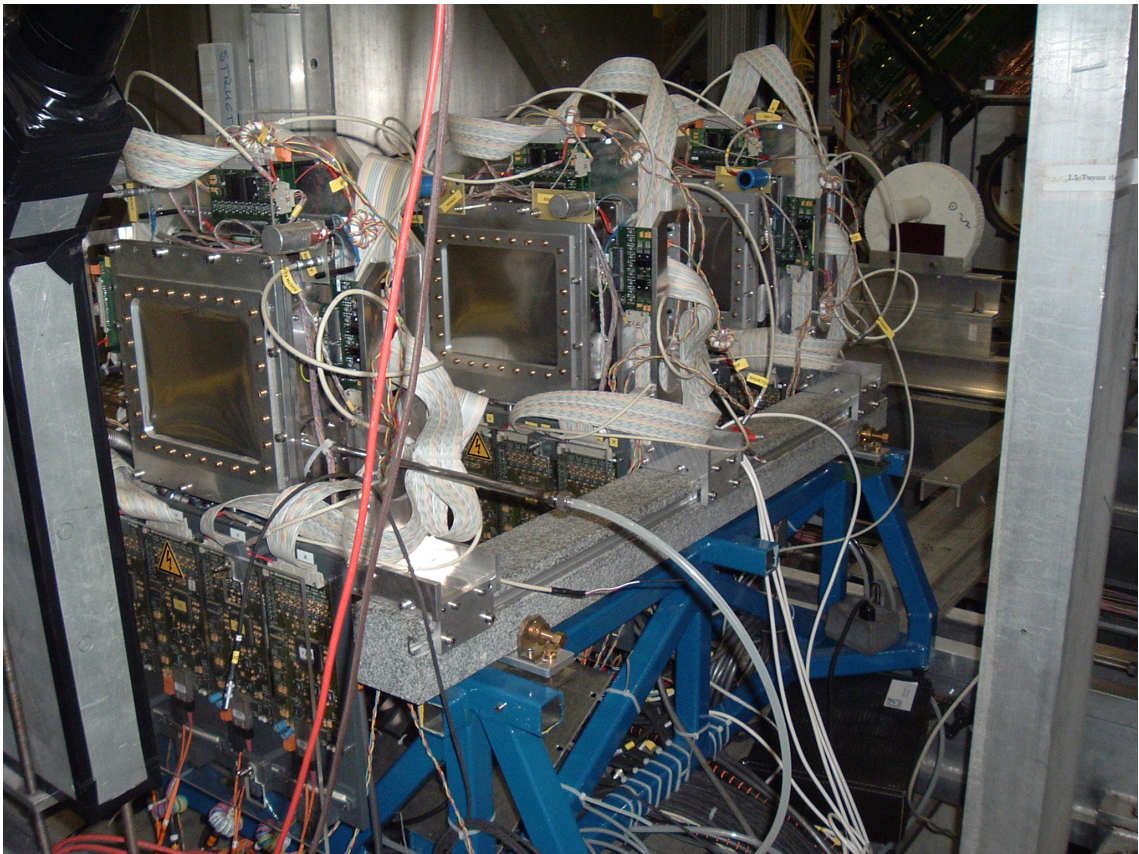


Figure C.1: Silicon stations SI03 to SI05 in hadron beam 2004.

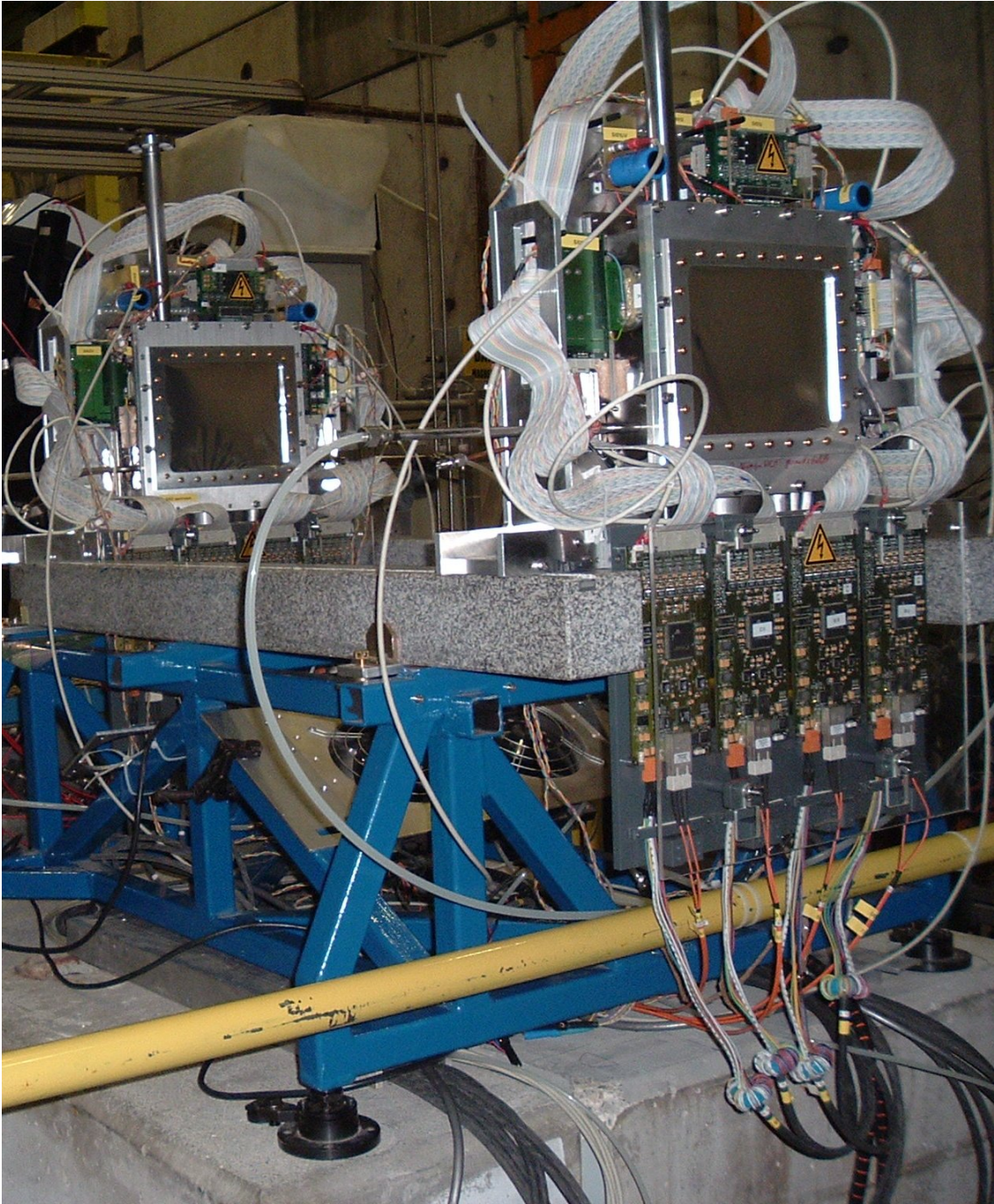


Figure C.2: Silicon stations SI01 and SI02 in hadron beam 2004.

SI plane	SI module	Z position [cm]		SI module	Z position [cm]
<i>2004 / 2006</i>		<i>Muon 2004</i>	<i>Muon 2006</i>	<i>Hadron 2004</i>	
Beam telescope					
SI01U	SIL11	-569.4600	-535.8800	SIL20	-534.5100
SI01V	SIL11	-569.4500	-535.8600	SIL20	-534.5080
SI01Y	SIL10	-568.4300	-534.8400	SIL18	-533.4720
SI01X	SIL10	-568.4100	-534.8200	SIL18	-533.4700
SI02U	SIL08	-501.3500	-430.9900	SIL22	-425.2900
SI02V	SIL08	-501.3300	-430.9700	SIL22	-425.2880
SI02Y	SIL12	-500.3100	-429.9500	SIL21	-424.2520
SI02X	SIL12	-500.2900	-429.9300	SIL21	-424.2500
SI05U / SI03U	SIL16	-352.6800	-326.4200	-	-
SI05V / SI03V	SIL16	-352.6700	-326.4000	-	-
SI05Y / SI03Y	SIL13	-351.6500	-325.3800	-	-
SI05X / SI03X	SIL13	-351.6300	-325.3600	-	-
Hadron target position					-309.000
Tracking telescope					
SI03U				SIL16	-203.2950
SI03V				SIL16	-203.2930
SI03Y				SIL13	-202.2570
SI03X				SIL13	-202.2550
SI04U				SIL11	-150.9100
SI04V				SIL11	-150.9080
SI04Y				SIL10	-149.8720
SI04X				SIL10	-149.8700
SI05U				SIL08	-101.5900
SI05V				SIL08	-101.5880
SI05Y				SIL12	-100.5520
SI05X				SIL12	-100.5500

Table C.1: Position and module names of silicon stations in 2004 - 2006.

Appendix D

Silicon Detector Analysis - Technical Information

All code, macros, scripts and information about the analysis of this thesis can be found in `ANALYSISPATH=/afs/e18.ph.tum.de/compass/analysis/primakoff/`. For the whole silicon analysis the ROOT version `root_v4.02.00.Linux.soversion.gcc33` was used and in case of CORAL and COOOL the Class Library for High Energy Physics (CLHEP) version 1.8.1.0.

D.1 Calibrations with COOOL

Information and documentation about COOOL can be found at the web page <http://cbernet.home.cern.ch/cbernet/Cool/>. On the E18-Wiki documentation page <https://www.e18.physik.tu-muenchen.de/cgi-bin/wiki.pl>, all important steps for the compilation of COOOL at the E18-environment are explained.

The COOOL used for the analysis was configured with the options `./configure --with-TRACK --with-DATABASE=/afs/e18/compass/silicon/mysql/`

If COOOL is executed in the bash mode `./bcool` the following options were used within this analysis:

- `geom` <detector geometry file/ alignment file detectors*.dat>
- `group` <group file: list of detectors which will take part in the tracking>
- `map` <standard COMPASS mapping file>
- `CompMon` <COOOL automatically generates a file `.CompMon` in the home directory which can be edited in order to deactivate detectors which are not in the focus of the analysis>

- `nevent` <number of events to analyse>
- `root` <output tree>

The straight line tracking routine of COOOL is very convenient for detector studies, especially in the target region, where no magnetic field introduces further challenges. For the time calibration, all silicon detectors and the SciFi stations (in muon run FI01 and FI02, for hadron run FI01 and FI03) located in the target region build one tracking group, listed in a `group_<name>.xml` file. It is possible to influence the tracking routine by setting some special parameters via an external file. The file is read by COOOL from the path `$ANALYSISPATH/timecalib/analysis_cool/configs/TrackPar`. The name of the tracking parameter file `Tracking_<name>.par` has to contain the same <name> sub-string like the group file `group_<name>.xml`. In the tracking parameter file, the following parameters for the track selection can be set and example configurations are given in Table D.1:

- **maxNumberOfCluster**: Sets the maximum numbers of clusters (cluster multiplicity) of those detector planes which are considered by the track finding algorithm (*active planes*).
- **minNumberofPlanes**: Choose the minimum number of active planes, which must have contributed to the track (Note: The algorithm needs at least hits from 5 active planes).
- **chi2probCut** : Cut on the χ^2 probability of the track
- **chi2Cut** : Cut on the χ^2/ndf of the track
- **scifiTimeDiffCut**: The hit-time of the particle for each active tracking SciFi plane has to be within a certain time window which is set by this cut. In case no time calibration or alignment of the silicon detectors exists, this cut is the most sensitive one in order to reduce background tracks.
- **scifiTriggerCut**: Sets the time window between the SciFi- and trigger-time. One can profit from off-time tracks in the calibration, if a big time window of e.g. 100 ns is set.
- **siliconTimeCutMode**: Cut on the silicon time of inactive planes
- **siliconActiveTimeCut**: Cut on the silicon time of active planes
- **<number of deactivated planes>**: The number of deactivated planes followed by a list of detector planes: `SI01X, SI02U, . . .`. Deactivated planes are those which should not be considered by the track finding algorithm, otherwise automatically all detectors are active planes which are listed in the group file.

Track selections	Alignment	Time calibration	Vertexing	Default
maxNumberOfCluster	6	6	3	6
minNumberofPlanes	8	8	8/12	min. 5
chi2probCut	10^{-8}	0.001	0.001	10^{-5}
chi2Cut	10^9	10	2	5
scifiTimeDiffCut	3	2	3	2
scifiTriggerCut	100	100	3	2
siliconTimeCutMode	100000	100000	100000	0
siliconActiveTimeCut	100000	100000	100000	0
active Tracker	FI01XY, FI02XY SI01UV, SI03UV	FI01XY, FI02XY SI01UV, SI03UV	SI01-02 SI03-05	all planes

Table D.1: Tracking configurations for the alignment and time calibration of the silicon telescope with COOOL as performed on 2006 muon data (section 4.4), and tracking options for the vertexing as it was used in hadron run 2004 (section 5.4).

D.1.1 Alignment

In case the tracking package of COOOL is activated, the residuals of the track position and the cluster of each silicon and SciFi plane are calculated and written in a ROOT-TTree. In the alignment procedure, the positions of these residuals are determined and the detector positions are shifted with respect to these values.

The new calculated detector positions are written in a new geometry file and alignment file, respectively, and the data sample is processed again for a new iteration. Usually the SciFi detectors and four silicon planes are chosen as active tracking detectors, due to the high spatial resolution of the silicon detectors they act like pivot elements. This step has to be iterated several times by changing the set of the active tracking silicon detectors. The procedure is finished, when the χ^2/ndf -distribution has its maximum at 1 and remains stable, see Fig. 4.8.

In the following, the single steps and the used scripts and programs are listed. If nothing else is explicitly mentioned, the main path is `$ANALYSISPATH/timecalib/cool_alignment/`.

- Analyse a run with COOOL in tracking mode by using the proper COMPASS geometry file (detectors.dat).
- The ROOT-macro `residuen_SI.C` in `makro_cool_tree` fits the residuum distributions of each plane with a Gauss. The mean value of the fit is written in a file `sortdat/respos.dat`.
- The C++ program `sortdat/sort` rearranges the values in the file `respos.dat` in the same directory and writes `sortdat/respos_new.dat`.

- A program written by Jan Friedrich (`sortdat/jandetdat/detdatc`) reads a `detectors.dat` file which can be chosen via a graphical user interface. Based on the values of `respos_new.dat`, new positions for the silicon detectors are calculated and written in a new file `detectors.dat`.

D.1.2 Time Calibration

With an aligned silicon telescope, one can analyse the data sample with COOOL and special tracking options, see Table D.1. The resulting ROOT-TTree has to be analysed by a special program generating the time calibration parameters. The sources of the program can be checked out from the repository by

```
svn co svn+ssh : //hamlet:/opt/svn/silicon/trunk/time_calib.
```

This checkout also includes a manual, where all necessary information about using this program is documented. This program executes all fitting routines mentioned in section 4.4. The output of the program is a text file, e.g. `SI01Y1__` with the calibration parameters in the final format, see Table D.2

Time calibration parameters									
1.	2.	3.	4.	5.	6.	7.	8.	9.	10.
0.05	0.717211	0.726909	1.12601	-1.59439	47.7655	-33.8891	-65.4215	0	0
0.05	0.757862	1.6614	15.5081	0.0492125	0.074364	10.0003	-0.344311		
0.69232	1.0879	1.28322	-4.17337	0.045026	0.0764297	17.1401	0.249168		
Parameter names									
$r0_{min}$	$r0_{max}$	$r1_{min}$	$r1_{max}$	T_{r0}	T_{r1}	S_{r0}	S_{r1}	tc_{r0}	tc_{r1}
$r0_{min}$	$r0_{max}$	r_0	t_0	a	c	b	d		
$r1_{min}$	$r1_{max}$	r_0	t_0	a	c	b	d		

Table D.2: Example of a time calibration of SI01Y for muon run 2006. rx_{min} and rx_{max} stand for the minimum and maximum signal amplitude ratio $r_{02} = r_0$ and $r_{12} = r_1$, respectively, within the 25 ns time window calculated by the corresponding time fit function. The first row contains the fit parameters for the straight line fit, the old timing fit routine, the parameter S is the slope and T the constant of the linear equation. tc is a possible additional time offset which has to be determined separately, but it is found not to be mandatory. In the second and the third row are listed the timing fit parameters 3. - 8. for the signal amplitude ratios respectively of eq. (4.5) on page 36 which are explained in section 4.2.

D.2 Silicon Detectors in CORAL

Within this thesis, the silicon clustering routine of the COMPASS reconstruction software CORAL (subsection 2.3.5) was revised. The time calculation and its error propagation as well as the clustering algorithm, which was firstly implemented in the online filter,

was integrated to the CORAL class `CsSiTrackerDetector`. From the online-filter, the files `silicon_timing.c`, `silicon_timing.h` and `silicon_timing_types.h` were taken and added to the CORAL repository. The results of the analysis of the spatial resolution as well as for the cluster charge distribution were considered in the updated clustering code. The underlying ideas and analysis are presented in chapter 4.

D.2.1 New Silicon CORAL Options

CORAL can be configured by the user via an *option file*. In this option file one can set e.g. the path for the calibration values, the detectors which should not be considered by the tracking algorithm, specific analysis options for detector experts, special options for the tracking algorithm. CORAL has an extra options interpreter class `CsOpt` which interprets this input string.

In the following, new CORAL options for the silicon detector part are explained. The option is composed by the detector name, a key name and the specific option.

- **SI ClusteringSelect cind/ratio:** By default, the new clustering algorithm (**cind**) is used. The previous algorithm, with a simpler treatment of the time calculation and cluster position can be activated with **ratio**. Since 2004 appropriate calibration values for the new clustering algorithm are available, option **cind** should be used.
- **SI AlignmentPatch on/off:** The result of the alignment procedure of the silicon telescope in hadron run 2004 which is discussed in section 5.2, is taken into account by calculating the cluster positions. The determined offsets for the ten silicon detectors of 264 runs from the interval 42320 to 43350 are stored as an array in the file `CsSiTrackerResCor.h`. By default this AlignmentPatch is **on**, but it can be switched **off**.
- **SI TimeCalibMunich on/off:** This option must be used with great care, since it is an option for the detector expert only. By activating this option a new time calibration can be tested, before it is submitted to the data-base. The calibrations are read from the directory `/afs/e18.ph.tum.de/compass/silicon/time_calib/timingfiles/` instead of reading from data-base. One has to ensure, that files to be tested are linked to this path.

D.2.2 CORAL Configurations for Silicon Data Analysis

Default option files with all standard configurations are in the CORAL repository. For muon runs it is the `trafdic.2004.opt` file, which is pre-configured for the user and adapted for each beam time. For hadron run the file is `hadron.opt`. Both can be found in the directory with the user settings. General and technical information for the user are given in [COR] and [Bed04].

D SILICON DETECTOR ANALYSIS - TECHNICAL INFORMATION

SI Plane	r_0	t_0	a	c	b	d
SI01U r_{02}	2.21155	-10.9645	0.00148814	0.168084	75.6866	-2.81788
SI01U r_{12}	1.48307	-23.8953	0.00245496	0.126036	92.704	-1.45523
SI01V r_{02}	2.06525	2.47841	0.00220851	0.107857	137.341	-1.74084
SI01V r_{12}	1.40841	31.1421	0.00402548	0.0771251	656.016	1.04752
SI01X r_{02}	2.38025	21.0033	0.00423383	0.0956122	55.1406	-0.678635
SI01X r_{12}	1.55608	-2.44572	0.00303674	0.0935325	67.0302	-0.262643
SI01Y r_{02}	2.0579	-11.0933	0.0409697	0.396774	10	-3.50221
SI01Y r_{12}	1.45742	12.0802	1.65351e-05	0.0817973	832.911	0.328644
SI02U r_{02}	2.03483	30.46	0.0205736	0.080222	49.9112	-0.307321
SI02U r_{12}	1.42306	-49.9939	0.0241908	0.185772	57.0874	-3.99898
SI02V r_{02}	2.5	9.96751	0.0364194	0.108175	10	-1.58846
SI02V r_{12}	2.05045	8.57665	0.0143186	0.0482383	23.5126	-0.280571
SI02X r_{02}	2.02236	38.2355	0.0409574	0.0530321	10	0.0691326
SI02X r_{12}	1.47407	-49.8902	0.0226409	0.14499	68.0434	-3.48041
SI02Y r_{02}	1.93776	25.863	0.0280357	0.0683463	37.4966	-0.577982
SI02Y r_{12}	1.3861	-49.4313	0.0265192	0.0950421	92.2456	-2.85124
SI03U r_{02}	2.18825	-7.46361	0.0289509	0.393194	10.0002	-2.4528
SI03U r_{12}	1.45049	-49.5134	0.0263666	0.344877	23.7155	-3.78997
SI03V r_{02}	1.87084	13.6794	0.0419551	0.111169	10	-1.28273
SI03V r_{12}	1.45986	-48.463	0.00219696	0.199002	86.6088	-3.97565
SI03X r_{02}	1.92643	21.9607	0.039209	0.0659978	10	-0.451649
SI03X r_{12}	1.54625	-50	3.91192e-06	0.26305	59.9944	-4.29357
SI03Y r_{02}	2.49487	8.24477	0.0220866	0.160485	16.1249	-1.7389
SI03Y r_{12}	1.52368	-17.1593	0.0164397	0.124275	39.1241	-1.3384
SI04U r_{02}	1.65381	20.2494	0.0422527	0.0924887	13.2748	-0.582966
SI04U r_{12}	1.24516	-26.0671	0.0486742	0.399984	11.2984	-2.83254
SI04V r_{02}	1.7431	8.99525	0.0423734	0.222979	10	-1.78052
SI04V r_{12}	1.23702	29.464	0.032388	0.0651545	12.0569	1.60022
SI04X r_{02}	2.40876	-1.37103	0.00660613	0.14395	36.0992	-1.26425
SI04X r_{12}	1.21362	-30.3488	0.0730836	0.114085	10	-1.2734
SI04Y r_{02}	1.62646	21.054	0.0485965	0.0761094	10	-0.509563
SI04Y r_{12}	1.27023	-46.3455	0.00133193	0.187754	121.416	-3.58262
SI05U r_{02}	2.5	18.3565	0.0195415	0.075384	14.8599	-0.322931
SI05U r_{12}	1.21802	-7.73377	0.0497535	0.102011	287.79	0.228363
SI05V r_{02}	2.41625	17.9987	0.00489605	0.123485	36.7791	-1.12984
SI05V r_{12}	1.21963	47.9364	0.000521942	0.111364	242.248	2.70738
SI05X r_{02}	1.70301	20.9439	0.0527572	0.0852525	10	-0.486345
SI05X r_{12}	1.23713	30.8269	0.030261	0.0723779	10	2.1113
SI05Y r_{02}	1.65598	24.3414	0.0470014	0.076097	10	-0.460841
SI05Y r_{12}	1.27601	32.6065	0.018918	0.0658735	20.5884	1.61124

Table D.3: Time calibration parameters of eq. (4.5) for hadron run 2004, see section 4.2. Note, the parameter sequence is here a, c, b, d.

Option string (general)	Argument
mDST hits SI FI	Measurements of tracking detectors (clusters) are stored in DST file
mDST digits SI FI	Raw information of each hit are stored
CDB server hamlet	Server is located in Munich TUM E18
CDB specialplace MUNICH	Location of calibration files at MUNICH
SI ClusteringSelect cind	Activates new clustering algorithm
Option string (muon run specific)	
TraF DetNameOff BM SI02X SI02Y	Deactivate a detector group or single planes from tracking
TraF iCut [20] 2	Min. number of SciFi-hits in beam telescope
TraF dCut [70] 0.5	Min. time resolution for Si (== 0 means Si timing disregarded)
TraF iPRpar [40 - 45] 4 3 9 4 3 8	Min. and max. hit requirements for tracking of beam telescope
Option string (hadron run specific)	
SI AlignmentPatch on	Alignment correction for silicon telescope
TraF DetNameOff FI03 SI04X SI04Y	Deactivate a detector group or single planes from tracking
TraF iCut [20] 0	Min. number of SciFi-hits in beam telescope
TraF iPRpar [0 - 5] 2 3 9 2 2 8	Min. and max. hit requirements for tracking of beam telescope of first zone after target
TraF dCut [66] 10000	Maximum momentum for fringe-field track
TraF ReMode [18] 0	Disables backtracking

Table D.4: Special CORAL options for the silicon detector analysis [Bed06] in order to achieve a tracking of the beam telescope only, as needed for the silicon detector analysis, both for muon and hadron run configuration, see section 4.6.

Appendix E

ECAL2 in COMPASS

E.1 ECAL2 Mapping

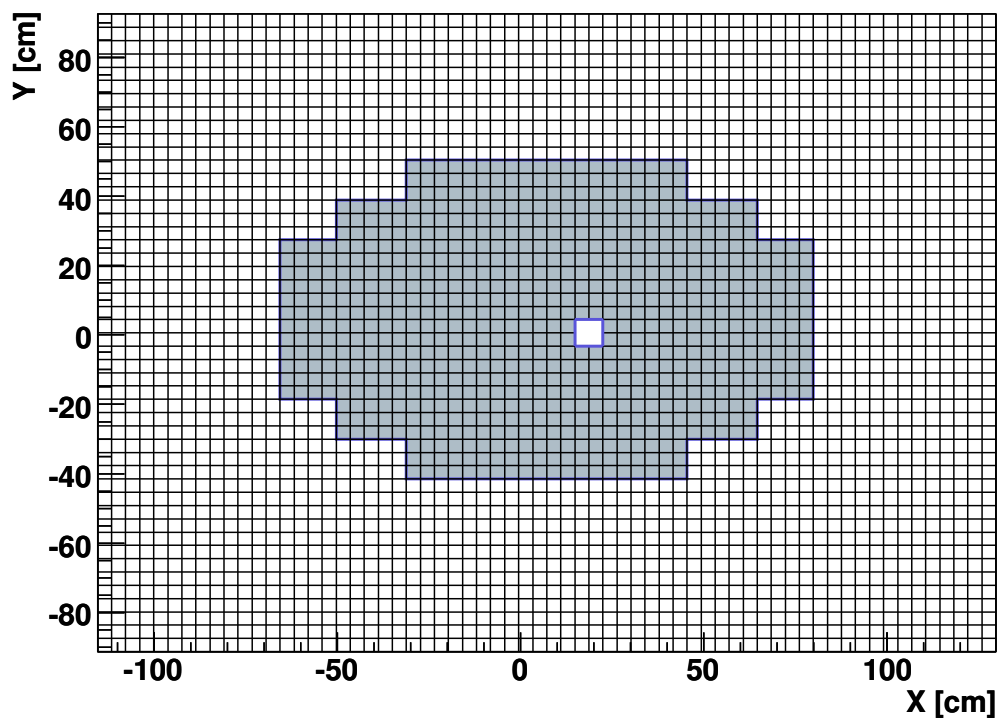


Figure E.1: Configuration of the 3068 (64×48) cells of ECAL2 in COMPASS hadron run 2004 of the size $38.3 \times 38.3 \times 450 \text{ mm}^3$. The radiation hard lead glass blocks (TF101) are installed in the central region which are coloured in grey [Pol07].

E.2 Technical Information for ECAL2 Calibration

All source code is archived in the E18 repository:

```
svn co svn+ssh://hamlet/opt/svn/analysis/primakoff/CalibEcal2/
```

E.2.1 Functions for Generating Energy Ratio Distributions

The following macros are used in order to generate log-energy-ratio distributions as it is discussed in subsection 6.4.2:

- Produce μ DST data which contain the raw information of a ECAL2 cell with PHAST user function USR50 (located in svn repository: `/afs/e18/svn/analysis/primakoff/phast_user`).
- Filter the data in order to reduce the TTree size with `srcfilter/myfilter_pDST.C` and correct the cell energies for the adequate calibration values.
- Create 3D log-energy-ratio distributions for the different energy and angle bins with `src3Dplot/makeplot.C`.
- Add for all runs the angle and energy bins which belong together, e.g. `ratio3D_00_00.root`.
- Determine by Gaussian-fits the mean value of the energy fraction for each of the X- and Y-bins of the 3D log-energy-ratio histogram by executing the function `srcfinal/Ecal_ratio_fit_new.C`.
- With the macro `Ebin0_symmetrieplotmaker.C`, one can increase the statistics for the energy fraction distributions by exploiting certain symmetries, see Table 6.2, and superposing the particular histograms.
- For energies above 120 GeV, further energy ratio distributions have to be combined according to the particular energy intervals, see Table 6.3, use the macros `Ebin8_symmetrieplotmaker.C`, `Ebin9_symmetrieplotmaker.C`, and `Ebin10_symmetrieplotmaker.C`.
- The functions `srcfinal/smooth3D.C` and `srcfinal/smooth3Dpart.C` smooth the log-energy-ratio distributions and store the 6 fit parameters of the quadratic 2D-function in 6 histograms.
- Set the borders of the log-energy-ratio distributions to a fixed value with the macro `setborder2.C`.
- Exploit the energy constraint that the sum of the energy fraction carried by the 5×5 ECAL2 cells has to be 1 with `srcfinal/CellSum.cc`.
- Final smoothing `srcfinal/smooth3DforclFit.cc`.

Angle bin	Bending parameter interval [GeV rad]	
0 ^A	bx -1.6 < 0.1	by < 0.1
1 ^A	bx +1.6 < 0.1	by < 0.1
2 ^A	bx +1.6 < 0.1	by -0.85 < 0.75
3 ^A	bx +1.6 < 0.1	by +0.85 < 0.75
4 ^A	bx -1.6 < 0.1	by +0.85 < 0.75
5 ^A	bx -1.6 < 0.1	by -0.85 < 0.75
6 ^A	bx -0.75 < 0.75	by -0.0 < 0.1
7 ^A	bx +0.75 < 0.75	by -0.0 < 0.1
8 ^A	bx +2.45 < 0.75	by -0.0 < 0.1
9 ^A	bx -2.45 < 0.75	by -0.0 < 0.1
10 ^A	bx -2.45 < 0.75	by +0.85 < 0.75
11 ^A	bx -2.45 < 0.75	by -0.85 < 0.75
12 ^A	bx +2.45 < 0.75	by -0.85 < 0.75
13 ^A	bx +2.45 < 0.75	by +0.85 < 0.75
14 ^A	bx +0.75 < 0.75	by +0.85 < 0.75
15 ^A	bx +0.75 < 0.75	by -0.85 < 0.75
16 ^A	bx -0.75 < 0.75	by -0.85 < 0.75
17 ^A	bx -0.75 < 0.75	by +0.85 < 0.75

Table E.1: List of angle bins for the energy ratio distributions.

Energy bin	Energy interval [GeV]
0 ^E	< 25
1 ^E	25 - 35
2 ^E	35 - 45
3 ^E	45 - 60
4 ^E	60 - 75
5 ^E	75 - 90
6 ^E	90 - 105
7 ^E	105 - 120
8 ^E	120 - 135
9 ^E	135 - 150
10 ^E	150 - 165
11 ^E	> 165

Table E.2: List of energy bins for the energy ratio distributions.

Column	Name	Function
1	<code>int cell_index</code>	Index off ECAL2 cell
2	<code>int cX</code>	Cell number in X
3	<code>int cY</code>	Cell number in Y
4	<code>double nb_smoothed</code>	Entries in fitted histogram including statistics due to smoothing
5	<code>double Sig</code>	Sigma of fitted Gauss on calibration plot
6	<code>double ErrSig</code>	Error of sigma
7	<code>double RatioGauss</code>	Ratio of amplitude between the two Gauss
8	<code>int nb_raw</code>	Raw entries in fit histogram
9	<code>int adc_sat</code>	ADC value in case of saturation, default value is 4500
10	<code>double calibconst</code>	Calibration value [MeV], mean value of Gauss
11	<code>double calibconstErr</code>	Error of the Gauss mean value

Table E.3: List of the values in the calibration files

E.2.2 Functions for Generating the Calibration Parameters

The following macros are used in order to generate the calibration parameters for ECAL2 based on the log-energy-ratio distributions, see subsection 6.4.3:

- Produce μ DST data which contain the raw information of a ECAL2 cell with PHAST user function `USR50` (located in svn repository: `/afs/e18/svn/analysis/primakoff/phast_user`).
- Filter the data in order to reduce the TTree size with `srcfilter/myfilter_pDST.C` and correct the cell energies by means of the log-energy-ratio distributions `calibsrc/filter4calib_pDST.cc`.
- Prepare the relevant histograms for each run with `calibsrc/createplot4calib.cc`.
- With `calibmaker/src/calibmaker.cc` evaluate the histograms and derive the calibration values.

E.2.3 Run Lists

42322	42482	42515	42609	42667	42800	43046	43097	43207	43262
42326	42483	42519	42614	42669	42803	43055	43099	43219	43271
42327	42484	42539	42619	42680	42810	43058	43103	43222	43279
42328	42485	42565	42631	42758	42820	43061	43106	43228	43285
42389	42486	42569	42634	42766	42824	43066	43114	43231	43296
42470	42489	42574	42638	42772	42827	43072	43117	43239	43305
42476	42491	42593	42640	42781	42830	43084	43120	43244	
42480	42495	42601	42653	42793	42838	43091	43122	43250	
42481	42496	42604	42658	42796	43043	43094	43196	43257	

Table E.4: 85 runs used for deriving the shower model

42322	42495	42592	42647	42772	42825	43076	43121	43191	43251
42324	42496	42593	42648	42774	42827	43077	43122	43193	43252
42325	42498	42594	42649	42776	42828	43078	43124	43194	43255
42326	42500	42596	42650	42777	42830	43079	43158	43196	43257
42327	42502	42597	42653	42779	42831	43081	43159	43198	43260
42328	42505	42598	42657	42781	42835	43082	43160	43200	43261
42342	42507	42599	42658	42784	42836	43084	43162	43202	43262
42385	42515	42601	42661	42785	42838	43085	43163	43203	43267
42386	42519	42604	42665	42793	42839	43086	43164	43204	43268
42388	42522	42607	42667	42794	42840	43087	43165	43205	43269
42389	42535	42609	42669	42796	43037	43089	43166	43207	43270
42397	42536	42610	42671	42797	43038	43091	43168	43209	43271
42398	42539	42612	42672	42798	43039	43092	43169	43219	43274
42456	42542	42614	42680	42800	43041	43093	43170	43220	43278
42470	42544	42615	42751	42801	43042	43094	43171	43221	43279
42476	42545	42616	42753	42802	43043	43096	43172	43222	43280
42478	42549	42617	42756	42803	43044	43097	43173	43227	43281
42480	42564	42619	42757	42804	43046	43098	43174	43228	43285
42481	42565	42630	42758	42809	43055	43099	43175	43230	43291
42482	42566	42631	42759	42810	43058	43100	43176	43231	43296
42483	42569	42634	42760	42811	43060	43103	43177	43234	43298
42484	42571	42636	42762	42812	43061	43106	43183	43239	43305
42485	42572	42637	42764	42813	43063	43111	43184	43241	43310
42486	42573	42638	42766	42816	43066	43112	43185	43244	43318
42489	42574	42640	42767	42820	43067	43114	43186	43246	43321
42491	42575	42642	42770	42821	43069	43117	43187	43247	43322
42494	42591	42645	42771	42824	43072	43120	43188	43250	

Table E.5: For these 269 runs new calibration parameters are determined. In addition these runs are scanned for saturated cells.

E.2.4 Description of the Cluster Refit

- **Ecalibshowerfit:** Main method for applying the new calibration constants and re-fitting the cluster which will be called by the PHAST `UserEventxx.cc` analysis function.
- **FindMaxCell:** Method to find the cell with the maximum energy content of the currently analysed ECAL2 cluster.
- **ApplyCalibration:** Method to apply the calibration value of the particular cell, the energy value is recalculated.
- **CalcError:** This method to calculate the error on the cell energy. The function is determined empirically and validated by the distribution of the pulls. It also gives an index to cells which are problematic, like dead cells or cells in saturation.
- **Cluster2Field:** This method sorts an ECAL2 cluster into an array/matrix structure of size 7×7 . Due to the preprocessing with CORAL the cluster array size is 3×3 or 5×5 maximum. In order to analyse special cases like dead cells, the basic array size is chosen to be 7×7 . Each cell has a unique cell index and can be mapped to a x-y cell information.
- **IsNotDeadCell:** Method to check whether a cell is dead.
- **SetDeadCells:** Method to do figure out if the cell is a dead cell, near the beam hole or close to the border of the detector within the region of the cluster. For each case a big error (see Table 6.4) for the cell is set and also a certain tag, e.g. saturated cell, hole, dead cell, maximum in dead cell, close to border.
- **FitMaker:** This method executes the fit on the clusters based on energy ratio distributions determined by the data of hadron run 2004. The distributions are generated depending on the impact angle (9×2 bins) and energy (12 bins) of the incoming particle. At first the method determines the right histogram of the shower distribution. The cell array is resorted in a 1D histogram and the fit is applied.
- **ReadEcalMap:** Method for reading the mapping of ECAL2 cells. The unique cell index is encoded in a 2D information like cell column (X) and cell row (Y).
- **ReadCalibConsts:** This method reads for a particular run number the file with the calibration constants.
- **OpenHist:** This method reads the histograms with the shower information which are in total 6 parameters of a 2D polygon for different energy and angle bins (L = Large Histograms, S = zoom into the shower centre). The histograms are derived from the experimental shower distribution, x-y position versus the carried energy ratio.
- **EABbin:** This method chooses the right energy ratio distribution depending on the energy of the particle and its impact angle at ECAL2.

- **SPSmooth:** This method is called by the fit. It calculates from the histogram parameters the energy ratio which should have been seen by the particular cell at a certain cluster energy.
- **GetHistoParameter:** Method to read out the parameter values for a particular x and y position of the energy ratio histograms.
- **wASFit:** This method is a wrapper function for the shower fit function.

E.3 Various Distributions of the Electron Analysis

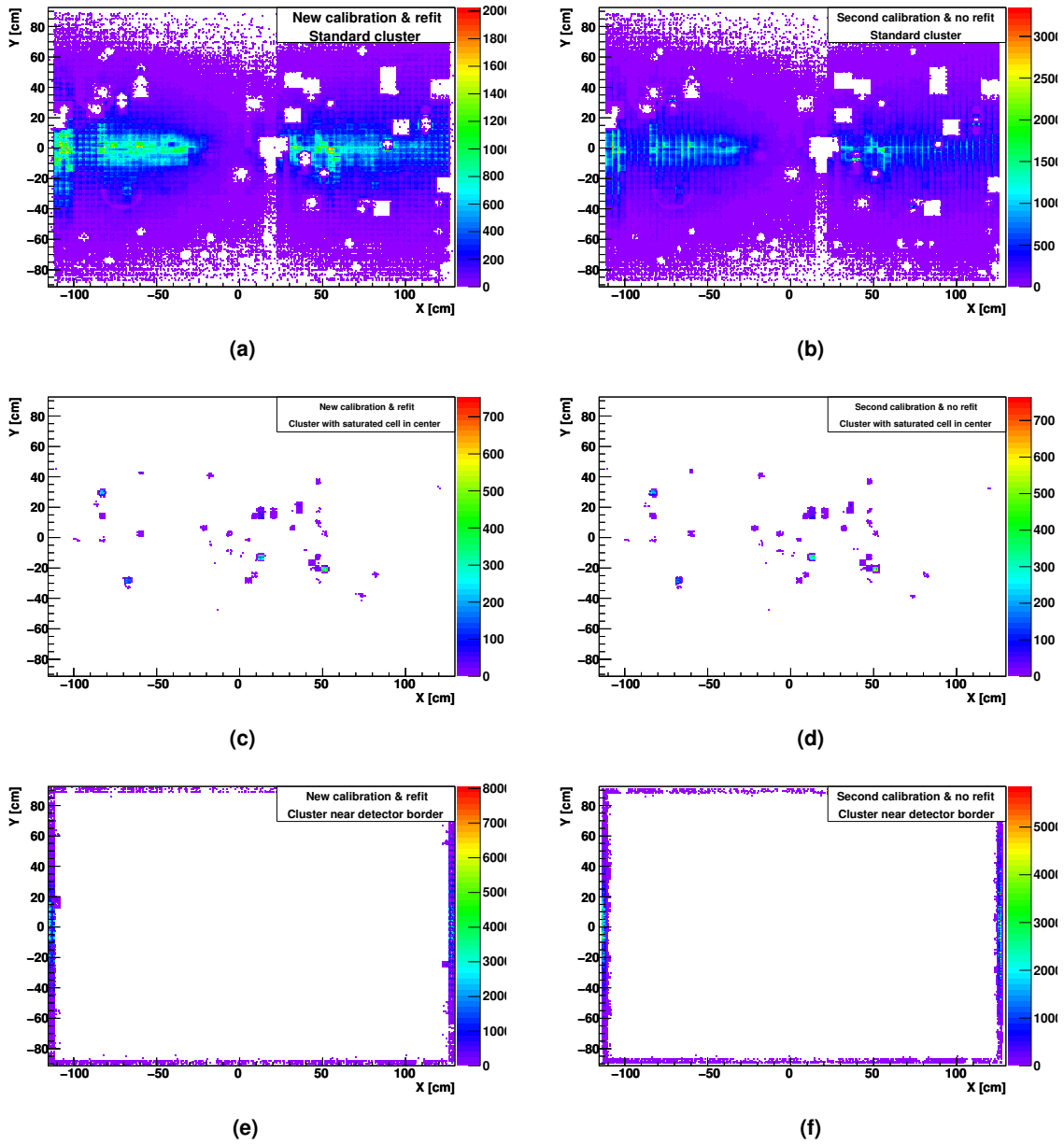


Figure E.2: Cluster position of 3 mm Pb-target period in ECAL2: (a) and (b) show standard clusters, (c) and (d) clusters with a saturated cell, (e) and (f) clusters close to the border. Right: Second calibration (position of primary calibration). Left: New calibration and cluster refit.

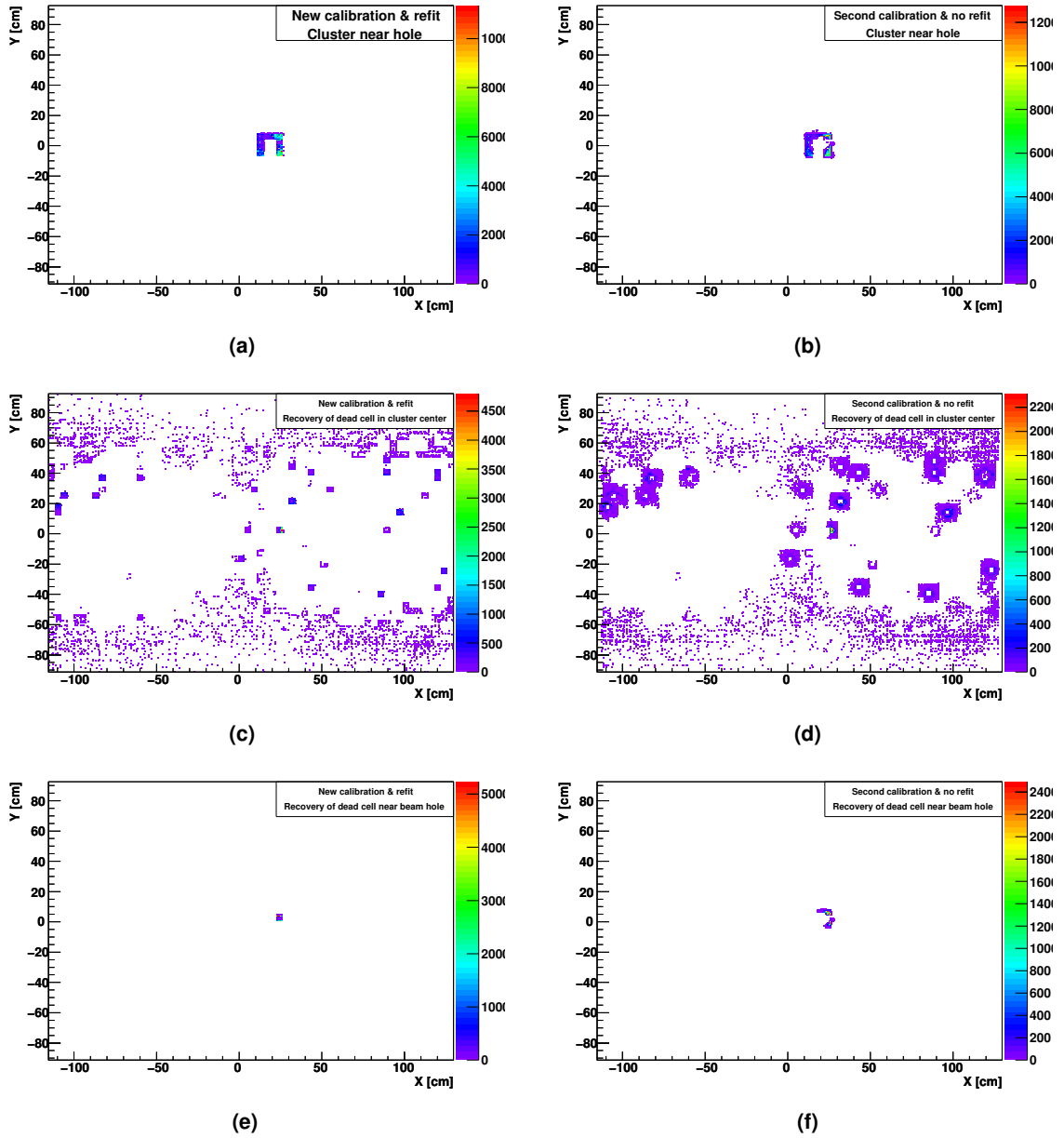


Figure E.3: Cluster position of 3 mm Pb-target period in ECAL2: (a) and (b) show clusters close to the beam hole, (c) and (d) clusters with a recovered dead cell in the centre, (e) and (f) recovery of the dead cell near the beam hole. Right: Second calibration (position of primary calibration). Left: New calibration and cluster refit.

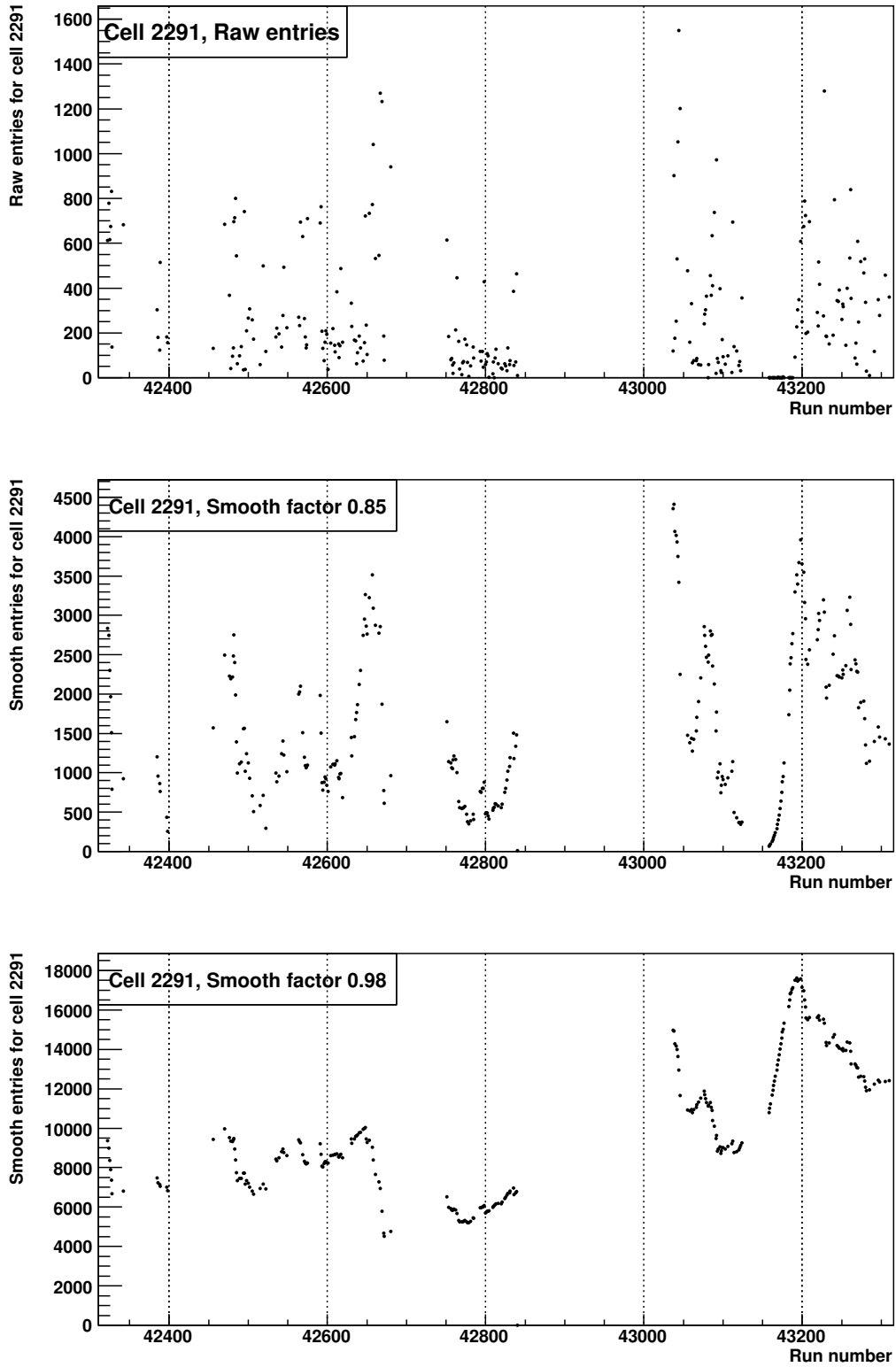


Figure E.4: Calibration statistics for cell 2291

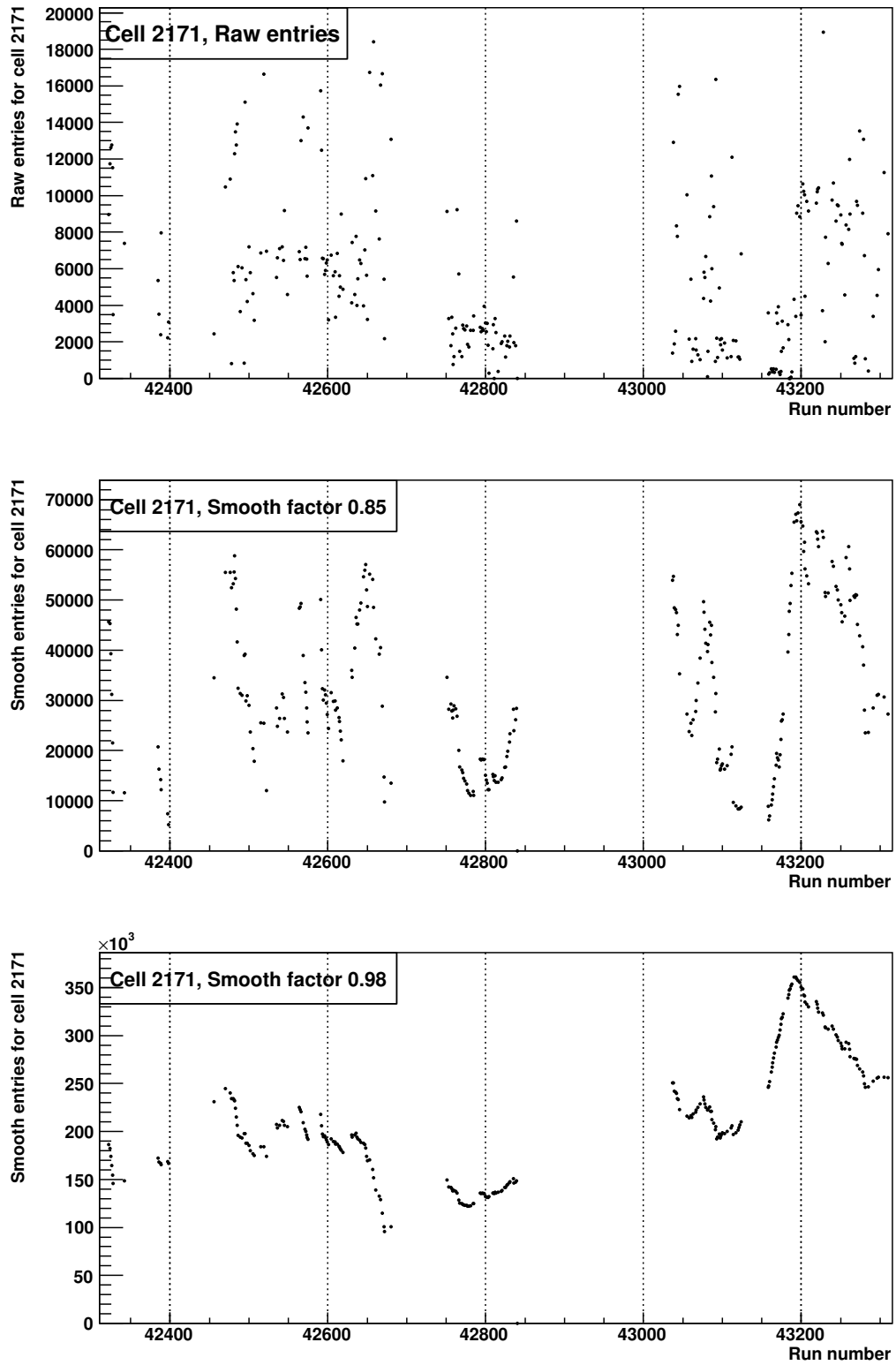


Figure E.5: Calibration statistics for cell 2171

Appendix F

Primakoff Statistics

Angle Bin [mrad]	Photon Energy [GeV]											
	40 < E < 60	60 < E < 80	80 < E < 100	100 < E < 120	120 < E < 140	140 < E < 160	160 < E < 180					
Pion (3 mm Pb target)												
5.0 < φ <= 8.0	5451	3889	2260	1815	1064	439	97					
2.5 < φ <= 5.0	4332	7082	8455	7481	5881	4070	1514					
1.5 < φ <= 2.5	3225	4929	5809	5737	6527	8390	4228					
1.0 < φ <= 1.5	2407	3801	4584	4173	3240	4451	4444					
0.7 < φ <= 1.0	1350	2511	3876	3277	2387	2369	2465					
0.4 < φ <= 0.7	1002	1869	3853	3908	2943	2020	1928					
0.2 < φ <= 0.4	350	581	1061	1141	1054	799	630					
Muon (2+1 mm Pb target)												
5.0 < φ <= 8.0	87	190	228	182	70	34	0					
2.5 < φ <= 5.0	279	946	1298	1039	756	323	49					
1.5 < φ <= 2.5	348	1636	2953	3015	2342	1450	304					
1.0 < φ <= 1.5	375	2103	4399	4267	3855	2883	971					
0.7 < φ <= 1.0	256	1745	5764	5137	4471	3806	1487					
0.4 < φ <= 0.7	164	1154	6537	8256	7126	5970	2392					
0.2 < φ <= 0.4	63	324	1798	2807	2995	2843	1012					

Table F.1: Statistics of Primakoff events of the pion and muon data on lead target in hadron run 2004.

List of Figures

The COMPASS Experiment

2.1	COMPASS muon spectrometer setup 2004	8
2.2	COMPASS hadron spectrometer setup 2004	8
2.3	COMPASS beam line	11
2.4	Schematic view of the hadron trigger system	14

The COMPASS Silicon Detector

3.1	Cross section of the silicon wafer	23
3.2	The silicon wafer surface of the n- and p-side	23
3.3	The COMPASS silicon detector module	24
3.4	Readout chain of the silicon detector	26
3.5	Scheme of the geometry of the silicon detector	28
3.6	A COMPASS detector station	29
3.7	Silicon stations in muon run 2004	31
3.8	Silicon stations in hadron run 2004	31

Characterisation of the COMPASS Silicon Detector

4.1	Signal current of a double-sided silicon strip detector	34
4.2	APV25 response to a δ -like signal shape	34
4.3	Walk of in-time signal ratios $r_{02}(t)$ and $r_{12}(t)$	36
4.4	Signal time structure determined by ratio functions	39
4.5	Amplitude ratio and signal plots for a latency scan	40
4.6	Commissioning phase of silicon detectors for COMPASS beam time	42
4.7	Correlation of amplitude ratios	43
4.8	χ^2 -distribution of after COOL alignment	44
4.9	Gauss fit on a amplitude ratio distribution	45
4.10	Stability of Gauss fits	45
4.11	Timing-fit on the signal amplitude ratio distribution	45
4.12	Effect of the calibration	46
4.13	Silicon cluster size for muon and hadron run 2004	48
4.14	Silicon cluster multiplicity for muon and hadron run 2004	48

LIST OF FIGURES

4.15	Signal amplitude for p- and n-side of muon run 2004	49
4.16	Correlation of signal amplitude and calculated time error	50
4.17	Charge distribution of silicon p- and n-planes	52
4.18	Effect of the cluster position correction	53
4.19	Silicon cluster time distributions	56
4.20	Calculated time error distributions	57
4.21	Timing and error distribution of the silicon telescope	58
4.22	Residuals for p- and n-side of muon and hadron run 2004	59
4.23	Residuals for p- and n-side and higher cluster sizes	60
4.24	Correlation between the signal amplitude and spatial resolution	61
Silicon Detectors in Hadron Run 2004		
5.1	Silicon hardware performance in hadron run 2004	64
5.2	Leakage current trending of SI05UV	65
5.3	Geometry for coordinate transformation	66
5.4	Residuals of silicon planes before and after alignment correction	68
5.5	Time trending of silicon planes in hadron run 2004	69
5.6	Target effect on pion scattering angle	71
5.7	Vertex position (in cm) of target region with COOOL	71
Calibration of the Electromagnetic Calorimeter		
6.1	Primakoff exclusivity peak for primary and second calibration set	74
6.2	Energy resolution with the primary calibration for different runs	74
6.3	Event selection for the shower model	80
6.4	Shower distribution	81
6.5	Selection of angle and energy bins for the shower model	83
6.6	2D- r -distribution of a particular angle and energy bin	84
6.7	Shower profile and single fit	85
6.8	r -distribution and its error after Gauss fit	86
6.9	Energy ratio distribution before and after symmetry exploitation	87
6.10	r -distribution after first smoothing	89
6.11	Summed energy ratio	90
6.12	r -distribution after energy correction	90
6.13	Distribution of the six parameters for r -distribution (large)	91
6.14	Distribution of the six parameters for r -distribution (zoom)	92
6.15	Correlation cluster energy and ADC-value	94
6.16	Position of tracks at ECAL2 after event selection for calibration	96
6.17	Trending of calibration value	96
6.18	Trending of LED based calibration	98

6.19	LED calibration comparison	99
6.20	Illustration for cluster fitting	101
6.21	Example of the cluster refit	103
6.22	Fit and calibration performance for standard cluster	106
6.23	Fit and calibration performance for clusters with saturated cells	107
6.24	Fit and calibration performance for clusters with a dead cell	108
6.25	Fit and calibration performance for clusters with a dead cell in the centre	109
6.26	Fit and calibration performance for clusters near the detector borders	110
6.27	Fit and calibration performance for clusters close at the beam hole	111
6.28	Fit and calibration performance for clusters with dead cell near beam hole	112
6.29	Cluster position at ECAL2 for clusters with dead cells	113
6.30	Correlation between the residual of the cluster and the detector position	114
6.31	Primakoff exclusivity peak for different ECAL2 calibrations	115
6.32	$E_\pi + E_\gamma$ for clusters with a dead cell in the cluster centre	116
6.33	Primakoff $\pi\gamma$ -invariant mass spectrum	116
6.34	Dependence of $E_\gamma + E_\pi$ on E_γ with different calibrations	118
6.35	Initial cluster position of Primakoff candidates	120
6.36	Refitted cluster position of Primakoff candidates	121
6.37	ECAL2 cell in saturation	123
6.38	Zoom into central part of ECAL2	123
6.39	Calibration trending over time for unstable cell 2191	124
6.40	Calibration trending over time for unstable cell 2117	124
6.41	Example Fit	125
6.42	Energy resolution for cluster with second calibration	126
6.43	Energy resolution for cluster refit	126
6.44	Spatial resolution in X for original cluster	127
6.45	Spatial resolution in X for cluster refit	127
6.46	Spatial resolution in Y for original cluster	128
6.47	Spatial resolution in Y for cluster refit	128
Pion Polarisability		
7.1	Classical analogon of the polarisabilities	132
7.2	Pion Compton scattering in the centre-of-mass system	132
7.3	Angular dependence of the Compton cross section	137
7.4	Pion Compton cross section	137
Data Analysis		
8.1	Vertex distribution as function of the pion scattering angle	140
8.2	Angular vertex resolution	140
		195

LIST OF FIGURES

8.3	p_{\perp} -distribution	141
8.4	Total energy distribution of the $\pi\gamma$ -system	142
8.5	Different kinematic distributions for pion and muon PCS	143
8.6	$R(x_{\gamma})$ obtained by the Serpukov experiment	146
8.7	Acceptance function $a(x_{\gamma})$ for Pb-target	146
8.8	Effect of He-gas pipe	146
8.9	Secondary vertex distributions of e^{\pm} along z-axis as function of R	148
8.10	Secondary vertices in the xy-plane for the RICH region	148
8.11	Secondary vertices in the xy-plane for the region in front of the RICH	148
8.12	Sketch of particles crossing He-gas pipe	149
8.13	Pion loss in RICH	149
8.14	Primakoff trigger efficiency	150
8.15	Zoom into central part of ECAL2	151
8.16	Efficiency of Primakoff Trigger	151
8.17	Q^2 and Q -distribution for different targets	153
8.18	Z^2 dependence of the Primakoff cross section	154
8.19	Pion Compton scattering cross section	155
8.20	Muon Compton scattering cross section	156
8.21	Primakoff events only with pions passing the RICH gas pipe	157
Appendix		
A.1	COMPASS coordinate systems	162
B.1	History of hadron run 2004	164
C.1	Photo of SI03 to SI05 in hadron run	167
C.2	Photo of SI01 and SI02 in hadron run	168
E.1	Cell configuration of ECAL2 in COMPASS hadron run 2004	179
E.2	Cluster position at ECAL2 for different calibrations and cluster types I	186
E.3	Cluster position at ECAL2 for different calibrations and cluster types II	187
E.4	Calibration statistics for cell 2291	188
E.5	Calibration statistics for cell 2171	189

List of Tables

The COMPASS Experiment

2.1	Beam parameters	12
2.2	Target configurations for hadron pilot run in 2004	13

The COMPASS Silicon Detector

3.1	Silicon modules in muon beam	30
3.2	Silicon modules in hadron beam	30

Characterisation of the COMPASS Silicon Detector

4.1	Spatial and time resolution of the silicon detectors	62
-----	--	----

Silicon Detectors in Hadron Run 2004

5.1	Production problems of silicon detectors	64
5.2	High voltage settings in hadron run	65

Calibration of the Electromagnetic Calorimeter

6.1	Properties of different lead glass types	76
6.2	Exploited shower symmetries	88
6.3	Shower symmetries for higher energy-bins	88
6.4	Cell and cluster errors applied for cluster fit	102
6.5	Number of Primakoff events for all periods	117
6.6	Energy and spatial resolution of ECAL2	129

Pion Polarisability

7.1	Experimental and predicted values for the pion polarisabilities	134
-----	---	-----

Data Analysis

8.1	Primakoff selection cuts	141
-----	------------------------------------	-----

Appendix

B.1	History of hadron run 2004	165
B.2	Detector list of 2004 hadron run	166
C.1	Position and module names of silicon stations in 2004 - 2006	169
D.1	Tracking configurations for silicon telescope in COOL	173

LIST OF TABLES

D.2	Example text file with time calibrations	174
D.3	Time calibration values for pilot hadron run 2004	176
D.4	CORAL options	177
E.1	List of angle bins for shower model	181
E.2	List of energy bins for shower model	181
E.3	List of the values in the calibration files	182
E.4	List of runs with LED information	183
E.5	List of runs with new calibration values	183
F.1	Primakoff statistics	192

Bibliography

- [Abt96] I. Abt et al. Irradiation tests of double-sided silicon strip detectors with a special guard ring structure. *IEEE Trans. Nucl. Sci.* **43**, 1113–1118 (1996).
(Cited on page 22.)
- [Abt00] I. Abt et al. Double-sided microstrip detectors for the high radiation environment in the HERA-B experiment. *Nucl. Instrum. Meth.* **A439**, 442–450 (2000).
(Cited on page 22.)
- [AG68] Henry D. I. Abarbanel and Marvin L. Goldberger. Low-energy theorems, dispersion relations, and superconvergence sum rules for Compton scattering. *Phys. Rev.* **165** 5, 1594–1609 Jan 1968.
(Cited on page 133.)
- [Ald85] D. Alde et al. Acquisition system for the hodoscope spectrometer GAMS-4000. *Nucl. Instr. Meth.* **A 240**, 343–362 (1985).
(Cited on page 77.)
- [Ald86] D. Alde et al. Production of $g(1590)$ and other mesons decaying into η pairs by 100 GeV/c π^- on protons. *Nucl. Phys.* **B 269**, 485–508 (1986).
(Cited on page 77.)
- [Ang03] H. Angerer et al. Present status of silicon detectors in COMPASS. *Nucl. Instr. Meth.* **A 512**, 229–238 (2003).
(Cited on pages 27 and 37.)
- [Ant83] Yu. M. Antipov et al. Measurement of π^- meson polarizability in pion Compton effect. *Phys. Lett.* **B121**, 445 (1983).
(Cited on pages 135, 145, and 154.)
- [Ant85] Yu. M. Antipov et al. Experimental estimation of the sum of pion electric and magnetic polarizabilities. *Z. Phys.* **C26**, 495 (1985).
(Cited on pages 135, 145, and 154.)
- [Ant86] Yu. M. Antipov et al. Investigation of Compton-effect on π -meson and charged pion polarizability. *JINR preprint* **P1-86-710** (1986).
(Cited on page 145.)
- [Bat70] G. Bathow et al. Measurements of the longitudinal and lateral development of electromagnetic cascades in lead, copper and aluminum at 6 GeV. *Nucl. Phys.* **B 20**, 592 (1970).
(Cited on page 75.)
- [Bau00] C. Bauer et al. The HERA-B vertex detector system. *Nucl. Instrum. Meth.* **A453**, 103–108 (2000).
(Cited on page 22.)

BIBLIOGRAPHY

- [Bau02] C. Bauer et al. Radiation hardness of the HERA-B double-sided silicon strip detectors. *Nucl. Instrum. Meth.* **A485**, 116–120 (2002). (Cited on page 22.)
- [Bec04] M. Becker. *Setup of a Cryogenic System for Silicon Microstrip Detectors in the COMPASS Experiment*. Diploma thesis, Technische Universität München, September 2004. (Cited on pages 29 and 32.)
- [Bed04] Y. Bedfer et al. COMPASS’s track reconstruction algorithm. *COMPASS Note 2004-1* (2004). (Cited on page 175.)
- [Bed06] Y. Bedfer, yann.bedfer@cern.ch. Private communication, 2006. (Cited on page 177.)
- [Ber04] C. Bernet. *Caractérisation des Micromégas et mesure de la polarisation des gluons sur COMPASS (in french)*. PhD thesis, Université Paris 7 - Denis Diderot, 2004. (Cited on page 17.)
- [Bin81] F. Binon et al. Hodoscope gamma spectrometer GAMS-200. *Nucl. Instr. Meth.* **188**, 507–516 (1981). (Cited on page 77.)
- [Bov82] C. Bovet et al. The cedar counters for particle identification in the sps secondary beams: A description and an operation manual. **CERN 82-13** (1982). (Cited on page 13.)
- [Bru97] R. Brun and F. Rademakers. ROOT: An object oriented data analysis framework. *Nucl. Inst. Meth.* **A389**, 81 (1997). (Cited on page 17.)
- [Bur96a] U. Burgi. Charged pion polarizabilities to two loops. *Phys. Lett.* **B377**, 147–152 (1996). (Cited on page 132.)
- [Bur96b] U. Burgi. Pion polarizabilities and charged pion pair production to two loops. *Nucl. Phys.* **B479**, 392–426 (1996). (Cited on page 133.)
- [CAS] CASTOR. Home page, <http://castor.web.cern.ch>. (Cited on page 16.)
- [CMS] CMS. Home page, <http://cmsinfo.cern.ch>. (Cited on page 25.)
- [Col05] M. L. Colantoni. Measurement of electric and magnetic polarizabilities with Primakoff reaction at COMPASS. *Czech. J. Phys* **55** (2005). (Cited on page 145.)
- [COM] COMgeant: COMpass monte carlo simulation program based on geant3, <http://valexakh.web.cern.ch/valexakh/wwwcomg/index.html>. (Cited on page 17.)
- [COM96] The COMPASS collaboration. A proposal for a Common Muon and Proton Apparatus for Structure and Spectroscopy. **CERN SPSLC 96-14** (1996). (Cited on pages 3 and 22.)
- [COM05a] The COMPASS collaboration. First measurement of the transverse spin asymmetries of the deuteron in semi-inclusive deep inelastic scattering. *Physical Review Letters* **94**, 202002 (2005). (Cited on page 6.)

- [COM05b] The COMPASS collaboration. Measurement of the spin structure of the deuteron in the dis region. *Physics Letters B* **612**, 154–164 (2005). (Cited on page 5.)
- [COM06] The COMPASS collaboration. Gluon polarization in the nucleon from quasi-real photoproduction of high-pT hadron pairs. *Physics Letters B* **633** **1**, 25–33 February 2006. (Cited on page 5.)
- [COM07a] The COMPASS collaboration. The COMPASS experiment at CERN. *Nucl. Inst. Meth. A* **577**, 455–518 (2007). (Cited on pages 7, 16, 26, 76, 77, 78, 125, 129, and 166.)
- [COM07b] The COMPASS collaboration. The deuteron spin-dependent structure function g_1^d and its first moment. *Physics Letters B* **647**, 8–17 (2007). (Cited on page 5.)
- [COM07c] The COMPASS collaboration. A new measurement of the collins and sivers asymmetry on a transversely polarized deuteron target. *Nuclear Physics B* **765**, 31–70 (2007). (Cited on page 6.)
- [COM07d] The COMPASS collaboration. Spin asymmetries A_1^d and the spin-dependent structure functions g_1^d of the deuteron at low values of x and Q^2 . *Physics Letters B* **647**, 330–340 (2007). (Cited on page 5.)
- [COM08a] The COMPASS collaboration. Direct measurement of the gluon polarisation in the nucleon via charmed meson production. *submitted to Physical Review Letters* **CERN-PH-EP/2008-003**, arXiv:0802.3023v1 (2008). (Cited on page 5.)
- [COM08b] The COMPASS collaboration. The polarised valence quark distribution from semi-inclusive DIS. *Physics Letters B* **660**, 458–465 (2008). (Cited on page 5.)
- [COM09a] The COMPASS collaboration. Collins and Sivers asymmetries for pions and kaons in muon-deuteron DIS. *Physics Letters B* **673**, 127–135 (2009). (Cited on page 6.)
- [COM09b] The COMPASS collaboration. Flavour separation of helicity distributions from deep inelastic muon-deuteron scattering. *accepted by Physics Letters B* **CERN-PH-EP/2009-008**, arXiv:0905.2828v1 (2009). (Cited on page 5.)
- [COM09c] The COMPASS collaboration. Gluon polarisation in the nucleon and longitudinal double spin asymmetries from open charm muoproduction. *Physics Letters B* **676**, 31–38 (2009). (Cited on page 5.)
- [COM09d] The COMPASS collaboration. Measurement of the longitudinal spin transfer to Λ and $\bar{\Lambda}$ hyperons in polarised muon DIS. *accepted by European Physics Journal C* **CERN-PH-EP/2009-011**, arXiv:0907.0388v1 (2009). (Cited on page 6.)
- [COM10] The COMPASS collaboration. COMPASS-II Proporsal. *CERN-SPSC-2010-014 ; SPSC-P-340* (2010). (Cited on pages 132 and 159.)

BIBLIOGRAPHY

- [COO] C. Bernet. COOOL: COmpass Objectoriented Online, <http://cbernet.home.cern.ch/cbernet/Cool>. (Cited on page 17.)
- [COR] CORAL: COmpass Reconstruction and AnaLysis program, <http://coral.web.cern.ch/coral>. (Cited on pages 18 and 175.)
- [Dav03] G. David et al. PHENIX calorimeter. *Nucl. Instr. and Meth.* **A 499**, 521–536 (2003). (Cited on page 76.)
- [DeM04] R. De Masi. *Development of a cryogenic silicon detector system and study of strange particle production in deep inelastic scattering*. Ph.D. thesis, Technische Universität München, November 2004. (Cited on pages 26, 27, and 32.)
- [Din03] A.-M. (Fuchs) Dinkelbach. *Setup of a low Temperature Silicon Detector for the COMPASS Experiment*. Diploma thesis, Technische Universität München, December 2003. (Cited on pages 27, 32, and 44.)
- [Evd05] A.V. Evdokimov et al. The lead-glass electromagnetic calorimeter for the selex experiment. *Nucl. Instr. and Meth.* **A 545**, 114–138 (2005). (Cited on page 76.)
- [Fer05] A. Ferrero. Soft hadronic interactions in the compass experiment. *Czech. J. Phys* **55** (2005). (Cited on page 12.)
- [FK06] L. V. Fil'kov and V. L. Kashevarov. Determination of π^\pm meson polarizabilities from the $\gamma\gamma \rightarrow \pi + \pi^-$ process. *Phys. Rev. C* **73 3**, 035210 Mar 2006. (Cited on page 133.)
- [Fri04] J. Friedrich, Jan.Friedrich@physik.tu-muenchen.de. Private communication, 2004. (Cited on page 36.)
- [Fri10] J. M. Friedrich. *Habilitation in preparation*. Habilitation thesis, Technische Universität München, December 2010. (Cited on pages 27, 32, 136, and 137.)
- [FT07] Göran Fäldt and Ulla Tengblad. Hard pion bremsstrahlung in the coulomb region. *Phys. Rev. C* **76 6**, 064607 Dec 2007. (Cited on page 144.)
- [Gat01] L. Gatignon. User guide for m2 beam, <http://gatignon.home.cern.ch/gatignon/M2manual.html>. (Cited on pages 11 and 12.)
- [GIS06] J. Gasser, M. A. Ivanov, and M. E. Sainio. Revisiting $\gamma\gamma \rightarrow \pi^+\pi^-$ at low energies. *Nucl. Phys.* **B745**, 84–108 (2006). (Cited on pages 132, 133, and 134.)
- [GL84] J. Gasser and H. Leutwyler. Chiral Perturbation Theory to One Loop. *Ann. Phys.* **158**, 142 (1984). (Cited on page 132.)
- [Gra09] S. Grabmüller, sgrabmue@e18.physik.tu-muenchen.de. Private communication, 2009. (Cited on page 30.)
- [Gra10] S. Grabmüller. *Ph. D. Thesis in Preparation*. Ph. d. thesis, Technische Universität München, December 2010. (Cited on page 32.)

- [Gri90] G. Grindhammer et al. The fast simulation of electromagnetic and hadronic showers. *Nucl. Instr. Meth. A* **290**, 469–488 (1990). (Cited on page 75.)
- [Gru01] B. Grube. *The Trigger Control System and the common GEM and Silicon Read-out for the COMPASS Experiment*. Diploma thesis, Technische Universität München, December 2001. (Cited on page 26.)
- [Gru06] B. Grube. *A Trigger System for COMPASS and A Measurement of the Transverse Polarization of Λ and Ξ Hyperons from Quasi-Real Photo-Production*. Ph.D. thesis, Technische Universität München, March 2006. (Cited on pages 6, 11, 16, 25, and 26.)
- [Gus10] A. Guskov. *Analysis of the charged pion polarisability measurement method at COMPASS experiment*. Ph.D. thesis, Universita degli Studi Torino, Jan 2010. (Cited on pages 134, 140, 145, 146, and 154.)
- [GVE93] M. A. Ivanov G. V. Efimov. *The quark confinement model of hadrons*. IOP Publishing Ltd., Bristol, 1993. (Cited on page 133.)
- [IM92] M. A. Ivanov and T. Mizutani. Pion and kaon polarizabilities in the quark confinement model. *Phys. Rev. D* **45** 5, 1580–1601 Mar 1992. (Cited on page 133.)
- [Jon] L. L. Jones et al. The APV25 deep submicron readout chip for CMS detectors. . Prepared for 5th Workshop on Electronics for the LHC Experiments (LEB 99), Snowmass, Colorado, 20-24 Sep 1999. (Cited on pages 24 and 25.)
- [KF08a] N. Kaiser and J. M. Friedrich. Cross sections for low-energy $\pi^- \gamma$ reactions. *Eur. Phys. J.* **A36**, 181–188 (2008). (Cited on pages 134, 135, 136, and 138.)
- [KF08b] N. Kaiser and J. M. Friedrich. Radiative corrections to pion Compton scattering. *Nucl. Phys.* **A812**, 186–200 (2008). (Cited on page 138.)
- [KF09] N. Kaiser and J. M. Friedrich. Radiative corrections to pion-nucleus bremsstrahlung. *Eur. Phys. J.* **A39**, 71–80 (2009). (Cited on pages 135 and 138.)
- [Kol06] V. Kolossov, vkolosov@mail.cern.ch. Private communication, 2006. (Cited on pages 73, 78, and 104.)
- [Kol09] V. Kolossov, vkolosov@mail.cern.ch. Private communication, 2009. (Cited on page 79.)
- [Kuh01] R. Kuhn. *Simulations for the Measurement of the Polarizabilities of the Pion at COMPASS*. Diploma thesis, Technische Universität München, November 2001. (Cited on page 145.)
- [Kuh07] R. Kuhn. *A Measurement of Spin Asymmetries in Quasi-Real Photo-Production of Hadrons with High Transverse Momentum at COMPASS*. Ph. d. thesis, Technische Universität München, October 2007. (Cited on page 16.)

BIBLIOGRAPHY

- [Led95] A. Lednev. Electron shower transverse profile measurement. *Nucl. Instr. Meth. A* **366**, 292 (1995). (Cited on page 78.)
- [Leo94] W. R. Leo. *Techniques for nuclear and particle physics experiments*. Springer, 1994. (Cited on page 21.)
- [Nag05] T. Nagel. *Cinderella: An Online Filter for the COMPASS Experiment*. Diploma thesis, Technische Universität München, January 2005. (Cited on pages 16, 37, 40, and 62.)
- [Nel66] W. R. Nelson et al. Electron-induced cascade showers in copper and lead at 1 gev. *Phys. Rev.* **149**, 201 (1966). (Cited on page 75.)
- [Pal98] V. Palmieri et al. Evidence for charge collection efficiency recovery in heavily irradiated silicon detectors operated at cryogenic temperatures. *Nucl. Instr. and Meth. A* **413**, 475–478 (1998). (Cited on page 32.)
- [PDG06] Particle Data Group. Review of particle physics. *Journal of Physics G* **33**, 1 (2006). (Cited on pages 33, 74, 75, and 76.)
- [Pei92] A. Peisert. Silicon microstrip detectors. *Adv. Ser. Direct. High Energy Phys.* **9**, 1–79 (1992). (Cited on pages 21, 46, 47, and 51.)
- [PHA] S. Gerassimov. PHAST: PHysics Analysis Software Tool, <http://ges.home.cern.ch/ges/phast>. (Cited on page 67.)
- [Po92] W. H. Press and other. *Numerical recipes in C*. Cambridge University Press, 1992. (Cited on page 102.)
- [Pol07] V. Poliakov, Vladimir.Poliakov@cern.ch. Private communication, 2007. (Cited on page 179.)
- [Pug99] V. M. Pugatch et al. Radiation hardness of the HERA-B silicon microstrip detectors. *Nuovo Cim.* **112A** (1999). (Cited on page 22.)
- [RIC] S. Dalla Torre. Rich 1 - materials and radiation length, http://wwwcompass2.cern.ch/compass/detector/rich/rich_locked/radlength.html. (Cited on page 147.)
- [Ric96] R. H. Richter et al. Strip detector design for ATLAS and HERA-B using two-dimensional device simulation. *Nucl. Instrum. Meth.* **A377**, 412–421 (1996). (Cited on page 22.)
- [Rie98] K. Riechmann. *Einsatz von Siliziumdetektoren in der Hochstrahlungsumgebung von HERA-B*. Phd thesis, MPI für Physik, Technische Universität München, November 1998. (Cited on page 22.)
- [ROO] R. Brun, F. Rademakers, et al. ROOT home page, <http://root.cern.ch>. (Cited on page 17.)

- [Ros65] B. Rossi. *High Energy Particles*. Prentice Hall, 1965. (Cited on page 75.)
- [Rud92] R. Rudolph. *Aufbau eines elektromagnetischen Kalorimeters und Messung der Polarisation inklusiv produzierter Λ^0 und Σ^+* . Ph.D. thesis, Universität Mainz, November 1992. (Cited on page 75.)
- [Sch03] S. Scherer. Introduction to Chiral Perturbation Theory. *Adv.Nucl.Phys.* **27**, 277 (2003). (Cited on page 131.)
- [See04] D. Seeharsch. *A Microcontroller based Steering Mechanism for the COMPASS Silicon Detector Cooling System*. Schriftliche Hausarbeit, Technische Universität München, August 2004. (Cited on page 32.)
- [Sin97] R. W. Bernstein and T. Westgaard. Technical and test specifications for MPI HERA-B doublesided silicon. Technical report, SINTEF Electronics & Cybernetics, 1997. (Cited on page 22.)
- [SP95] W. Schmidt-Parzefall. HERA-B: An Experiment to study CP violation at the HERA proton ring using an internal target. *Nucl. Instrum. Meth.* **A368**, 124–132 (1995). (Cited on page 22.)
- [Spi05] H. Spieler. *Semiconductor Detector Systems*. Oxford Science Publications, 2005. (Cited on pages 21, 33, and 34.)
- [Tri] Compass hadron analysis wiki, <http://lxfsr6103.cern.ch/twiki/bin/view/HadronAnalysis/Trigger>. (Cited on page 15.)
- [Tsa74] Y. S. Tsai. Pair production and bremsstrahlung of charged leptons. *Rev. Mod. Phys.* **46**, 815–851 (1974). (Cited on page 74.)
- [Wag01] R. Wagner. *Commissioning of Silicon Detectors for the COMPASS Experiment at CERN*. Diploma thesis, Technische Universität München, December 2001. (Cited on pages 27 and 40.)
- [Wie04] M. Wiesmann. *A Silicon Microstrip Detector for COMPASS and a first Measurement of the transverse Polarization of Λ -Hyperons from quasi-real Photo-Production*. Ph.D. thesis, Technische Universität München, February 2004. (Cited on pages 6, 16, 26, 27, 32, and 34.)
- [Wik] Wikipedia, <http://www.wikipedia.org>. (Cited on page 25.)

Own contributions

Within this Ph.D. thesis I continued my work on the COMPASS silicon detectors of my diploma thesis. I took over the project in 2004 from the preceding Ph.D. students Michael Wiesmann and Rita De Masi.

For the hadron pilot run in 2004 two more detector stations (and a spare station) had to be built beside the three existing ones. Under my guidance the new detectors were produced. This included the assembly of the silicon modules at an external company, the manufacturing of all cables, cryostats and mechanical components. Igor Konorov provided all electronic components. Assistance came from the diploma student Matthias Becker, who helped in commissioning these new detectors both in our lab and at CERN. The new detectors had to be adapted to all existing frameworks, DAQ, data-base, safety system etc. .

I implemented the correct treatment of the time information of the silicon detectors (at first used by the online-filter) in the analysis software CORAL as well as corrections on the charge sharing. I realized the fruitful ideas and advises from Jan Friedrich concerning the characterisation of the silicon detectors, particularly the silicon time calibration and realignment of the beam telescope in the hadron run 2004.

For 2004 and 2006 muon beam time, I set up the three silicon detector stations and provided all necessary calibrations. I took regularly shift-duties for the complete spectrometer operation and was in charge as "expert on call" for GEM and silicon detectors for several weeks per year.

Under the supervision of Stephan Paul and Jan Friedrich, I started the analysis of determining the pion polarisabilities. During this analysis it turned out that a better understanding of the electromagnetic calorimeter was necessary. Under their guidance I recalibrated for 269 runs the 3068 cells of the calorimeter with already processed data of the hadron run 2004. The new calibration is based on a data-driven shower model. Besides the new calibration I developed a fit procedure which is based on this shower model, in order to refit the calorimeter clusters. I studied the stability of the calorimeter cells, analysed the LED signals and their potential for a run-dependent calibration. With the new cluster fit, I was able to recover clusters with unstable or dead cells. I extracted Primakoff candidates from the hadron data 2004 and I presented the necessary steps to obtain the pion polarisabilities. The measurement of the pion polarisabilities was limited by systematic effects of the apparatus, in particular I studied also the influences of the He-gas pipe of the RICH detector and a trigger inefficiency.

Acknowledgements

Thanks to Stephan Paul for giving me the opportunity to work in the COMPASS collaboration, letting study me an interesting topic and for his support and patience while finishing this work.

Thanks to Jan Friedrich for his extraordinary engagement, his guidance, fruitful ideas and showing me fun in physics and calibration issues. I really learned a lot from him.

Thanks to my silicon colleagues, Steffi Grabmüller and Matthias Becker, for the excellent team work.

Thanks to Igor Konorov and Heinz Angerer for their support during the annual commissioning of the silicon detectors.

Thanks to the COMPASS collaboration for the interesting discussions and the team spirit.

Thanks to Martin Aigner and all his colleagues from the machine shop for their great work and support.

Thanks to Roland, Boris, Thiemo, Alexander and Markus for your patience in answering my various computer and programming related questions. Boris, thanks for your \TeX framework used for this thesis.

Thanks to Matthias, Rita, Boris, Alexander, Steffi, Daniele and Suh-Urk, it was a pleasure sharing the office with you.

Thanks to all technical students who made work easier.

Thanks to all members of E18 for the nice time. I appreciated the warm and friendly atmosphere at E18. Special thanks to Karin.

Thanks to my colleagues at Prüftechnik Alignment Systems for their support while finishing this thesis.

Danke sage ich meiner Familie und meinen Eltern, die mich immer gefördert und darin bestärkt haben meinen Interessen nachzugehen.

Danke lieber Horst, für Dein Verständnis, Deine Ausdauer, Deine Unterstützung und Deine Liebe.